Time-domain Compressive Beamforming for Medical Ultrasound Imaging

Guillaume David

Submitted in partial fulfillment of the
requirements for the degree of
Doctor of Philosophy
in the Graduate School of Arts and Sciences

Columbia University

2017

ABSTRACT

Time-domain Compressive Beamforming

for Medical Ultrasound Imaging

Guillaume David

Over the past 10 years, Compressive Sensing has gained a lot of visibility from the medical imaging research community. The most compelling feature for the use of Compressive Sensing is its ability to perform perfect reconstructions of under-sampled signals using l_1-minimization. Of course, that counter-intuitive feature has a cost. The lacking information is compensated for by *a priori* knowledge of the signal under certain mathematical conditions. This technology is currently used in some commercial MRI scanners to increase the acquisition rate hence decreasing discomfort for the patient while increasing patient turnover. For echography, the applications could go from fast 3D echocardiography to simplified, cheaper echography systems.

Real-time ultrasound imaging scanners have been available for nearly 50 years. During these 50 years of existence, much has changed in their architecture, electronics, and technologies. However one component remains present: the beamformer. From analog beamformers to software beamformers, the technology has evolved and brought much diversity to the world of beam formation. Currently, most commercial scanners use several focalized ultrasonic pulses to probe tissue. The time between two consecutive focalized pulses is not compressible, limiting the frame rate. Indeed, one must wait for a pulse to propagate back and forth from the probe to the deepest point imaged before firing a new pulse.

In this work, we propose to outline the development of a novel software beamforming technique that uses Compressive Sensing. Time-domain Compressive Beamforming (t-CBF) uses computational models and regularization to reconstruct de-cluttered ultrasound images. One of the main features of t-CBF is its use of only one transmit wave to insonify the

tissue. Single-wave imaging brings high frame rates to the modality, for example allowing a physician to see precisely the movements of the heart walls or valves during a heart cycle. t-CBF takes into account the geometry of the probe as well as its physical parameters to improve resolution and attenuate artifacts commonly seen in single-wave imaging such as side lobes.

In this thesis, we define a mathematical framework for the beamforming of ultrasonic data compatible with Compressive Sensing. Then, we investigate its capabilities on simple simulations in terms of resolution and super-resolution. Finally, we adapt t-CBF to real-life ultrasonic data. In particular, we reconstruct 2D cardiac images at a frame rate 100-fold higher than typical values.

Contents

List of Figures

List of Tables

Acknowledgments

This work was funded by the Van der Pol Award from Philips Research North America.

Preface

I discovered the fascinating world of medical imaging while I was studying at ESPCI Paris where I had the opportunity to work at the LANGEVIN Institute under the supervision of Professor Claude BOCCARA. He introduced me to Optical Coherence Tomography and its application to monitoring sentinel lymph nodes in breast cancer patients. This project instilled a sense of purpose in me that hasn't left since.

After a few more experiences in medical imaging at Philips Research North America and Columbia University, I was awarded the VAN DER POL Fellowship from Philips Research to pursue a PhD in Biomedical Engineering at Columbia University where I had the opportunity to work alongside bright and motivated people.

For five years I worked on computational methods that would allow a more efficient use of the information provided by echography. Namely, the goal of this work was to increase the frame rate of the modality without impacting the image quality. It is one of the many challenges ultrasound imaging faces today. High frame rates are necessary to detect the subtle and fast movements of the different parts of the beating heart. It would allow for a better and earlier diagnostic of cardiovascular disease and positively impact the many people affected every year. Unfortunately, increasing the frame rate means losing resolution in the current framework. Thus my work was to define a new framework that would preserve resolution while increasing the frame rate using computational methods.

Many people made this difficult task possible. The following is a brief list of the persons I would like to acknowledge.

Doctor Jean-luc ROBERT from Philips Research gave me the opportunity to collaborate with an industry leader in the field of ultrasound imaging. He has been my greatest supporter and advisor throughout the years. Professor Andrew F. LAINE gave me the honor of accepting me in the HEFFNER Biomedical Imaging Lab and being my dissertation sponsor.

Doctor Michael PASHLEY, Head of the Ultrasound Imaging and Interventions department at Philips Research, awarded me the VAN DER POL Fellowship that supported my work for five years.

I have had the pleasure of working alongside great colleagues and friends at the HEFFNER Biomedical Imaging Lab. In particular, Doctor Viktor GAMARNIK and Doctor Yrjö HÄME have had a tremendous positive influence in-and-outside the lab, as well as an unfaltering support in both my work and my personal life. Doctor Antonio ALBANESE, Doctor Arthur MIKHNO, Doctor Jack PO, Doctor Frank PROVENZANO, and Nikolaos KARAMOLEGKOS have also been of great help and made going to work every day all the more enjoyable.

Several people at Philips Research also influenced me during lunchtime or hallway conversations: Doctor Ladislav YANKOVIC, Doctor Emil RADULESCU, Doctor François VIGNON, Doctor Sheng-Wen HUANG, Doctor Nick CHBAT, Doctor Francesco VICARIO, Roberto BUIZZA, Viktor GORNSTEIN, Flavia WHITE.

Thomas DELOR, Christophe WILHELM, and Jacem JOOBEUR have been great friends and even greater support over the years.

All of this would not have been possible without the support of my parents Denis and Michèle DAVID, as well as my brother Thomas.

Finally, the most important person has been my lovely fiancée Glynnis KING-ANCEL. She proofread all this work, offering corrections and suggestions, and her unwavering support and patience have been extremely comforting in the most challenging times.

I owe a great deal of gratitude to each and every person mentioned here, and I thank you from the bottom of my heart.

Oh, and our three cats Al, Estella, and Gil, as well.

Guillaume David

December 18, 2016

Chapter 1

Introduction: Ultrasounds in medicine

1.1 A brief history

Researchers started working on ultrasounds during World War I as a technique to reliably detect German submarines. Nearly 40 years earlier, Pierre and Jacques Curie had discovered the piezoelectric effect [1]: a class of crystals that has the ability to deform and vibrate under an electric current, and that can produce an electric current when deformed. Paul Langevin and Constantin Chilowski used this effect to generate ultrasonic waves in water and detect subsequent echoes [2]. The innovation that resulted from this research, the SONAR system, could indeed detect German submarines and was therefore quickly classified. At the end of the war, the interest for ultrasound technology seemed to fade and research on ultrasound imaging slowed down.

The interest for ultrasound imaging was revived in 1942 when Dr. Karl Theo Dussik, an Austrian medical doctor, published a founding paper on using ultrasounds for diagnostic purposes [3]. He called his technique "hyperphonography" and used it to make images of the human brain [4] by transmission of ultrasonic waves through the skull. However, even though Dussik believed he was imaging the ventricles of his patients' brain, researchers at MIT showed that his images were the result of artifacts. They proved that similar images could be obtained from an empty skull in a water bath [5]. The structures DUSSIK uncovered were the result of multiple reflection on the skull and the wall of the water tank he was using. This discover was an important setback for the development of diagnostic ultrasound techniques.

Meanwhile, a Scottish researcher named Ian DONALD tried using an ultrasonic metal flaw detector to differentiate a cyst from a myoma in the human body. The idea came to him after he observed such an apparatus being used in the Glasgow shipyards. The successful experiment eventually led to one of the founding papers on medical ultrasounds [6].

The basis of ultrasound imaging as we know it today was introduced to the medical world in the late 1940s by Dr. George D. LUDWIG from the Naval Medical Research Institute in Bethesda, Maryland. Originally described as a method to detect and localize gallstones and other foreign bodies in soft tissues of the body [7] superseding X-ray imaging, this revolutionary technique used reflection of ultrasonic pulses. It quickly evolved to become the modality of choice in obstetrics, pediatrics, and cardiology.

1.2 EMERGENCE OF BEAMFORMING

Before the mid-1970s, scanners used single element probes and displayed a 1D signal showing the amplitude of the echoes as a function of depth (figure 1.1). This ultrasound mode is known as A-mode, the "A" standing for amplitude. This type of scan does not need any kind of beamforming.

Around the same time, M-mode scanning (M for motion) appeared. It is obtained by displaying the traces of the peaks of the A-lines swept in time (figure 1.2).

Starting around 1975, transducer arrays were developed in an effort to produce true 2D images of a section of tissue. Ultrasonic arrays allow focusing and steering of beams by finely controlling the delays between the elements.

From figure 1.3, one can understand how the technology moved from a single transducer

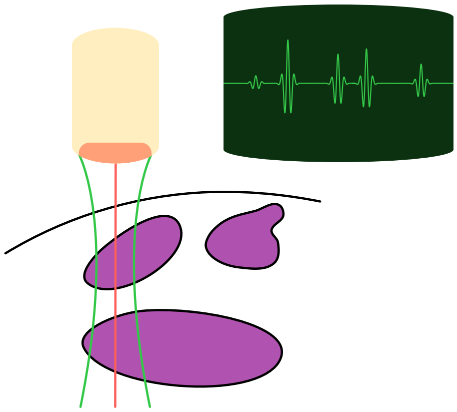

Figure 1.1: *A-mode ultrasound: the signal shown on the screen corresponds to the amplitude of the echoes along the red A-line.*

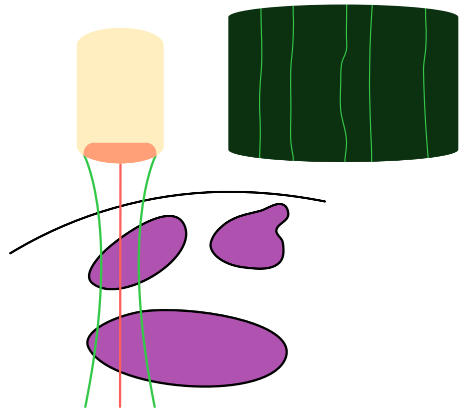

Figure 1.2: *Swept M-mode ultrasound: the signal on the screen corresponds to the trace of the peaks of the red A-line linearly swept in time.*

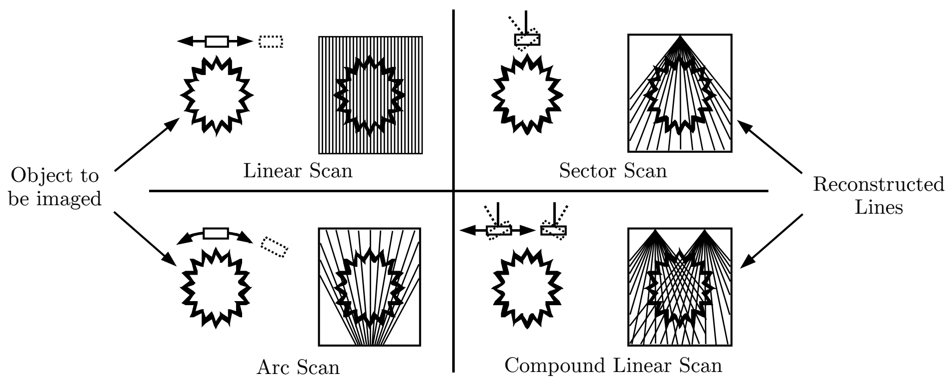

Figure 1.3: *Single element image formation. The transducer is mechanically translated, rotated, and tilted to reconstruct the lines of the image. Figure courtesy of E.* Brunner *[8].*

to arrays of several transducers. The action formerly performed with a single transducer by translating, rotating and tilting it is replaced by an array of elements that does the same process electronically with greater accuracy and speed.

1.2.1 Focusing in transmission

Focusing in a homogeneous medium is currently achieved on most commercial scanners by using ultrasonic probes made of an array of independent transducers. Each transducer is connected to a separate delay line as presented on figure 1.4. They are commonly referred to as "channels". The size of the elements of the array and the spacing between them are

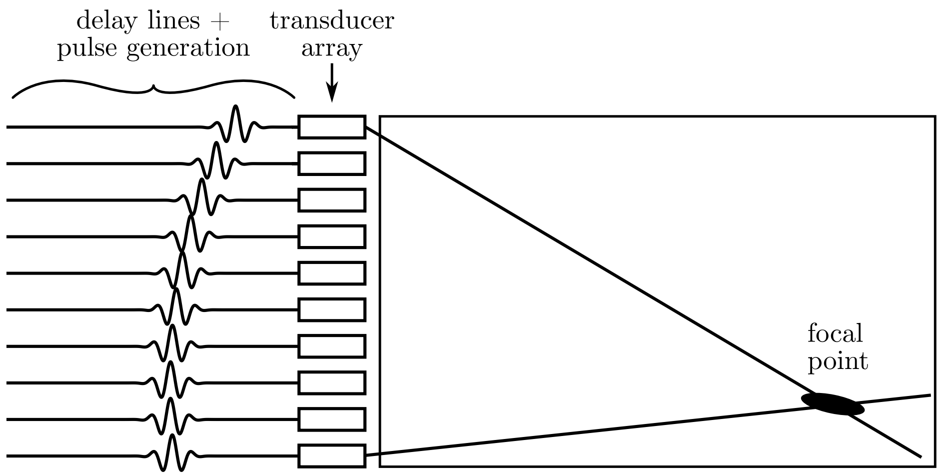

Figure 1.4: *Beam steering in transmission: delays are calculated so that the waves emitted by each independent element reach the target focal point at the same time, interfering constructively.*

about the size of the central wavelength of the probe or smaller. Under those conditions, the sidelobes remain small and the grating lobes are minimized [9] ensuring proper focalization of the energy in the medium. Each element emits the same pulse but at different times chosen so that each pulse reaches the focal point at the same time. The propagation times or times-of-flight between each element and the focal point are calculated. From those values, delays are inferred and applied in emission so that the pulses emitted by each individual element reach the target focal point at the same time, thus interfering constructively at that location. To obtain a sharp image with the least amount of noise, a sequence of focalized pulses is emitted in different directions, and the acquired echoes are combined off-line to form an image. That last step relies on *in silico* focalization easily made possible by a direct access to the phase of the sound waves.

1.2.2 Beamforming in reception

Beamforming in reception or image formation is a similar process. The final image is an echo intensity map that shows the acoustic echogenicity of the medium. The greater the echogenicity, the more intense the echo. The intensity is computed using off-line focusing. The intensity of the sound reflected in a particular point (x_i, z_i) of the medium being imaged

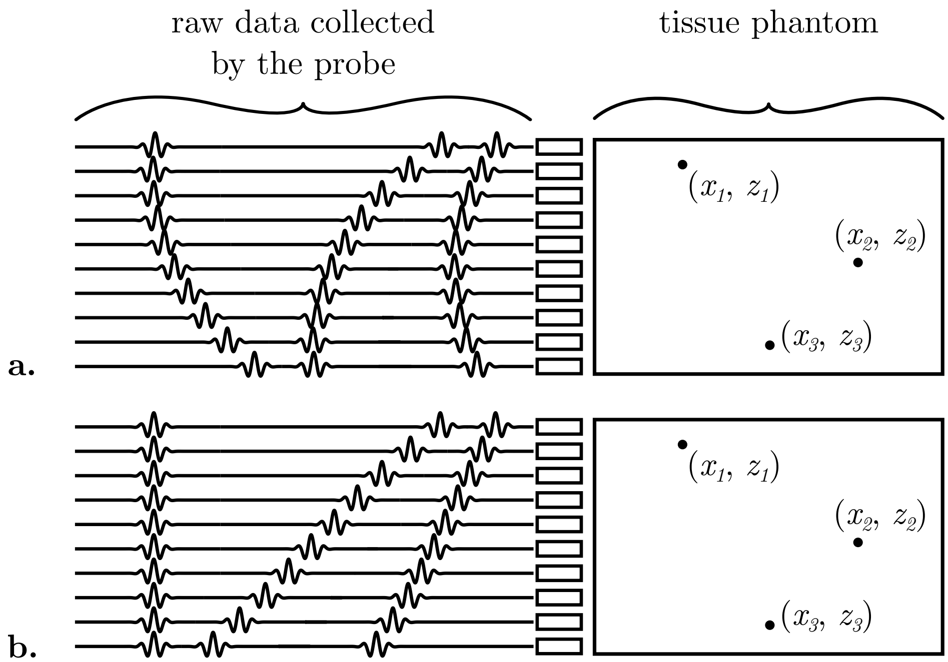

Figure 1.5: *Beamforming in reception:* a. *the echoes coming from three point scatterers are acquired by the probe;* b. *time-of-flights from* (x_1, z_1) *to each transducer are calculated and applied to the channels, aligning the phase of the wavefronts coming from that point.*

is obtained by computing the time-of-flight from the point (x_i, z_i) to each element of the ultrasonic probe. From those values, delays are inferred and applied in reception so that all the echoes originating from (x_i, z_i) are propagated back to that point. As shown on figure 1.5, applying the calculated delays to each channel aligns the waveforms originating from (x_i, z_i), whereas the echoes originating from other locations do not get aligned. Finally, the aligned channels are summed together. The waves originating from (x_i, z_i) interfere constructively whereas the other waves get averaged out to small values. This process is known as *coherent summation*. It is repeated for all the points (x_i, z_i) of the final image, and the amplitude value for each point is stored in the corresponding pixel. This algorithm is the so-called Delay-and-Sum [10]. It is worth noting that to the best of the author's knowledge it has not been proven that Delay-and-Sum is the best way to solve this inverse problem, leaving a lot of potential for new algorithms and innovation.

1.3 Evolution of beamformers

Real-time ultrasound imaging scanners have been available for nearly 50 years. During these 50 years of existence, much has changed in their architecture, electronics, and technologies. However one component remains present: the beamformer. From analog and hardware beamformers to digital and software beamformers, the technology has evolved and paradigms have shifted and brought much diversity to the world of beam formation. In this section, we propose to review briefly the different beamforming technologies that have been developed over the years. We choose to focus on beamforming with linear and phased arrays, since those are the two types of probes that were used in this work.

According to Thomenius [10],

> *The goal [...] is to create as narrow and uniform a beam with as low sidelobes over as long a depth as possible.*

In both transmit and receive modes, delays are applied to each individual channel to achieve beam focusing and beam steering as desired.

When dealing with medical ultrasound imaging a few challenges arise. For example, the maximum amplitude of the pressure one can apply at the source is limited and regulated by the FDA to ensure the imaged tissues are not damaged in the process. Typically, pressure amplitudes of a few hundred kiloPascal are used. As the generated wave propagates in the tissue, it is attenuated by about 0.5 $dB.cm^{-1}.MHz^{-1}$. One must also take into consideration that less than 10% of the incident pressure actually gets reflected back to the probe. Moreover, the conversion efficiency of the piezoelectric elements is usually of 50 - 75%. As a result, it is estimated that in order to display 40 dB of information, the scanner has to be able to handle over 100 dB of dynamic range.

1.3.1 Basics

The functions of a basic beamformer are presented in figure 1.6. The beamformer must be able to generate a transmit wave, either focalized, plane, diverging, etc. It must be able to steer the generated wave in different directions. When the emission is complete, it must process the received signal in order to obtain the best image quality possible.

It is assumed that the elements behave as point-like sources, and generate a continuous wavefront such as the one represented in figure 1.4. In general, the received signal is assumed to have to following form [10]

$$r(t) = \sum_{i=1}^{N} A_{r_i} \sum_{j=1}^{N} A_{x_j} s\left(t - \tau_{r_i} - \tau_{x_j} + \frac{2R_f(t)}{c}\right) \tag{1.1}$$

where N is the number of elements in transmission and reception. The transmitted wave is $s(t)$, and the factors A_{x_j} and A_{r_i} represent a potential apodization function in transmission and in reception, respectively. The delays τ_{x_j} and τ_{r_i} refer to the transmit and receive delays applied during the transmit and receive beamforming, respectively. The four parameters A_{x_j}, A_{r_i}, τ_{x_j}, and τ_{r_i} are of critical importance in beamforming and their value greatly influences the quality of the reconstruction, as we will discuss in the remainder of this section.

It can be proven easily that [10]

$$\tau_{x_i} = \frac{1}{c}\left(\sqrt{(x_i - x_f)^2 + {z_f}^2} - R_f\right) \tag{1.2}$$

where c is the speed of sound, τ_{x_i} is the transmit delay (a similar formula can be computed for the receive delay), (x_f, z_f) are the coordinates of the focal point, and R_f is the distance between the origin and the focal point. The focal point can be alternatively:

- a single transmit focal point,
- a series of focal points in the case of dynamic focusing,

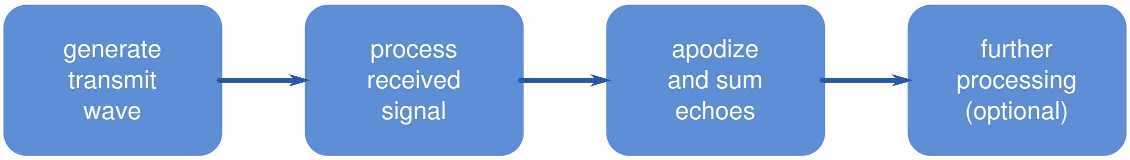

Figure 1.6: *Block diagram of a basic beamformer.*

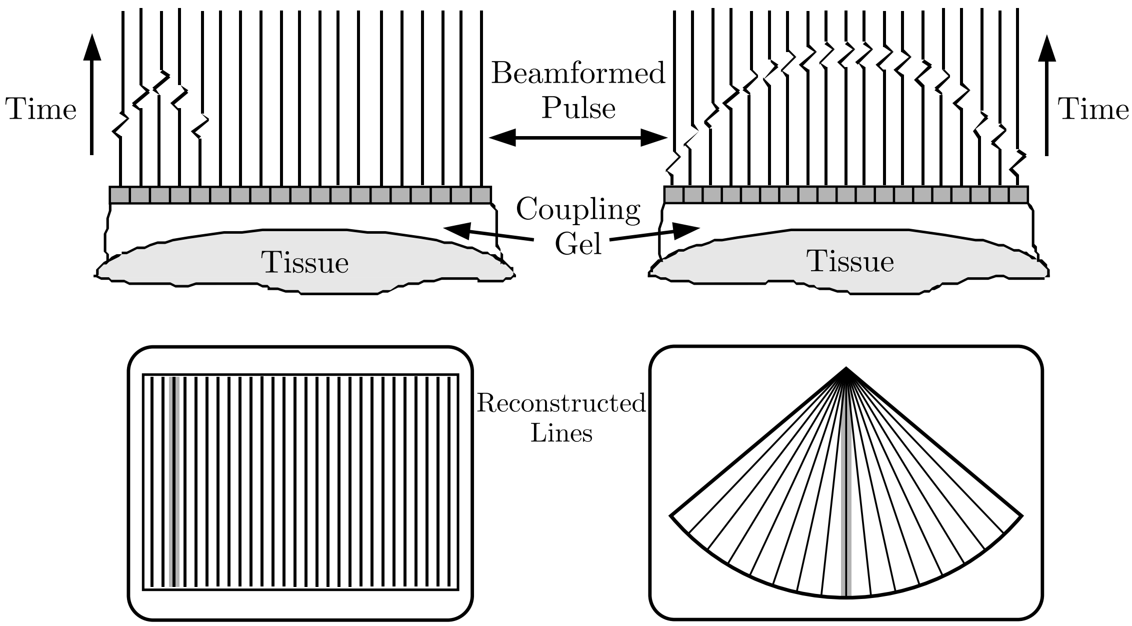

Figure 1.7: *Linear array acquisition versus phased array acquisition. Figure courtesy of* E. Brunner *[8].*

- the location of a pixel in the reconstructed image.

In figure 1.7, one can understand the difference between a linear array acquisition and a phased array acquisition. With a linear probe, a sub-aperture with optional apodization is used. The sub-aperture is translated across the entire width of the probe to produce a single image. In the case of the phased array, the full aperture is used to focalize a wave in the medium at different angles. This results in multiple scans at angles that span a sector of the tissue.

1.3.2 Development

Linear [11, 12] and phased [13–16] array systems were initially developed for brain imaging, echocardiography, and obstetrics. These systems were simple, and some of them did not incorporate a focusing mechanism. Instead, they relied on the natural narrowing that occurred during the propagation of a collimated beam. This design presents several limitations such as a limited focal area, high sidelobes, and high energy in the near-field. In that case, equation 1.1 becomes

$$r(t) = \sum_{j=1}^{N} A_{x_j} s\left(t - \tau_{x_j} + \frac{2R_f(t)}{c}\right) \tag{1.3}$$

which is a transmit only beamformer with constant τ_{x_j} that can therefore cancel the term $\frac{2R_f(t)}{c}$ in a single location only. Furthermore, in order to yield an acceptable depth-of-field, the f-number has to be fairly high.

The need to eliminate sidelobes became an evidence early on [17]. To that end, *apodization* functions were applied to the aperture [17–20], and a combination of both transmit and receive beamforming was applied.

Dynamic focusing was introduced to medical ultrasound with the first Duke University phased array system [14, 15]. Dynamic focusing along with apodization allow a great reduction of the sidelobes. Dynamic focusing also adds the advantage of keeping the f-number low and relatively constant

The Gold Standard beamformer is the one associated with a complete dataset. To acquire such a dataset, one has to fire each element independently and acquire the echoes with each element independently, leading to a N^2 dataset. Since the acquisition of such a dataset would require at least $N^2/2$ transmits and receives, assuming that reciprocity holds, it is infeasible *in-vivo*.

As a result, several methods have been developed to approach the performance of the Gold Standard beamformer, some of them being:

- using multiple transmits at different focal points,

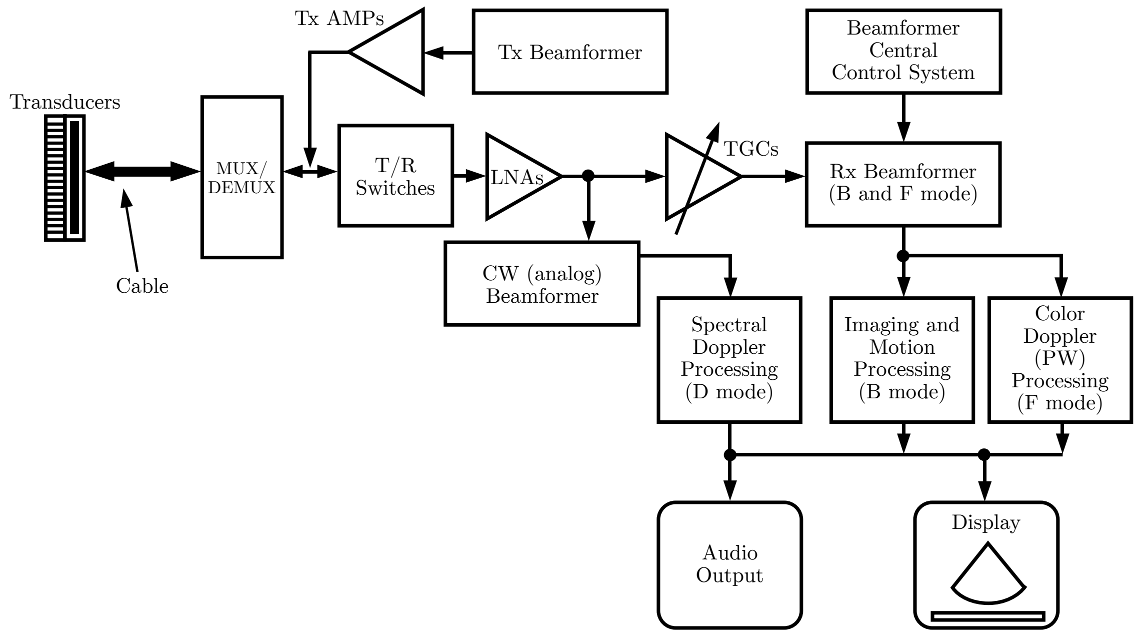

Figure 1.8: *Complete block diagram of a state-of-the-art beamformer. Figure courtesy of E.* Brunner *[8].*

- using synthetic aperture approaches,
- creating non-diffracting transmit beams [21],
- deconvolving the transmit beam pattern [22].

Figure 1.8 shows a complete block diagram of a state-of-the-art beamformer. The acquisition happens as follows:

- The transmit beamformer produces a signal which is amplified and sent to the probe,
- the scanner then switches to reception mode and records echoes from the medium,
- the signal is amplified and pre-processed before being sent to the receive beamformer that generates an image.

1.3.3 Capon beamformer

The idea behind the Capon beamformer comes from the observation that the quality of B-mode images is limited not only by the resolution, but also by the interference suppression capabilities of the system. These in turn depend on the beam pattern of the system which depends on the geometry of the probe and the weight applied to each individual element. Classical weighting techniques such as static apodization are used to lower sidelobes at the cost of a wider main lobe. In other words, static apodization sacrifices resolution to decrease interferences. Adaptive techniques however, adapt the weights to the situation by using data already acquired to estimate the distribution of noise and interferences [23]. The Capon beamformer is one such technique.

Let us consider an array of n sensors. $\mathbf{a}(\theta)$ is the response of the array to a plane wave of unit amplitude, coming from direction θ. The set $\{\mathbf{a}(\theta) \mid \theta\}$ is commonly referred to as the array manifold. We assume that there is a source in the far field in direction θ emitting a signal $s(t)$. Then, the array output is given by

$$y(t) = \mathbf{a}(\theta)s(t) + v(t) \tag{1.4}$$

where v represents the noise as well as the effects of undesired signals. Denoting discrete samples of y by $\mathbf{y}[k]$, we have

$$\mathbf{y}[k] = a[\theta]\mathbf{s}[k] + \mathbf{v}[k] \tag{1.5}$$

The weighted output of the beamformer $\mathbf{y}_{\mathrm{BF}}$ is given by

$$\mathbf{y}_{\mathrm{BF}}[k] = \mathbf{w}^\top \mathbf{y}[k] = \mathbf{w}^\top \mathbf{a}[\theta]\mathbf{s}[k] + \mathbf{w}^\top \mathbf{v}[k] \tag{1.6}$$

where $\mathbf{w}^\top$ denotes the transpose of the weight vector $\mathbf{w}$.

The goal is to have

$$\begin{cases} \mathbf{w}^\top \mathbf{a}[\theta] \sim & \mathbf{1} \text{ and} \\ \mathbf{w}^\top \mathbf{v}[k] = & o\left(\mathbf{w}^\top \mathbf{a}[\theta]\mathbf{s}[k]\right) \end{cases} \tag{1.7}$$

which amounts to saying that we want to maximize the array response in the direction θ while making sure the contributions from the undesired signals are as small as possible. The expected contribution of the noise and interferences is given by

$$\mathbf{w}^\top R_y \mathbf{w} \tag{1.8}$$

where R_y is the *covariance matrix* of the signal y. The covariance matrix is given by the expected value of the autocorrelation of the signal y:

$$R_y[k] = E[yy^\top] \tag{1.9}$$

The Minimum Variance Beamformer (MVB) is chosen as the optimal solution of

$$\min \mathbf{w}^\top R_y \mathbf{w} \quad \text{s.t.} \quad \mathbf{w}^\top \mathbf{a}[\theta] = \mathbf{1} \tag{1.10}$$

This is commonly referred to as the Capon beamformer [24]. Problem 1.10 has an analytic solution given by

$$\mathbf{w}_{\text{MVB}} = \frac{{R_y}^{-1}\mathbf{a}[\theta]}{\mathbf{a}[\theta]^\top {R_y}^{-1}\mathbf{a}[\theta]} \tag{1.11}$$

In practice, we do not have direct access to R_y, and it is replaced by an estimate of the covariance matrix of the signal y, calculated from the available samples:

$$\hat{R_y} = \frac{1}{N} \sum_{i=k-N+1}^{k} \mathbf{y}[i]\mathbf{y}[i]^\top \tag{1.12}$$

for a signal y of length N.

The original Capon beamformer is very sensitive to mismatches between the assumed array response and the actual array response, and numerous methods have been proposed to make it more robust [25–27].

1.3.4 Beamspace beamforming

Beamspace beamforming builds on the MVB previously developed by taking some of its principles into the beamspace, as opposed to the element space, where MVB was originally defined. The advantage is a reduction in computational complexity which is one of the main drawbacks of Capon's method.

The Capon beamformer relies on the inversion of the covariance matrix of the array, which has dimensions equal to the number of elements in the array. This step is computationally intensive, making the Capon beamformer less attractive despite its advantages.

Beamspace beamforming uses the same constraints and optimality criterion as the Capon beamformer, but from the point-of-view of beams, as opposed to elements. The beamspace beamformer effectively combines the outputs of several Delay-and-Sum beamformers steered in different directions instead of combining elements. This allows for a reduction in complexity since the beams can be chosen to mostly cover problematic regions and effectively cancel the underlying interferences, whereas the number of elements is fixed for a given probe. It has been found that a low number of beams (3 beams) compared to the number of elements (usually about 128 elements) is enough to obtain results with beamspace-Capon beamforming that are comparable to elementspace-Capon beamforming.

A beamspace beamformer combines the outputs of several beamformers to generate orthogonal beams. To that end, a Butler matrix is used:

$$\mathbf{x}_{\mathrm{BS}} = B\mathbf{x} \tag{1.13}$$

where $B \in \mathcal{M}_{m,n}(\mathbb{C})$ is the matrix such that

$$B_{m,n} = \frac{1}{\sqrt{M}} e^{-j\frac{2\pi mn}{M}} \tag{1.14}$$

The Butler matrix generates M orthogonal beams that have their main response lobe in the direction θ_m given in reference [28]. In this case, the BUTLER matrix from equation 1.14 is equivalent to an M-point Discrete FOURIER Transform matrix. In practice, the result of the products of B by another vector is computed using the FFT algorithm, which is faster than a matrix multiplication.

This transform corresponds to the beamspace transform, and is applied to both the signal and the weights in the element space to find their beamspace counterparts:

$$\begin{cases} \mathbf{y}_{\mathrm{BS}} = & B\mathbf{y} \\ \mathbf{w}_{\mathrm{BS}} = & B\mathbf{w} \\ \mathbf{x}_{\mathrm{BS}} = & B\mathbf{x} \end{cases} \tag{1.15}$$

As an example, consider the beamspace transform of the uniformly weighted Delay-and-Sum beamformer $\mathbf{w}_{\mathrm{DAS}} = \mathbf{1}$:

$$\mathbf{w}_{\text{BS-DAS}} = B\mathbf{1} = \mathbf{e}_1 \tag{1.16}$$

where $\mathbf{e}_1$ is the vector with 1 as its first coordinate, and 0 otherwise.

The final step is to find the optimal selection of beams in the beamspace. This is done using CAPON's method:

$$\min \mathbf{w}_{\mathrm{BS}}^{\top} R_{\mathrm{BS}} \mathbf{w}_{\mathrm{BS}} \;\; \text{s.t.} \;\; \mathbf{w}_{\mathrm{BS}}^{\top} \mathbf{a}[\theta] = \mathbf{1} \tag{1.17}$$

which analytic solution is given by

$$\mathbf{w}_{\mathrm{BS}} = \frac{{R_{\mathrm{BS}}}^{-1}\mathbf{e}_1}{{\mathbf{e}_1}^{\top}{R_{\mathrm{BS}}}^{-1}\mathbf{e}_1} \tag{1.18}$$

where $R_{\mathrm{BS}} = E[\mathbf{x}_{\mathrm{BS}}{\mathbf{x}_{\mathrm{BS}}}^{\top}]$. The beamspace CAPON beamformer is indeed the FOURIER domain version of the element space CAPON beamformer. Beamspace beamforming is developed in further details in reference [29].

1.3.5 Multi-beam Capon beamforming

In multibeam Capon beamforming [30], the goal is to form a single covariance matrix R covering all the angles we need for reconstruction, as seen in figure 1.7. In fact, regular Capon beamforming requires to build a separate covariance matrix R for each image sample. It is also possible to build a radial covariance matrix, or per-beam covariance matrix as seen in section 1.3.4, to decrease the computational power needed for the method.

Building a single covariance matrix for all the angles required to compute the final image involves going back to problem 1.10 and its analytic solution 1.11. Indeed, we want to define a far-field steering vector $\mathbf{a}[\theta]$ such that

$$\mathbf{a}[\theta] = [1 \ e^{-j\pi \sin\theta} \ e^{-j2\pi \sin\theta} \ \cdots \ e^{-j(M-1)\pi \sin\theta}] \tag{1.19}$$

The phase shift introduced by 1.19 allows the building of a single matrix R capable of covering all the necessary angles in the image. Therefore, the weights for a given direction and a given range of depth can be computed using

$$\min \ \mathbf{w}_{\theta,n}^{\top} R \mathbf{w}_{\theta,n} \ \text{ s.t. } \ \mathbf{w}_{\theta,n}^{\top} \mathbf{a}_n[\theta] = \mathbf{1} \tag{1.20}$$

which has the following analytic solution:

$$\mathbf{w}_{\theta,n} = \frac{R^{-1}\mathbf{a}_n[\theta]}{\mathbf{a}_n[\theta]^{\top} R^{-1} \mathbf{a}_n[\theta]} \tag{1.21}$$

The goal is to reduce the computational cost as much as possible, to make those methods more attractive for real-life applications. The constant evolution of computers and the development of new tools such as cloud computing that make clusters affordable and available to everyone may increase the interest for software beamformers and accelerate their development and implementation in commercial scanners.

1.3.6 Spatial compounding

The first implementation of Real-Time Spatial Compounding in a commercial scanner was introduced in 1999 by Philips [31]. The development of Spatial Compounding comes from the observation that ultrasound images are subject to inherent artifacts that have a negative impact on image quality and resolution. Common acoustic artifacts include:

- *speckle* that gives a salt-and-pepper texture to tissue and is due to coherent wave interference,
- *sidelobes* and *grating lobes* that are due to the architecture of the probe and correspond fundamentally to the propagation of acoustic energy in a different direction than the one intended, causing significant echoes coming away from the focal axis and artifacts in the reconstruction or *clutter*,
- *multiple scattering* which is commonly neglected in commercials scanners and corresponds to signal generated by a scatterer from an echo coming from another scatterer, causing artifacts in the reconstruction known as *clutter*,
- *shadows* generally observed below a bright structure, and due to the fact that the energy available to insonify a region right below a hyperechoic structure is greatly diminished, therefore creating a shadow below the structure.

The combination of all these artifacts decreases both the resolution and the contrast of the image.

Spatial compounding consists in acquiring several overlapping images of the same structure but from different angles, and then combining them to form a final image. This technique has a positive averaging effect on the image because the artifacts produced from different view angles are different and uncorrelated. The underlying structure imaged however remains constant. The effect of shadowing is also decreased by the technique. The advantages of spatial compounding include:

- **contrast improvement** making structures more differentiable,
- **clutter reduction** by averaging noise and combining incoherent artifacts together,
- **sharpness improvement** making interfaces between structures clearer.

The direct consequence of the aforementioned improvements is to increase the diagnostic confidence.

1.3.7 Tissue Harmonic Imaging

The goal of Tissue Harmonic Imaging (THI) [32–36] is to improve the image quality in patients that are difficult to scan with traditional techniques, such as obese patients, [37–46].

Conventional ultrasound imaging uses echoes generated by the tissue at the emitted frequency f_c. Whereas THI uses the second harmonic signal, thus at frequency $2f_c$. The second harmonic is actually not present in the original signal. It is created through non-linear propagation of the emitted pulse in the body [47, 48]. Traditionally, it is assumed that the propagation of ultrasonic waves in the body is within the linear range of pressures. This implies that the pressure applied to the body is small enough that the tissue is perfectly elastic. In reality, pressures used in ultrasound imaging are frequently outside of the elastic domain of the tissue [49].

In non-linear propagation, the propagation speed, or speed of sound, depends on the pressure in the body. The speed of sound is higher in areas where there is tissue compression, and lower in areas where the tissue is relaxed. Since the sound wave is a pressure wave, the higher pressure parts of the emitted pulse will travel faster than its lower pressure parts, resulting in a distortion of the signal. The distortion makes the peaks of the signal look steeper and sharper than the emitted pulse. In signal analysis, this is explained by the generation of harmonics, as depicted in figure 1.9. In practice, the generation of harmonics is not as efficient as shown on figure 1.9, and only the second harmonic is actually usable.

Indeed, the second harmonic is much weaker than the fundamental, and drastic improvements in transducer technology and manufacturing as well as in signal processing and de-noising had to be made before THI could be used in clinical scanners.

The main advantage of harmonic imaging is that the second harmonic is generated directly in the tissue, and is most prominent where the acoustic energy is concentrated: at the focal point. As we know, an ultrasonic pulse generated by the probe has to go through superficial layers of fat and muscle. Since the thickness of such layers is not the same for all patients, they are generally assumed to be negligible. As such, the different speed of sound of those layers is not taken into account. Since they tend to be irregular, the layers of fat and muscle distort the wavefront emitted by the probe, degrading the focalization and introducing artifacts. The echoes generated by the medium as a response for the excitation pulse have to go through the exact same layers of fat and muscle, doubling the distortion and subsequent artifacts. With THI however, the distortion due to those layers happens only during echo reception since the second harmonic is generated deep within the tissue. It has been shown that the profile of the harmonic beam at the focal point is narrower and its sidelobes are lower than that of the fundamental beam [50]. Therefore, the lateral resolution is improved. There is also an improvement of the contrast due to the fact that the amplitude of the second harmonic signal varies with the square of the amplitude of the fundamental. Thus, small local variations that are barely visible with the fundamental signal can be made more obvious with THI.

1.3.8 Plane wave imaging and coherent compounding

Plane wave imaging is fairly new to the world of ultrasound, and its development comes from the emergence of other modalities such as transient elastography. In transient elastography, the goal is to image the propagation of a shear wave in the body, which requires a high frame rate of over 1,000 Hz [51]. Doing so allows one to compute the speed of the shear wave which depends on the bulk modulus of the tissue. As a result, a map of the elasticity of the

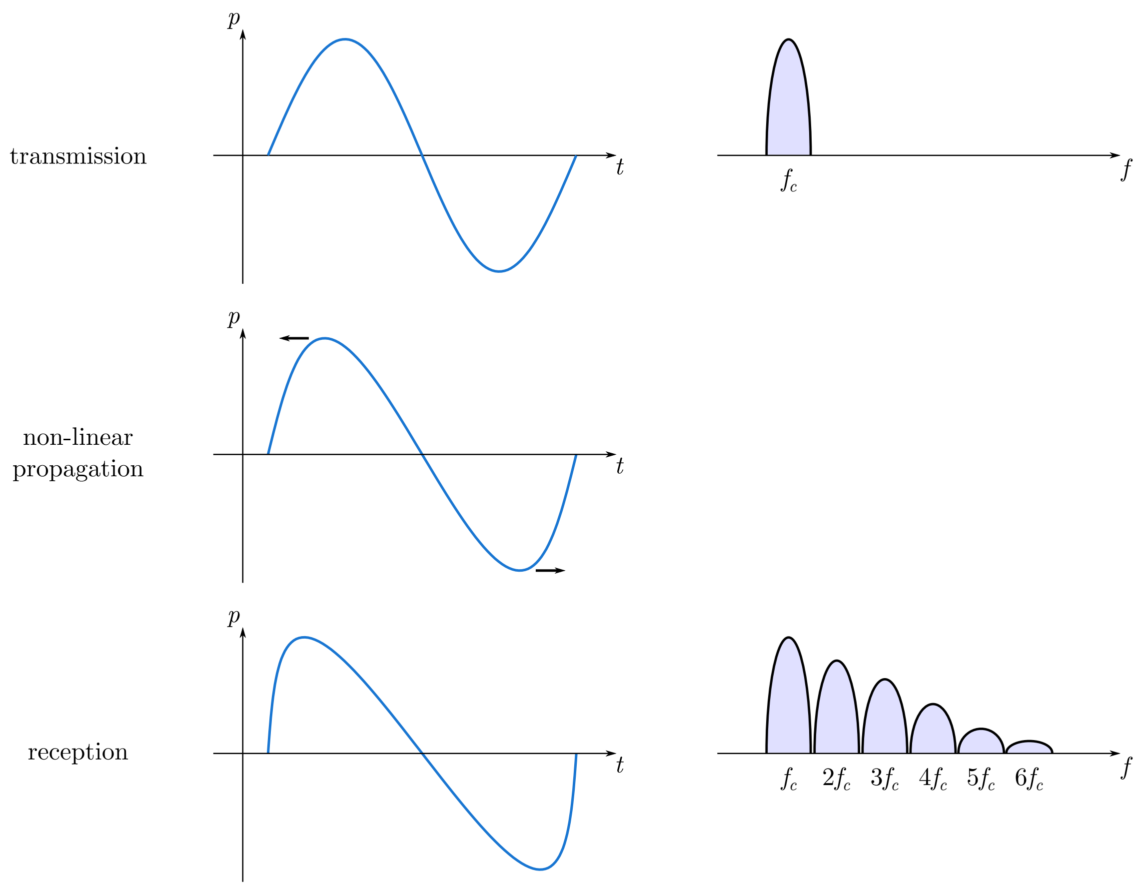

Figure 1.9: *Tissue Harmonic Imaging: the propagation of ultrasound in the body is non-linear, due to the tissue not being perfectly elastic. The pressure peaks travel faster than the valleys, making the signal look steeper and sharper. This is due to the creation of higher frequencies in the tissue.*

tissue and its underlying structures can be computed and shown to the user. Some lesions or cancers are stiffer than regular structures in the body. For that reason and others not developed here, transient elastography is used to characterize non-invasively the elasticity of tissue [52]. For more details on transient elastography, the interested reader can refer to publications [53–59].

To achieve the necessary frame rate of over 1,000 Hz, transient elastography relies on plane wave imaging [60, 61], and coherent image compounding [62]. We saw that in incoherent image compounding, several images of the same tissue region are acquired at different angles. Then individual images are computed from those different angles. Finally, all the images are summed together and the final image is the average image, exhibiting attenuated artifacts, better contrasts, less clutter, etc.

In coherent compounding, the first step remains the same: the tissue is probed with plane waves at different angles of inclination. However, the data acquired is combined coherently, thus before envelope detection, to focus in the medium. The simple diagram in figure 1.10 shows the acquisition process in red: a set of plane waves steered in different directions are emitted and the echoes are recorded for each one of them. Knowing what the plane wave angles are, one can combine the different datasets to refocus within the tissue by applying the correct delays to form the focalized waves shown in yellow. This method gives the ability to focalize both in depth and laterally.

This method achieves good results with a limited number of plane wave, typically 3 to 5. As a result, the frame rate is greatly increased.

1.4 Challenges

Since the inception of ultrasound imaging for diagnostic purposes, the technology and the concepts have evolved toward computational methods. Modern methods such as Capon beamforming or beamspace beamforming rely on computational power to increase the image

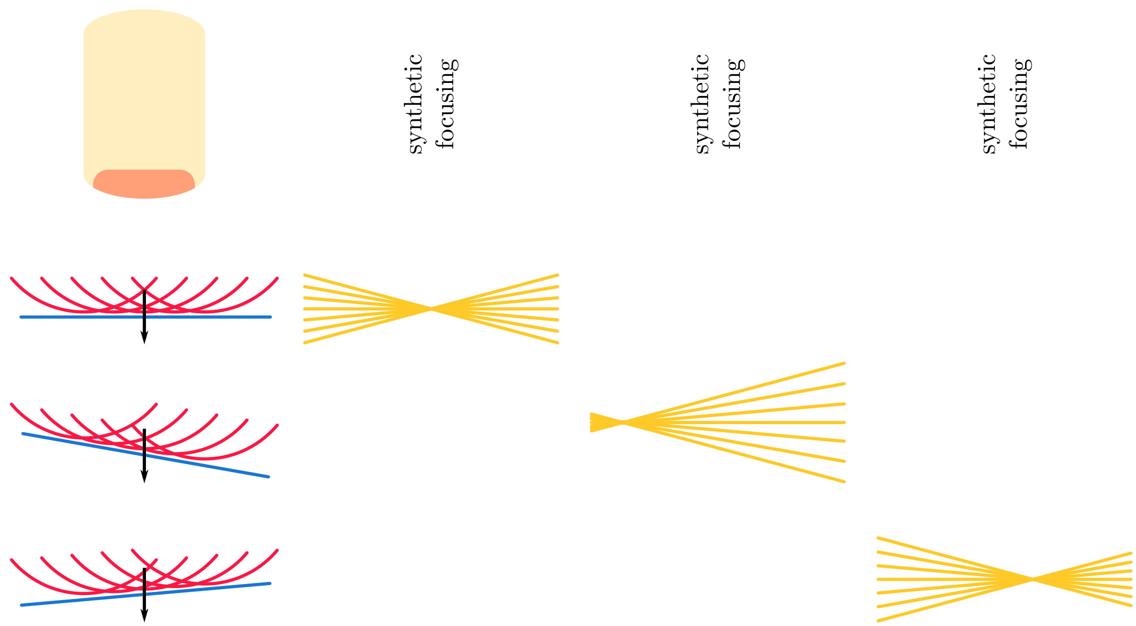

Figure 1.10: *Coherent compounding: a. The tissue is probed with several plane waves steered in different directions, one at a time, b., c., and d. The datasets are combined together with appropriate delays to focalize* a posteriori *synthetically. The delays are calculated to cover all the width and depth of the image.*

quality. As computational cost decreases, digital beamforming becomes more and more attractive. The emphasis on increasing the number of cores in CPUs as well as GPU computing is an opportunity for digital beamforming, adaptive and computational methods to emerge and become more compelling.

In the next 10 years, it is possible that beamforming techniques based on machine learning and deep learning along with cloud computing will supercede current beamforming technologies. This work is at the interface between these technologies. The beamformer we developed, the so-called time-domain Compressive Beamformer (t-CBF), relies on physical models as well as computational power to extract as much information as possible from the data. It is fully compatible with machine learning techniques and its compression capabilities can be exploited in a cloud computing setting.

Nowadays, ultrasound imaging is faced with the following challenges:

- Most ultrasound commercial scanners rely on expensive custom built hardware. Originally, specific hardware was needed since technology was not advanced enough to allow the use of software beamforming. However this bridge has been gapped. Modern computers have several CPU cores, and hundreds of GPU cores. They have the ability to speed up calculations dramatically, making software beamformers and computational techniques increasingly attractive.

- The use of several focalized transmit events to compute a single image brings more complexity to beamforming. This makes the hardware all the more difficult to build and therefore expensive.

- The frame rate of the modality is limited by the number of transmit events needed to compute a single image. The time between two transmit events is not compressible. It is equal to the propagation time between the probe and the deepest point imaged, back and forth. Using less transmit events is then the only way to increase the frame rate. However, it leads to artifacts and reconstruction errors with classic beamforming techniques.

- 3D brings another technological challenge to ultrasound imaging. It is increasingly used in echocardiography to assess the movements of the heart walls and valves. However it requires more transmit events than 2D imaging, decreasing the frame rate significantly.

The method proposed in this work aims to address those challenges. Regarding 3D imaging, much remains to be done but this work establishes the preliminary and necessary steps toward this goal.

1.5 Impact

Cardiovascular diseases have a tremendous impact worldwide. In the US, it is estimated that as many as 85.6 million American adults were living with at least one type of cardiovascular disease in 2016 [63]. Cardiovascular diseases include:

- High Blood Pressure: 80 million people.
- Coronary Heart Disease: 15.5 million people divided into 4 subcategories (with overlap):
  - Myocardial Infarction: 7.6 million.
  - Angina Pectoris: 8.2 million.
  - Heart Failure: 5.7 million.
  - Stroke: 6.6 million.

Cardiovascular disease is the leading cause of death, with a global cost of $863 billion in 2010.

Echocardiography is an increasingly used modality to diagnose cardiovascular disease due to its low cost, non-invasiveness, and high temporal resolution compared to CT or MRI. During a single cardiac cycle several events take place and it has been shown that a temporal resolution of 2-5 ms is required to observe them [64, 65]. Abnormalities could be an indicator of cardiac disease. Early detection of ischemia, arrhythmia, etc could be made possible by the measurements of transient deformations of the myocardium at a high temporal resolution. Indeed heart disease changes the mechanical properties of the heart dramatically.

Increasing the frame rate of the modality could help detect small, transient deformations of the cardiac muscle that could in turn by used to diagnose early onset heart disease. Early diagnosis is critical for early treatment and improvement of patient outcome. To that end, frame rates of at least 200-500 frames per second are needed.

1.6 Aims

Ultrasound imaging has been used in the medical field for over 20 years for applications ranging from fetus monitoring to tumor ablation, hence spanning both the diagnostic and therapeutic worlds. Its versatility and cost-effectiveness with respect to other imaging modalities such as MRI and X-ray make it a great tool in the medical imaging arsenal. However in spite of recent developments and enhancements, ultrasound imaging still has several drawbacks. In order to compute a single image, a vast amount of data has to be acquired and processed by the scanner impacting the frame rate of the machine among other aspects.

Independently, Compressive Sensing has emerged as an inverse problem technique and gained a lot of interest from researchers quickly because of its ability to recover under-sampled signals under some mathematical assumptions. After being thoroughly developed and supported as a mathematical theory, it was successfully applied to MRI, effectively decreasing the acquisition time significantly. Naturally, researchers from other fields have been trying to adapt Compressive Sensing to their own problems.

This work adapts Compressive Sensing to ultrasound imaging and outlines the development of a method that decreases the amount of data acquired while maintaining the image quality. It relies on models, wavelets, and processing power to fill-in the gaps, so to speak.

The aims of this work are:

Aim 1: Develop a mathematical framework for beamforming that is compatible with Compressive Sensing

Challenge To write beamforming as a matrix product to ensure compatibility with Compressive Sensing, and show the theoretical equivalence with classic beamforming techniques such as Delay-and-Sum.

Approach The medium or biological tissue is modeled as a collection of point scatterers in an otherwise homogeneous surrounding. The pressure field resulting from a specific excitation pulse is calculated using temporal GREEN's functions of the 2D wave propagation equation. A one-to-one correspondence between a given point scatterer and an excitation pulse, and the resulting pressure field is explicitly written as a matrix product.

Impact The aforementioned approach is a theoretical proof that Compressive Sensing can be used for the beamforming of ultrasound signals. The framework developed is used throughout this work as a fundamental basis for all image reconstructions.

Aim 2: Investigate the capabilities of the method through simulations, and apply it to a phantom

Challenge To adapt the theory to *in-silico* and practical experiments under simple, restrictive conditions.

Approach The framework developed in Aim 1 is *a priori* designed to reconstruct images of point scatterers. Before moving to media displaying a more complicated structure such as *speckle*, its performance has to be assessed on simulated, sparse wave fields. The predicted capabilities of Compressive Sensing such as super-resolution are also investigated.

Impact The limits of the approach are defined and used to improve on the results.

Aim 3: Develop an algorithm for ultrasound image reconstruction based on the previous framework and the use of wavelets

Challenge To adapt the previous point scatterer-based theoretical framework to tissue imaging displaying continuous structures and ultrasonic *speckle* using wavelets to enhance sparsity.

Approach Several flavors of the wavelet transform are used and their performance in the framework assessed. The images reconstructed are more sparse in the wavelet domain, enabling the Compressive Sensing framework to work optimally. Different families of wavelets are investigated to find an optimal transform. Different types of wavelet transform algorithms are also investigated: decimated and undecimated wavelet transform, as well as wavelet packet transform.

Impact The theoretical ability to reconstruct real life images is proven in ideal conditions.

Aim 4: Apply the algorithm to *in-silico* then *in-vivo* data to illustrate its advantages and limits

Challenge To acquire data in accordance with the previously developed framework, and modify the algorithm so it can handle the big amount of data needed for real life applications.

Approach The excitation pulse has to be coded in an ultrasonic scanner. A software and hardware modified scanner enables the extraction of pre-beamformed raw data, necessary to run the algorithm. The HILBERT transform is used extensively to downsample the raw data and allow the algorithm to run on real life data.

Impact The performance of the algorithm is assessed and improved.

1.7 Contributions

This work is organized into seven chapters. The first three chapters are meant to be an introduction to the field of ultrasound imaging and Compressive Sensing. The following four chapters focus on our work. It outlines how the theory of Compressive Sensing was used in the context of ultrasound imaging.

- In **chapter 2** we outline the evolution of signal representations. We focus on signal representation that are the most efficient in terms of compression. Namely, an efficient representation can capture most of the signal information in just a few coefficients.

- In **chapter 3** we give the reader the basic information needed to understand Compressive Sensing and its tools. We explain in what way Compressive Sensing is interesting, and how it can be adapted to the solving of inverse problems.

- In **chapter 4** we develop the theory of Time-domain Compressive Beamforming. Starting with a simplistic 1D example, we eventually describe a 2D beamforming framework for the reconstruction of point scatterers that uses the tools of Compressive Sensing.
- In **chapter 5** we show that the framework developed in chapter 4 can be adapted to tissue imaging. We discuss the challenges of memory usage and speckle imaging, as well as the robustness to noise.
- In **chapter 6** we apply our algorithm to patient data.
- In **chapter 7** we conclude this work by outlining some of the next steps possible for t-CBF.

Chapter 2

From signal representation to image compression

Any discrete signal can be viewed as a collection of values in a vector. The values are filled out by measurements during the acquisition process. As a result, the measurement vector lives in a vector space that we choose to refer to as the *acquisition space*. Associated with this acquisition space is an *acquisition basis*, which is the natural basis of the space as dictated by the acquisition process. In an effort to clarify this statement, we provide the following two examples:

Sound acquisition The recording of a sound is usually done by discretely sampling a continuous signal acquired by a microphone. The samples are usually equispaced and measured at a rate corresponding to the minimum sampling frequency dictated by the Nyquist-Shannon theorem [66]. Namely, in order to avoid any aliasing, the sampling frequency of the signal must be at least twice the maximum frequency exhibited by the signal. In this case, the acquisition can be seen as the convolution of a continuous signal $s(t)$ by a Dirac δ comb $\delta_{f_s}(t)$, as shown in figure 2.1. The result is a series of values that can be organized in a vector $s[t]$, where the brackets symbolize discrete time. From this, we can deduct that the natural acquisition basis is made of a collection of Dirac δ functions translated by a value

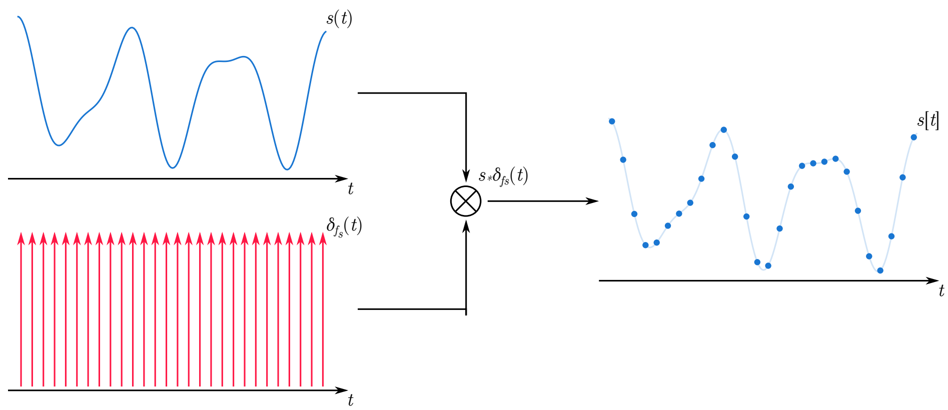

Figure 2.1: *Digital acquisition of an acoustic signal: the signal value is sampled regularly f_s times per second.*

imposed by the sampling frequency.

MRI acquisition In the case of MRI, the acquisition happens in the k-space (as will be briefly developed in section 3.2.4). The MRI inverse problem is solved by applying the inverse FOURIER transform to the acquired signal. Subsequently, the natural acquisition basis in that case is a FOURIER basis.

However, linear algebra teaches us that there are many more ways to represent a vector. In fact, any invertible transform applied to the acquisition vector leads to a new representation of the same information. This new representation then lives in the so-called *transform space*. Not all transforms are made equal and some are more useful than others. In this chapter, we focus on transforms that can help us compress a signal or an image. Such transforms will have the desirable property of being able to give a *sparse* representation of the image, meaning that few non-zero coefficients in the transform vector will be necessary to capture all or most of the information of the image in the acquisition space.

We will see that beyond data compression, a sparse representation can be used in conjunction with *regularization* to recover signals from an incomplete set of measurements.

2.1 Evolution of representations

2.1.1 Fourier representation

In 1822, Joseph Fourier proved that some signals could be written has an infinite sum of their weighted frequencies or harmonics. The Fourier transform comes from the study of Fourier series where an arbitrary periodic function or signal is expanded as an infinite sum of sines and cosines.

Definition 1. *The* Fourier *series of a P-periodic function f is given by*

$$f(t) = \sum_{n=-\infty}^{+\infty} F[n] e^{i\frac{2\pi n}{P}t} \tag{2.1}$$

where $F[n]$ are the frequency weights.

The extension of this discrete transform to a continuous frequency variable gives the Fourier transform. The discreet variable n designating the index of a harmonic of the signal becomes the continuous variable ω that designates the angular frequency or angular velocity.

Definition 2. *Within the framework of the* Lebesgue *integral, we have:*

$$f(t) = \frac{1}{\sqrt{2\pi}} \int F(\omega) e^{i\omega t} d\omega = \mathcal{F}^{-1}[F](t) \tag{2.2}$$

where F is Lebesgue *integrable, hence if $F \in \mathcal{L}^1(\mathbb{R})$.*

The transform exists if $f \in \mathcal{L}^1(\mathbb{R})$, and if $F \in \mathcal{L}^1(\mathbb{R})$ as well. This condition ensures one can take the Fourier transform of a function and its inverse.

Definition 3. *The* Fourier *transform of a function f is given by*

$$F(\omega) = \frac{1}{\sqrt{2\pi}} \int f(t) e^{-i\omega t} dt = \mathcal{F}[f](\omega) \tag{2.3}$$

Corollary 1. *If $f \in \mathcal{L}^1(\mathbb{R})$ and $F \in \mathcal{L}^1(\mathbb{R})$ then the transform is fully invertible and we have:*

$$f(t) = \mathcal{F}^{-1}\left[\mathcal{F}[f]\right](t) \tag{2.4}$$

almost everywhere.

The FOURIER transform is a representation of a signal from the frequency standpoint.

2.1.2 Time-frequency representation

The FOURIER transform is a very powerful tool that represents all the frequencies in a signal. However, it is not adapted to non-stationary signals by construction. It has no time resolution which means it does not provide information about when a frequency is present in the signal and when it is not. To alleviate this issue the Short-Time FOURIER Transform (STFT) [67] was developed by GABOR in 1946. The STFT is essentially a FOURIER transform of the signal multiplied by a moving windowing function. The signal is divided into short segments of equal length with an optional overlap between segments. An optional windowing function can also be applied to the segments to minimize aliasing. Then the FOURIER transform of each segment is calculated. How to cut and window the signal is a non-trivial problem in itself. Indeed, windowing the signal corresponds to a multiplication by a windowing function in the temporal space, which becomes a convolution in the frequency space. As a result, the windowing function has tremendous repercussions on the result of the STFT.

In this method, time and frequency play a symmetrical role as opposed to the FOURIER transform, where it is one or the other. To illustrate this, let us consider the signal in figure 2.2. It is an audio recording of a person speaking. The time representation gives us information on the variation of the amplitude of the signal in time only. The STFT representation allows us to see the frequencies that compose the signal and their variations in time. For example we notice a change in the frequency content around 0.5 s and then again around 0.85 sec. Those two changes correspond to the pronunciation of fricatives

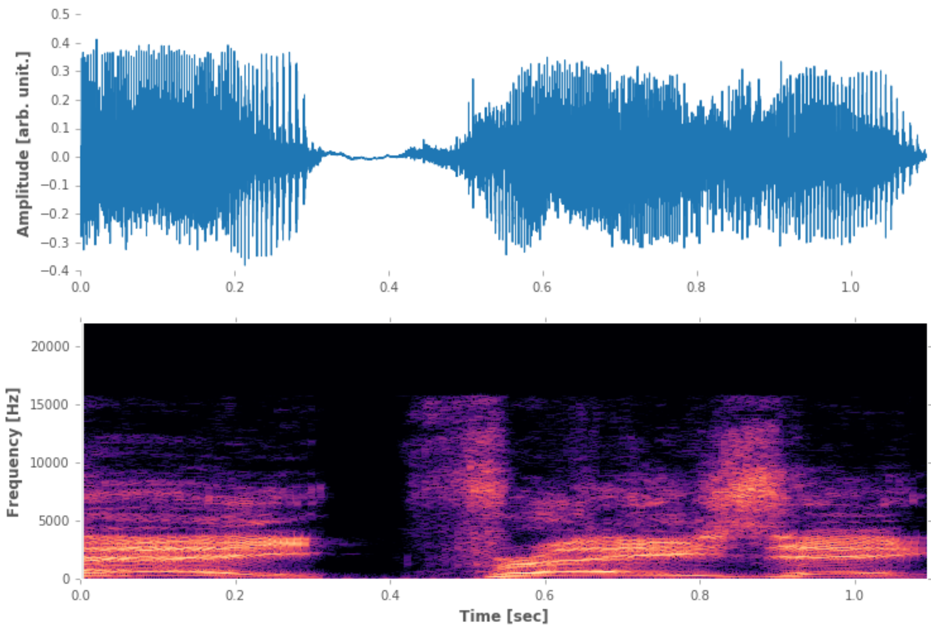

Figure 2.2: (Top) *Time representation of an audio signal.* (Bottom) *Time-frequency representation of the same signal using the STFT.*

which contain higher frequencies. The rest of the signal contains mostly vowels which contain mostly lower frequencies. Locating the fricatives in time would be difficult from a simple observation of the signal. The STFT makes it effortless. However, the time-frequency analysis allowed by the STFT is limited: according to HEISENBERG's uncertainty principle [68], it is impossible to define a windowing function which is compactly supported both in the time domain and in the frequency domain. In other words, a windowing function designed to give good frequency resolution will have poor time resolution and *vice versa*.

2.1.3 Space-scale representation

The wavelet viewpoint is conceptually similar to the time-frequency analysis. In this framework, signals and images alike can be built from a sum of multi-scale wavelets. The idea originated from the analysis of seismic data by an engineer working for an oil company, Jean MORLET. Petroleum geologists usually locate oil trapped underground by generating seismic waves in the ground and measuring their propagation times. The analysis is usually performed using FOURIER analysis tools. However, MORLET first analyzed the data using the STFT to locate transient, abrupt changes in the seismic signal. The transients contain invaluable information for the geologists since they are due to reflections at the interface of layers of different acoustic impedance, therefore of different content. Unfortunately, MORLET could not find a window of constant width that would allow the elucidation of the transients. As a result he started experimenting with windows of varying widths. He called them "wavelets of constant shape" [69]. The wavelets were obtained by dilations and shifts of a mother wavelet. This way, he built the first wavelet family. Many more were to come. The shape of the wavelet affects the existence of the transform and its inverse, as well as the compression properties of the decomposition. The compression properties of the wavelet transform are going to be extremely important for the application developed in this document. We will describe why in the following section.

Definition 4. *Let f be a time signal. Then*

$$g(s,\tau) = \frac{1}{\sqrt{s}} \int_{-\infty}^{+\infty} f(t)\overline{\psi_{s,\tau}}(t)dt \quad \forall s \neq 0 \tag{2.5}$$

is the Continuous Wavelet Transform (CWT) of f.

It is the inner product of a function of interest f with a wavelet function $\psi_{s,\tau}$ in $\mathcal{L}^1(\mathbb{R})$.

Definition 5. *The function $\psi_{s,\tau}$ is obtained by translations and dilations of the so-called* mother wavelet *Ψ:*

$$\psi_{s,\tau}(t) = \frac{1}{\sqrt{s}}\Psi\left(\frac{t-\tau}{s}\right) \tag{2.6}$$

τ is the translation factor and s is the scale factor.

More specifically in the case of a time signal s is the frequency and τ the time. Thus the signal-windowing problem is alleviated in wavelet analysis by the use of a fully scalable modulated windowing function.

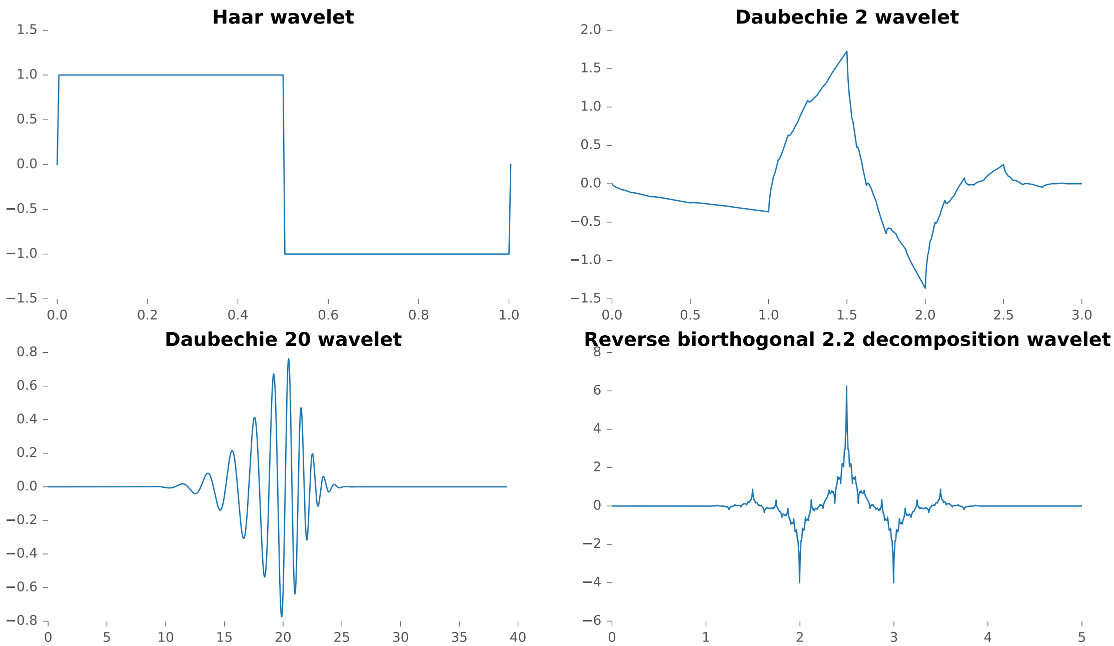

Figure 2.3: *Plots of a few different types of wavelets. From the top left corner clockwise:* Haar *wavelet,* Daubechie 2 *wavelet,* Daubechie 20 *wavelet, reverse biorthogonal* 2.2 *decomposition wavelet.*

2.2 The wavelet transform

We now know the mathematical definition of the wavelet transform (equation 2.5), and we know that it involves a mother wavelet (equation 2.6). However, what exactly constitutes a wavelet from a mathematical standpoint?

2.2.1 Properties of the mother wavelet

For the transform to exist, the mother wavelet Ψ must have the following properties:

- Ψ must oscillate and its integral over its support must be equal to zero,
- Ψ must be square integrable ($\Psi \in \mathcal{L}^2(\mathbb{C})$).

The mother wavelet must also satisfy the *admissibility* and *regularity* conditions.

Definition 6. ***Admissibility*** *A square integrable function Ψ satisfies the admissibility condition if:*

$$\int \frac{|\mathcal{F}[\Psi](\omega)|^2}{|\omega|} d\omega < +\infty \tag{2.7}$$

A wavelet Ψ satisfying the admissibility condition guarantees a signal analysis and reconstruction without loss of information.

Corollary 2. *The admissibility condition implies that the* FOURIER *transform of Ψ vanishes at the zero frequency:*

$$|\mathcal{F}[\Psi](\omega)|^2\Big|_{\omega=0} = 0 \tag{2.8}$$

This observation means that wavelets have a band-pass spectrum and have to oscillate since the average value of the wavelet in time is zero.

A desirable property of wavelets for compression is the fast decaying of the coefficients of the transform. This is related to the regularity condition by the notion of vanishing moments [70]. If a wavelet has N vanishing moments, then the approximation order of the transform is also N. The number of vanishing moments heavily depends on the application and relates to the smoothness of the wavelet.

Definition 7. ***Regularity*** *The wavelet Ψ is said to be r-regular if for any $\alpha \in \mathbb{Z}$:*

$$|\Psi^{(k)}(t)| < \frac{C}{(1 + |t|^\alpha)} \tag{2.9}$$

for $f = 0, \cdots, r$.

2.2.2 Inversion

Definition 8. *If g is the wavelet transform of a function f, then f can be reconstructed from g using the following formula:*

$$f(t) = \frac{1}{C_\psi} \iint\limits_{\mathbb{R}} \frac{g(s,\tau)}{s^2} \psi_{s,\tau}(t) ds d\tau \tag{2.10}$$

where C_ψ is a constant related to the type of wavelet used.

In practice, the uniqueness of the invert transform is guaranteed by the orthonormality of the wavelet basis. Overcomplete wavelet bases can also be used.

2.2.3 In practice

Equations 2.5 and 2.10 give us a theoretical way to apply the wavelet transform. In practice however, those integrals are difficult to compute.

First of all, according to equation 2.5 the wavelet transform is computed by convolving a continuous scalable function and a continuous signal. As a result the wavelet coefficients will be highly redundant. This is not desirable in this case. Also, the signals we are interested in are discrete. Therefore we are going to have to formulate a wavelet transform for discrete signals.

Then, the CWT is computed with an infinite number of wavelets, since s and τ are continuous variables. The mother wavelet is continuously dilated and translated. This makes the transform computation intractable, on top of being redundant.

Finally, equation 2.5 has no analytical solution in most cases and must be computed numerically. These issues can be alleviated, and one way to do that is to use the so-called *dyadic* wavelet transform introduced in the next section.

2.2.4 Dyadic transform

The dyadic transform was derived to make the computation of the wavelet transform tractable. It defines a series of countable dilations and translations of the mother wavelet that ensures full coverage of the spectrum of the function to be analyzed. In practice, the functions ψ are generated from a mother wavelet by:

- dyadic dilation or contraction by a factor $s = 2^j$,
- binary translations: $\tau = ks = 2^j k \quad \forall k \in \mathbb{Z}$.

The location of the wavelet coefficients is shown in figure 2.4. Subsequently, the wavelet functions $\psi_{j,k}$ can be computed simply from the mother wavelet Ψ

Definition 9. *The wavelet function $\psi_{j,k}$ are derived from the mother wavelet Ψ using the following relationship:*

$$\psi_{j,k}(t) = \frac{1}{\sqrt{2^j}} \Psi \left(\frac{t - 2^j k}{2^j} \right) \tag{2.11}$$

Corollary 3. *For a given j and for all k in $\mathbb{Z}$, the supports of the functions $\psi_{j,k}$ are* disjoint *and* contiguous.

Each function $\psi_{j,k}$ is characterized by its scale 2^{-j} and its position k.

Property 1. *In this case, the function f can be reconstructed with the following formula:*

$$f(t) = \sum_{j,k} g(j,k)\psi_{j,k}(t) \tag{2.12}$$

Theorem 1. *The reconstruction is stable under the condition that the energy of the wavelet coefficients is bounded.*

$$A\|f\|^2 \leqslant \sum_{j,k} |\langle f, \psi_{j,k} \rangle|^2 \leqslant B\|f\|^2 \tag{2.13}$$

where $\|f\|^2$ is the energy of the signal f which must be finite, and $0 < A < B < +\infty$. When equation 2.13 is satisfied, the family of wavelets $((\psi_{j,k}))_{j,k}$ is a *frame*. If $A = B$ the frame is said to be *tight* and the wavelet family behaves like an orthonormal basis. If $A \neq B$, exact reconstruction is possible if a dual frame is used, meaning the decomposition wavelet is different from the reconstruction wavelet. To minimize redundancy even further, we can choose discrete wavelets that are orthogonal to their own dilations and translations. However, orthogonality is not essential.

This decomposition avoids the redundancy inherent to equation 2.10. The decomposition corresponds to the analysis of f in vector spaces of different scales $V_0 \subseteq V_1 \subseteq \cdots \subseteq V_m$. The reconstruction of f from its wavelet coefficients is done by taking its mean (scale or resolution

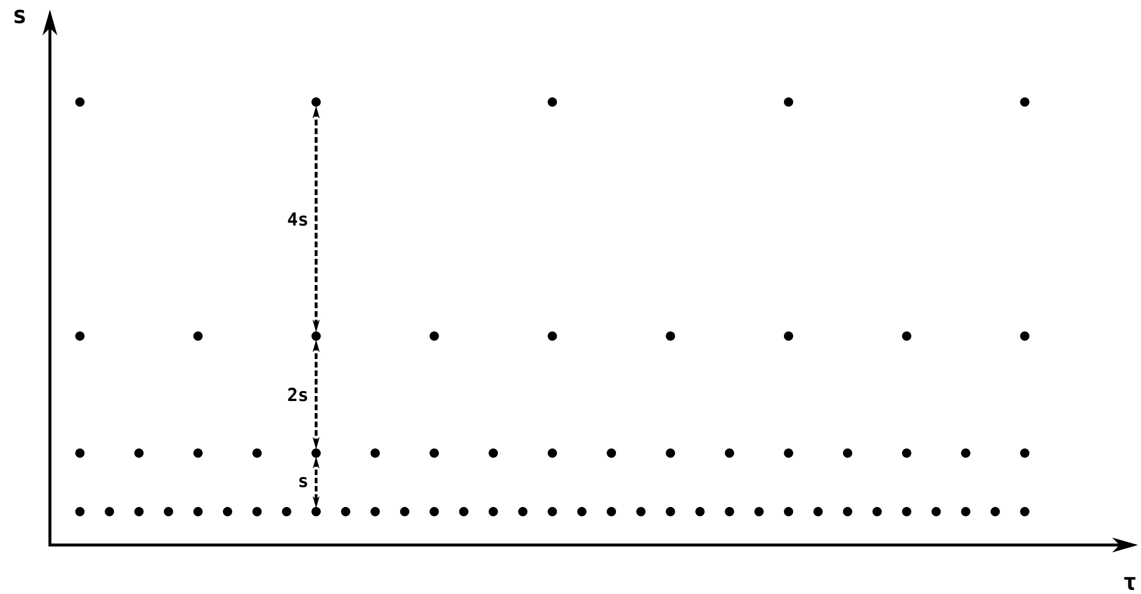

Figure 2.4: *Plots of the location of the wavelet coefficients for the dyadic transform.*

0) and adding the details at finer resolutions recursively. The transform thusly defined is commonly referred to as multi-resolution analysis.

2.2.5 Haar wavelets

Definitions and proofs The Haar wavelet is the first wavelet that was discovered and was described in a 1910 paper [71] as a piecewise constant function.

Definition 10. *The* Haar *mother wavelet is the function* Ψ *such that*

$$\Psi(t) = \begin{cases} 1 & \text{if } 0 \leqslant t < \frac{1}{2} \\ -1 & \text{if } \frac{1}{2} \leqslant t < 1 \\ 0 & \text{otherwise} \end{cases} \tag{2.14}$$

Corollary 4. *The dilations and translations of Ψ generate an orthonormal basis:*

$$\psi_{j,k}(t) = \begin{cases} 1 & \text{if } \frac{k}{2^j} \leqslant t < \frac{k}{2^j} + \frac{1}{2^{j+1}}, \\ -1 & \text{if } \frac{k}{2^j} + \frac{1}{2^{j+1}} \leqslant t < \frac{k+1}{2^j}, \\ 0 & \text{otherwise.} \end{cases} \tag{2.15}$$

that can be written more concisely as:

$$\left(\psi_{j,k}(t) = \frac{1}{\sqrt{2^j}}\Psi(2^j t - k)\right)_{j,k} \tag{2.16}$$

HAAR gave this family of functions as an example of an orthonormal basis for the space of square-integrable functions on $[0, 1]$. It is the simplest wavelet but has the significant disadvantage of being discontinuous and therefore not differentiable.

From equation 2.15, we see that the HAAR functions are supported on the interval $I_{j,k} = \left[\frac{k}{2^j}, \frac{k+1}{2^j}\right[$, therefore they vanish to zero outside of the interval.

Property 2. *The* HAAR *functions verify both conditions to be a wavelet, as described in section 2.2.1. We verify easily that*

$$\forall (j,k) \quad \int_{\mathbb{R}} \psi_{j,k}(t)dt = 0 \tag{2.17}$$

and

$$\forall (j,k) \quad \|\psi_{j,k}\|_2^2 = \int_{\mathbb{R}} \psi_{j,k}(t)^2 dt = 1 \tag{2.18}$$

Moreover, the HAAR functions are pairwise orthogonal.

Property 3. *For all (j_1, k_1) and (j_2, k_2),*

$$\int_{\mathbb{R}} \psi_{j_1,k_1}(t)\overline{\psi_{j_2,k_2}}(t)dt = \delta_{j_1,j_2}\delta_{k_1,k_2} \tag{2.19}$$

where $\delta_{m,n}$ is the KRONECKER *delta.*

The orthogonality comes from the fact that if intervals I_{j_1,k_1} and I_{j_2,k_2} are not equal they are either disjoint or the smaller of the two supports is contained fully in the lower or upper half of the other on which the widest HAAR function is constant. In this case, it follows that the inner product of the two functions is simply equal to the integral of the narrowest HAAR function on its support. This integral is equal to zero according to equation 2.17.

As a result, the family of HAAR functions $((\psi_{j,k}))$ is complete in $\mathcal{L}^2(\mathbb{R})$. In addition, it is a orthonormal family, and therefore a basis of $\mathcal{L}^2(\mathbb{R})$.

This basis spans the space $\mathcal{L}^2(\mathbb{R})$ of functions of finite energy.

Definition 11. *A function f is said to have finite energy if:*

$$\|f\|^2 = \int_{\mathbb{R}} |f(t)|^2 dt < +\infty \tag{2.20}$$

For the remainder of the work, we will need an inner product.

Definition 12. *The inner product $\langle , \rangle$ on $[0, 1[$ is the linear application such that:*

$$\langle f, g \rangle = \int_0^1 f(t)\overline{g}(t)dt \tag{2.21}$$

then any finite energy signal can be represented by its wavelet coefficients.

Property 4. *The wavelet coefficients of f correspond to the projection of f on the wavelet basis using the inner product:*

$$\langle f, \psi_{j,k} \rangle = \int_{\mathbb{R}} f(t)\overline{\psi_{j,k}}(t)dt \tag{2.22}$$

Corollary 5. *The signal can be easily recovered from these coefficients:*

$$f(t) = \sum_j \sum_k \langle f, \psi_{j,k} \rangle \, \psi_{j,k}(t) \tag{2.23}$$

Scaling function The wavelet function is a band-pass filter. The goal of the transform is to cover the full spectrum of a function f with the band-pass spectrum of the wavelet by scaling and dilating it. However, an infinite number of dilations would be require to cover the spectrum down to the 0 frequency. The scaling function associated with a given wavelet is a low-pass filter that is used for the lowest level of the transform to ensure all the spectrum of f is covered. The scaling function associated with the HAAR wavelet is

$$\phi(t) = \begin{cases} 1 & 0 \leqslant t < 1, \\ 0 & \text{otherwise.} \end{cases} \tag{2.24}$$

More information on the wavelet transform as a filter bank and on the scaling function is given in sections 2.2.6, 2.2.7, and 2.2.8.

Properties The HAAR wavelet has several famous properties:

Property 5. *Any continuous real function with compact support can be approximated uniformly by linear combinations of $\phi(t)$, $\phi(2t)$, $\cdots$, $\phi(2^j t)$, $\cdots$ and their shifted functions.*

Property 6. *Any continuous real function on $[0,1]$ can be approximated uniformly on $[0,1]$ by linear combinations of the constant function 1, $\psi(t)$, $\psi(2t)$, $\cdots$, $\psi(2^j t)$, $\cdots$ and their shifted functions [71].*

Property 7. *The HAAR wavelet has a HAAR matrix associated with it:*

$$H_2 = \begin{bmatrix} 1 & 1 \\ 1 & -1 \end{bmatrix} \tag{2.25}$$

and

$$H_{2N} = \begin{bmatrix} H_N \otimes [1,1] \\ I_N \otimes [1,-1] \end{bmatrix} \tag{2.26}$$

where $\otimes$ is the KRONECKER product.

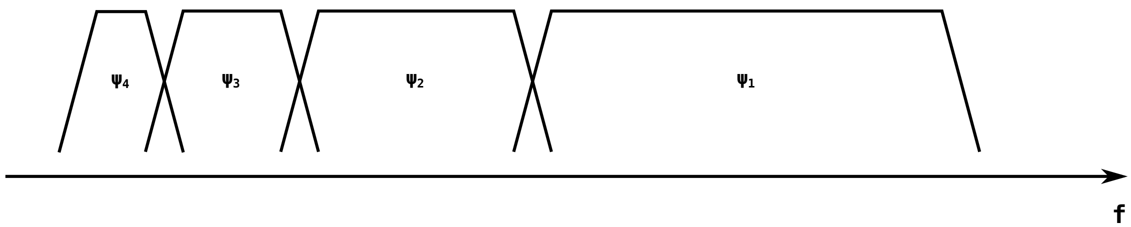

Figure 2.5: *Spectra of correctly designed dilated wavelets.*

The HAAR wavelet transform has noteworthy image compression capabilities. It is used in the JPEG200 file format for image compression [72].

2.2.6 The wavelet transform as a band-pass filter

To make the wavelet transform efficient, we try to reduce the number of wavelets needed, which is in theory infinite. The number of translations is evidently limited by the length of our signal. However how many scales do we need to analyze it properly? From FOURIER theory, we know that scaling in time is equivalent to scaling the spectrum and shifting it.

Property 8. *The* FOURIER *transform of $f(at)$ with $a \neq 0$ is related to the* FOURIER *transform F of $f(t)$ by the following relationship:*

$$\mathcal{F}[f(at)](\omega) = \frac{1}{|a|} F\left(\frac{\omega}{a}\right) \tag{2.27}$$

where F is the FOURIER transform of f. Hence, a compression in time by a factor 2 will translate into a stretching of the spectrum by a factor 2 as well as a frequency shift by a factor 2. We can use this property to cover the full finite spectrum of our signal with the spectra of our dilated wavelets. A correct wavelet design will give the coverage shown in figure 2.5. As a result, if we see a wavelet as a band-pass filter, then a series of wavelets can be seen as a band-pass filter bank.

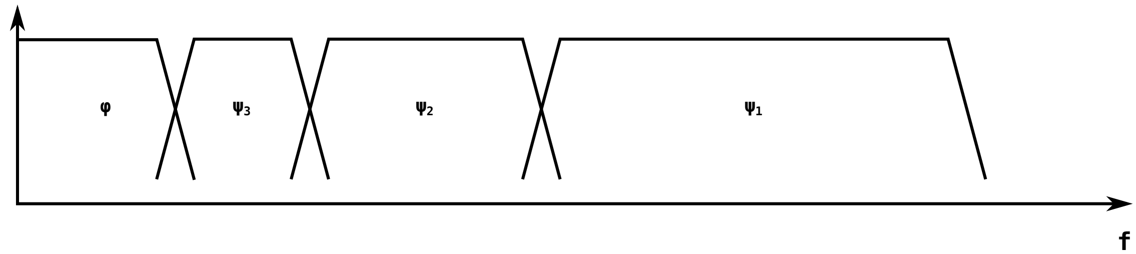

Figure 2.6: *Role of the scaling function φ: how to cover frequencies all the way down to zero.*

2.2.7 Covering the spectrum down to the null frequency: the scaling function

Using the previous technique, we cover the spectrum of a band limited function by stretching and translating a wavelet by a factor 2. However, this technique would require an infinite amount of wavelets to cover all the frequencies down to zero.

The solution to this problem is to use wavelets to cover most of the spectrum, and then use a function that acts as a low pass filter to cover the frequencies all the way down to zero. That function is the *scaling function* and its spectrum is represented in figure 2.6. From the analysis standpoint, the width of the scaling function is very important. It must cover the spectrum from the lowest frequency covered by the wavelet down to the numm frequency to ensure no valuable spectral information is discarded.

The dilated and translated wavelets along with the scaling function form a filter bank.

2.2.8 Calculating the wavelet transform: subband coding

Building on what was explained in the previous paragraph, we consider the wavelet transform as a filter bank made of wavelet functions and a scaling function. Taking the wavelet transform of a signal can thus be seen as passing it through this filter bank. This process is known as *subband coding* and predates the theory of wavelet analysis.

The filter bank needed in the subband coding framework can be derived in different ways. One way is to build a set of bandpass filters that split the spectrum into frequency bands of interest. In that case, we could imagine building the filters so that the spectrum of the signal to analyze is covered where we are expecting the information to be. The main disadvantage of that approach is that the filters have to be designed individually, and they can only work for a particular type of signals.

Another way is to make the process as general as possible. The filter bank is not tailored to the signal of interest. Instead, the spectrum of the signal is divided into two equal parts: a low-pass and a high-pass part. The high-pass contains all the smallest details of the image and the low-pass contains all the rest. One could stop here, but the low-pass part still contains some details. In order to discriminate the details by scale, the low-pass is split in two again, a high-pass and a low-pass part. The high pass contains the next level of details, and so on until we reach the desired number of subbands. The filter bank hence created is an *iterated filter bank*. The process is displayed in figure 2.7. The advantage is that we only have to design two filters. The drawback is that the transform is not adaptive and the spectrum coverage is fixed.

At the end of the process, we are left with a set of band-pass bands with doubling bandwidths and one low-pass bands, as depicted in figure 2.7. This kind of analysis is generally referred to as multi-resolution analysis.

2.2.9 Decimated and non-decimated wavelet transform

After splitting the spectrum in two, the low-pass and the high-pass can be safely subsampled, or decimated, since the sampling frequency needed to preserve the details in the signal or the image is thereby decreased. In particular, since we arranged the filter bank to split the spectrum in two equal parts, the low-pass and the high-pass parts can be subsampled by a factor of 2. In that case, the iteration stops when the length of the subsampled low-pass becomes smaller than the length of the filter. This has become standard in wavelet transform implementations. It has the advantage of limiting redundancy and providing a *de facto* stopping criteria for the decomposition algorithm. However in some cases, we will see

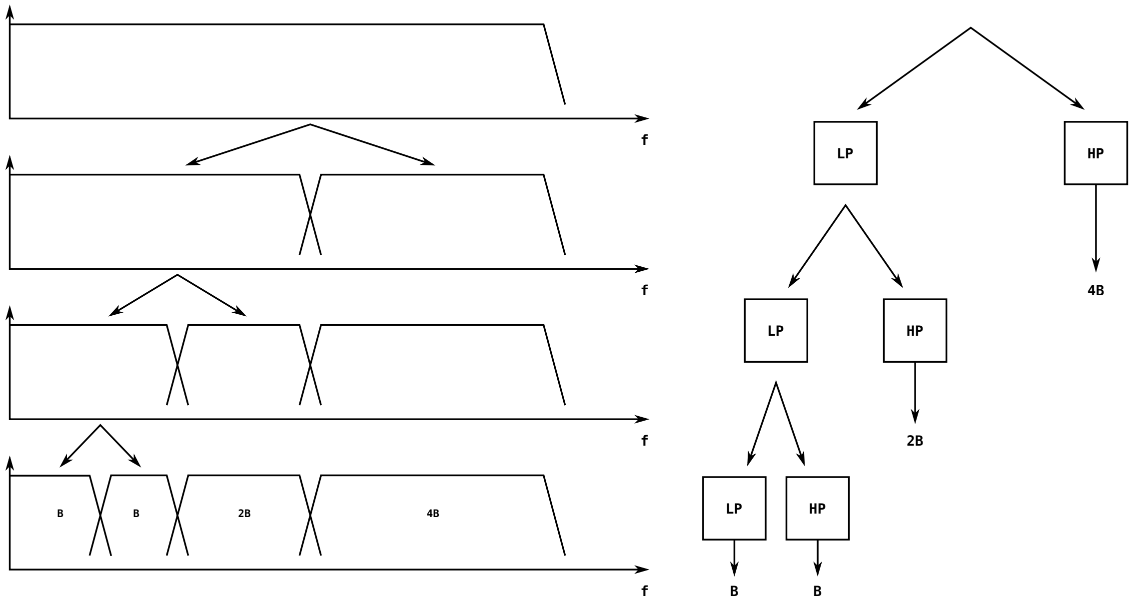

Figure 2.7: *Process of splitting the spectrum of our signal using an iterated filter bank.*

that the added redundancy of the undecimated wavelet transform can be beneficial.

2.3 Extending the wavelet theory: wavelet packet analysis

2.3.1 Wavelet packets

The wavelet packet decomposition is a generalization of the wavelet analysis. Richer than regular wavelets, wavelet packets are an invaluable tool to expand a signal in a variety of ways. The most suitable representation for a signal f can be selected using an entropy-based criterion chosen by the user. Depending on the application, the entropy function, which can also be seen as some form of penalty or cost function, can be adapted to the situation.

As explained in 2.2.8, the wavelet transform is calculated by splitting the approximation coefficients into two parts: the high frequency part with the detail coefficients and the low frequency part with the approximation coefficients at a coarser scale. Then the process is iterated on the approximation coefficients that get split again. The information lost in

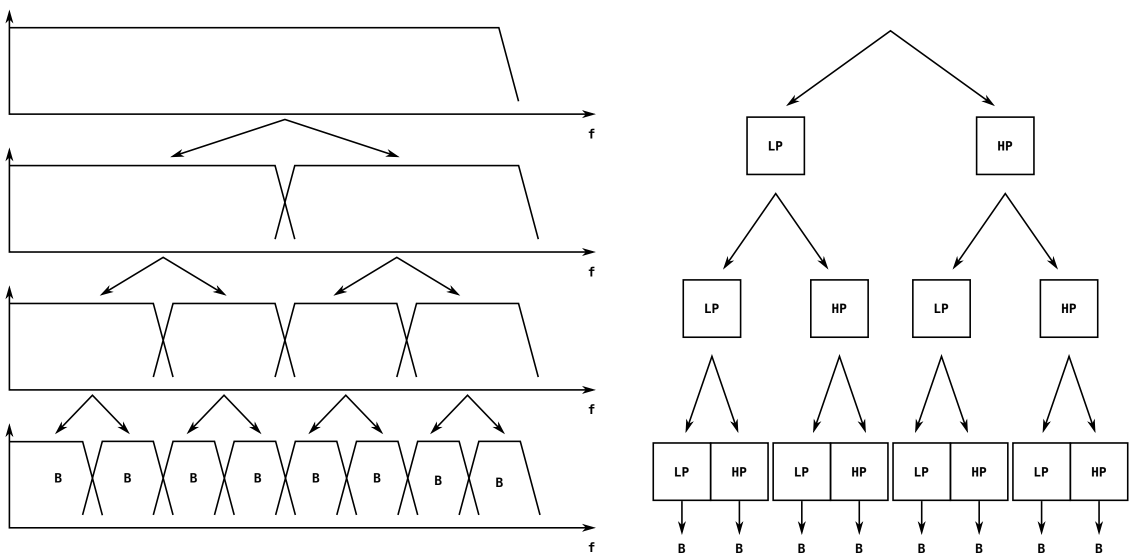

Figure 2.8: *Decomposition of the spectrum of a signal using wavelet packets.*

the approximation is retained in the detail coefficients. However, the details never get re-analyzed.

In the wavelet packet framework, the process of splitting coefficients into two parts, approximation and detail coefficients, is also applied to the detail coefficients. This produces a complete, binary tree as shown in figure 2.8.

The first fundamental observation we can make is that the wavelet packet tree contains the wavelet tree, as well as several other bases. The leaves of every connected binary subtree form an orthogonal basis of the initial space. As a result, any finite energy signal can be exactly reconstructed from any wavelet packet basis, offering an adapted way to code the signal.

2.3.2 Choosing a decomposition

The number of admissible trees can be extremely large, and explicit enumeration of all of them is not an option. Therefore, finding an optimal decomposition with respect to a given, efficiently computable criterion is of particular interest. In general, the criterion corresponds to the minimization of a cost function. The goal is to reduce the redundant wavelet packet tree to the best basis with respect to a given criterion.

Many criteria or penalties can be used depending on the application considered and what the user is trying to achieve. However, criterion functions verifying an additivity property are more desirable in the case of a binary tree structure. Indeed, additivity makes updating of the penalty easier when splitting or merging coefficients.

Theorem 2. *The entropy E must be an additive cost function such that $E(0) = 0$ and*

$$E(s) = \sum_i E(s_i) \tag{2.28}$$

where s is the signal considered and s_i its wavelet packet coefficients.

A list of a few general entropy-based criteria is given below.

Definition 13. **Shannon *entropy***

$$E_{Shannon}(s) = -\sum_i s_i^2 log(s_i^2) \tag{2.29}$$

with the convention that $0log(0) = 0$.

Definition 14. ***l_p-norm entropy***

$$E_{l_p}(s) = \sum_i |s_i|^p \tag{2.30}$$

with $p \in]0, 1]$.

Definition 15. ***Logarithm of the energy entropy***

$$E_{log}(s) = log(s_i^2) \tag{2.31}$$

with the convention that $log(0) = 0$.

Definition 16. ***Threshold entropy***

$$E_\epsilon(s) = \# \{i||s_i| > \epsilon\} \tag{2.32}$$

for a certain threshold ϵ, where # is the cardinality of the set. It corresponds to the number of times the coefficients s_i are greater than the threshold ϵ.

2.3.3 Best basis algorithm

The best basis algorithm was derived by Coifman and Wickerhauser and presented in reference [73]. Essentially, it consists in starting from the bottom of the tree and comparing for each terminal node the entropy of the parent node with the sum of the entropies of the two child nodes. If the entropy of the parent node is smaller than the sum of the entropies of the child nodes, then the child nodes are merged together. Otherwise they remain terminal nodes. This process is iterated over all the terminal nodes until an optimal decomposition is reached. The algorithm is presented in pseudocode in algorithm 1.

Algorithm 1: Best Basis Algorithm

```
Data: a signal s of finite energy.
Result: the best wavelet basis with respect to a certain entropy criterion E.
begin
    compute full binary tree up to level N to get the set w_{n,k} of detail and
      approximation coefficients
    for n ⟵ [N, 1] do
        for k ⟵ [0, n − 1] do
            if node (n, 2k) is a terminal node then
                e_{n,2k} ⟵ E(w_{n,2k})
                e_{n,2k+1} ⟵ E(w_{n,2k+1})
                e_{n−1,k} ⟵ E(w_{n−1,k})
                if e_{n,2k} + e_{n,2k+1} ⩾ e_{n−1,k} then
                    merge nodes (n, 2k) and (n, 2k + 1)
```

2.3.4 Application to l_1-minimization

Depending on the application the user is envisioning, some entropy or cost functions can be more advantageous than others. For some applications the choice is obvious. In the case of Compressive Sensing we want the wavelet packet transform to be a the best sparsifying transform possible. In other words, we are looking for the basis that will lead to the signal expansion with the lowest l_1-norm.

Using the wavelet packet framework, one can improve on the wavelet decomposition. We can choose the l_p-norm entropy described in 3.21 with $p = 1$. Then we can derive the wavelet expansion with the lowest l_1-norm that will lead to a perfect reconstruction using the best basis algorithm described in 2.3.3.

2.3.5 Concluding remarks

There are many more image representations available: curvelets, chirplets, etc. For the purpose of this document, we will not develop on those. However more information can be found in the literature [74–78].

2.4 Sparse representations and compression

Most signals are somewhat structured. That is, if we consider an image with a given number of pixels with values uniformly distributed in the integer interval $[\![0, 255]\!]$, the probability of that image to represent a given scene, object, or person is zero. Intuitively, the subset of signals that are interpretable as "meaningful" is very small compared to the set of all possible signals. A picture of a given scene will have structures such as recognizable shapes, shadows, textures, etc. These features are extremely unlikely to be present in a random image.

2.4.1 Coding images efficiently

From this observation and the fact that it is true for most signals, we can build coding schemes for specific signals that display a given set of features with a high probability. This is the idea behind signal compression. Taking advantage of the knowledge we have on a set of features of a given type of signal, we can derive very efficient coding strategies. In terms of compression, an efficient coding strategy will take advantage of the features of the signal to find a basis in which it can be expressed with the smallest amount of non-zero coefficients. In other words, the signal possesses a sparse expansion in that basis.

Most real-life signals are not directly sparse in their acquisition basis. Also, most signals do not have a purely sparse expansion, for example because of the presence of noise. However, those signals are very often compressible. This means that there exists a basis in which the signal coefficients decay rapidly. A compelling example is the compression of images. Most natural images can be reconstructed from very few of their wavelet coefficients, making the wavelet transform suitable for image compression. Such an example is shown in figure 2.9.

A good representation is efficient. This means it uses few coefficients to describe the full signal or image. An image is then compressible in a certain representation space if its sparse approximation in the transform domain yields a good reconstruction. Mathematically we want the mean squared error of the reconstruction to be small. It is the case with the wavelet transform. By construction it separates the details of an image from the rest at different scales. The sparsification is inherent to this construction: the detail coefficients are generally sparse even for complex images, and the slowly varying content is captured by the scaling function on very few pixels as can be seen in figure 2.9.

Even though it has never been adopted by the general public, wavelet compression is routinely used in the JPEG2000 format. Thanks to the properties of wavelets, it is more efficient in terms of data compression than the older JPEG format that relies on the Discrete Cosine Transform to compress images. However, it requires a lot more computational power which explains why its use is primarily limited to the medical imaging field. At the time the format was developed, personal computers were not powerful enough to render a JPEG2000 image in a timely fashion.

2.4.2 Sparsity and image compression

A vector is said to be k-sparse if and only if it has k non-zero coefficients. As a result a k-sparse vector has only k degrees of freedom and lives in a k-dimensional space. Moreover

Figure 2.9: *(Left) Original picture. (Center) Log-scaled wavelet transform of the image, displayed DR: 60 dB. (Right) Reconstruction of the image from 26% of its most significant wavelet coefficients, energy retained: 99.8%.*

there are $C(n,k) = \frac{n!}{(n-k)!k!}$ k-combinations of n, or ways to fill a k-sparse vector.

If we look at the cost of coding any n float vector, we get $\mathcal{O}(n)$. Now if we look at the cost of coding a k-sparse vector, we get $\mathcal{O}\left(k \log_2(\frac{n}{k})\right)$. The advantage is clear: the sparser the signal the cheaper it gets to store it. What if that was true for the acquisition as well? In many applications, a lot of data is acquired to produce a final "object" for the user, for example an image. Then comes a compression step. That step usually involves performing a lossy compression, hence discarding some of the data that was acquired earlier. What if instead of acquiring the signal in a traditional, evident acquisition basis it were possible to only acquire its largest coefficient in a basis were the signal is guaranteed to be sparse? Then the number of acquisitions needed would decrease drastically, and the information acquired would be used more efficiently, rendering the well-known SHANNON sampling theory [79] obsolete. It is one of the aspect of signal acquisition that Compressive Sensing addresses.

Chapter 3

Compressive Sensing and l_1-regularization

3.1 Introduction

Over the past 10 years, Compressive Sensing has gained a lot of visibility from the medical imaging research community. The most compelling feature for the use of Compressive Sensing is its ability to perform perfect reconstructions of under-sampled signals using l_1-minimization. Of course, that counter-intuitive feature has a cost. The lacking information is compensated for by *a priori* knowledge of the signal, as well as certain mathematical conditions detailed further in this work.

So far, Compressive Sensing has proven to be particularly well suited for MRI, where the assumptions of the Compressive Sensing theory can easily be justified, and the implementation is fairly straightforward [80]. It has allowed for faster image acquisition without loss in image quality and resolution, which is critical for applications such as cardiac MRI. The application of Compressive Sensing to ultrasound imaging is not as straightforward due to the very nature of the acquired signal and the inverse problem that needs to be solved.

This section presents the basics of Compressive Sensing and aims at giving the reader the minimal background necessary to understand the assumptions and underlying constraints of this technique.

3.2 Motivation

In this section, we present a simple, compelling example of why compressive acquisition can be beneficial. Then we focus on MR imaging as a hands-on example of how Compressive Sensing can be implemented in real-life applications. MRI is inherently a slow acquisition modality where a patient needs to be immobilized for a long period of time to produce good images [81]. The natural question one might ask is: is there a way to make it faster?

3.2.1 A little bit of intuition

In many applications, solving a problem requires finding a solution to an underdetermined set of linear equations. A problem is said to be underdetermined when then number of equations is less than the number of unknowns. There exists many examples of such cases, and this section aims at giving a simple illustration.

Definition 17. *Let us consider a signal $x[t]$, with $t = 0, \cdots, n-1$. The Discrete* Fourier *Transform (DFT) of x is given by*

$$\mathcal{F}\{x[\omega]\} = \sum_{t=0}^{n-1} x[t] e^{-2j\pi \frac{\omega t}{n}} \tag{3.1}$$

for $\omega = 0, \cdots, n-1$.

We assume that the signal is acquired in the Fourier domain, meaning that we sample the DFT of x. This is the case for MRI, for example, as we will see later. In many applications, there is not enough time to acquire all the coefficients of the DFT of x. So let us assume that we collected $m \ll n$ DFT coefficients. We end up with an underdetermined system $y = Ax$ where y corresponds to the coefficients of the DFT of x that we have acquired, and A is the equally under-sampled DFT matrix. How does one recover x from what appears to be a highly incomplete view of its spectrum?

The general form of the problems we are tackling is a n-dimensional vector x, a m-dimensional measurement vector y with $m \ll n$, and a linear operator A that links x to y

$$y_k = \langle a_k, x \rangle \quad \text{with} \quad k = 1, \cdots, m \ll n \tag{3.2}$$

where $\langle , \rangle$ is the inner product and a_k is the k^{th} row of A. Since A is not invertible and we have no additional information on the missing data, there is an infinite number of solutions to this problem. It is seemingly impossible to choose which one is the correct one without additional information. The theory of Compressive Sensing was designed for this particular purpose. It was shown [82] that with a "*bit of structure*" [83], it is possible to find the desired solution in most cases using convex programming techniques.

By structure, the instigators of Compressive Sensing mean sparsity, or the knowledge that a sparse expansion of the signal exists in a known basis. Sparsity can be seen as the true number of degrees of freedom of a signal. In the case of matrix completion, a domain also tackled by Compressive Sensing, structure means low-rank. Again it can be linked to the number of degrees of freedom of the matrix. But is this knowledge of the structure of the signal sufficient?

Naturally, the answer is no. As a simple counter example, consider a 1-sparse 10-dimensional vector x whose only non-zero coefficients is the tenth. Suppose the acquisition consists in sampling the first 5 coefficient values. The matrix A has the form

$$\begin{pmatrix} I_5 & 0_5 \\ 0_5 & 0_5 \end{pmatrix} \tag{3.3}$$

where I_5 is the 5×5 identity matrix and 0_5 is the 5×5 null matrix. The acquisition of our vector x can be expressed as

$$y = Ax = 0 \tag{3.4}$$

Since $y = 0$, it will be impossible to recover x no matter what we do. Thus it is important for x to not be in the null space of A to ensure some information about x is acquired.

One way to make certain of this is to consider an incoherence property which states that while x is sparse, the rows of A must not. Each measurement y_k is a weighted sum of all the components of x. Another way to look at it is to say that each a_k in A must not correlate well with x. As a result, all the y_k contain a little bit of the information in x.

Under such conditions, the number of equations needed to solve the problem is roughly equivalent to the number of degrees of freedom of the original signal.

3.2.2 Digital photography and the sensor waste

The sensor of a digital camera is made out of millions of photosites. Each photosite is a unique sensor that acquires a tiny part of the image projected on its surface by the lens while exposing a shot. After the light intensity value is recorded by the sensor, the data is processed in the memory of the camera to output a compressed file, generally a JPEG.

JPEG compression is lossy. The raw data is decomposed on a discrete cosine basis, the most significant coefficients are encoded into the JPEG file while the others are purely and simply discarded. So we go from *data* acquired with millions of photosites to *information* encoded in a few kilobytes. Obviously, this is a wasteful process.

Compressive Sensing is a technology that takes advantage of the compressibility of a photograph, for example, to perform the data acquisition in an already compressed form. Since only a few discrete cosine coefficients (typically a 10^5 order of magnitude) can describe most million pixel images, why not try to acquire those coefficients, and not the others since they are to be discarded anyway? Another way to look at it is to realize that most images have a number of degrees of freedom in a discrete cosine space that is much smaller than the number of sensors used for the acquisition.

Compressive Sensing offers a way to acquire just the amount of data needed by sampling and compressing at the same time and by providing efficient decompression algorithms.

3.2.3 MR imaging: the ideal case for Compressive Sensing

MRI is a good candidate for Compressive Sensing, mostly for two reasons:

- MR images are compressible by sparse coding in an appropriate transform domain, the wavelet domain in most cases,
- MRI scanners acquire encoded information, as opposed to pixels for example, since the acquisition takes place in the FOURIER domain.

Hence, an MRI system can be used in a Compressive Sensing configuration:

- The user controls the gradients, as well as the RF pulses, which in turn control the phase of the voxels in the image,
- The MR signal is received by a coil in the encoded form of k-space samples,
- Therefore the user can modify the MRI pulse sequence to perform incoherent measurements of the k-space,
- Non-linear reconstruction with a sparsity condition allows the reconstruction of an image.

3.2.4 Theory of MRI in brief

The MRI signal comes from the resonance of protons in the body. The main contribution to the signal comes from water. The patient is placed in a strong, static magnetic field $\mathbf{B_0}$ that polarizes the protons. A radio-frequency (RF) excitation $\mathbf{B_1}$ is then applied, producing a transverse magnetization $m(\mathbf{r})$ that precesses, generating an emission of RF signal detected

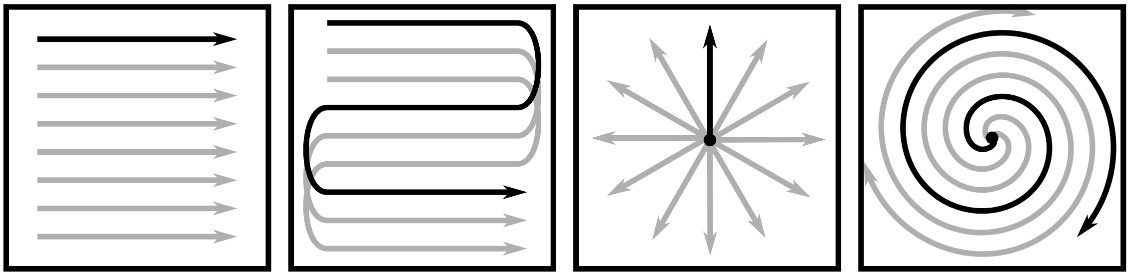

Figure 3.1: *A few common acquistion trajectories in the k-space: the resolution of the reconstructed image depends on the coverage of the k-space, and the field-of-view by the sampling density. If the* NYQUIST *criterion is not respected, artifacts of shapes dictated by the sampling strategy appear.*

by receiver coils. The transverse magnetization $m(\mathbf{r})$ can be made proportional to the proton density in the body, as well as other properties [81]. The goal of the MR reconstruction process is to visualize $m(\mathbf{r})$.

The information is spatially encoded using linear gradients of magnetic fields: $\mathbf{G} = \begin{pmatrix} G_x \\ G_y \\ G_z \end{pmatrix}$. The gradient changes to resonance frequency of the protons, based on their location in the body, making spatial discrimination of the signals possible. It can be shown that an MR measurement signal s can be expressed as:

$$s(t) = \iiint_{\mathcal{V}} m(\mathbf{r}) e^{-i2\pi\mathbf{k}(t)\cdot\mathbf{r}} d\mathbf{r} \tag{3.5}$$

where $\mathcal{V}$ is the volume of the reconstructed area [81]. Equation 3.5 visibly corresponds to the FOURIER transform of $m(\mathbf{r})$ sampled at the spatial frequency $\mathbf{k}(t)$. Many sampling strategies exist, and the result of the engineering of a magnetic gradient for MRI is commonly referred to as a pulse sequence [84–86].

3.2.5 MR acquisition and image reconstruction

The pulse sequence drives the acquisition in the k-space which is the FOURIER domain. In the MR lingo, 1 acquisition corresponds to 1 RF pulse sequence, hence 1 point in the

k-space. The sampling of the k-space follows a specific trajectory designed to meet the NYQUIST criterion. The coverage and density of the trajectory dictates the resolution and the field-of-view. If the trajectories are lines, the reconstruction algorithm is conveniently a simple inverse Fast FOURIER Transform (FFT).

If a trajectory does not meet the NYQUIST criterion, artifacts appear. The shape and strength of the artifacts depend on the shape of the trajectory. For example aliasing if the density is too low for a linear trajectory. One should note here that a random downsampling of the k-space will lead to a multitude of weak artifacts that will look just like noise. This is the phenomenon of incoherent aliasing: since the downsampling is random, each contribution leads to different artifacts that do not add up. This phenomenon will be exploited in the MRI implementation of Compressive Sensing.

3.2.6 Limitations

Beter performace can be obtained with higher gradient amplitude. However, it is a well-known and demonstrated fact that high gradient amplitudes in conjunction with rapid switching of the magnetization can lead to peripheral nerve stimulation causing negative effects to the patient. From a minor discomfort to actual pain, this phenomenon can present a risk when imaging the heart, for example. As a result, physiology imposes a limit to the system's performance [81].

Naturally, the question of overcoming this limitation arises. The benefit is clear: make MR acquisitions faster, without degrading the image quality. Compressive Sensing is one of the efforts that have been developed in that direction over the past 10 years.

3.2.7 Application of Compressive Sensing to MRI

Natural images are often compressible by encoding of their information in an appropriate transform space. A few common transform-based compression schemes are JPEG, JPEG2000, and MPEG [72, 87]. The strategy of such transform-based compression algorithms is to apply a sparsifying transform to the image or video in order to get a vector of rapidly decaying coefficients. The image is then compressed by selecting the largest coefficients and encoding their location. The smaller coefficients are discarded. Depending on the image and the application, one such transform can be the Discrete Wavelet Transform (DWT), finite-differencing, the Discrete Cosine Transform (DCT), etc. In the case of dynamic imaging, a potential pseudo-periodicity of the signal can also be exploited.

MRI has the advantage of:

- the encoded nature of the acquisition,
- the sparsity of the images (for example angiography) or their compressibility.

The basic principle of Compressive Sensing is to make a small number of measurements, that are random-like linear combinations of signal values. By small, we mean smaller than the number of samples that are necessary under SHANNON's theory. This makes sense only if the signal is compressible since less samples are needed in the transform domain, where the number of degrees of freedom is reduced. Thus good reconstruction is possible from fewer measurements through a non-linear process. In the case of MRI, this would mean acquiring random samples in the k-space rather than the entire grid.

In order to be successful, a Compressive Sensing acquisition scheme must have:

- **Transform sparsity**: the image we are reconstructing must have a sparse expansion in a known transform domain. In other words, it must be compressible by transform coding.
- **Incoherence of undersampling artifacts**: the undersampling artifacts that appear when linearly reconstructing the image must be incoherent in the transform domain. In other words, the artifacts must be noise-like.
- **Non-linear reconstruction**: the reconstruction method should be non-linear and enforce sparsity of the reconstruction as well as its consistency with the data acquired.

The question of how to randomly sample the k-space is not trivial, and is beyond the scope of this document. We will just accept that a pseudo-random sampling of the k-space leading to low coherence of the artifacts exists. Then the image I can be recovered. Let Ψ be the transform coding matrix, and $\mathcal{F}_S$ the under-sampled FOURIER transform. The image I is recovered by solving the problem:

$$\min \|\Psi I\|_1 \;\text{ s.t. }\; \|\mathcal{F}_S I - y\|_2 < \epsilon \tag{3.6}$$

where y is the measured k-space data that we acquired, and ϵ governs the fidelity of the reconstruction to the data.

Definition 18. *The l_1-norm of a vector x is defined by*

$$\|x\|_1 = \sum_i |x_i| \tag{3.7}$$

The first term in equation 3.6 promotes sparsity [82, 88, 89]. The second term enforces data consistency.

This reconstruction scheme can be used for:

- **Angiography**: a contrast agent is injected into the patient's blood stream, effectively increasing the blood signal, and imaged in 3D. Capturing the dynamics of the contrast agent is crucial to this application. However it requires high spatial and temporal resolution as well as a large field-of-view. Traditional sampling fails at accomplishing this task, but Compressive Sensing is perfectly suitable for it.

- **Coronary imaging**: imaging coronary arteries is a challenging task since they are constantly in motion. The number of acquisitions is generally limited to the number of heart beats during one breath hold. Each acquisition needs to be very short to avoid motion blurring. Compressive Sensing can be used to decrease acquisition time, allowing the whole heart to be imaged in a single breath hold.

- **Brain imaging**: Compressive Sensing can reduce acquisition time while improving resolution of the most common clinical application of MRI.

3.3 A Compressive Sensing primer

Compressive Sensing relies mainly on two fundamental assumptions related to the acquired signal: *sparsity* and *incoherence*. The sparsity assumption is exploited in the form of an l_1-norm minimization algorithm that reconstructs the signal. The attentive reader might notice a discrepancy here. In fact, a good question to ask is: since we are trying to reconstruct a sparse vector, shouldn't we try to minimize the number of non-zero coefficients it has?

3.3.1 The sensing framework

We consider a continuous time domain signal of interest f that we want to sample. We assume that the information about f is acquired by inner products with a set of waveforms φ_k:

$$y_k = \langle f, \varphi_k \rangle \ \ \forall k = 1, \cdots, m \tag{3.8}$$

where m is the number of waveforms used to sample f, and thus the number of measurements. This process is equivalent to correlating the signal f with the waveforms φ_k. This is indeed a classic sampling scheme. For example, if the waveforms φ_k are spikes, or Dirac δ functions δ_k, we find that the above process is equivalent to traditional sampling:

$$y_k = \langle f, \delta_k \rangle = f[k] \tag{3.9}$$

Similarly, if φ_k is a sinusoid, then y_k is a Fourier coefficient, which is found for example in MR imaging. The theory of Compressive Sensing focuses on under-sampled signals, such that $m \ll n$ where n is the dimension of the signal f. In the case of traditional sampling, n is the number of samples imposed by the Nyquist-Shannon criteria.

The questions that arise from this are the following:

- Is it possible to accurately reconstruct f from $m \ll n$ measurements?
- How to design $m \ll n$ waveforms φ_k that capture most of the information of the signal?
- If so, how can we approximate f from this information?

If A denotes a $m \times n$ sensing matrix with the vectors $\overline{\varphi_1}, \cdots, \overline{\varphi_m}$ as rows, then the acquisition process is given by

$$y = Af \tag{3.10}$$

In general, recovering f from y is ill-posed when $m < n$ since there is an infinity of solutions. However, if we know about the structure of the signal, we can find a solution. Compressive Sensing is based on two fundamental premises: sparsity and incoherence.

3.3.2 Sparsity

Many natural signals have a sparse representation in some basis as we saw with figure 2.9, which makes them compressible by transform coding.

A vector $x \in \mathbb{R}^n$ is said to be S-sparse if all but S of its coefficients are equal to zero. Considering a basis $\Psi = (\psi_i)_{i=1,\cdots,n}$ of the signal space, we have:

$$x = \sum_{i=1}^{n} x_k \psi_i \tag{3.11}$$

where the $(x_i)_{i \in (1,\ldots,n)}$ are the coefficients of x in the basis Ψ.

In that framework, x is said to be S-sparse if the subset $\Omega = \{i \mid x_i \neq 0\}$ is of cardinality S. Equivalently the condition $\|x\|_{l_0} \leqslant S$ must hold true. $\|x\|_{l_0}$ is the l_0-pseudonorm defined as the number of non-zero coefficients of x.

The energy of a sparse signal in a certain basis is concentrated on a few samples. The target number of acquisition being low, each measurement has to provide as much information as possible. For that reason the acquisition is performed in a different basis where the energy of the signal is spread out on as many samples as possible. Intuitively, the two bases are incoherent, enabling fewer measurements containing all the information required for accurate reconstruction.

As mentioned by ROMBERG in [90],

A good signal representation can fundamentally aid the acquisition process.

3.3.3 Incoherence

The coherence between two bases Φ and Ψ is usually defined as the maximum absolute value of the cross-correlation between the elements of the two bases [91]:

$$\mu(\Phi, \Psi) = \sqrt{n} \cdot \max_{1 \leqslant k,j \leqslant n} | < \varphi_k, \psi_j > | \tag{3.12}$$

This value corresponds to the maximum of correlation between any two vectors of Φ and Ψ. If the vectors are correlated, then μ is large. If they are uncorrelated, μ is small. The value of μ is always between 1 and $\sqrt{n}$.

In Compressive Sensing, we are looking at low μ values which corresponds to *incoherent* bases. To clarify the notion of incoherence, consider the following three examples:

Φ is a spike basis, Ψ is the FOURIER basis Quick calculation shows that in that case $\mu = 1$, the maximal incoherence. Indeed, spikes and sinusoids are incoherent in any dimension.

Φ is the noiselet basis, Ψ is the HAAR wavelet basis Noiselets were derived to be as incoherent as possible with HAAR wavelets. It has be shown that in that case $\mu = \sqrt{2}$. Noiselets are also maximally incoherent with spikes and incoherent with the FOURIER basis.

Φ is an orthonormal basis picked at random, Ψ is any basis Then μ is approximately $\sqrt{2\log n}$.

3.3.4 The reconstruction of under-sampled sparse signals

Assuming that the acquisition is limited to $m \ll n$ samples, we collect the data y_k according to the following process:

$$y_k = \langle f, \varphi_k \rangle \quad k \in M \tag{3.13}$$

where M is a subset of $\{1, \cdots, n\}$ of cardinality $m \ll n$. We decide to recover the signal from the information at hand by l_1-minimiation. The reconstruction f^* is $f^* = \Psi x^*$ where x^* is the solution to the problem

$$\min \|x\|_{l_1} \quad \text{s.t.} \quad y_k = \langle \varphi_k, \Psi x \rangle \quad \forall k \in M \tag{3.14}$$

This means that among all the possible solutions $f = \Psi x$ consistent with the data, we choose the one with the minimal l_1-norm. If f is sparse enough, then the reconstruction is exact.

3.3.5 Why minimizing the l_1-norm?

In practice, the number of non-zero coefficients in a vector is given by the so-called l_0-norm.

Definition 19. *The l_0-norm is defined by:*

$$\forall x, \quad \|x\|_{l_0} = \#\{x_i | x_i \neq 0\} \tag{3.15}$$

Unfortunately, the "l_0-norm" is in fact not a norm in the mathematical sense. It is a pseudonorm since it does not satisfy the homogeneity requirement. In fact, we have:

$$\|\lambda x\|_{l_0} = \|x\|_{l_0} \quad \forall x \tag{3.16}$$

Therefore, the expectation that one could solve the following problem:

$$\min \|\Psi I\|_0 \ \text{ s.t. } \ \|\mathcal{F}_S I - y\|_2 < \epsilon \tag{3.17}$$

falls flat. This problem is infamously computationally intractable. It is a NP-hard problem.

The l_1-norm is used as an approximation of the l_0-pseudonorm to make the computation tractable. Historically, the l_1-norm has been used in various applications as a natural promoter of sparsity. One way to understand how the l_1-norm promotes sparsity is to consider a vector $\mathbf{x} = (1, \epsilon) \in \mathbb{R}^2$ with $\epsilon \ll 1$. Then the l_1- and l_2-norms of $\mathbf{x}$ are given by, respectively:

$$\|\mathbf{x}\|_{l_1} = 1 + \epsilon \qquad \text{and} \qquad \|\mathbf{x}\|_{l_2}^2 = 1 + \epsilon^2 \tag{3.18}$$

Now if we reduce, as part of the regularization procedure, the magnitude of one of the coefficients of $\mathbf{x}$ by $\delta \leqslant \epsilon$, say x_1, the resulting norms become:

$$\|\mathbf{x}\|_{l_1} = 1 - \delta + \epsilon \qquad \text{and} \qquad \|\mathbf{x}\|_{l_2}^2 = 1 - 2\delta + \delta^2 + \epsilon^2 \tag{3.19}$$

On the other hand, reducing x_2 by δ gives:

$$\|\mathbf{x}\|_{l_1} = 1 - \delta + \epsilon \qquad \text{and} \qquad \|\mathbf{x}\|_{l_2}^2 = 1 - 2\epsilon\delta + \delta^2 + \epsilon^2 \tag{3.20}$$

As a result, in the case of a l_2-penalty, reducing the larger term x_1 leads to a much greater reduction in norm than doing so to the smaller term x_2. In the case of the l_1-penalty, the reduction in norm is the same for both coefficients.

Thus, a model using an l_2-penalty is very unlikely to set any coefficients to zero, since the reduction in coefficients approaches zero when the coefficient is small. On the other hand, a model based on a l_1-penalty will see a reduction by δ in both cases.

Considering the l_p-norm:

$$\|\mathbf{x}\|_p = \left(\sum_i |x_i|^p \right)^{\frac{1}{p}}, \qquad \forall p \in]0,1] \tag{3.21}$$

we observe that the more p approaches zero, the more the norm promotes sparsity.

3.3.6 How sparse should a signal be?

A natural question that arises from the previous observation is: how do we know that a signal is sufficiently sparse?

Theorem 3. *Let f be a signal, and x its coefficients in the basis Ψ such that x is a S-sparse vector. Suppose that we perform m measurements of f uniformly at random in the domain Φ. Then if*

$$m \geqslant C \cdot \mu^2(\Phi, \Psi) \cdot S \cdot \log n \tag{3.22}$$

for $C > 0$, the solution to the minimization problem 3.14 is exact with overwhelming probability [92].

Corollary 6. *The probability of exact recovery is greater than $1 - \delta$ if*

$$m \geqslant C \cdot \mu^2(\Phi, \Psi) \cdot S \cdot \log n \tag{3.23}$$

A few comments can be made of theorem 3 and equation 3.22:

1. The lower the coherence, the fewer measurements we need, making the significance of incoherence evident.

2. The entirety of the information is preserved if we make any m measurements.

3. The signal can be recovered from the compressed dataset by convex minimization without further assumptions on the total number of non-zero coefficients of x, their location, and their amplitude.

We can see a data acquisition protocol emerge from all this:

- **sample** non-adaptively in an incoherent domain,
- **decode** the data using l_1-minimization.

We have shown that Compressive Sensing could recover sparse under-sampled signals from a few measurements. However, in order to be useful as an acquisition paradigm, Compressive Sensing has to be robust to signals that are only nearly sparse, as well as noise. In fact, most natural signals are compressible, or approximately sparse in a certain basis, but not exactly sparse. Can Compressive Sensing reconstruct *compressible* signals from just a few measurements? And since most acquisitions are corrupted by a certain level of noise, can Compressive Sensing accurately reconstruct compressible signals from *noisy* data? Finally, another desirable feature is *stability*: does a small perturbation in the data translate to a small perturbation in the reconstruction?

3.3.7 Robustness to non-sparse signals

From now on, we will assume that the acquisition takes the form

$$y = Ax + z \tag{3.24}$$

where z is the additive noise vector. We have $f = \Psi x$, and $y = D\Phi f$ where D is a decimation, or undersampling, matrix that selects m coefficients at random. Thus the sensing matrix A is given by $A = D\Phi\Psi$.

For the rest of this development, we need to introduce a new, useful tool: the so-called *Restricted Isometry Property*, or RIP.

Definition 20. $\forall S \in \{1, 2, \cdots\}$, *the isometry constant* δ_S *of a matrix* A *is defined to be the smallest number such that*

$$(1 - \delta_S)\, \|x\|_{l_2}^2 \leqslant \|Ax\|_{l_2}^2 \leqslant (1 + \delta_S)\, \|x\|_{l_2}^2 \tag{3.25}$$

holds for all S-sparse vectors x [93].

Hence, a matrix A obeys the RIP of order S if δ_S is not too close to 1. It follows from this that if the RIP holds, then A approximately preserves the Euclidean length of S-sparse vectors, which in turn implies that any S-sparse vector cannot be in the null space of A, which would make any attempt to reconstruct such a vector unsuccessful.

This result is fundamental. In fact, if we consider two S-sparse vectors x_1 and x_2, we have that $x_1 - x_2$ is $2S$-sparse. Then if the $2S$-RIP holds for A, we have

$$(1-\delta_{2S})\left\|x_1 - x_2\right\|_{l_2}^2 \leqslant \left\|Ax_1 - Ax_2\right\|_{l_2}^2 \leqslant (1+\delta_{2S})\left\|x_1 - x_2\right\|_{l_2}^2 \tag{3.26}$$

with δ_{2S} not too close to 1. This means that the sensing matrix A approximately preserves Euclidean distances, guaranteeing the possibility of algorithmically discriminating S-sparse vectors or signals based on their compressed measurements.

Theorem 4. *If $\delta_{2S} < \sqrt{2} - 1$, then the solution x^* to 3.14 obeys*

$$\begin{cases} \|x^* - x\|_{l_2} \leqslant & C_0 \cdot \frac{\|x - x_S\|_{l_2}}{\sqrt{S}} \quad \textit{and} \\ \|x^* - x\|_{l_1} \leqslant & C_0 \cdot \|x - X_S\|_{l_1} \end{cases} \tag{3.27}$$

for $C > 0$, where x_S is the S-sparse approximation of x, that is the vector x with all but its largest S coefficients set to 0 [94–96].

Theorem 4 states that if x is not S-sparse, then the Compressive Sensing reconstruction is at least as good the S-sparse approximation of x, denoted by x_S. The previous results are strong, but raise a new question: how to design a matrix A that is S-RIP with S close to m? Before giving examples of such matrices, we examine the robustness of Compressive Sensing to noisy data.

3.3.8 Robustness to noisy data

In the presence of noise, we relax the constraint to solve the following problem:

$$\min \|x\|_{l_1} \quad \text{s.t.} \quad \|Ax - y\|_{l_2} \leqslant \epsilon \tag{3.28}$$

This problem is the so-called LASSO [97].

Theorem 5. *Assuming that $\delta_{2S} < \sqrt{2} - 1$, the solution x^* to 3.28 obeys*

$$\|x^* - x\|_{l_2} \leqslant C_0 \cdot \frac{\|x - x_S\|_{l_1}}{\sqrt{S}} + C_1 \cdot \epsilon \tag{3.29}$$

for $C_0 > 0$ and $C_1 > 0$ [95].

The interpretation of theorem 5 is fairly straightforward: the reconstruction error is bounded by the sum of the reconstruction error from noiseless data, and the noise level.

It follows that Compressive Sensing is robust to noisy data.

3.3.9 Examples of random sensing matrices

One can obtain a sensing matrix A that obeys the RIP by

- sampling n columns uniformly at random on the unit sphere of $\mathbb{R}^m$,
- sampling i.i.d. entries from the normal distribution with mean 0 and variance $\frac{1}{m}$,
- sampling a random projection P,
- sampling i.i.d. entries from a symmetric BERNOULLI distribution.

All the previous strategies lead to RIP compliant sensing matrices if

$$m \geqslant C \cdot S \cdot \log\left(\frac{n}{S}\right) \tag{3.30}$$

3.3.10 Non-linear reconstruction

To give the reader intuition on how Compressive Sensing reconstruction actually works, a one-dimensional heuristic case is presented in this section. Figure 3.2 shows how a signal can be recovered from random under-sampled acquisitions using the iterative thresholding algorithm.

Figure 3.2.a shows a sparse signal. The data acquisition happens in the k-space, shown in figure 3.2.b. In the case of an equispaced undersampling of the k-space, the reconstructed signal will show aliasing leading to ambiguity. If the undersampling is somewhat random then the artifacts generated in the signal space are not coherent and create a noise-like pattern added to the signal we are reconstructing, as shown in figure 3.2.c.

The first step of the iterative thresholding algorithm is to select the most significant coefficients in the signal space (figure 3.2.d), and set the other ones to zero (figure 3.2.e). This first approximation of the signal is then used to calculate what the acquisition data would look like if only those coefficients were present. The result is subtracted from the data, and thresholded again, as shown in figure 3.2.g, allowing the recovery of smaller coefficients [98].

Algorithm 2: Iterative Thresholding Algorithm

Data: a randomly sampled signal x of finite energy.
Result: the recovery of the full signal x.
begin
  error $\longleftarrow \|Ax - y\|_{l_2}$
  set threshold to given value
  while *error* > 0 **do**
    $x_n \longleftarrow x\,(x \geqslant \text{threshold})$
    $y_n \longleftarrow Ax_n - y$
    update threshold

From this example, it is clear that Compressive Sensing can help recover signals from under-sampled data that would otherwise be lost in the noise caused by the undersampling.

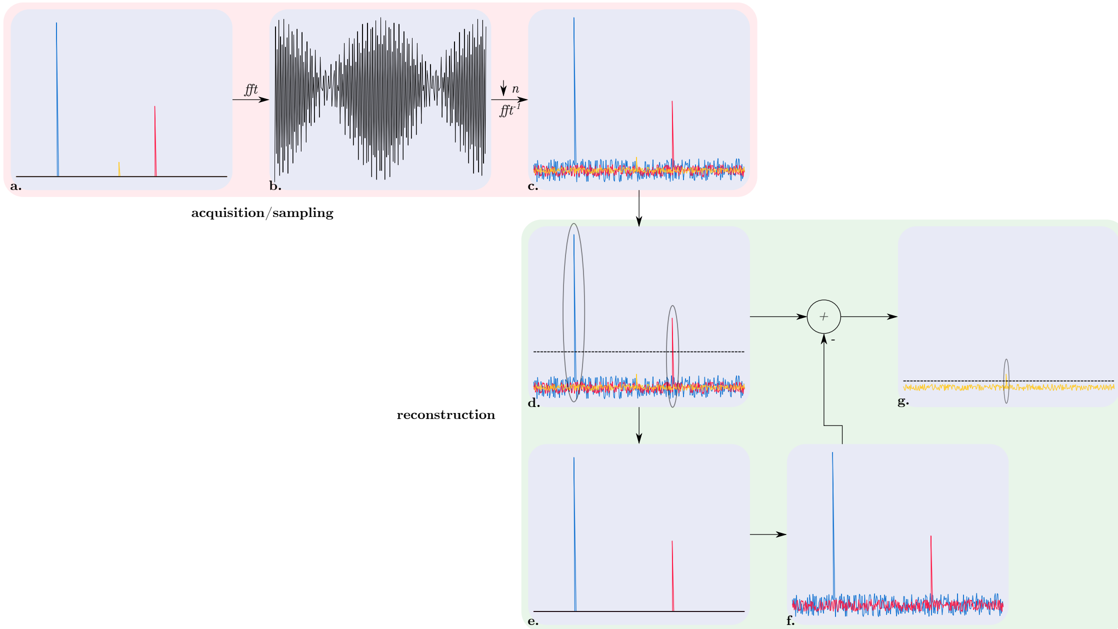

Figure 3.2: *Iterative thresholding algorithm for signal reconstruction from under-sampled data.*

3.3.11 Wrap-up

The classic data acquisition paradigm is extremely wasteful. It starts with the acquisition of a huge amount of data that usually gets compressed for ease of storage. In the compression process a lot of the data gets discarded. The Compressive Sensing paradigm works as if we could acquire only the necessary encoded compression coefficients of the signal. Just the right amount of data gets collected by using $\mathcal{O}\left(S \cdot \log\left(\frac{n}{S}\right)\right)$ random projections. This data collection in an already compressed form coupled with efficient decoding algorithms allows us to obtain potentially super-resolved signals from just a few measurements.

Herein, we introduce some of the notation that we will use for the remainder of this work, in an effort to bridge the gap between the Compressive Sensing theory and the application we developed.

Let us consider a continuous object we wish to acquire represented by the function f.

We assume that f has a sparse representation I in the basis Ψ

$$f = \Psi I \tag{3.31}$$

The acquisition is performed in the basis Φ. Let R_0 denote the complete dataset acquired at the NYQUIST rate. We have

$$R_0 = \Phi f \tag{3.32}$$

The coherence between Φ and Ψ is assumed to be low.

Compressive Sensing focuses on under-sampled signals. Thus, if R_0 is a vector sampled at the NYQUIST frequency and has n samples, we only consider a subset Ω_u of samples with a cardinality $m < n$. The under-sampling or decimation is modeled by the matrix denoted $D \in \mathcal{M}_{m,n}(\mathbb{R})$. We will loosely define D as the matrix that picks m coefficients out of n. The under-sampled data R is obtained from R_0 by multiplication with the matrix D. Using the expression for R_0 from equation 3.32, we find that:

$$R = DR_0 = D\,\Phi f \tag{3.33}$$

Subsequently, we have a linear relationship between the under-sampled data R and the representation of the original object we want to acquire I, given by:

$$R = D\,\Phi\,\Psi I = GI \tag{3.34}$$

with $G = D\,\Phi\,\Psi$. G is the linear application that links the sparse representation of the signal I, and the under-sampled data R.

Under the previous assumptions, the theory of Compressive Sensing states that the original signal f can be reconstructed from the under-sampled subset of coefficients R using

l_1-minimization [99]. That is, the problem:

$$\min_{\hat{I}\in\mathbb{R}^N} \|\hat{I}\|_{l_1} \text{ subject to } G\hat{I} = R \tag{3.35}$$

has a unique solution, and that solution is exactly I. This result can then be used to recover f using equation 3.32.

Equation 3.35 simply states that we aim at iteratively minimizing the l_1-norm of a vector $\hat{I}$ under the constraint $G\hat{I} = R$. That constraint ensures that $\hat{I}$ stays consistent with the acquired data throughout the minimization process. This problem is known as the Basis Pursuit (BP) [100].

In the presence of noise, the constraint may be relaxed and the problem becomes:

$$\min_{\hat{I}\in\mathbb{R}^N} \|\hat{I}\|_{l_1} \text{ subject to } \|G\hat{I} - R\|_{l_2} \leqslant \epsilon \tag{3.36}$$

where ϵ is the noise level. This minimization problem is known as the Basis Pursuit De-Noising (BPDN) [100].

As a last remark, we will note that the signal doesn't have to be exactly sparse in some basis. In fact, it is almost never the case with physical signals. Compressibility is sufficient: a signal f is compressible in the basis Ψ if its coefficients ordered by magnitude decay relatively fast. In that perspective, Compressive Sensing is a more efficient way to acquire the same amount of information from a signal.

For more information on the theory of Compressive Sensing, the interested reader could refer to [82, 91, 99, 101, 102], and [103].

3.4 Solving the inverse problem

3.4.1 What is an inverse problem?

It is generally admitted that a problem is inverse when:

- the output is known, either everywhere or on a certain domain,
- the input is the unknown.

The acquisition can be modeled by a measurement operator $\mathcal{G}$ such that:

$$R = \mathcal{G}(I) \tag{3.37}$$

where R is the output, the data acquired, and I is the input, the information we are trying to determine. It corresponds to the forward process. In the case of linear measurements, the operator $\mathcal{G}$ becomes the matrix G and we have:

$$R = GI \tag{3.38}$$

Of course, the above equality must be taken with a grain of salt. It is only valid if the model employed perfectly describes the problem, and in the absence of noise. Those two conditions are seldom verified in real-life.

With that in mind, we can now focus on the necessary conditions to solve inverse problems. Hadamard [104, 105] has described a set of conditions for well-posedness of inverse problems. This set of conditions is generally accepted to be necessary:

- **Existence**: a solution must exist,
- **Uniqueness**: the solution must be unique, or at least in limited number,

- **Stability**: the solution must depend continuously on the data, meaning that a small perturbation in the data must result in a small perturbation in the solution.

For the measurement operator $\mathcal{G}$, this means that:

- $\mathcal{G}$ must be **injective**: $\mathcal{G}(x_1) = \mathcal{G}(x_2) \implies x_1 = x_2$,
- $\mathcal{G}$ must be **stable**: if we have $y_1 = \mathcal{G}(x_1)$ and $y_2 = \mathcal{G}(x_2)$ then $\mathcal{G}(x_1) \underset{x_1 \to x_2}{\longrightarrow} \mathcal{G}(x_2)$.

Unfortunately, most inverse problems are ill-posed, or well-posed but badly conditioned. The echography inverse problem is no exception to that rule. However, if the class of the solution is known the restriction of the problem to that particular class might be solvable. It is a regularization of the problem.

3.4.2 The ultrasound imaging inverse problem

Ultrasound imaging is based on the probing of tissue with a sound wave. For that purpose, the human body is generally considered like a homogeneous fluid, such as water.

Variables and equations on hand The independent variables are time t and space $\mathbf{x}$. The dependent variables that we want to determine are:

- the wave propagation speed: $\mathbf{v}(\mathbf{x}, t)$,
- the pressure field: $p(\mathbf{x}, t)$,
- the density: $\rho(\mathbf{x}, t)$.

These variables are linked by equations such as:

- the conservation of mass,
- EULER's equation,
- an equation of state,

that we will develop in this section.

Conservation of mass First of all, let us consider a volume V_0 of fluid bounded by the closed surface S_0. The mass of the fluid is given by:

$$m = \iiint_{V_0} \rho dV \tag{3.39}$$

The amount of fluid that flows through a surface element $\mathbf{dS}$ with its normal pointing outward is given by $\rho\mathbf{v} \cdot \mathbf{dS}$. Thus, the total variation of the fluid mass is given by:

$$\frac{\partial m}{\partial t} = -\oint\!\!\!\oint_{S_0} \rho\mathbf{v} \cdot \mathbf{dS} \tag{3.40}$$

Using equation 3.39 and differentiating under the integral sign (since t and $\mathbf{x}$ are independent), we get:

$$\forall V_0 \quad \iiint_{V_0} \left(\frac{\partial \rho}{\partial t} + \mathrm{div}\rho\mathbf{v} \right) dV = 0 \tag{3.41}$$

This relationship must hold true for any volume of fluid V_0 which means the integrand must be equal to 0. We can write:

$$\frac{\partial \rho}{\partial t} + \mathrm{div}\rho\mathbf{v} = 0 \tag{3.42}$$

Equation 3.42 is known as the *conservation of mass*.

EULER's equation EULER's equation is obtained by balancing the forces being applied to a volume V_0 of fluid. To that end, we need a volumic expression of the pressure forces. Considering the surface S_0 bounding the volume V_0, the total pressure at the surface P_{tot} is given by:

$$P_{\text{tot}} = -\oint\!\!\!\oint_{S_0} p\mathbf{dS} \tag{3.43}$$

Using GAUSS-OSTROGRADSKY's theorem [106] that relates the flux of a vector field through a surface to the vector field in the volume defined by that surface, we find that:

$$P_{\text{tot}} = -\iiint_{V_0} \nabla p dV \tag{3.44}$$

Therefore the pressure forces in the volume V_0 can be expressed using the vector ∇p. We use this expression in EULER's equation:

$$\rho \frac{D\mathbf{v}}{Dt} = -\nabla p \tag{3.45}$$

where $\frac{D}{Dt}$ is the material derivative [107] defined by:

$$\frac{D}{Dt} = \frac{\partial}{\partial t} + (\mathbf{v} \cdot \nabla) \tag{3.46}$$

This yields the *conservation of the linear momentum* also known as EULER's equation:

$$\frac{\partial \mathbf{v}}{\partial t} + (\mathbf{v} \cdot \nabla)\, \mathbf{v} = -\frac{1}{\rho} \nabla p \tag{3.47}$$

At this point, we have derived a set of 3 + 1 equations: 3 of those come from EULER's equation, while the other one is the conservation of mass. However, we are working with 5 unknowns: $\mathbf{v}$, p, and ρ. Evidently, we need another equation to ensure the problem is well-posed. One such equation is the equation of state.

Equation of state The equation of state describes the thermodynamic behavior of the fluid and can be written $p = f(\rho, s)$, where s is the entropy of the system, for a certain function f. In the case of an ideal gas for example, we can invoke the reversible and adiabatic nature of the wave propagation to show that the entropy is constant, yielding:

$$\frac{p}{p_0} = \left(\frac{\rho}{\rho_0}\right)^{\gamma} \tag{3.48}$$

with p_0 and ρ_0 describing the pressure and density at a reference state, and $\gamma = \frac{C_P}{C_V}$ the adiabatic index, corresponding to the ratio of the heat capacity at constant pressure C_P and the heat capacity at constant volume C_V [107].

However, this relationship is not true in the case of an ideal liquid. In fact, there is no general equation of state for an ideal liquid. Fortunately, we can expand p in a TAYLOR series:

$$\begin{aligned} p(\rho, s) = p_0 + (\rho - \rho_0) \left.\frac{\partial p}{\partial \rho}\right|_{s_0,\rho_0} + (s - s_0) \left.\frac{\partial p}{\partial s}\right|_{s_0,\rho_0} + \frac{1}{2}(\rho - \rho_0)(s - s_0) \left.\frac{\partial^2 p}{\partial s \partial \rho}\right|_{s_0,\rho_0} \\ + \frac{1}{2}(\rho - \rho_0)^2 \left.\frac{\partial^2 p}{\partial \rho^2}\right|_{s_0,\rho_0} + \frac{1}{2}(s - s_0)^2 \left.\frac{\partial^2 p}{\partial s^2}\right|_{s_0,\rho_0} + o(\rho^2, s^2) \end{aligned} \tag{3.49}$$

We have already established that the sound wave propagation is isentropic, so the previous equation becomes:

$$p = p_0 + A\frac{\rho - \rho_0}{\rho_0} + \frac{B}{2}\left(\frac{\rho - \rho_0}{\rho_0}\right)^2 + o(\rho^2) \tag{3.50}$$

with $A = \rho_0 \left.\frac{\partial p}{\partial \rho}\right|_{s_0,\rho_0}$ and $B = \rho_0^2 \left.\frac{\partial^2 p}{\partial \rho^2}\right|_{s_0,\rho_0}$. A is actually the isentropic bulk modulus of the fluid χ_s: $A = \chi_s$.

Wave equation We now have 5 relationships that describe the behavior of our 5 variables, ensuring the well-posedness of the *forward* problem. To derive the wave equation, we assume that a sound wave is a small perturbation of the state of the system at equilibrium. This way we have $\frac{p - p_0}{p_0} \ll 1$, $\frac{\rho - \rho_0}{\rho_0} \ll 1$, and $\|\mathbf{v}\| \ll 1$. We denote the perturbation ρ_1, p_1, $\mathbf{v_1}$, then we have:

$$p = p_0 + p_1 \tag{3.51}$$

$$\rho = \rho_0 + \rho_1 \tag{3.52}$$

$$\mathbf{v} = \mathbf{0} + \mathbf{v_1} \tag{3.53}$$

EULER's equation becomes:

$$(\rho_0 + \rho_1)\left[\frac{\partial \mathbf{v_1}}{\partial t} + (\mathbf{v_1} \cdot \nabla)\mathbf{v_1}\right] = -\nabla p_1 \tag{3.54}$$

Limiting the devlopment to the first order, we get:

$$\rho_0 \frac{\partial \mathbf{v_1}}{\partial t} = -\nabla p_1 \tag{3.55}$$

Simliarly, the conservation of mass becomes:

$$\frac{\partial \rho_1}{\partial t} + (\rho_0 + \rho_1)\text{div } \mathbf{v_1} + \mathbf{v_1} \cdot \nabla \rho_1 = 0 \tag{3.56}$$

yielding, when keeping only first order terms:

$$\frac{\partial \rho_1}{\partial t} + \rho_0 \text{div } \mathbf{v_1} = 0 \tag{3.57}$$

The equation of state gives:

$$p = p_0 + \chi_s \frac{\rho_1}{\rho_0} \tag{3.58}$$

Since we have $p = p_0 + p_1$, we get:

$$p_1 = \chi_s \frac{\rho_1}{\rho_0} \tag{3.59}$$

Inputing equation 3.59 in equation 3.57, we get:

$$\frac{1}{\chi_s} \frac{\partial p_1}{\partial t} + \text{div } \mathbf{v_1} = 0 \tag{3.60}$$

We can then differentiate equation 3.55 with respect to time and use equation 3.60 to eliminate p_1 and find the propagation equation for $\mathbf{v_1}$:

$$\frac{\partial^2 \mathbf{v_1}}{\partial t^2} - \frac{\chi_s}{\rho_0} \Delta \mathbf{v_1} = 0 \tag{3.61}$$

since $\nabla \mathrm{div} = \Delta$.

Speed of sound Equation 3.61 is the wave equation for speed, also known as D'ALEMBERT's equation. Similarly, the wave equation for pressure can be derived by differentiating equation 3.60 with respect to time and use equation 3.55 to eliminate $\mathbf{v_1}$ and find the wave equation for pressure:

$$\frac{\partial^2 p_1}{\partial t^2} - \frac{\chi_s}{\rho_0}\Delta p_1 = 0 \tag{3.62}$$

A dimensional analysis of $\frac{\chi_s}{\rho_0}$ shows that this quantity has the physical dimensions of a squared speed. Thus, let c_0 be the speed of sound defined by:

$$c_0 = \sqrt{\frac{\chi_s}{\rho_0}} \tag{3.63}$$

Equation 3.63 shows that the speed of sound in a fluid depends on the inverse of its density ρ_0 and on the its isentropic bulk modulus χ_s. Subsequently, the speed of sound in a medium increases with its stiffness and decreases with its density. The velocity c_0 represents the maximum propagation speed of a wave in a homogeneous medium.

Solutions to the wave equation Therefore, we have a set of two equations that govern the pressure and the speed associated with an acoustic wave propagating in a homogeneous medium. In practice we define the D'ALEMBERT operator or d'Alembertian $\Box$ such that equations 3.61 and 3.62 can be written

$$\Box p = 0 \tag{3.64}$$

$$\Box \mathbf{v} = \mathbf{0} \tag{3.65}$$

The most general solution of D'ALEMBERT's equation can be found exactly using D'ALEMBERT's solution [108] for example:

$$\varphi_i(x_i, t) = f\left(t - \frac{x_i}{c}\right) + g\left(t + \frac{x_i}{c}\right) \tag{3.66}$$

where the φ_i are the projections of φ on each of the coordinate system axes. Here, f corresponds to a wave that propagates toward increasing values of x_i whereas g is a wave that propagates toward decreasing values of x_i.

The HELMHOLTZ equation We can apply the FOURIER transform as a way to simplify the resolution of equation 3.62. It allows us to study monochromatic solutions of equation 3.62. And since any signal can be written as a sum of sines and cosines, we can then derive more general solutions.

In the FOURIER domain, the derivatives with respect to time can be simplified since

$$\begin{cases} \frac{\partial}{\partial t} & \text{becomes } \; i\omega \\ \frac{\partial^2}{\partial t^2} & \text{becomes } \; -\omega^2 \end{cases} \tag{3.67}$$

As a result, the FOURIER transform of equation 3.62 is

$$\left(\Delta + k^2\right) P = 0 \tag{3.68}$$

where P is the FOURIER transform of p and $k = \frac{\omega^2}{c^2}$ is the wave number. This is commonly known as the HELMHOLTZ equation.

Let us consider a monochromatic plane wave $p_0 e^{j\omega t + \phi_0}$, where p_0 and ϕ_0 are constant. Then based on D'ALEMBERT's solution,

$$p = p_0 e^{j\left(\omega t - \frac{x}{c}\right) + \phi_0} \tag{3.69}$$

is solution of equation 3.62. Therefore it also verifies the HELMHOLTZ equation. Inputing the plane wave 3.69 into equation 3.68, we find that

$$k = \pm\frac{\omega}{c} \tag{3.70}$$

which is the dispersion relation for plane waves and gives the relationship between the wave number, the pulsation, and the speed of sound. In 2D or 3D, the previous relationship becomes

$$\mathbf{k} = \frac{\omega}{c}\mathbf{n} = k\mathbf{n} \tag{3.71}$$

where $\mathbf{n}$ is the unit vector in the direction of propagation, leading to the pressure field

$$p = p_0 e^{j\phi_0} e^{j(\omega t - \mathbf{k}\cdot\mathbf{x})} \tag{3.72}$$

Equation 3.72 shows that a monochromatic plane wave is not only cyclic in time with a period of $\frac{1}{f}$, but is also cyclic with the distance of propagation, with a repetition length $\frac{2\pi}{k}$, commonly known as the *wavelength* λ. Since we have $k = \frac{\omega}{c}$ and $\omega = 2\pi f$, we find that

$$\lambda f = c \tag{3.73}$$

first coined in NEWTON's *Principia* [109].

Reminder on GREEN's functions The d'Alembertian is a linear, hyperbolic differential operator. As such, we can calculate its GREEN's function. The GREEN's function of an operator corresponds to its impulse response, that is to say the solution of the differential equation if the source were replaced by an impulse in time and space: $\delta(\mathbf{x} - \mathbf{x_0}, t - t_0) = \delta(\mathbf{x} - \mathbf{x_0})\delta(t - t_0)$. In the case of the d'Alembertian, it is the solution to the following inhomogeneous equation:

$$\Box\, g(\mathbf{x}, t|\mathbf{x_0}, t_0) = \delta(\mathbf{x} - \mathbf{x_0})\delta(t - t_0) \tag{3.74}$$

where the source is located in $\mathbf{x_0}$ and emits at t_0. The motivation for the GREEN's function is to solve the general equation

$$\Box\, u(\mathbf{x}, t) = s(\mathbf{x}, t) \tag{3.75}$$

for u, where s is a given source in the medium. It can be justified by multiplying equation 3.74 by $s(\mathbf{x_0}, t_0)$ first, and then integrate with respect to $\mathbf{x_0}$ and t_0 to obtain

$$\iint \Box g(\mathbf{x}, t|\mathbf{x_0}, t_0) s(\mathbf{x_0}, t_0) d\mathbf{x_0} dt_0 = \iint \delta(\mathbf{x} - \mathbf{x_0})\delta(t - t_0) s(\mathbf{x_0}, t_0) d\mathbf{x_0} dt_0 = s(\mathbf{x}, t) \tag{3.76}$$

The right hand side is given by equation 3.75 to be equal to $\Box u(\mathbf{x}, t)$, yielding

$$\Box\, u(\mathbf{x}, t) = \iint \Box g(\mathbf{x}, t|\mathbf{x_0}, t_0) s(\mathbf{x_0}, t_0) d\mathbf{x_0} dt_0 \tag{3.77}$$

The double integral acts on $\mathbf{x_0}$ and t_0, whereas the linear operator $\Box$ acts on $\mathbf{x}$ and t alone. Therefore the operator $\Box$ can be taken outside the double integration. We obtain

$$\Box\, u(\mathbf{x}, t) = \Box \left(\iint g(\mathbf{x}, t|\mathbf{x_0}, t_0) s(\mathbf{x_0}, t_0) d\mathbf{x_0} dt_0 \right) \tag{3.78}$$

which in turn suggests

$$u(\mathbf{x}, t) = \iint g(\mathbf{x}, t|\mathbf{x_0}, t_0) s(\mathbf{x_0}, t_0) d\mathbf{x_0} dt_0 \tag{3.79}$$

Finally, since the D'ALEMBERT operator has constant coefficients with respect to both $\mathbf{x}$ and t, the GREEN's function can be written

$$g(\mathbf{x}, t|\mathbf{x_0}, t_0) = g(\mathbf{x} - \mathbf{x_0}, t - t_0) \tag{3.80}$$

and we find that the solution u to equation 3.75 is given by

$$u(\mathbf{x}, t) = \iint g(\mathbf{x} - \mathbf{x_0}, t - t_0) s(\mathbf{x_0}, t_0) d\mathbf{x_0} dt_0 = (g \otimes s)(\mathbf{x}, t) \tag{3.81}$$

Free-space GREEN's function of the wave equation In this paragraph we compute the GREEN's function associated with the equation

$$\Box\, g(\mathbf{r}, t) = -\delta(\mathbf{r})\delta(t) \tag{3.82}$$

The choice of putting the source in $\mathbf{r_0} = \mathbf{0}$ and emitting at $t_0 = 0$ yields no loss of generality since g is the free-space GREEN's function. We choose the source to emit a negative pulse for convenience and without loss of generality.

First, we take the temporal FOURIER transform of equation 3.82 to obtain the HELMHOLTZ equation [110]

$$\Delta G_t(\mathbf{r}, \omega) - \frac{\omega^2}{c_0^2} G_t(\mathbf{r}, \omega) = -\delta(\mathbf{r}) \tag{3.83}$$

where G_t is the temporal FOURIER transform of g. Then we take the spatial FOURIER transform of equation 3.83 to find

$$G(\mathbf{k}, \omega) = -\frac{1}{k^2 - k_p^2} = -\frac{1}{(k - k_p)(k + k_p)} \tag{3.84}$$

where $k = \|\mathbf{k}\|$ and $k_p = \frac{\omega}{c}$ is the wave number for a plane wave and is a function of ω. By convention, the FOURIER transform of g is denoted by G.

In order to calculate g, we need to invert the spatial FOURIER transform, and then the temporal FOURIER transform. Indeed we have

$$G_t(\mathbf{r}, \omega) = -\frac{1}{(2\pi)^3} \iiint \frac{e^{-j\mathbf{k}\cdot\mathbf{r}}}{k^2 - k_p^2} d^3\mathbf{k} \tag{3.85}$$

and then

$$g(\mathbf{r},t) = -\frac{1}{2\pi}\int G_t(\mathbf{r},\omega)e^{j\omega t}d\omega = \frac{1}{(2\pi)^4}\int\iiint \frac{e^{j(\omega t-\mathbf{k}\cdot\mathbf{r})}}{k^2-k_p^2(\omega)}d^3\mathbf{k}d\omega \tag{3.86}$$

To compute equation 3.85 we use the spherical coordinate system oriented such that the third component of $\mathbf{k}$ is parallel to $\mathbf{r}$ as shown on figure 3.3 without loss of generality. Expression 3.85 then becomes

$$G_t(\mathbf{r},\omega) = -\frac{1}{(2\pi)^3}\int\limits_{k=-\infty}^{+\infty}\int\limits_{\theta=0}^{2\pi}\int\limits_{\varphi=0}^{\pi/2} k^2\mathrm{sin}\varphi\frac{e^{-jkr\mathrm{cos}\varphi}}{(k-k_p)(k+k_p)}dkd\theta d\varphi \tag{3.87}$$

where $r = \|\mathbf{r}\|$. Furthermore, it is easy to prove, with the change of variable $\psi = -\mathrm{cos}\varphi$ for example, that

$$\int\limits_0^{\pi/2}\mathrm{sin}\varphi e^{-jkr\mathrm{cos}\varphi}d\varphi = \frac{1}{jkr} - \frac{e^{jkr}}{jkr} \tag{3.88}$$

The term $\frac{1}{jkr}$ is anti-symmetrical in k and vanishes in the k-integration. Using this and the fact that the integrand is independent from the variable θ, we find

$$G_t(\mathbf{r},\omega) = -\frac{j}{(2\pi)^2 r}\int\limits_{-\infty}^{+\infty}\frac{ke^{-jkr}}{(k-k_p)(k+k_p)}dk \tag{3.89}$$

The integral in 3.89 can be computed using the residue theorem [111]. To that end, we extend the integrand to the complex plane and integrate on the closed contour $\mathcal{C} = \mathcal{C}_1 \cup \mathcal{C}_2$. $\mathcal{C}_1$ follows the $\mathfrak{Re}(k)$ axis, whereas $\mathcal{C}_2$ is a semi-circle in the $\mathfrak{Im}(k) < 0$ plane, defined by $k = ae^{j\beta}$. On $\mathcal{C}_2$, we have

$$e^{-jkr} = e^{-jar\mathrm{cos}\beta}e^{ar\mathrm{sin}\beta} \tag{3.90}$$

Since $\mathcal{C}_2$ is in the lower half-plane, $\mathrm{sin}\beta < 0$, and equation 3.90 shows us that the integrand thus vanishes when $a \to +\infty$, proving that

$$\lim_{a\to+\infty} \oint_{\mathcal{C}} \frac{ke^{-jkr}}{(k-k_p)(k+k_p)}dk = \int_{-\infty}^{+\infty} \frac{ke^{-jkr}}{(k-k_p)(k+k_p)}dk \tag{3.91}$$

The integrand has two simple poles in $\mathbb{R}$: $k = k_p$ and $k = -k_p$. Knowing that for a given function f with a simple pole c we have, $\mathrm{Res}(f, c) = \lim_{x\to c}(x - c)f(x)$, the residues of the integrand are

$$\frac{e^{-jk_pr}}{2} \quad \text{and} \quad \frac{e^{jk_pr}}{2} \tag{3.92}$$

Finally, we are ready to apply the residue theorem. The integrand $i(k, r)$ is compatible with the existence of the CAUCHY principal values, so we have

$$\int_{-\infty}^{+\infty} i(k,r)dk = 2j\pi \sum_{\mathrm{Im}\ z_j<0} \mathrm{Res}(i, z_j) + j\pi \sum_{x_j} \mathrm{Res}(i, x_j) = 0 + \frac{j\pi}{2}\left(e^{-jk_pr} + e^{jk_pr}\right) \tag{3.93}$$

The term e^{jk_pr} corresponds to a wave converging at the source, which is a contradiction. In fact, according to the SOMMERFELD radiation condition the energy of the total wave is radiated outward [110]. Thus we choose to only consider the diverging term e^{-jk_pr}. This yields

$$G_t(\mathbf{r}, \omega) = \frac{e^{-jk_pr}}{4\pi r} \tag{3.94}$$

which can be inverted using the invert temporal FOURIER transform to get the GREEN's function of the time-space wave equation

$$g(\mathbf{r}, t) = \frac{\delta(t - \frac{r}{c})}{4\pi r} \tag{3.95}$$

Since we are in the free-space, the GREEN's function for a source located in $\mathbf{r_0}$ and emitting at $t_0 = 0$ can be derived by shifting or translating the previous function.

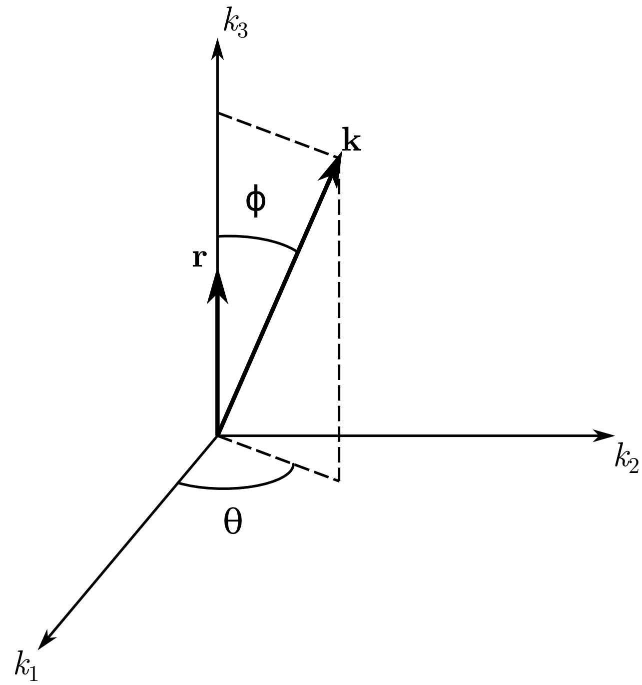

Figure 3.3: *Coordinate system chosen to compute integral 3.85.*

Theorem 6. *The* GREEN*'s function associated with the d'Alembertian operator is given by:*

$$g(\mathbf{r}, t|\mathbf{r_0}, t_0) = \frac{\delta(t - \frac{\|\mathbf{r}-\mathbf{r_0}\|}{c})}{4\pi\|\mathbf{r} - \mathbf{r_0}\|} \tag{3.96}$$

Throughout the remainder of this work, we will use the mathematical objects hereby defined as well as algorithmics to solve the ultrasound inverse problem in the context of medical imaging.

3.5 Conclusion

Traditionally, the ultrasonic inverse problem is solved using the Delay-and-Sum (DAS) algorithm. Delay-and-Sum assumes that the human body is homogeneous almost everywhere with a constant speed of sound. The scatterers embedded in tissue that reflect the excitation pulse are seen as sources of short ultrasonic waves emitting with a relative delay that corresponds to their location in the tissue. Using this assumption, Delay-and-Sum can com-

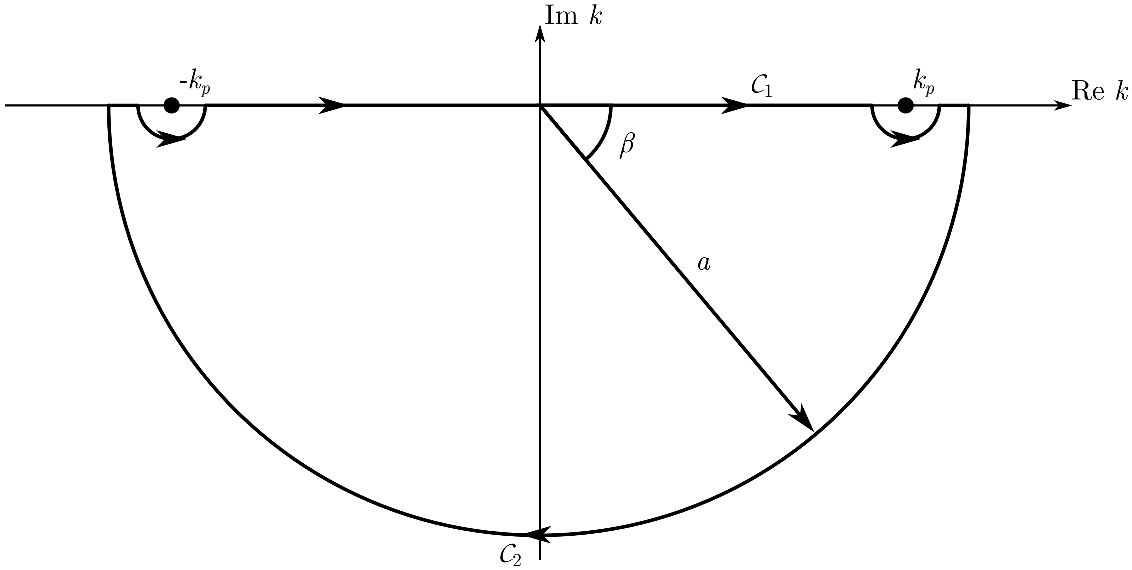

Figure 3.4: *Contour designed to compute integral 3.89.*

pute the intensity at a certain location by synthetically focusing *a posteriori*. This is done by applying the appropriate delays across the acquisition channels, aligning the wavefronts coming from that particular location, and adding the channels with one another. The exact architecture of the Delay-and-Sum algorithm depends on the application and the probe used.

However it has not been demonstrated that Delay-and-Sum is the best way to solve this problem, mathematically speaking, leaving much room for improvement. The Capon beamformer along with other algorithmic alternatives are efforts in the direction of finding an optimum beamformer. In this work, we are trying to address a few limitations of current approaches.

Single wave insonification The approach herein introduced is based on a mathematical framework called Compressive Sensing. The compression will intervene on the acquisition side. We want to be able to acquire just the right amount of ultrasonic data to reconstruct an image. Hence, we are focusing on single wave imaging, assuming that we can insonify the whole medium in one ultrasonic pulse firing.

Sidelobe suppression In this approach, we will build a model of the acquisition process. The model will take into account the geometry of the probe and the physics of the acquisition. By doing so, we can expect to observe an attenuation of the sidelobes since their cause will be inherently included in the model.

Grating lobes suppression In the case of grating lobes, a similar argument can be used. We expect potential grating lobes to be at least attenuated since the geometry of the probe is taken into account in the model.

Chapter 4

Compressive Sensing and ultrasound imaging: the theory of t-CBF

4.1 Introduction

Over the past decade, Compressive Sensing (CS) has gained a lot of visibility and recognition from the signal processing community. This inverse problem technique allows for drastic down-sampling of a signal. It relies on computational power as well as *a priori* information on the signal in the form of the knowledge of a basis where the signal has a *sparse* representation to account for the missing samples. The signal recovery is performed using convex optimization.

The seminal work of Candès [99], Baraniuk [101], and Romberg [103] has led to innovations in a lot of different fields ranging from astronomy to seismology and radars. This technology is currently used in some commercial MRI scanners. In MR imaging, the gain for a higher acquisition rate is obvious: by allowing a smaller number of measurements, it enables shorter acquisition times [80], resulting in less discomfort for the patient, less artifacts and a higher daily patient turnover. For echography, the applications could go from fast 3D echocardiography to simplified echography systems.

Classic beamforming schemes use many transmit waves to insonify a medium [112] and sample echoes at a high acquisition rate of tens of millions of samples per second. While many successful attempts to reduce the number of transmit waves have been made, several beams are still necessary to maintain good image quality [113, 114]. One of the advantages of Compressive Sensing is its ability to require less information for accurate reconstruction when certain mathematical conditions hold. As far as ultrasound imaging is concerned, two aspects of beamforming or image formation could benefit from this new approach. In medical echography, the reconstruction of an image classically requires expensive arrays made of hundreds to thousands of transducers that emit sequences of focalized transmit pulses [112]. First, Compressive Sensing could mean implementing simplified hardware such as an ultrasonic probe with a small number of independent transducers, making ultrasonic systems more affordable. Then, it could mean using less transmit pulses, making the acquisition faster and the frame rate higher.

Compressive Sensing has started to get the attention of acoustic physicists. It has been successfully implemented in the frequency domain by Schiffner [115], it has been used with wave atoms and wavelets by Friboulet [116], and in the *Xampling* framework by Eldar [117]. Our approach is different in the sense that it is a time domain implementation of Compressive Beamforming, and aims at reducing both the number of transmit waves and the number of receiving transducers, while decreasing the sampling frequency. This work is the first of its kind to justify formally the Compressive Sensing framework for ultrasound imaging in the time domain. It can be put into the perspective of the work of Schiffner [115], as the time and frequency domains are related to each other by the Fourier transform.

This section focuses on the beamforming of ultrasonic fields and introduces the Compressive Sensing approach in a medium containing only a few point scatterers. First, a simple 1D example is given. Then, the approach is justified using the theory of wave propagation in a homogeneous medium, and the fundamentals of the theory are laid out. In addition, simulation results are presented alongside the limitations of the described approach. Further developments to overcome these limitations are proposed. Finally, images of a phantom are shown and compared again a state-of-the-art reconstruction algorithm.

4.2 A simple 1D example

In this section we explore a simple 1D setup. The purpose of this is to introduce the concepts of Compressive Sensing into the field of beamforming. The 1D model is greatly simplified compared to a real-life 2D situation but it provides some ground work and basis to build upon.

4.2.1 Description of the experimental setup

In order to simplify the technical aspects of beamforming, we consider a simple setup that we will reduce to a 1-dimensional problem. The setup is described in figure 4.1 and consists in a generic ultrasonic probe made of a collection of individual transducers. The probe emits a monochromatic plane wave.

A small number of scatterers are located in the focal plane of the probe and in the focal plane only. To reduce the setup to a 1-dimensional problem, we reconstruct the distribution of scatterers in the focal plane. As a result, the reconstruction will be a cross-sectional amplitude profile of the medium at the focal depth.

In transmit mode (figure 4.1.a), the probe emits a monochromatic plane wave. In receive mode (figure 4.1.b), the incident plane wave is reflected back to the probe by the scatterers located in the focal plane. Since we are in the far-field approximation, the scattered waves can be approximated by plane waves. The far-field approximation, or Fraunhofer approximation [118], is justified because we are observing the pressure field at the focal plane of the probe. Depending on the position and echogenicity of the scatterers, the probe will see a sum of plane waves of different amplitudes and coming from different angles propagating back to it.

From this description of the process, we can understand that to each scatterer in the focal plane corresponds a unique reflected plane wave characterized by the angle its wave vector makes with the axis of the probe and its amplitude. Those two parameters depend on the echogenicity of the scatterers as well as their location.

In terms of mathematical framework, the scatterers in the focal plane can be described by a Dirac δ basis. Indeed, if a scatterer is present at a certain location, then the corresponding coefficient in the Dirac δ basis will be non-zero, and equal to the echogenicity of the scatterer. This way, the two parameters aforementioned, location and echogenicity, are fully taken into account.

On the acquisition side, the plane waves seen by the probe can be characterized by their amplitude and the angle of their wave vector with respect to the axis of the probe. These two parameters can be described by a basis of complex exponentials which are typically used in the study of monochromatic plane waves.

As a result, we can see clearly what the acquisition and the reconstruction spaces will be. On the one hand, we have the focal plane of the probe, where scatterers will be simulated. The reconstructed profile of the focal plane will be the "image". Thus, the focal plane is the reconstruction space. On the other hand, we have the probe and more specifically its surface divided into individual piezoelectric transducers, or elements. Each element acquires a small portion of the echoed wavefronts coming from the focal plane. This second 1D space will be our acquisition space.

4.2.2 Acquisition and reconstruction bases

According to Fraunhofer's diffraction theory, the transverse amplitude of the focal point is a sinc function of width $\frac{\lambda F}{A}$ where F is the focal length and A the size of the aperture, centered at the focal point. For the purpose of this experiment we choose $\frac{F}{A} = 1$. Therefore, the resolution in the focal plane is limited by the wavelength λ. Namely, a focalized ultrasonic pulse emitted by the probe will have, after propagation to the focal plane, a transverse

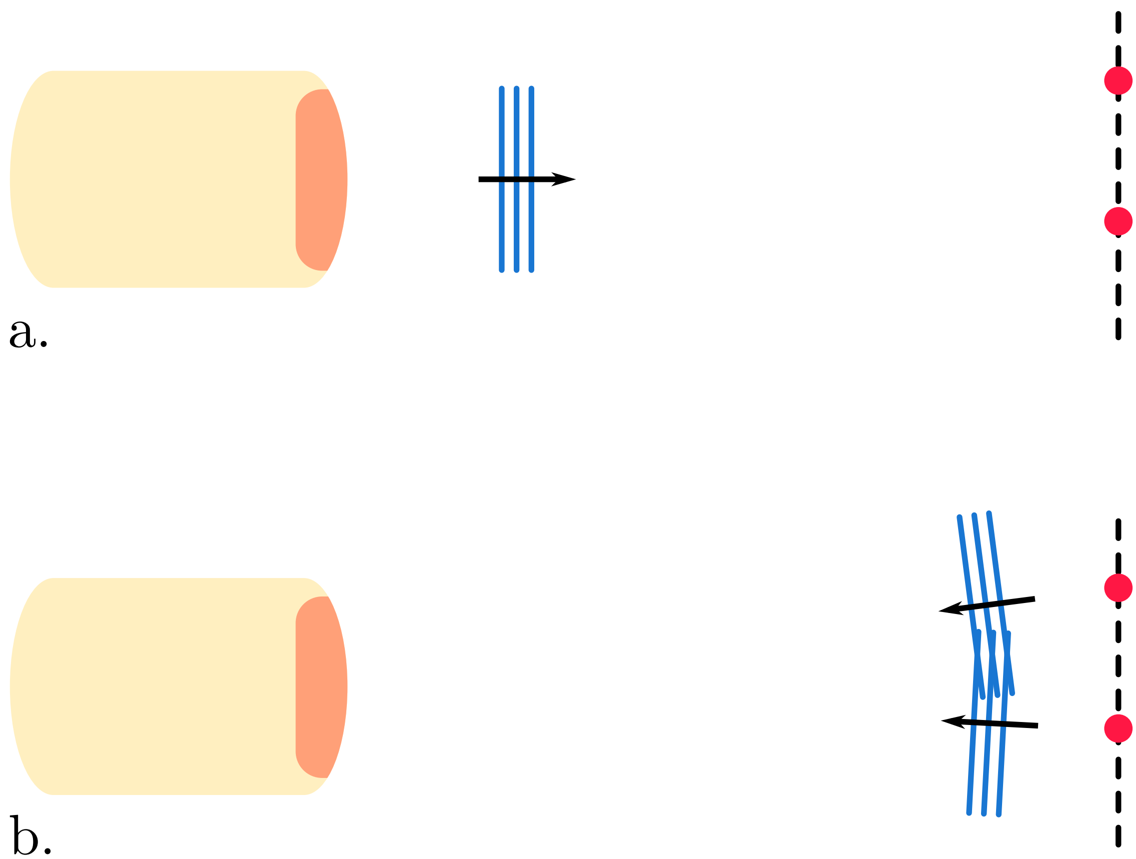

Figure 4.1: a. ***Transmit mode****: a single plane wave is emitted by the probe; 2 scatterers (in red) are in the focal plane, symbolized by the black dashed line.* b. ***Receive mode****: In the far-field approximation, the 2 echoes produced by the scattering can be seen as plane waves angled with respect of the axis of the probe; to each scatterer position in the focal plane corresponds a single angled plane wave.*

amplitude profile described by a sinc function: a central main lobe of width λ, and secondary lobes spaced $\frac{\lambda}{2}$ from each other. A spatial sampling frequency of $\frac{\lambda}{2}$ is then well adapted, since a scatterer in the focal plane can be efficiently represented as a DIRAC δ function as shown in figure 4.2:

$$\psi_j(x) = \delta\left(x - j\frac{\lambda}{2}\right) \tag{4.1}$$

where j is an integer. A discrete basis of the focal plane can thus be derived by calculating the family of functions 4.1 for $x_i = i\frac{\lambda}{2}$ and storing it in a matrix Ψ:

$$\Psi_{ij} = \psi_j(x_i) = \delta\left(x_i - j\frac{\lambda}{2}\right) = \delta(i-j) \tag{4.2}$$

The columns of Ψ are orthonormal.

Now that an efficient basis of the representation space is derived, we can focus our effort on the derivation of a basis for the acquisition space. To do so, we select a point in the focal plane to have a scatterer. When insonified, the scatterer reflects the incident wave yielding a reflected spherical wave that propagates back to the probe. This wave gets recorded by the elements of the probe. In the far field approximation, it can be approximated as a plane wave. As a result, there is a one to one correspondence between a scatterer in the focal plane of the probe and the plane wave it generated, as seen by the probe. In the case of the FRAUNHOFER [118] approximation, the two bases are linked by the FOURIER transform. This guarantees the orthogonality of the plane wave basis. Let us consider a scatterer located in $\mathbf{r_l} = \begin{pmatrix} x_l \\ F \end{pmatrix}$. It yields a plane wave of wave vector $\mathbf{k_l}$:

$$\varphi_l(\mathbf{r}) = e^{i\mathbf{k_l}\cdot(\mathbf{r}-\mathbf{r_l})} = e^{-i\mathbf{k_l}\cdot\mathbf{r_l}} e^{i\mathbf{k_l}\cdot\mathbf{r}} \tag{4.3}$$

where $\mathbf{k_l}$ is a propagation vector, $\mathbf{r}$ is a position vector, and l is an integer. The field is observed at the surface of the transducer $\mathbf{r_k} = \begin{pmatrix} x_k \\ 0 \end{pmatrix}$ where k is the index of a transducer

Parameter	f_c	bw	λ	N_{elements}	p	F	c_{sound}	f_s
Value	3.08 MHz	0.6	500 μm	128	$\lambda/2$	6.4 cm	1540 m.s^{-1}	32 MHz

Table 4.1: *Parameters used to build G for the 1D experiment.*

of the probe. The phase term in equation 4.3 can be safely omitted since it is constant for a given scatterer. The wave vector can be expressed as:

$$\mathbf{k_l} = -\frac{2\pi}{\lambda}\frac{\mathbf{r_l}}{\|\mathbf{r_l}\|} \tag{4.4}$$

For the sake of simplicity, the projection of the propagation vector onto the x-axis is denoted k_l. Let Φ be the acquisition basis. Then we have:

$$\Phi_{kl} = \varphi_l(\mathbf{r_k}) = e^{ik_l x_k} \tag{4.5}$$

A diagram of the bases is shown on figure 4.2. The signification of those two bases is straightforward: each column of Ψ is a vector that represents a scatterer at a given location in the focal plane, each column of Φ is a plane wave coming from a scatterer in the focal plane. A point scatterer in the image is represented by a Dirac δ function. From this we see that there is a one-to-one correspondence between a point scatterer in the reconstruction space and a plane wave in the acquisition space. It is common knowledge that when the Nyquist criterion holds the two bases are orthonormal and linked by the Fourier transform.

4.2.3 Application to simulation

We apply the theoretical framework previously derived to an *in silico* experiment. The parameters of the simulation are presented in table 4.1, including the physical parameters of the ultrasonic probe.

The goal of the experiment is first of all didactic. We want to understand how Compressive Sensing can be applied in the context of medical ultrasound imaging. Then, we want to explore the different ways we can take advantage of the data compression capabilities of Compressive Sensing. To that end, we simulate a data acquisition using only 32 central elements out of the 128 the probe has. We are expecting to preserve the resolution of the full aperture.

We are reconstructing 4 scatterers located in the focal plane. The amplitudes of the scatterers are stored in a vector I for "image". We obtain the simulated data by multiplying I by the acquisition matrix G. G is a combination of a sparsifying basis for I and a model for our data. Thus, we are using Compressive Sensing to solve the inverse problem from incomplete ultrasonic measurements.

To derive G, we go back to 4.2.2, where we derived the acquisition and the reconstruction bases. Since we are reconstructing 4 scatterers, the image I is directly sparse. As a result we choose the reconstruction basis Ψ to be the identity matrix. We saw that in our case, the columns of the acquisition basis Φ are the $e^{ik_l x_k}$. If we stop our reasoning here and define G such that:

$$G = \Psi\Phi \tag{4.6}$$

the data $R = GI$ is complete. In the case of Compressive Sensing, the goal is to reconstruct missing data. As a result, we need to define a decimation operator D. Here, D is the operator that chooses which transducers are acquiring signals, and which are left out. There are several ways of selecting acquiring transducers and we will develop some of them in the following section. This way, we have:

$$R = D\,\Psi\Phi I = GI \tag{4.7}$$

where R is the data vector as acquired by our system, and I is a map of scatterers in the focal plane. We are then all set to use l_1-regularization in the form of the BP algorithm to reconstruct the image. The l_1-minimization is performed using SPGL1 [119, 120].

4.2.4 SPGL1

SPGL1 (Spectral Projection-Gradient for l_1-minimization) [119] is a general purpose convex minimization algorithm. It was chosen to carry out this work because of its flexibility, and its ability to handle large-scale sparse reconstructions in the complex domain.

The flexibility of SPGL1 comes from its capability to solve the basis pursuit problem (equation 3.35), the basis pursuit denoising problem (equation 3.36) as well as the LASSO (equation 4.9) [120]. Despite its name, SPGL1 is not limited to the l_1-norm and can solve the previous three problems for any norm providing that the user specifies scripts to compute:

1. the norm $\|x\|$
2. its dual norm $\|x\|^*$
3. the Euclidian projection

$$P_\tau(x) = \min_p \ \|p - x\|_{l_2} \ \text{ s.t. } \ \|p\| \leqslant \tau \tag{4.8}$$

SPGL1 relies only on the applications GI and $G^\top R$ and accepts both explicit matrices and functions that evaluate these products. In the worst case scenario, the authors claim the algorithm runs in $\mathcal{O}(N \log N)$ operations [121].

It is also compatible with multiple measurement vectors [122, 123], where the vector I becomes a matrix containing as many columns as measurements, as well as group sparsity [120, 124].

The approach of SPGL1 is to efficiently solve a succession of LASSO problems

$$\min_x \|Ax - b\|_{l_2} \ \text{ s.t. } \ \|x\|_{l_1} \leqslant \tau \tag{4.9}$$

using a spectral gradient-projection method. The solution of each LASSO subproblem brings information on how to update the parameter τ so that the solutions of the LASSO get closer and closer to the solution of the BPDN at each iteration.

4.2.5 Results

To allow for a clear assessment of resolution and contrast evolution between the undersampled image and the Compressive Sensing reconstruction, we compute a reference image vector. In this case the reference image can be computed easily since the relationship between I and R is the FOURIER transform. We expect the resolution of the reference image to be the same as the resolution of a 32-element probe. By using Compressive Sensing, we hope to recover the full resolution of the original 128-element probe. The results are compiled in figure 4.3, which shows a resolution and contrast comparison between the reference image and the Compressive Sensing reconstruction both acquired under the same conditions. Unsurprisingly, the direct image exhibits the resolution of a narrower 32 transducer probe. Nevertheless, Compressive Sensing was able to perform the reconstruction with the resolution of the wider 128 transducer probe. The full contrast has also been recovered and the closest scatterers are well separated.

4.2.6 Conclusion

The purpose of this simulation was to illustrate with a simplistic example the capabilities and potential of Compressive Sensing for ultrasound image reconstruction. This simple simulation suggests that Compressive Sensing could be used in the field of ultrasonic imaging and would contribute toward simpler hardware, among other things. A simpler probe with less transducers could reduce costs while Compressive Sensing would preserve the resolution of the final image.

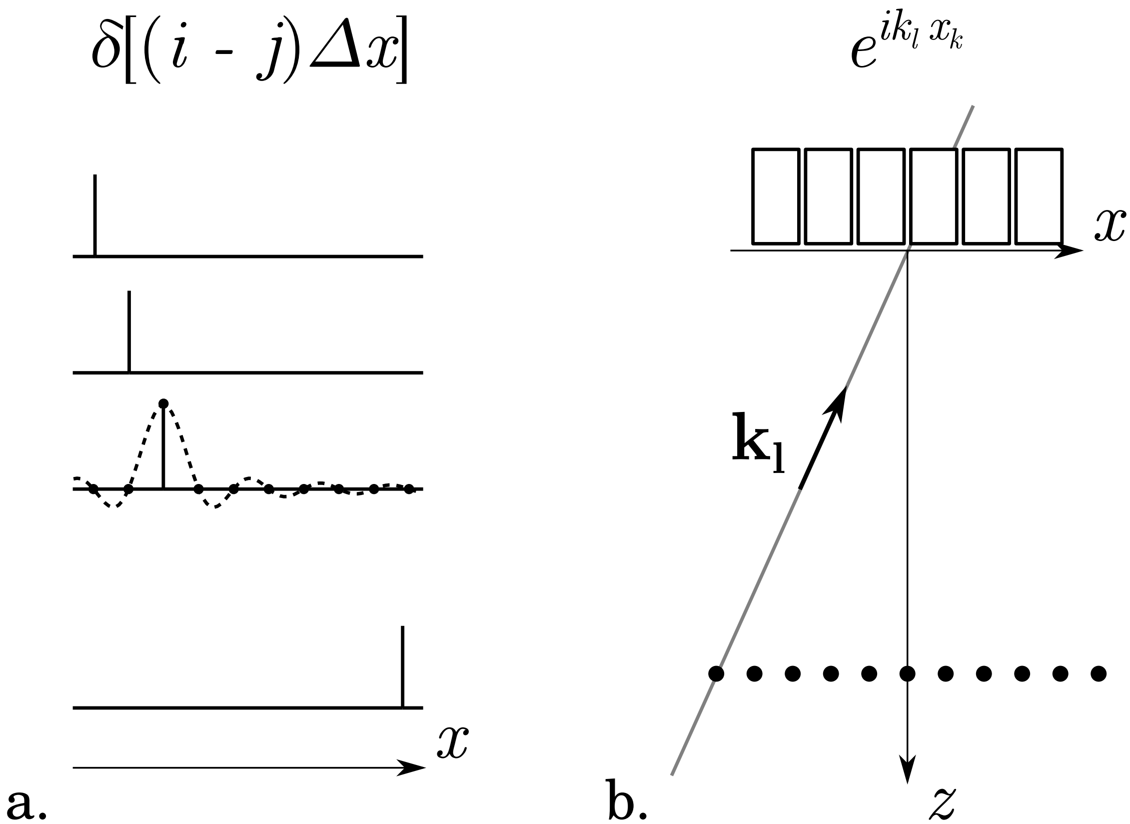

Figure 4.2: a. *Basis of the focal plane of the probe, here a Dirac δ function basis with $\Delta x = \frac{\lambda}{2}$; the continuous intensity distribution at the focal point is also given.* b. *Plane wave basis, the first $\mathbf{k_l}$ is represented. The transducers are represented by the rectangles along the x-axis .*

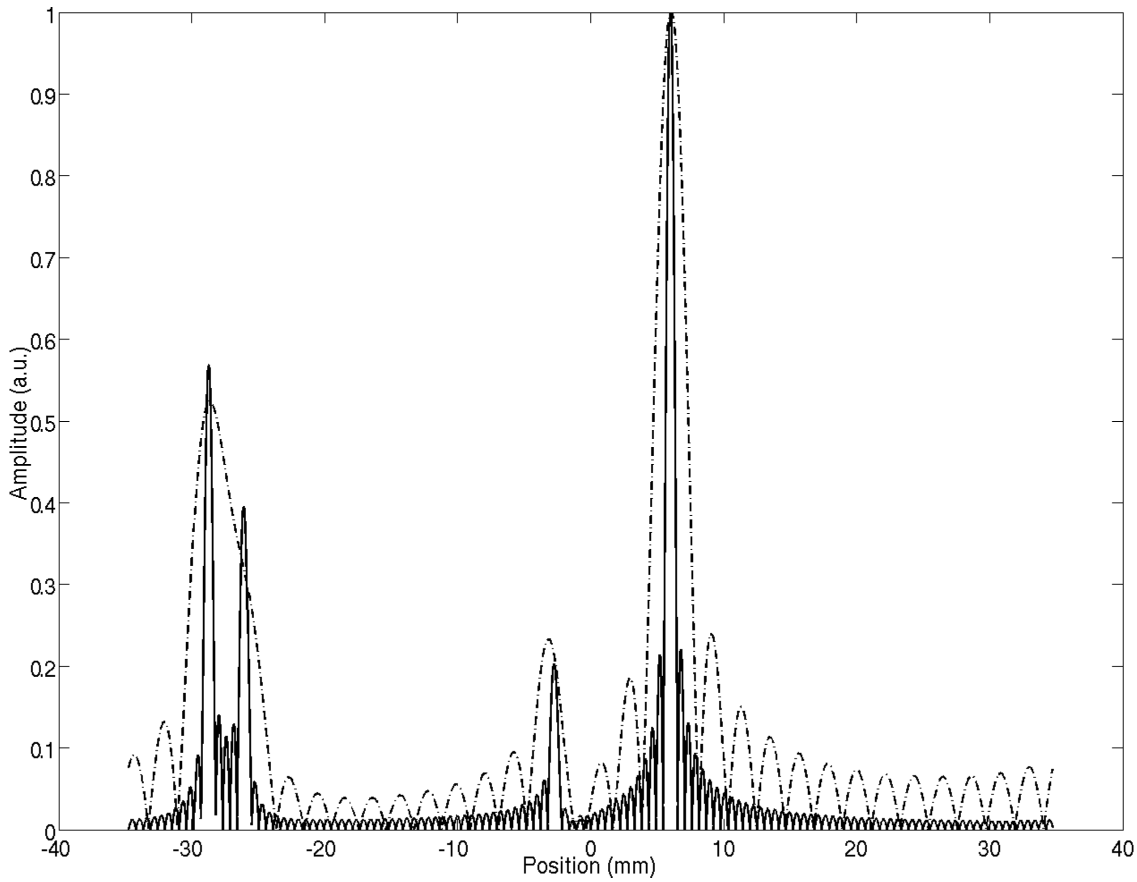

Figure 4.3: *1D projection of the focal plane with 4 scatterers using only 32 of the central transducers of the probe. The signal is interpolated in the Fourier domain to show the difference in resolution: the dashed line corresponds to the image without Compressive Sensing, the continuous line shows the image with Compressive Sensing. The two scatterers on the far left are separated only when Compressive Sensing is used.*

4.3 2D Time-domain Compressive Beamforming

In the field of medical ultrasound imaging, images live in a 2D or a 3D space. In this section, we introduce a Compressive Sensing approach to the 2D image formation paradigm. We demonstrate how we can use simulated Green's functions to define a linear beamforming operator G. G will live in our computer's memory as a wavefront dictionary, a matrix containing the wavefronts resulting from the insonification of every single scatterer located on the image grid. We show that the operator G defines a linear relationship $R = GI$ between the raw data R and the image I compatible with Compressive Sensing. Therefore, we will show that this beamforming operator G can be used in the context of Compressive Sensing to solve the ultrasound inverse problem from incomplete data. We will also give a more precise definition of "incomplete" in this case. Time-domain Compressive Beamforming (t-CBF) will be built upon this basis. Finally, we will show the equivalence between beamforming using G and the classic Delay-and-Sum algorithm.

4.3.1 Linear beamforming operator G

One of the burning issues of Compressive Sensing is to find a suitable matrix G that follows the mathematical conditions of Compressive Sensing. It must link a sparse representation of our image and the data in the acquisition space. Let us consider a homogeneous medium with a distribution of scatterers of reflectivity $I(\mathbf{r})$, where $\mathbf{r} = \begin{pmatrix} x \\ z \end{pmatrix}$ denotes a position vector. An array of transducers is used for the acquisition. The array emits a sound wave that propagates through the medium to the scatterers. The scatterers reflect the excitation wave and these echoes, propagating back to the array, are acquired by the transducers. The acquisition is thus bidimensional, as each sample corresponds to a particular instant in time and a particular position in space. We consider each spatio-temporal sample acquired after insonification of the medium by a single wave as a measurement, in the Compressive

Sensing terminology. Classic beamforming schemes use many transmit waves to insonify the medium, and sample the echoes at a high rate of several million samples per second. Thus, some strategies can be envisioned and combined to compress the acquisition: first the acquisition of a single image could be done with less transmit waves, then the hardware could be simplified to use less independent transducers. Finally, a lower sampling frequency could reduce the amount of data transferred to the scanner. In the following development, we focus on a single plane wave excitation of the medium. However, the formalism hence introduced can be easily generalized to any kind of excitation wave.

Let $R \in \mathcal{M}_{N_t,N_{\text{el}}}(\mathbb{R})$ be a matrix containing the raw data after only one insonification. N_t is the number of time samples, N_{el} is the number of transducers used during the acquisition. $I \in \mathcal{M}_{N_x,N_z}(\mathbb{R})$ is the original distribution of scatterers corresponding to our final image. N_x and N_z are the number of pixels in azimuth and depth respectively. To apply the principles of Compressive Sensing, we need to define a linear relationship between the data R and the image I. Namely we are looking for a tensor $G \in \mathcal{M}_{N_t,N_{\text{el}},N_x,N_z}(\mathbb{R})$ such that:

$$R = GI \tag{4.10}$$

In order to define the matrix G, the acquisition process is broken down into the following steps. First, the transducers of the array are excited by an electrical temporal impulse denoted by $h^i_{\text{ex}}(t)$ for the i^{th} transducer. The transducers are considered to have equivalent physical properties, and have the same impulse response denoted by $h_{\text{trans}}(t)$. As a result, the impulse response of the acquisition system in emission is:

$$h^i_{\text{sys,Tx}}(t) = \left(h^i_{\text{ex}} \underset{t}{\otimes} h_{\text{trans}}\right)(t) \tag{4.11}$$

Expression 4.11 takes into account the impulse response of the acquisition system in emission which includes the central frequency and bandwidth of the probe as well as the transmitted amplitude.

The sound wave thus emitted propagates through the medium from the array to each scatterer. The impulse response of the forward propagation process of the emitted wave is denoted by $h_{\text{fwd}}(t_c, \mathbf{r})$. Part of the energy of the wave gets reflected by the scatterers in the form of spherical waves. The reflected amplitude for each scatterer is given by the reflectivity $I(\mathbf{r})$. The impulse response of the backward propagation process is denoted by $h^i_{\text{bwd}}(t_c, \mathbf{r})$, the index i corresponding to the index of the transducer used for the acquisition. Finally, the pressure field is converted into an electrical signal by the probe and acquired by the scanner, with the impulse response $h_{\text{trans}}(t)$ mentioned earlier.

We can now infer the mathematical expression of the total pressure field recorded by the probe by convolving in time the different terms aforementioned and summing over space:

$$R^i(t) = \int_{\mathbf{r}} \left(h^i_{\text{sys,Tx}}(t_c) \underset{t_c}{\otimes} h_{\text{fwd}}(t_c, \mathbf{r}) \underset{t_c}{\otimes} h^i_{\text{bwd}}(t_c, \mathbf{r}) \underset{t_c}{\otimes} h_{\text{trans}}(t_c) \right)(t) \cdot I(\mathbf{r}) d\mathbf{r} \tag{4.12}$$

under the assumption that multiple scattering is negligible which is a classic approximation in medical ultrasound imaging.

In equation 4.12, the terms $h^i_{\text{sys,Tx}}$ and h_{trans} can be grouped: they describe the impulse response of the acquisition system, denoted $h^i_{\text{sys, TxRx}}$. The term $h^i_{\text{sys, TxRx}}$ takes into account the central frequency of the probe, as well as its bandwidth, usually modeled by a Gaussian function. As a result, for the sake of simplicity we can leave that term out of the development, keeping in mind that depending on the parameters of the probe, those terms have to be added back when calculating the matrix G. This leads to:

$$R^i(t) = \int_{\mathbf{r}} \left(h_{\text{fwd}}(t_c, \mathbf{r}) \underset{t_c}{\otimes} h^i_{\text{bwd}}(t_c, \mathbf{r}) \right)(t) \cdot I(\mathbf{r}) d\mathbf{r} \tag{4.13}$$

The next step is to discretize the simplified equation 4.13. The time variable t becomes $t_j = j\Delta t$ where $\Delta t = \frac{1}{f_s}$, f_s being the sampling frequency of the system. The spatial variable $\mathbf{r}$ becomes $\mathbf{r_{kl}} = \begin{pmatrix} x_k \\ z_l \end{pmatrix} = \begin{pmatrix} k\Delta x \\ l\Delta z \end{pmatrix}$ where Δx and Δz are the grid spacing in azimuth and depth respectively. This yields to:

$$R_{ij} = \sum_{k=1}^{N_x} \sum_{l=1}^{N_z} \cdot \left(h_{\mathrm{fwd}}(t_c; k, l) \underset{t_c}{\otimes} h^i_{\mathrm{bwd}}(t_c; k, l) \right) (j) I_{kl} \tag{4.14}$$

Equation 4.14 is indeed a tensor product between a bi-dimensional matrix $I = (I_{kl})_{k,l}$ and a four-dimensional tensor $G = (G_{ijkl})_{i,j,k,l}$. Following this notation, we have:

$$G_{ijkl} = \left(h_{\mathrm{fwd}}(t_c; k, l) \underset{t_c}{\otimes} h^i_{\mathrm{bwd}}(t_c; k, l) \right) (j) \tag{4.15}$$

which may be discretized to:

$$G_{ijkl} = \sum_{u=1}^{N_t} h_{\mathrm{fwd}}(j - u; k, l) h^i_{\mathrm{bwd}}(u; k, l) \tag{4.16}$$

Based on this framework, we can particularize the solution. For a plane wave excitation propagating along the axis of the probe in a homogeneous medium, the propagation to a scatterer in $\mathbf{r} = \begin{pmatrix} x \\ z \end{pmatrix}$ can be modeled by the following forward impulse response:

$$h^i_{\mathrm{fwd}}(t, \mathbf{r}) = \delta \left(t - \frac{z}{c} \right) \tag{4.17}$$

which doesn't depend on the emitting transducer i in the case of a plane wave excitation: the individual excitation pulses are synchronized on all the channels.

After propagation through the medium, the plane wave reaches a scatterer in $\mathbf{r}$ and gets reflected. The scatterer is assumed to be smaller than λ, thus generating a spherical wave which yields to the following backward impulse response that describes the propagation from the scatterer in $\mathbf{r}$ back to the i^{th} transducer of the array [110]:

$$h^i_{\mathrm{bwd}}(t, \mathbf{r}) = \frac{\delta \left(t - \frac{\|\mathbf{r} - \mathbf{r_i}\|}{c} \right)}{4\pi \|\mathbf{r} - \mathbf{r_i}\|} \tag{4.18}$$

which is the GREEN's function of the homogeneous medium.

From equations 4.17 and 4.18, we can infer the mathematical expression of the pressure field resulting from an excitation of the medium by a plane wave and its reflection on a scatterer located in $\mathbf{r}$:

$$h_{\mathrm{fwd}}(t_c, \mathbf{r}) \underset{t_c}{\otimes} h^i_{\mathrm{bwd}}(t_c, \mathbf{r})(t) = \frac{\delta\left(t - \frac{z}{c} - \frac{\|\mathbf{r}-\mathbf{r_i}\|}{c}\right)}{4\pi\|\mathbf{r}-\mathbf{r_i}\|} \tag{4.19}$$

Discretizing equation 4.19 leads to the following expression for G_{ijkl}:

$$G_{ijkl} = \frac{\delta\left(t_j - \frac{z_l}{c} - \frac{\|\mathbf{r_{kl}}-\mathbf{r_i}\|}{c}\right)}{4\pi\|\mathbf{r_{kl}}-\mathbf{r_i}\|} \tag{4.20}$$

Equation 4.20 corresponds to the diffraction impulse response of a homogeneous medium with one point scatterer located at $\mathbf{r_{kl}}$, in other words the GREEN's function of the medium that takes into account both the transmission and the reception parts. Therefore, G_{ijkl} is the GREEN's function of the medium, observed at the time sample j by the i^{th} transducer when a point scatterer is at the position $\mathbf{r_{kl}}$ in space.

We have defined a 4-dimensional tensor G that gives a linear relationship between a map of scatterers I in a homogeneous medium, and the raw data R acquired by the array of transducers:

$$R = GI \tag{4.21}$$

For Compressive Sensing, we need to write equation 4.21 in the form of a matrix product. To that end, we perform a change of indexes going from (i, j, k, l) to (α, β) with:

$$\left\{\begin{array}{lcl} \alpha & = & j + N_t(i-1) \\ \beta & = & l + N_z(k-1) \end{array}\right. \tag{4.22}$$

which is a bijective $\mathcal{C}^1$ change of variable. The change of variable allows the unwrapping of matrices R and I into vectors as shown in figure 4.4, and of tensor G into a matrix.

By remapping the indices, the 4-dimensional problem is transformed into an equivalent 2-dimensional problem adapted to the Compressive Sensing framework.

With that notation, we have:

$$R_\alpha = G_{\alpha\beta} I_\beta \tag{4.23}$$

using Einstein's convention, where the repeated index β is implicitly summed across all its accessible values.

4.3.2 Relationship with Delay-and-Sum

The standard beamforming algorithm described in the literature and widely used in available commercial scanners, called the Delay-and-Sum, is a reconstruction algorithm that computes an image D based on the raw data R by using the principle of coherent summation [10]. In that framework, the propagation delays from the surface of the transducers to the different points of the final image defined by the grid $\mathcal{G}$ are applied to each channel of the raw data before summation and detection. Thus, the level value of the pixel (k, l) in the image D is given by:

$$D_{kl} = \sum_{i=1}^{N_{\mathrm{el}}} R\left(\mathbf{r_i}, \frac{z_l}{c} + \frac{\|\mathbf{r_{kl}} - \mathbf{r_i}\|}{c}\right) \tag{4.24}$$

where the term $\frac{z_l}{c} + \frac{\|\mathbf{r_{kl}} - \mathbf{r_i}\|}{c}$ corresponds to the propagation time, back and forth, from the probe's i^{th} element to the position $\mathbf{r_{kl}}$ for a plane wave excitation.

The right hand side of equation 4.24 can be interpreted as a convolution product of $R(\mathbf{r_i}, t)$ and $\delta\left(t - \frac{z_l}{c} + \frac{\|\mathbf{r_{kl}} - \mathbf{r_i}\|}{c}\right)$. In discrete time, we have:

$$D_{kl} = \sum_{i=1}^{N_{\mathrm{el}}} \sum_{j=1}^{N_t} \delta\left(t_j - \frac{z_l}{c} - \frac{\|\mathbf{r_{kl}} - \mathbf{r_i}\|}{c}\right) \cdot R(\mathbf{r_i}, t_j) \tag{4.25}$$

Delay-and-Sum classically neglects the amplitude term $\frac{1}{4\pi\|\mathbf{r_{kl}} - \mathbf{r_i}\|}$ that is due to propagation [10] as well as the impulse response of the transducer. The interested reader can refer to reference [125] which describes a back propagation beamforming algorithm that does not

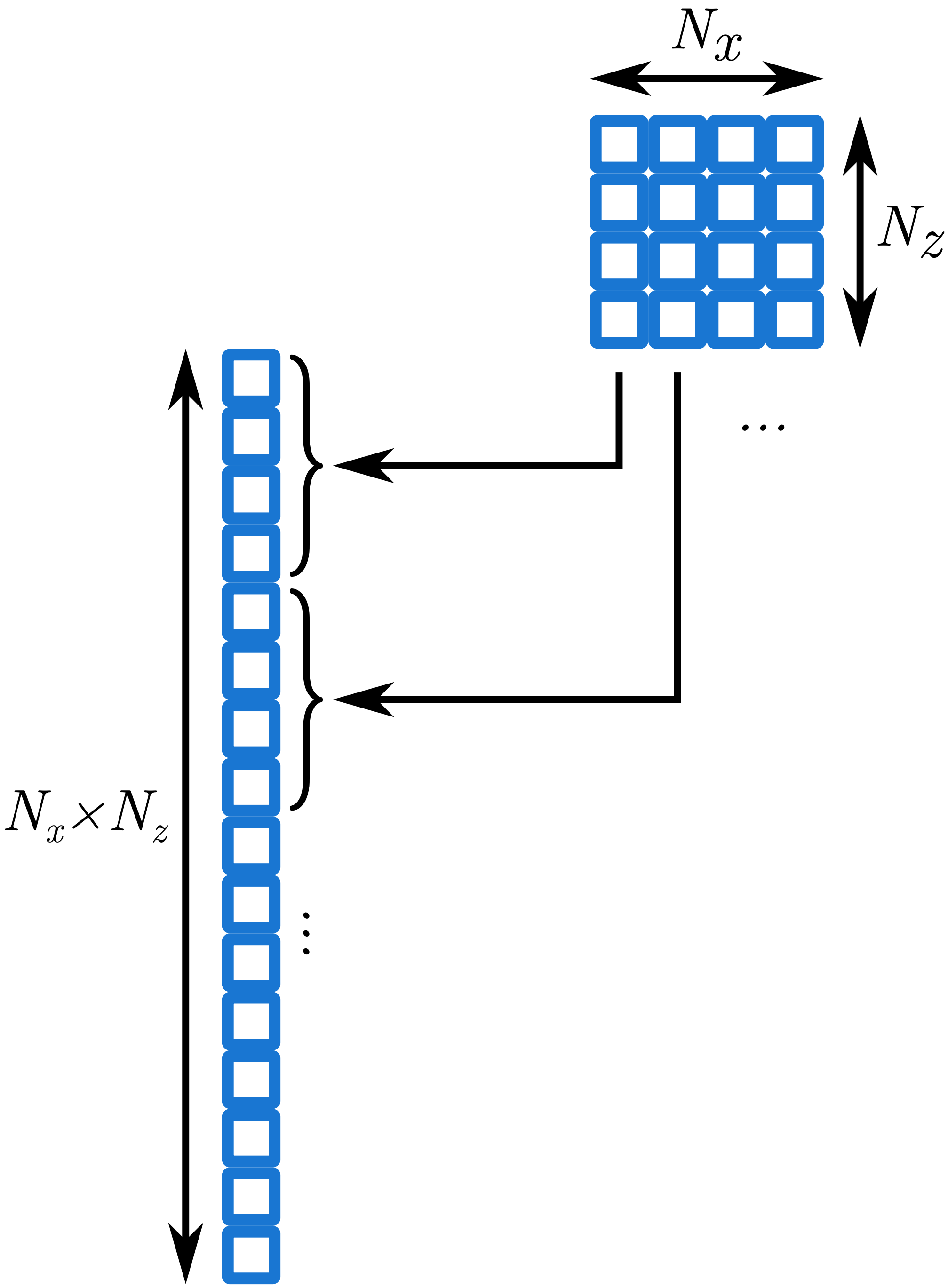

Figure 4.4: *Unwrapping of a matrix into a vector. This simple remapping allows the transformation of our image and data, which are 2-dimensional matrices, into 1-dimensional vectors. Similarly, the 4-dimensional tensor G can be remapped into a 2-dimensional matrix, making the problem dimensionally suited for the tools of Compressive Sensing.*

neglect the amplitude term and the impulse response of the transducer, and [126] which describes a matched filter approach to beamforming that also accounts for the amplitude term by modeling the wavefront propagation. Adding that term back in equation 4.25, we find that Delay-and-Sum is equivalent to:

$$D = G^{\mathsf{T}} R \tag{4.26}$$

which involves the same matrix G as we are using in the t-CBF framework. Subsequently, G can be interpreted as a beamforming matrix.The final image D is obtained by successive projections of the raw data on the columns of dictionary G.

Equations 4.21 and 4.26 combined together define a direct relationship between the Delay-and-Sum image D and the scatterer distribution I:

$$D = G^{\mathsf{T}} G I \tag{4.27}$$

From this, we can sense the importance of the matrix $G^{\mathsf{T}}G$: it links the scatterer distribution to the final Delay-and-Sum image and can therefore be seen as a Point Spread Function (PSF) of the acquisition system. In the Compressive Sensing framework, it is often called the *mutual coherence* of G.

Equation 4.27 also shows that we should expect the Delay-and-Sum and the t-CBF images to be different in nature.

4.3.3 Practical implementation

In the previous development, we established a formal expression for G_{ijkl} leaving out the influence of the parameters of the acquisition system such as the central frequency f_c, and the bandwidth bw of the probe. The bandwidth is generally modeled by a Gaussian function. Usually, the electrical excitation pulse h^i_{ex} is a simple temporal Dirac δ pulse. In the case of a plane wave, the pulses are synchronized on all the channels, therefore $h^i_{\text{sys, Tx}}$ does not depend on i and is equal to h_{trans}. Finally, the term $h^i_{\text{sys, TxRx}}$ from equation 4.12 is the auto-convolution of the Gaussian pulse, which can be approximated by another Gaussian pulse of same central frequency f_c and bandwidth $\frac{\sqrt{2}}{2}bw$:

$$h_{\text{sys, TxRx}}(t) \approx \text{gauspuls}(t, f_c, \frac{\sqrt{2}}{2}bw) \tag{4.28}$$

where the function gauspuls is the modulated pulse with a Gaussian bandwidth defined by:

$$\text{gauspuls}(t, f_c, bw) = e^{-\frac{t^2}{2t_v}} \cos(2\pi f_c t) \tag{4.29}$$

with $t_v = -\frac{8\log\left(10^{-6/20}\right)}{4\pi^2 bw^2 f_c^2}$.

To get the final expression for G_{ijkl}, expression 4.20 is convolved with $h_{\text{sys, TxRx}}$:

$$G_{ijkl} = \text{gauspuls}\left(t_j - \frac{z_l}{c} - \frac{\|\mathbf{r_{kl}} - \mathbf{r_i}\|}{c}, f_c, \frac{\sqrt{2}}{2}bw\right) \tag{4.30}$$

which is the expression used in the experiments section.

Therefore, in this particular setting, we can link a point scatterer at a certain location with a wavefront recorded by the probe, or simulated, as shown on figure 4.6. By repeating this process for all the points of a grid $\mathcal{G}$ that spans the whole final image space, one can populate a dictionary of wavefronts G that links a map of scatterers in a medium to the pressure field generated by them and acquired by the probe. Intuitively, one can expect this dictionary to be suitable for Compressive Sensing as long as the number of scatterers in the medium is small enough to ensure sparsity, and the grid spacing in depth and azimuth is chosen wisely, to ensure that the dictionary has a low coherence.

4.3.4 Towards a compressed beamforming algorithm

According to the definition of G, each of its columns contains the Green's function of a given scatterer. In that sense, it is a dictionary of Green's functions that associate a diffraction

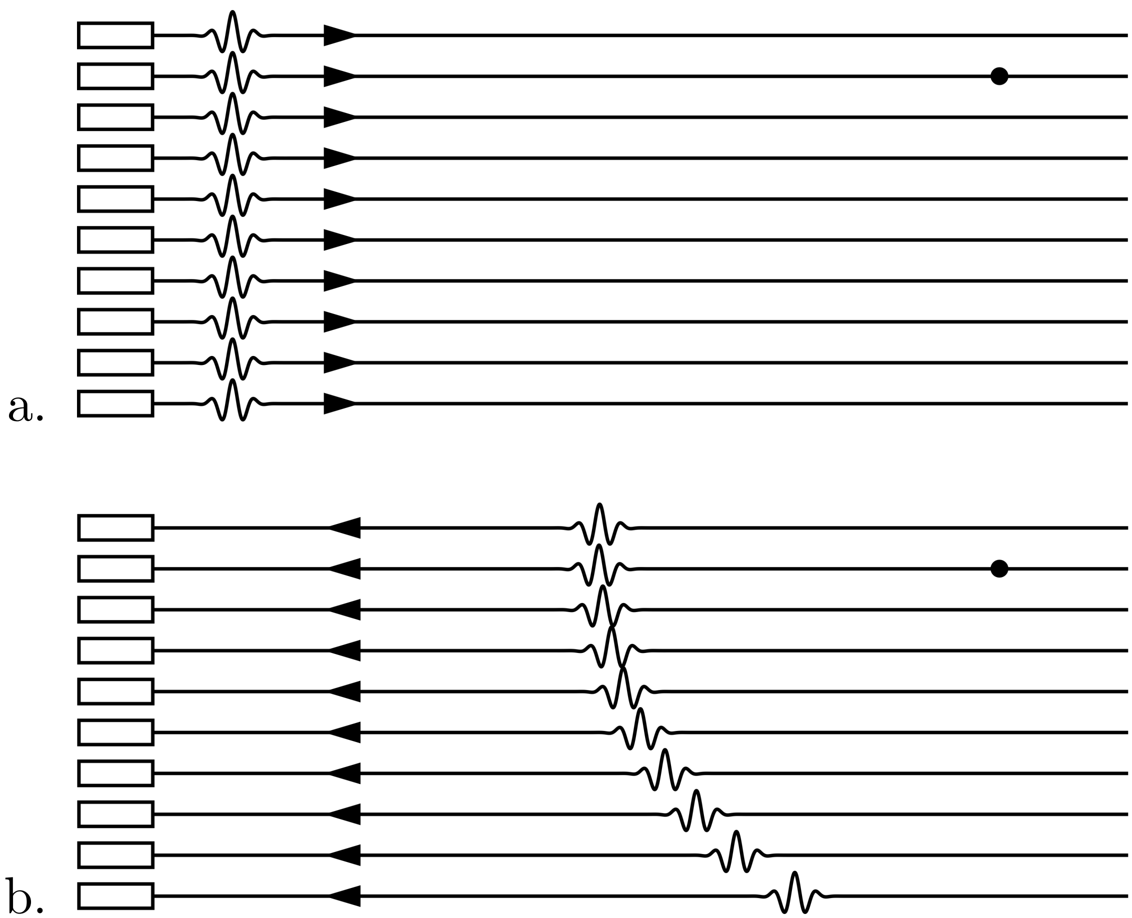

Figure 4.5: a. *The pressure field in the medium after emission by the ultrasonic probe. The black dot is a scatterer. The arrow indicates the direction of propagation of the ultrasonic wave.* b. *The pressure field after reflection on the scatterer.*

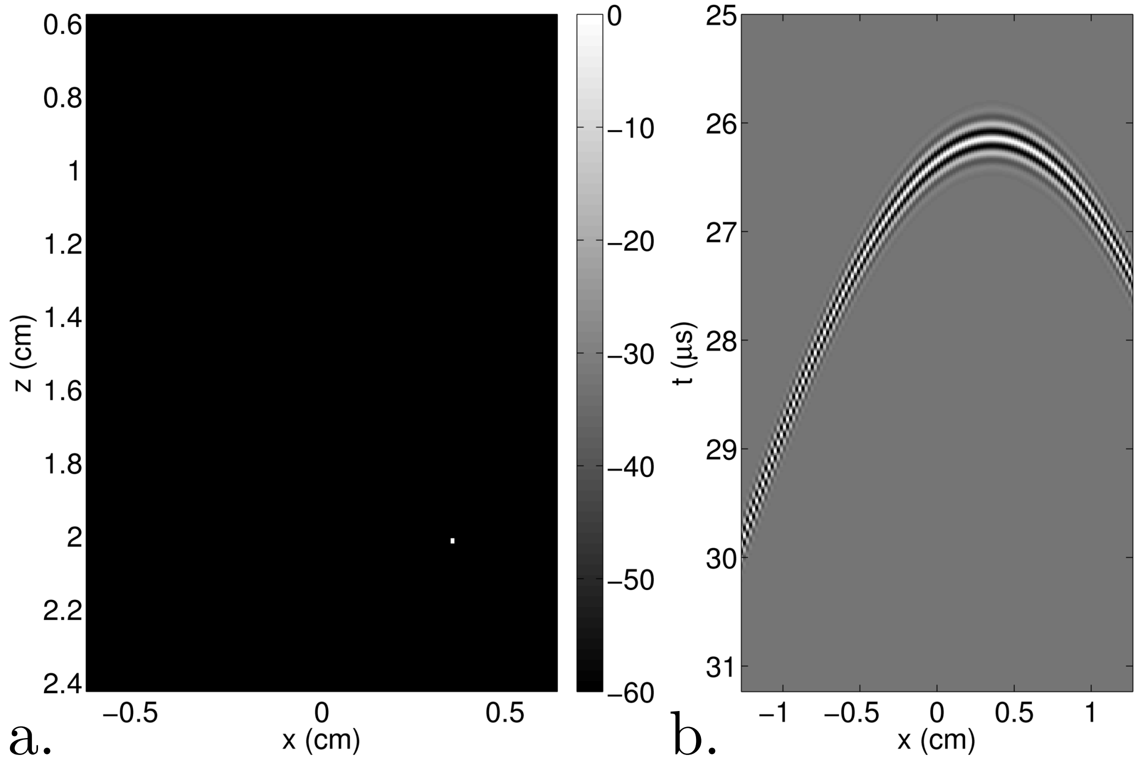

Figure 4.6: *Representation of a point scatterer in:* a. *the image space,* b. *the acquisition space.*

impulse response to a distribution of scatterers.

So within the limitations of our model, if R is a signal acquired with the ultrasonic probe, then there exists a spatial distribution of scatterers I such that:

$$R = GI \tag{4.31}$$

Using equation 4.31, we may infer a BP beamforming algorithm based on l_1-minimization:

$$\min_{\hat{I} \in \mathbb{R}^{\mathbb{N}_{\mathrm{img}}}} \|\hat{I}\|_{l_1} \text{ such that } R = G\hat{I} \tag{4.32}$$

in the absence of noise and if the distribution of scatterers I is *sparse*.

In order to take into account the acquisition noise and the inaccuracies of our model, one can relax the constraint with an inequality:

$$\min_{\hat{I} \in \mathbb{R}^{\mathbb{N}_{\text{img}}}} \|\hat{I}\|_{l_1} \text{ such that } \|G\hat{I} - R\|_{l_2} \leqslant \epsilon \tag{4.33}$$

where the parameter ϵ accounts for the noise and the model inaccuracies. This yields a BPDN beamforming algorithm, that is tat the very core of t-CBF.

4.4 Simulations and under-sampling performance

In this section, we present and discuss simulation results. We simulated a linear ultrasonic probe (table 4.2) made of $N_{\text{el}} = 128$ elements. The central frequency is $f_c = 7.3$ MHz, which gives $\lambda = 211$ μm at $c = 1540$ m.s^{-1}. The distance between the center of two consecutive elements is equal to λ in order to minimize the grating lobes. The sampling frequency is set to $f_s = 40$ MHz, which means that if the final image is a sector that spans 7 cm in azimuth and 7 cm in depth, each simulated Green's functions will be a 128×2000 sample matrix at least. After the column-wise *unwrapping*, this gives a $256,000$ value vector. Now if we work on a grid $\mathcal{G}$ defined by the pitches $\Delta x = \lambda/2$ in azimuth and $\Delta z = \lambda/2$ in depth, we need to simulate roughly $670 \times 670 = 448,900$ Green's functions. Using these parameters, the final matrix G will be a $256,000 \times 448,900$ matrix of double precision floating point numbers. Hence, the size of the entire matrix G would be roughly 920 GB. Having that matrix readily accessible in the RAM of the system is unrealistic. This first limitation could be mitigated by the use of a multi-core GPU card to compute the coefficients of G on-the-fly as opposed to storing them in the RAM. Another solution, that we chose to pursue in this chapter, is to restrain the simulation to a small domain of 192×192 pixels. In the next chapter, we will derive a method to work on a larger field-of-view by using the Hilbert transform.

Another important aspect is the computation time needed to calculate a single image. Here, Matlab is used to carry out the computation for proof of concept. As a result, processing times can be significant. In the long run, a few strategies could be pursued to improve

Parameter	f_c	bw	λ	N_{elements}	p	c_{sound}	f_s
Value	7.3 MHz	0.6	211 μm	128	211 μm	1540 m.s^{-1}	40 MHz

Table 4.2: *Simulation and experimental parameters used in the reconstruction of the images in figure 4.7 and generally throughout this chapter.*

on this: the algorithm could be adapted to C language, heavy GPU parallelization could be used, etc. The following development focuses on off-line reconstruction only.

All the pressure fields are simulated using Jensen's Field II [127].

4.4.1 t-CBF using a plane wave excitation and 128 transducers in reception

In this section we simulate a homogeneous medium containing a finite number of point scatterers and we investigate the influence of the scatterers' position on the reconstruction.

1 point scatterer simulation

For this simulation, a unique point scatterer is considered. The field-of-view (FOV) is a 192×192 pixel image and the pitch in azimuth and depth is $\Delta x = \frac{5\lambda}{2}$ and $\Delta z = \frac{3\lambda}{2}$ respectively. Attenuation is neglected as a first approximation, and the image is centered on $x = 0$ cm, $z = 2.5$ cm. The excitation is a plane wave: all the transducers fire the same pulse at the same time. The full aperture is used in reception. On figure 4.7, the point scatterer is located in the center of the image, at $x = 0$ cm, $z = 2.5$ cm. The results from both the l_1-minimization and the dynamic focusing Delay-and-Sum [10] are presented on figure 4.7.

The l_1-minimization recovers the map of the scatterers in the medium. The appearance of the image computed with Delay-and-Sum is different: it displays sidelobes and a coarser resolution. The differences between the two reconstructions can be explained by equation 4.27. The t-CBF would be a de-convolved version of the Delay-and-Sum image to a certain extent. For that reason, the result obtained through l_1-minimization is a single white pixel, whereas the image obtained using Delay-and-Sum shows sidelobes on each side of the point scatterer. Obtaining a comparable resolution with Delay-and-Sum would require many focalized transmit beams (typically 84, figure 4.7), or many plane wave excitations in the case of plane wave compounding (typically 12) [62] as well as a wide aperture.

Point scatterers selected at random

In this section we briefly look into the limits of the sparsity constraint. One of the main assumptions we have made so far is that the number of scatterers is relatively small. In that section, the ultrasonic field generated by 128 scatterers was simulated. The position and reflectivity of each scatterer are chosen at random on the grid $\mathcal{G}$. On figure 4.8, the images obtained using Delay-and-Sum, projections on the matrix G, and l_1-minimization are given for comparison. The reconstruction on figure 4.8.c was very accurate, as the amplitude of each scatterer was recovered as well as their position. However, when the number of scatterers increases, the quality of the recovery decreases and the convergence time of the algorithm increases.

The resolution is much better than in the case of 84 transmit beams (figure 4.8.b). For that simulation, the point scatterers were located on a known grid, which made it easier for the algorithm to recover the map. However, the model was not perfect and the wavefronts generated for the simulation differed from the wavefronts stored in the dictionary G. The attenuation was not considered, and neither was the influence of the directivity of the transducers.

4.4.2 t-CBF using a plane wave excitation and 16 transducers in reception

One of the great benefits of Compressive Sensing is the ability to decrease the number of measurements necessary to perform an accurate reconstruction. In our case, that could mean acquiring less samples in time, or less samples in space, or both. It could also mean imaging

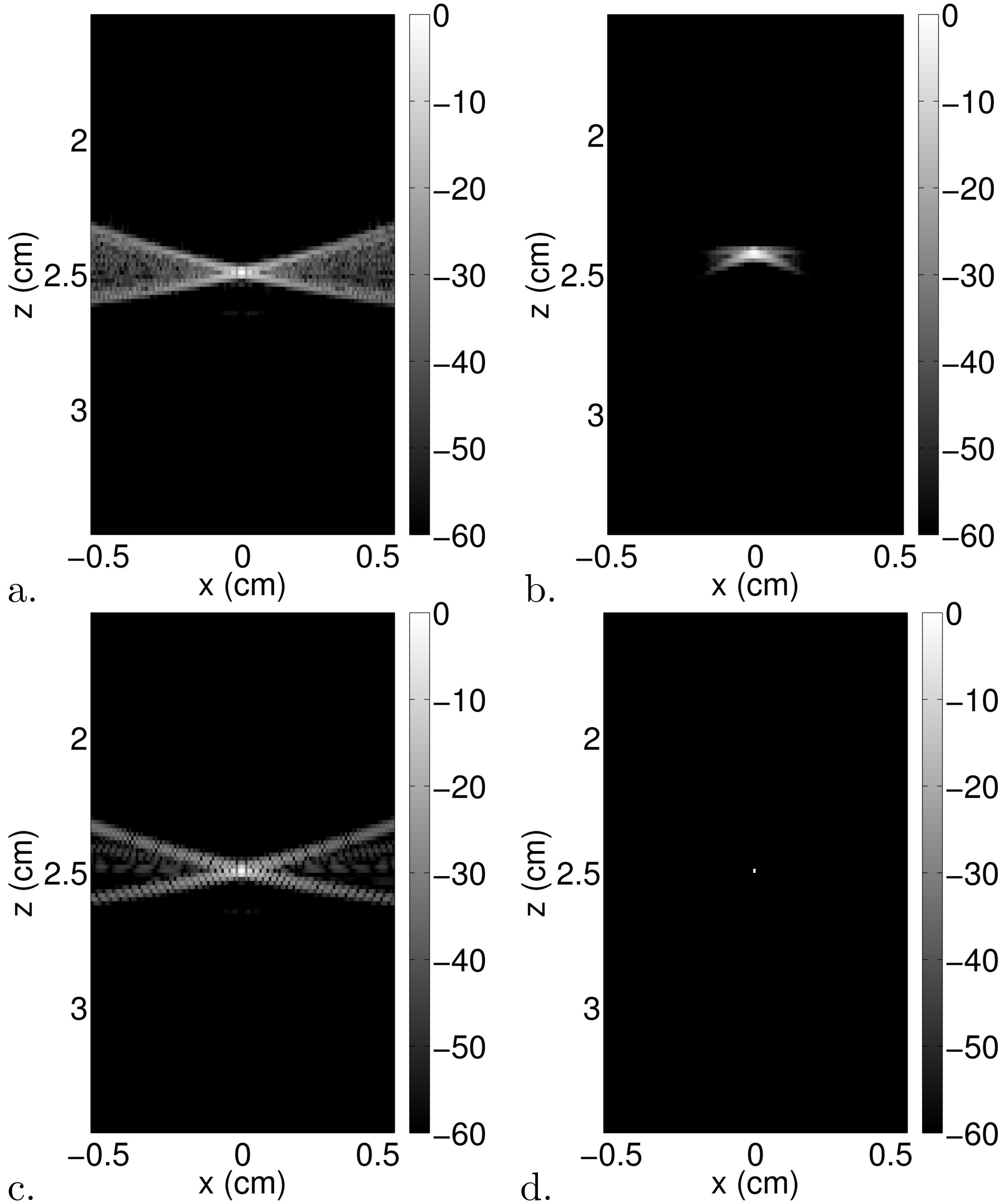

Figure 4.7: *Simulation of one point scatterer at azimuth 0 and depth 25 mm. Images obtained using:* a. *plane wave Delay-and-Sum,* b. *conventional Delay-and-Sum with 84 focalized transmit beams,* c. *projection of the raw data on the matrix G,* d. *l_1-minimization.*

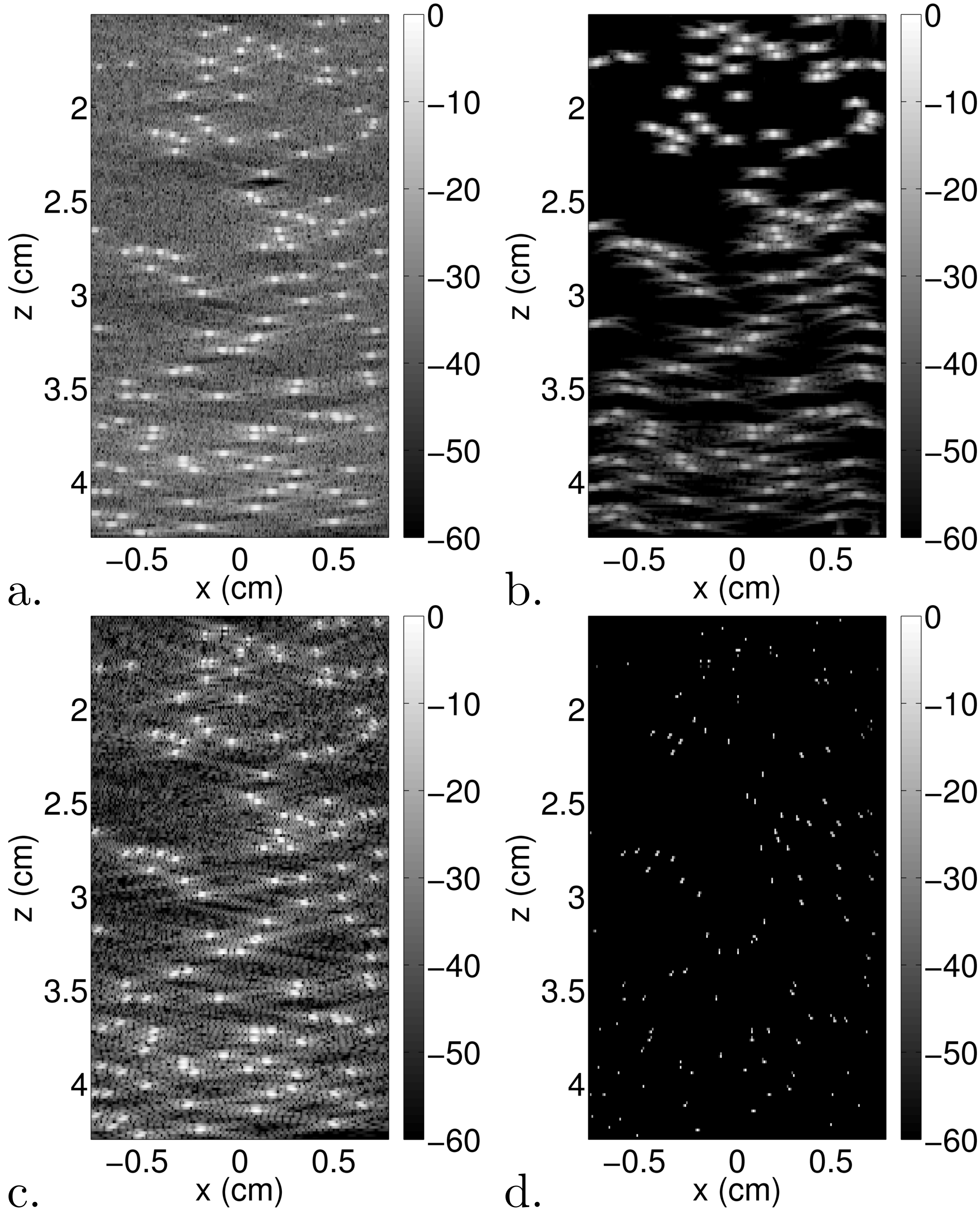

Figure 4.8: *Simulation of 128 point scatterers chosen at random on the grid $\mathcal{G}$. Images obtained using:* a. *plane wave Delay-and-Sum,* b. *conventional Delay-and-Sum with 84 focalized transmit beams,* c. *projection of the raw data on the matrix G,* d. *l_1-minimization.*

a medium using less transmits. In this section, we focus on acquiring less spatial samples, and less transmits, as it seems to be the most beneficial way to use Compressive Sensing for ultrasound beamforming.

The reduction of the number of transmits was implicitly used in the beginning of the paper: we assumed that the medium was insonified by a single plane wave. Usually, many focalized transmits are used to generate a single image, affecting the frame rate. The use of one, or a few, non-focalized transmits would allow for higher frame rates.

Reducing the number of transducers in acquisition can take several forms. In fact, using less elements in the probe raises a simple question: how to select the elements in a way that satisfies the principles of Compressive Sensing. The selection process is not trivial, as it directly impacts the mutual coherence of the measurement matrix. Figure 4.9 shows the evolution of the *mutual coherence* of the matrix G. It is generated by computing the scalar products of all the columns of G and sorting them by descending order of magnitude. The mutual coherence μ of a matrix G is commonly defined as the maximum absolute value of the cross-correlations of the columns of G. In this case:

$$\mu_G = \max_{1 \leqslant i,j \leqslant N_{\text{img}}} |G_i^\mathsf{T} G_j| \tag{4.34}$$

The acquisition using the entire aperture of 128 elements is here taken as a reference and compared against different element selection strategies: the signal is acquired using *a*) the N_{acq} central transducers; or *b*) N_{acq} transducers equally spaced, and spanning the entire aperture; or *c*) N_{acq} transducers selected at random, and spanning the entire aperture, used throughout the acquisition; or finally *d*) N_{acq} transducers selected at random at each time sample.

We simulate two scatterers: one is positioned on the grid $\mathcal{G}$ while the other one is off the grid. The reason for that experiment is that when the expansion of a wavefront originating from a point on $\mathcal{G}$ is evident, the expansion of the wavefront coming from a point off grid is not. It is expected to be wider.

On selecting the central transducers

A first strategy would be to select the central transducers of the probe, and to try to recover the image as if it had been acquired with the entire aperture. However, this approach leads to a high coherence of the measurement matrix and proves to be inefficient, as shown on figures 4.9 and 4.10.a. Using a smaller aperture means a loss in resolution as the main lobe of the PSF of the system becomes wider [128]. Therefore, if we consider a distribution of neighboring scatterers located in the vicinity of each other's main lobes it becomes evident that discriminating them would be a daunting task. The vectors of G corresponding to those points are highly coherent as the signals coming from them are very similar. Intuitively, we know that using a smaller aperture causes the far-field of the probe to be shallower [110]. Hence, the deepest wavefronts acquired by the probe are very close to plane waves. The points considered being close to the axis of the probe, the waveforms generated by scatterers located within a few wavelengths from each other are highly correlated, making it harder for the algorithm to discriminate point scatterers in azimuth for a given depth. The result, shown on figure 4.10.a, is that the main lobe of the point on-grid is a few pixels wide, and the PSF of the off-grid point is wider and somewhat noisy. The algorithm was able to detect a scatterer at the right depth but it had more troubles discriminating it in azimuth.

On selecting equally spaced transducers spanning the whole aperture

To alleviate the limitation aforementioned, a second strategy would be selecting transducers across the entire aperture. It should be beneficial for discriminating scatterers in azimuth. This way, the algorithm is still using only a small subset of transducers, but the entire physical aperture is used. At first, we selected equally spaced transducers. In a classic setting and if the distance between transducers is greater than λ, the issue with using equally spaced transducers is the appearance of grating lobes [128]. In fact, the space between two transducers in an ultrasonic probe is calculated so that the angle at which the grating lobes exist is about 90° from the axis of the probe, minimizing their effect on image quality.

Surprisingly, the grating lobe artifact didn't seem to affect the image quality too much, as can be observed on figure 4.10.b. The results are much better as the two PSFs are equivalent. The PSF of the point on-grid is almost a single pixel, as expected, whereas the PSF of the point off-grid is much narrower than in the previous case.

However, it is to be expected that due to the sidelobes, the coherence of G will be higher for points located in the secondary lobes of each other. As a result, an image with more scatterers would be less accurately reconstructed.

On selecting randomly spaced transducers spanning the whole aperture

In order to attenuate the grating lobe effect, another selection strategy would be to use a subset of randomly spaced transducers to make sure the grating lobe issue doesn't occur. Before acquisition, a subset of elements is chosen at random and used in the generation of the matrix G as well as in the acquisition process.

Figure 4.10.c shows a result that is not fundamentally different from what was obtained previously, because the two scatterers are not located in the vicinity of each other's grating lobes.

On selecting randomly spaced transducers for each time sample

In order to decrease mutual coherence even further, one could think of using a different random set of transducers for each time sample. For example, if the user wants to acquire 1600 time samples with 16 transducers, a 16×1600 map of transducer numbers can be generated and used in the generation of G, as well as to perform the acquisition. This way, the acquisition basis is well-known and well-defined.

From figure 4.9, we can see that the performance improves in terms of coherence. For the neighboring scatterers, the coherence of the sub-sampled basis follows the one of the original one. In azimuth, the coherence decreases faster than what we observed in the previous cases.

The end result, shown on figure 4.10.d, displays an improvement in the focalization of

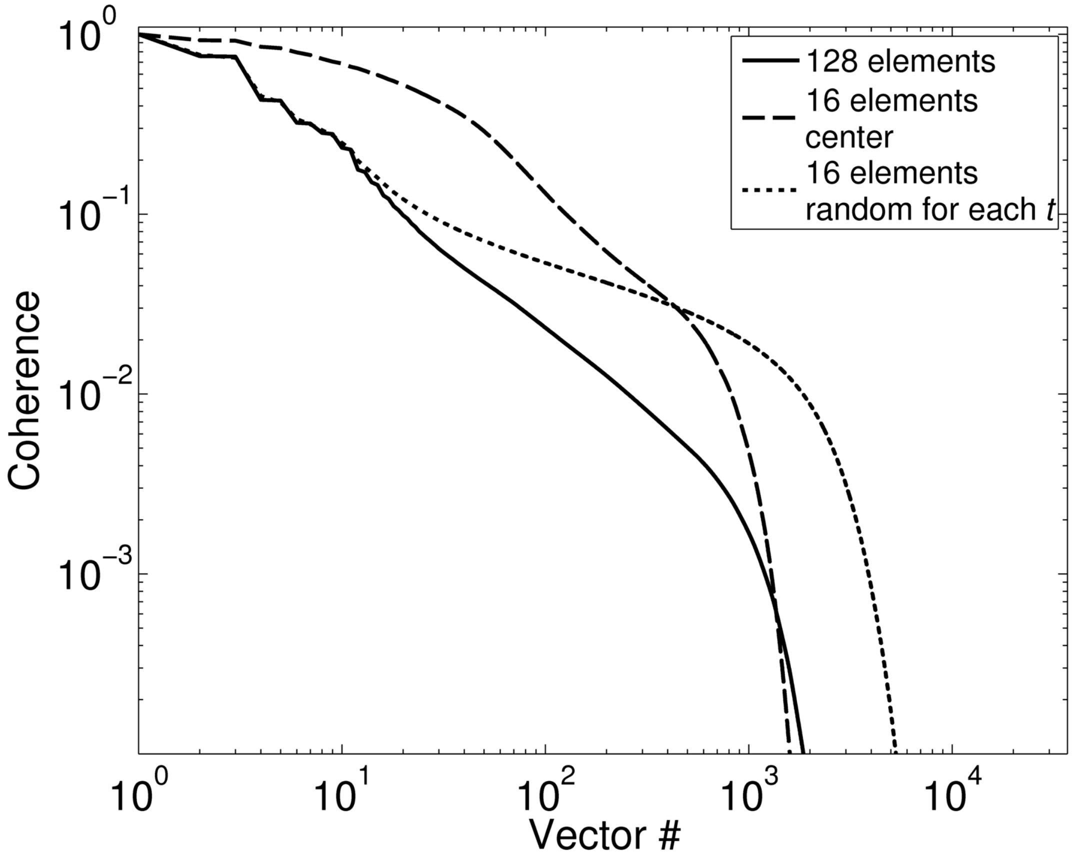

Figure 4.9: *Sorted coherence of sub-sampled G (dashed lines) vs. complete G (continuous line): selecting only the central transducers leads to high coherence and a slow decay of μ, whereas selecting random transducers .*

the energy as the PSF is this time a single pixel exactly for both the on-grid and the off-grid points. The incoherence of G greatly improves the quality of the reconstruction.

4.5 Super-resolution

4.5.1 Principle

In very specific conditions, we can hope to use Compressive Sensing to achieve super-resolution. In fact, the matrix G links a pixel to a wavefront like a dictionary. If the dictionary includes wavefronts originating from scatterers closer than $\frac{\lambda}{2}$, we can hope to separate them. Of course, one could object that with such a fine grid, the coherence of G will

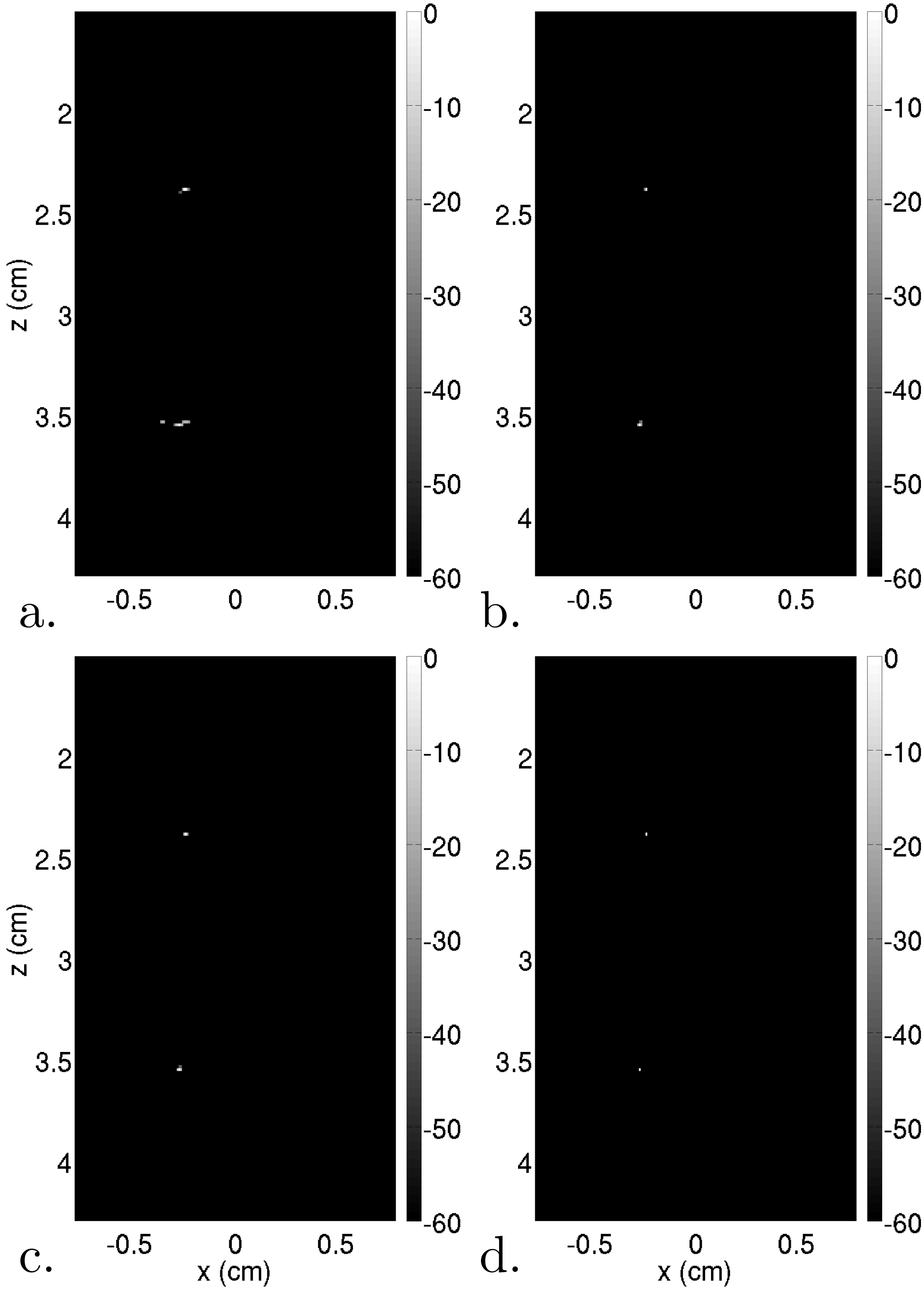

Figure 4.10: *Results obtained from sub-sampled data:* a. *using 16 central transducers;* b. *using 16 equally-spaced transducers spanning the entire aperture;* c. *16 randomly-spaced transducers spanning the entire aperture;* d. *using a different set of 16 randomly-chosen transducers for each time sample.*

increase drastically. However, *in silico* experiments suggest that in the case of a model G that describes the data R exactly, super-resolution is indeed achievable. Similarly, the PSF of a point scatterer should be a single pixel without sidelobes. In that very specific case, the raw data R is generated using the same function gauspuls mentioned in 4.30 than the matrix G. This way, we know that the raw data R corresponds to an image that is exactly sparse.

4.5.2 Results

For this experiment, a finer grid spacing of $\Delta x = \frac{\lambda}{10}$ in azimuth and $\Delta z = \frac{\lambda}{10}$ is used. The other parameters remain unchanged. We consider a homogeneous medium with two point scatterers located at the same depth but at different azimuths. The reconstruction algorithm is applied to the raw data generated analytically using equation 4.30. The Delay-and-Sum image is generated using a standard pulse sequence for a linear array such as the Philips L12-5 : a translating aperture of 64 elements is used resulting in 64 focalized pulses fired *en face* the probe. The two scatterers are located at depth $z_s = 15$ mm. Figure 4.11 shows a performance comparison in terms of resolution between t-CBF and Delay-and-Sum. Four cases are presented: *a*) the two scatterers are distant enough to be perfectly separated by Delay-and-Sum: the distance between the two scatterers is $\Delta x_s = 8\lambda$, *b*) the scatterers are at the limit of separation as defined by the Rayleigh criterion: $\Delta x_s = 2\lambda$, *c*) the scatterers are no longer separated by Delay-and-Sum but t-CBF can still separate the points, the classic reconstruction showing only one main lobe: $\Delta x_s = 2\lambda/3$, and *d*) neither of the reconstructions can separate the scatterers: $\Delta x_s = \lambda/2$. Overall, the contrast seems better as it is not affected by sidelobes.

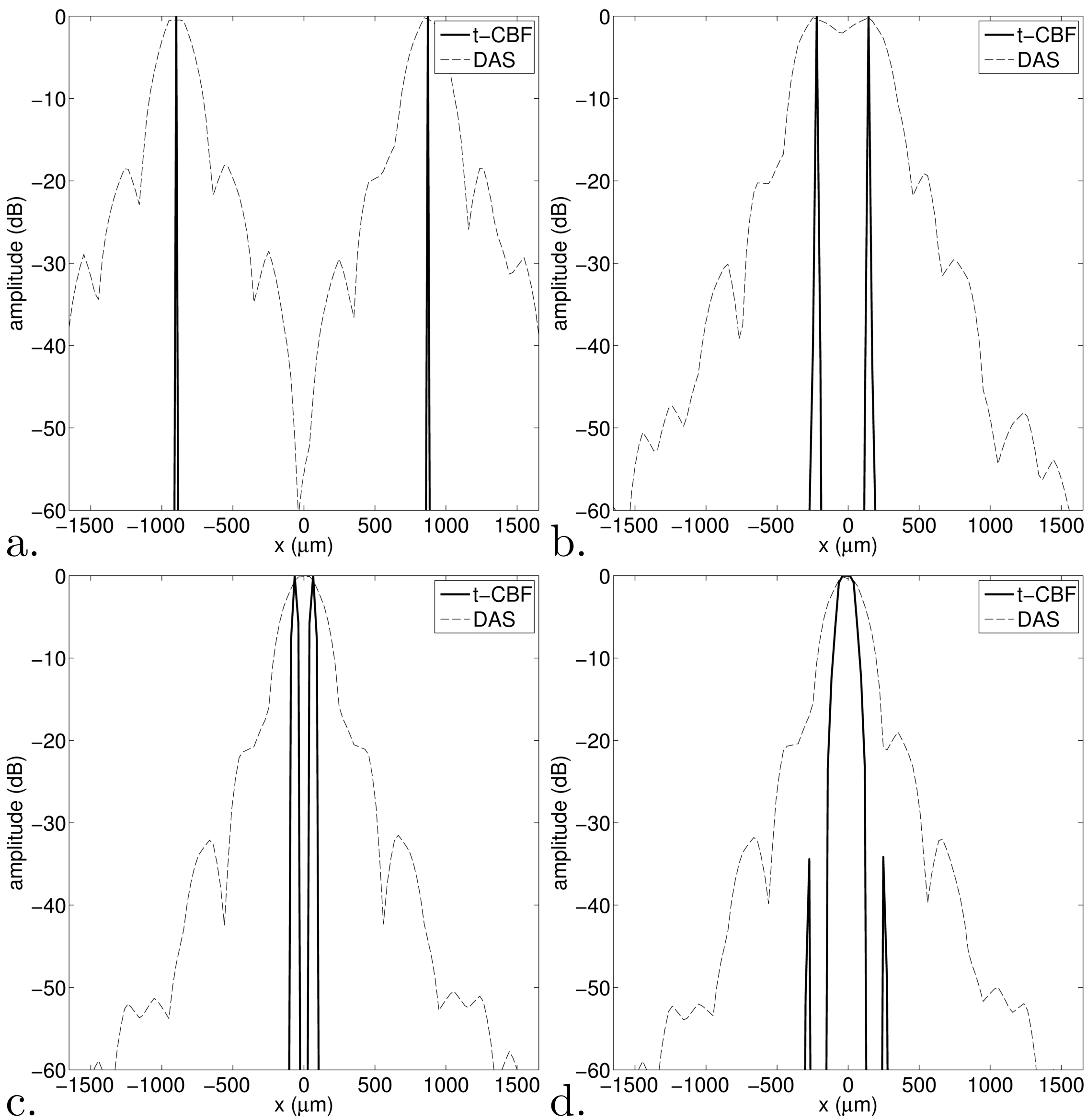

Figure 4.11: *Delay-and-Sum is used as a reference:* a. *separated points:* $\Delta x_s = 8\lambda$*;* b. *at the limit of separation for Delay-and-Sum according to the Rayleigh criterion:* $\Delta x_s = 2\lambda$*;* c. *Delay-and-Sum no longer separates the two scatterers:* $\Delta x_s = 2\lambda/3$*;* d. *t-CBF and Delay-and-Sum cannot separate the two scatterers:* $\Delta x_s = \lambda/2$

4.6 Imaging a sparse wire phantom

4.6.1 Introduction

The last experiment is realized using an iU22 ultrasound scanner from Philips (Bothell WA, USA) with a modified hardware that allows the collection of the raw data. The acquisition is done using a Philips S5-1 sector probe. The phantom is made of a series of taut fishing lines of diameter close to λ parallel to each other, in a water tank. The speed of sound in water is assumed to be unchanged throughout the experiment. S5-1 acquires echoes in a 2D plane perpendicular to the orientation of the fishing lines so that each of them acts as a point scatterer. This way, the expected image should be a set of aligned bright spots on a dark background, ensuring the sparsity we need for Compressive Sensing.

4.6.2 Results

Figure 4.12 shows the images obtained using Delay-and-Sum (figure 4.12.a) and t-CBF (figure 4.12.b). For this particular experiment and because we are using a sector probe, the excitation wave is a diverging wave. The advantage of using a diverging wave is that if the parameters are chosen wisely the entire sector can be insonified at once. The image obtained with t-CBF appears more resolved, there are no sidelobes, and each wire is separated from the next and well-defined in space. The Delay-and-Sum image displays a lower resolution and intertwined sidelobes.

4.7 Conclusion

Over the past decade, the importance of Compressive Sensing in the medical imaging world has increased drastically. So far and to the best of our knowledge, that revolutionary inverse problem technique had never been applied for time-domain beamforming of ultrasonic

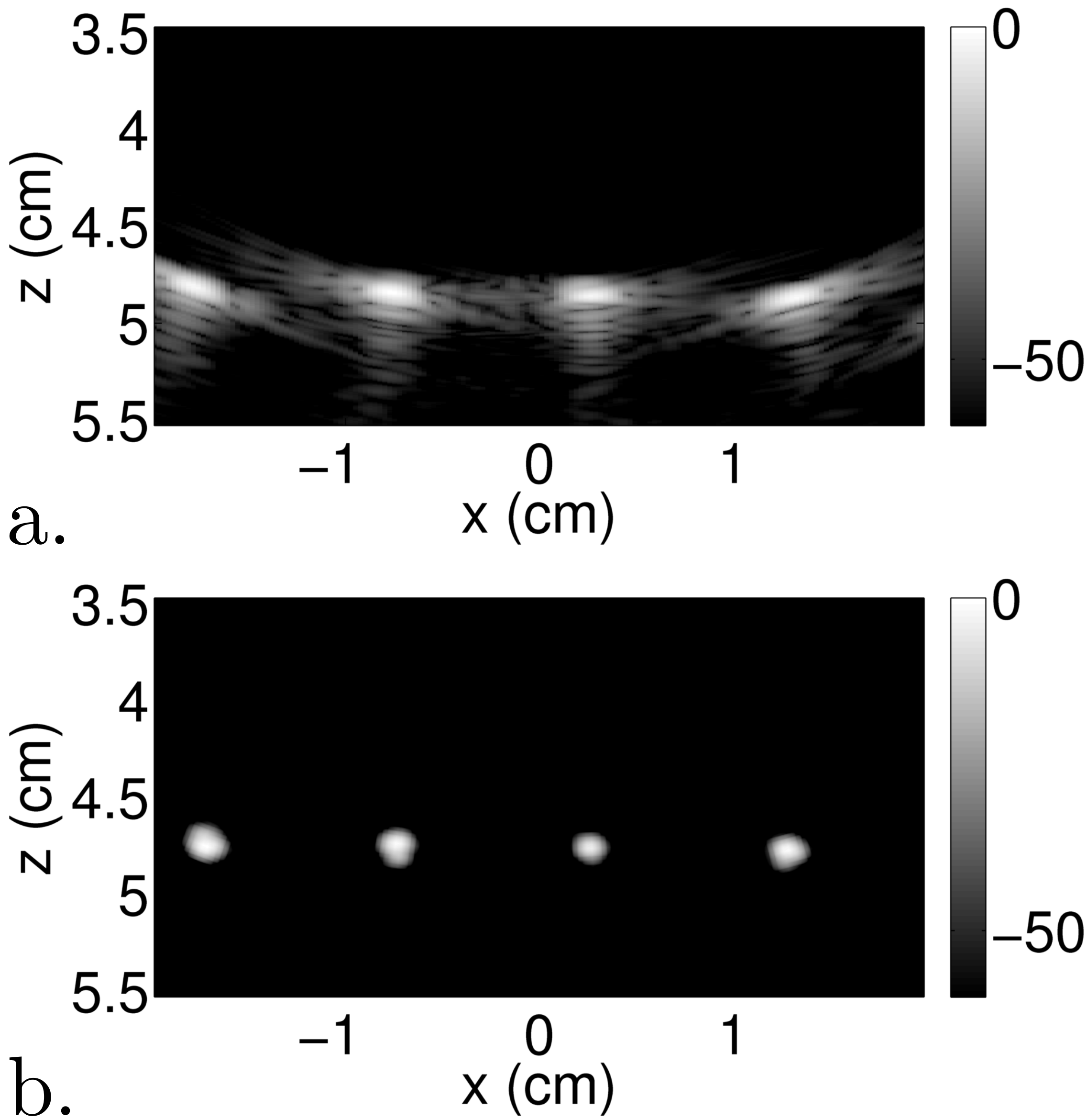

Figure 4.12: *Wire phantom*

fields. We presented a brief overview of Compressive Sensing, and more importantly we justified theoretically the feasibility and validity of the framework. Through simulations and experimentations we showed that an image of point scatterers can be recovered from the insonification of a medium by a single plane wave, when in the case of conventional Delay-and-Sum, more than a hundred focalized excitation pulses would be necessary and, in the case of plane wave compounding, more than ten excitation pulses would be required. We showed that the number of transducers in reception can be reduced from 128 to 16 transducers without significant loss of image quality. Finally, we showed that in specific, controlled conditions (near-perfect model, point scatterers on a known grid) t-CBF can be used to achieve super resolution of point scatterers.

The technique presented here is for time-domain beamforming. Other groups such as Schiffner *et al* have proposed a Compressive Sensing framework in the frequency domain. However, the relationship between the two frameworks is direct. In fact, the matrix G used by Schiffner *et al* is an under-sampled Fourier transform of the matrix G described in this paper.

As a result, the great potential of Compressive Sensing for ultrasonic beamforming has been formally proven. The next steps include, but are not limited to, working on decreasing the size of the matrix G while retaining all the information needed for the reconstruction, finding bases better suited to describing speckle and tissue structures, applying the algorithm to medical phantom, and eventually use the technique *in-vivo*. Those aspects are the subject of the remainder of this work.

Chapter 5

On adapting t-CBF to tissue imaging

5.1 Introduction

The frame rate of pulse echo imaging is limited by factors such as the number of focalized pulses used to compute an image and the imaging depth [118]. Indeed, the time elapsed between two consecutive ultrasonic pulses is incompressible: before emitting another pulse, one must wait for all the echoes up to a certain depth to travel back to the probe. As a result, the time delay separating two consecutive pulses is the time corresponding to a round-trip propagation of the emitted pulse from the surface of the probe to the deepest point imaged.

In the case of cardiac imaging where a typical field-of-view can go as deep as 14 cm, the maximum frame rate achievable is about 10 Hz for 2D and less than 1 Hz for 3D if no further method, like volume stitching, is in use. The straightforward way to increase the frame rate is to use less pulses to probe the medium. Unfortunately, doing so can lead to increased artifacts and a spatial under-sampling of the medium. Decreasing the number of transmit events while maintaining the image quality is thus a particularly arduous challenge.

Over the past few years, Compressive Sensing [99, 101] has gained interest from the beamforming community as it allows the reconstruction of images from less measurements than conventional techniques such as Delay-and-Sum. In this chapter, we propose to study how t-CBF performs on images displaying a speckle pattern and *in-vivo* data using a single diverging wave as the excitation pulse.

5.2 Decreasing the size of G

As stated in 4.4, the size of G can be prohibitive, even to recover small images. For t-CBF to be viable and applicable to clinical imaging problems, its size has to be made manageable.

The Hilbert transform is not unfamiliar to beamforming scientists. It is classically used as an envelope detector, after the Delay-and-Sum algorithm is applied. Indeed, the Delay-and-Sum reconstructs an image that is still modulated at the carrier frequency since it simply combines modulated wavefronts to focalize *a posteriori*. The demodulation is thus performed with the Hilbert transform [129]: the transform is used to calculate the analytic extension of the signal, which absolute value gives the demodulated signal.

However, envelope detection is only one of the many uses of the Hilbert transform. It is especially useful when applied to the analysis of real signals, which have a spectrum that is symmetrical about the $f = 0$ Hz axis. The Hilbert transform extends a real signal into the complex plane in a way that satisfies the Cauchy-Riemann equations [130–132]. The complex extension hence obtained is therefore analytic in $\mathbb{C}$.

Before we explain further in what way the Hilbert transform can help us decrease the size of the matrix G, we need a few basics.

Definition 21. *The* Hilbert *transform of $f \in \mathbb{R}^{\mathbb{R}}$ is given by [133]*

$$\mathcal{H}\left\{f(x')\right\}(x) = \frac{1}{\pi}\ \mathbf{p.v.} \int_{-\infty}^{+\infty} \frac{f(x')}{x'-x} dx' = \mathcal{H}f(x) \tag{5.1}$$

where the divergence at $x = x'$ is allowed for by taking the Cauchy *principal value of the integral, denoted* ***p.v.*** *in equation 5.1.*

Corollary 7. *The* Hilbert *transform is given by the convolution of $f(x)$ with the function*

$-1/\pi x$

$$\mathcal{H}f(x) = f \otimes \left(-\frac{1}{\pi x}\right) \tag{5.2}$$

Based on equations 5.1 and 5.2, applying the HILBERT transform may not seem straightforward. However, its interpretation is made easier in the FOURIER domain. To show this, let us take the FOURIER transform of definition 5.2. We know that the FOURIER transform of the convolution of two functions is equal to the product of their respective FOURIER transforms.

Property 9. *The* FOURIER *transform of the convolution of f and g is the product of the* FOURIER *transform of f by the* FOURIER *transform of g:*

$$\mathcal{F}\mathcal{H}f(\omega) = \mathcal{F}f \times \mathcal{F}\left\{-\frac{1}{\pi x}\right\} \tag{5.3}$$

The FOURIER transform of $-1/\pi x$ is given by

$$\mathcal{F}\left\{-\frac{1}{\pi x}\right\} = -\frac{1}{\pi}\ \textbf{p.v.} \int_{-\infty}^{+\infty} \frac{e^{-i\omega x}}{x} dx \tag{5.4}$$

We can simplify this integral by writing $e^{-i\omega x} = \cos(\omega x) - i\sin(\omega x)$. Additionally, $\frac{\cos(\omega x)}{x}$ is anti-symmetrical with respect to x, so its integral over $\mathbb{R}$ vanishes to zero, and we are left with

$$\mathcal{F}\left\{-\frac{1}{\pi x}\right\} = \frac{i}{\pi} \int_{\mathbb{R}} \frac{\sin(\omega x)}{x} dx \tag{5.5}$$

The integral in equation 5.5 is well-known and we have

$$\int_{\mathbb{R}} \frac{\sin(\omega x)}{x} dx = \left\{\begin{array}{ll} -\pi & \text{for } \omega < 0 \\ 0 & \text{for } \omega = 0 \\ \pi & \text{for } \omega > 0 \end{array}\right\} = \pi\ \mathrm{sgn}(\omega) \tag{5.6}$$

where sgn is the signum function. This brings, finally

$$\mathcal{F}\left\{-\frac{1}{\pi x}\right\} = i\ \mathrm{sgn}(\omega) \tag{5.7}$$

Therefore, we have proven theorem 7.

Theorem 7. *The* HILBERT *transform is a multiplier of the* FOURIER *transform and*

$$\mathcal{F}\mathcal{H}f(\omega) = i\ sgn(\omega)\mathcal{F}f \tag{5.8}$$

Equation 5.8 shows that applying the HILBERT transform to a signal f amounts to shifting the phase of its negative frequency components by $-\pi/2$, and to shifting the phase of its positive frequency component by $\pi/2$.

Definition 22. *The analytic function associated with $f \in \mathbb{R}^{\mathbb{R}}$ is the complex function $f_a \in \mathbb{C}^{\mathbb{R}}$ given by*

$$f_a(t) = f(t) - i\mathcal{H}f(t) \tag{5.9}$$

The HILBERT transform of f is commonly referred to as the *quadrature function* of f. Taking the FOURIER transform of f_a to analyze its frequency components, we get

$$\mathcal{F}(f_a)(\omega) = \mathcal{F}(f)(\omega) - i\mathcal{F}\mathcal{H}(f)(\omega) \tag{5.10}$$

Knowing that the HILBERT transform is a multiplier of the FOURIER transform (equation 5.8), we prove theorem 8.

Theorem 8. *The spectrum of the analytic continuation f_a is obtained by multiplying the spectrum of f with the* HEAVISIDE *step function:*

$$\mathcal{F}(f_a)(\omega) = [1 + sgn(\omega)]\,\mathcal{F}(f)(\omega) \tag{5.11}$$

Therefore, it is clear from 5.11 that the analytic continuation f_a contains no negative frequency components. Hence, the simplest way to compute the analytical signal f_a is to discard all the negative frequency components of f.

This last property is particularly interesting in our case. Recalling SHANNON's sampling theorem [79], we know we have to ensure the sampling frequency of our system is at least twice as fast as the highest frequency component present in our signal. One can easily understand that boundary by considering the frequency spectrum of a real, band-limited signal represented in figure 5.1. The signal studied is a Gaussian model of an ultrasonic pulse of central frequency f_0 and limited bandwidth. In order to make sure that the entire spectrum is covered in the acquisition process, the sampling frequency must span it entirely. Since the signal is in $\mathbb{R}$, its spectrum is symmetrical about the $f = 0$ Hz axis. As a result, the sampling frequency must span frequency components from $f_{\max}$ all the way to its symmetric about the $f = 0$ Hz axis $-f_{\max}$, yielding the famous $f_s \geqslant 2f_{\max}$. For a signal such as a narrow band RF signal, this process is far from optimal since many empty frequency components are covered.

That is where the HILBERT transform becomes extremely advantageous. As shown by equation 5.11, the HILBERT transform of a real signal is equivalent to discarding the signal's negative frequency content, with no loss of information. However, as shown in figure 5.2, the sampling only needs to span the frequency components in the bandwidth of the signal, around the central frequency. This way, we only need $f_s^{\mathrm{Hi}} \geqslant f_{\max} - f_{\min}$, where f_s^{Hi} is the sampling frequency of the HILBERT transform of the signal.

According to the parameters in table 5.1 for example, the scanner samples the signal at 32 MHz. Using the analytic signal obtained thanks to the HILBERT transform, we find that the minimum sampling frequency for our application is

$$f_s^{\mathrm{Hi}} = 2f_c\mathrm{bw} = 2 \times 2.7\ \mathrm{MHz} \times 0.6 = 6.24\ \mathrm{MHz} \tag{5.12}$$

which is 5 times lower than 32 MHz. As a result, if we image 5 cm deep, we decrease

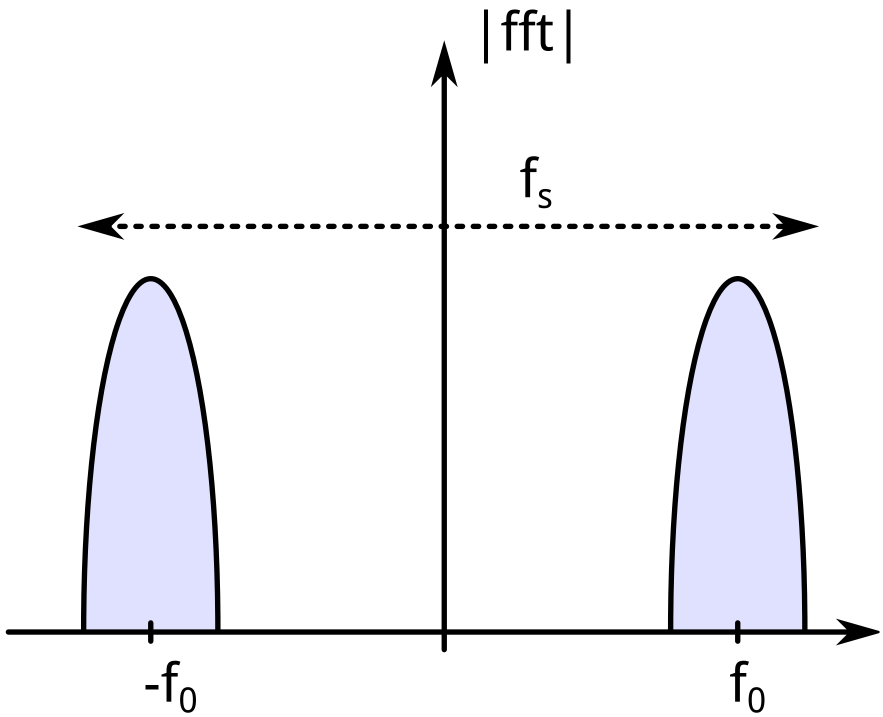

Figure 5.1: *Spectrum of the Gaussian pulse emitted by an ultrasonic probe. The sampling frequency has to be at least* $2f_{max}$.

Parameter	f_c	bw	λ	N_{elements}	p	c_{sound}	f_s
Value	5.2 MHz	0.6	295.7 μm	128	300 μm	1540 m.s^{-1}	20.8 MHz

Table 5.1: *Simulation and experimental parameters used in the reconstruction of the images in figure 5.4.*

the number of time samples from 2078 to 405. The images in figure 5.4 are reconstructed on a 305 by 386 pixel grid. Since we simulate the per-channel data for each pixel on the grid to populate G, we end up with a 250.5 gigabyte (GB) matrix G if we use the pre-Hilbert transform data. Using the post-Hilbert transform data, G is only 48.8 GB which is manageable by our server.

5.3 Tissue image compression

In chapter 4, we used t-CBF to recover images of point scatterers in a homogeneous medium. Since the number of point scatterers was kept low, we were expecting the images to be

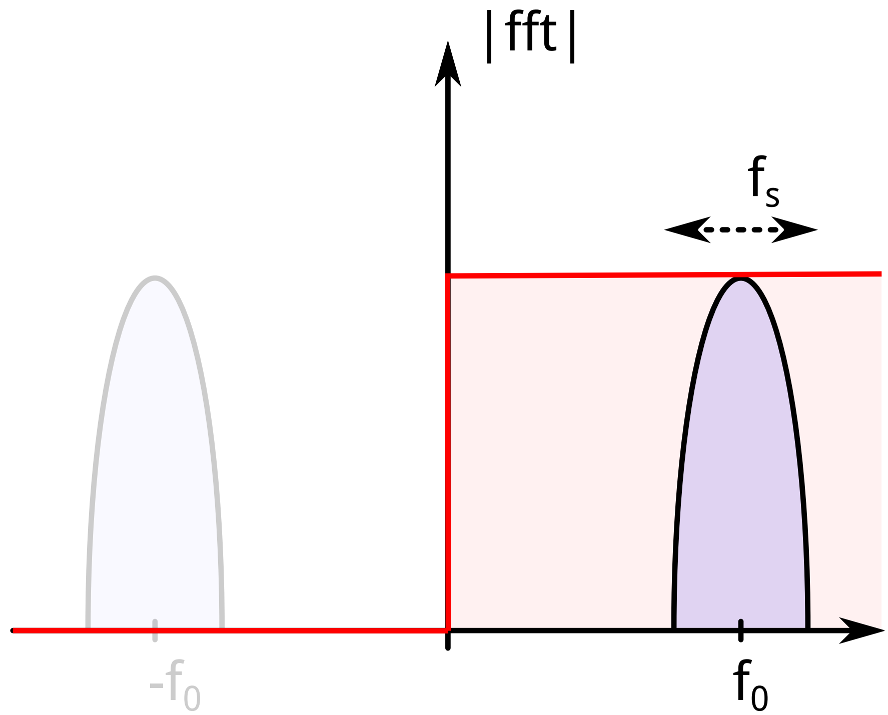

Figure 5.2: *Spectrum of the same signal processed with the* HILBERT *transform. The negative frequencies are discarded, leading to a complex signal that requires a smaller sampling frequency imposed by its bandwidth.*

extremely sparse in the image domain. That is, we needed not apply a sparsifying transform. This specific case is not common in tissue imaging. Images of tissue usually display a *speckle pattern*, due to the medium being a collection of several thousand randomly positioned point scatterers. The reflection of the transmit wave on this dense collection of scatterers produce reflected waves that randomly interfere with each other, giving a salt-and-pepper aspect to the image.

As we are moving from a few point scatterers to thousands of them, we are losing the sparsity in the pixel domain. A sparsifying transform needs to be used to successfully apply t-CBF. As mentioned in chapter 2, the wavelet transform is one of the best promoters of sparsity.

5.3.1 Sparsifying speckle with wavelets

The wavelet transform famously provides us with sparse representations and is not specific to a particular type of images. It is widely used in image compression for example in the JPEG2000 format [134]. It separates details in an image at various scales from the bulk of the image.

The wavelet transform is classically used in Compressive Sensing to recover *unsparse* signals or images. It is an efficient way to represent a signal, thanks to its ability to encode most of the information of the signal in a few coefficients. Moreover, the wavelet transform is fully compatible with the Compressive Sensing framework, and requires only minor modifications to work.

Let Ψ be a generic wavelet transform operator. By generic, we mean that we are not specifying a particular wavelet family or decomposition level at this point. Applying the wavelet transform to a vector-image I then amounts to computing ΨI. To understand fully how the wavelet transform can be used together with t-CBF to recover unsparse images, one should consider that if the vector I we want to recover is now unsparse, the vector ΨI is, indeed, sparse. Thus, we can apply the minimization algorithm 4.33 to ΨI:

$$\min_{I \in \mathbb{R}^N} \|\Psi I\|_{l_1} \text{ subject to } \|GI - R\|_{l_2} \leqslant \epsilon \tag{5.13}$$

This problems amounts to minimizing the l_1-norm of the wavelet transform of I under the constraint $\|GI - R\|_{l_2} \leqslant \epsilon$. Similarly, we can also solve

$$\min_{I \in \mathbb{R}^N} \|W\|_{l_1} \text{ subject to } \|G_\Psi W - R\|_{l_2} \leqslant \epsilon \tag{5.14}$$

where $W = \Psi I$ is the wavelet transform of I, and $G_\Psi = G\Psi^{-1}$ is the linear operator that relates the wavelet transform of I to the raw acquired data R.

5.3.2 Choosing a wavelet family

There are several flavors of the wavelet transform: different wavelet families (Haar, Daubechie, splines, etc), different ways to compute it, decimate the result, etc. As a result, choosing the transform that is the most suitable for our problem is not trivial.

One naive way of choosing a transform would be to run t-CBF on a set of phantoms a number of times, and changing the sparsifying transform every time with the hope that one transform will stand out. As a first step towards a more robust way of selecting a sparsifying transform, that is what we did. For example, figure 5.3 shows the results of t-CBF applied to a phantom displaying equispaced point scatterers, as well as walls made out of speckle. At first, no sparsifying transform was applied. We notice that the image has a lot of holes in the speckle. This is directly due to the fact that no sparsifying transform was applied: the algorithm is looking for the most significant coefficients that lead to a bounded error and a sparse solution. As a result, the parts of the speckle that would have a very low intensity are simply thresholded out and set to zero. The image works as a first approximation, but is certainly not suitable for clinical applications.

Then we went on to apply the wavelet transform using a Haar mother wavelet. The reconstructed image has a less hole-y speckle structure, which is desirable. This is directly related to the compression capabilities of the wavelet transform. We also note that the image is generally smoother, making it more appealing. This is due to the fact that thresholding in the wavelet space produces a smoother result than thresholding in the pixel domain directly.

First and third order spline wavelets were also tried. Their smoothness is an advantage in the reconstruction, since they produce a smoother image. However, the fact that they are not orthogonal raises an issue. The point scatterers are not well-reconstructed. One can see in figure 2.15 that in fact, the reconstructed point scatterers are asymmetrical.

The choice of a wavelet family is inherent to the type of images we need to reconstruct. Different structures in an image can be represented efficiently in different wavelet bases. For those reasons, there is probably not an absolute best basis choice to apply t-CBF.

Using wavelets helps improve the aspect of the speckle pattern. On figure 5.3.a we can see that the speckle has a lot of zero-valued pixels and its texture is off. Figures 5.3.b, c, and d have a smoother speckle pattern that looks more similar to what sonographers are accustomed to.

Then, the resolution seems to be affected by the size of the support of the wavelet basis. More compact supports lead to better resolution: the more compact Haar wavelets used in figure 5.3.c lead to better resolution of the point scatterers.

From this very preliminary glimpse into the world of t-CBF reconstructions, it appears that using an orthonormal wavelet family with a compact support is the best option.

5.3.3 Description of the phantoms

Another way to look at the problem is to consider the amount of compression that such a transform can bring to our image. To achieve that goal, we chose to work on four phantoms: two simulated phantoms, and two physical phantoms. Reconstructions using Delay-and-Sum are displayed in figure 5.4.

Phantoms 5.4.a and 5.4.c allows assessment of resolution. They incorporate point scatterers that give an idea of the Point Spread Function (PSF) [128] of the system. Furthermore, phantom 5.4.c is a physical phantom that has point scatterers in a matrix of tissue that produces a typical speckle pattern.

Phantoms 5.4.b and 5.4.d are designed to assess the contrast of the reconstruction, with cysts and lesions. Moreover, phantom 5.4.d is a physical phantom that incorporates different kinds of cysts: anechoic, hypoechoic, and hyperechoic.

Those four phantoms are then taken to the transform space. Namely, we apply the wavelet transform, and study the compressibility of the result. In order to do so, a criteria is imposed: we want the compressed image to retain at least 99% of the energy of the original image.

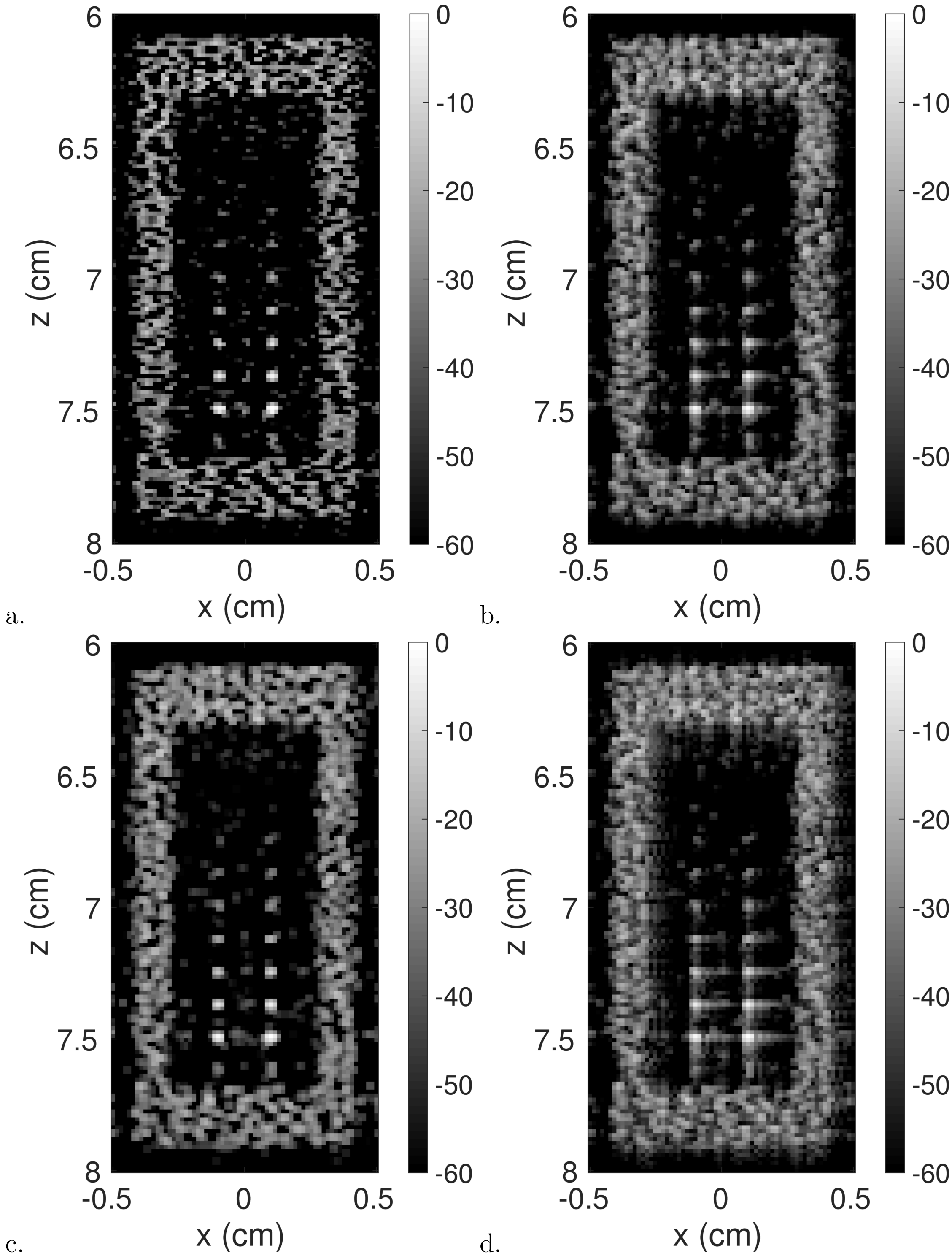

Figure 5.3: *Numerical phantom recovered with t-CBF:* a. *without wavelet transform,* b. *with first order spline wavelets,* c. *with* HAAR *wavelets,* d. *with third order spline wavelets.*

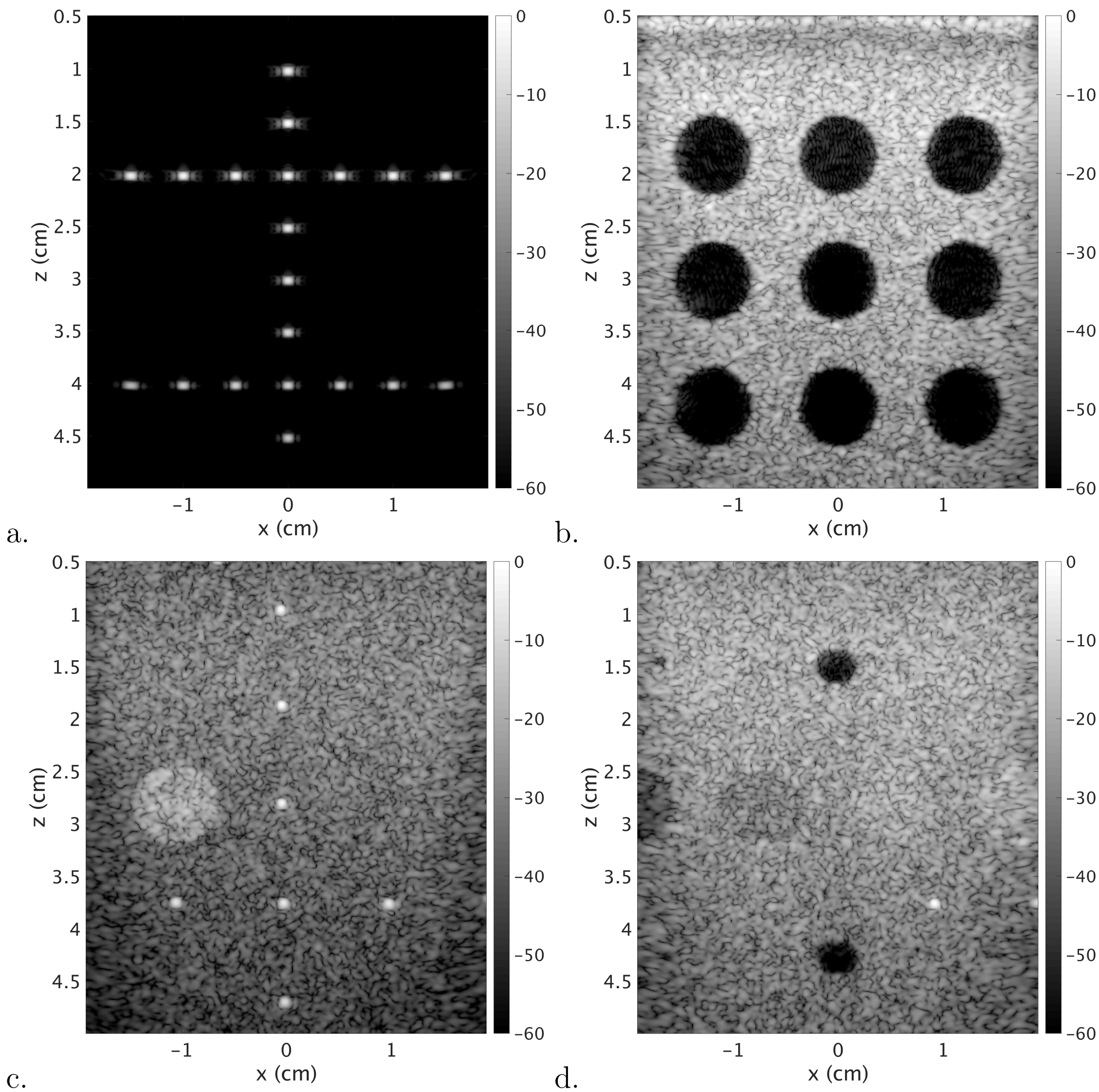

Figure 5.4: *Phantoms used in the assessment of wavelet bases. The simulations or acquisitions are done with 75 plane waves. The reconstructions are performed using the classic Delay-and-Sum algorithm. The phantoms allow the observation of a wide range of acoustic structures, from point scatterers to speckle patterns.*

5.3.4 Definition of the parameters

Definition 23. *In the case of orthogonal wavelets, the retained energy is given by*

$$e_{wavelet} = 100\frac{\|X^{wavelet}\|^2}{\|X\|^2} \tag{5.15}$$

where "wavelet" is the wavelet family used for the decomposition $X^{wavelet}$ of image X. $e_{wavelet}$ is the l_2-norm recovery score.

On the other hand, we need the compression score to be as high as possible.

Definition 24. *Similarly, a compression score is defined by*

$$c_{wavelet} = 100\frac{\#\{i \ / \ X_i^{wavelet} \neq 0\}}{\#\{i \ / \ X_i \neq 0\}} \tag{5.16}$$

where # is the cardinality of the set, that is the number of individual elements in the set.

The parameters used in the simulations and the experiments are summarized in table 5.1.

Since the condition we impose is on the retained energy, we only display the compression performance. It is worth noticing that for this first exploration, the classic dyadic wavelet transform, or critically sampled wavelet transform, has been used. The wavelet families we study are orthonormal and exhibit compact support

- **Haar wavelets**, commonly used in the JPEG2000 format,
- **Daubechie wavelets**, which are a higher order expansion of the Haar wavelets,
- **Symmlets**, also spelled symlets, which introduce more symmetry to Daubechie wavelets, and are used for image coding where symmetrical errors are believed to be less perceptible to the human eye,
- **Coiflets**, used in the sampling approximation of smooth functions [135], which is of particular interest in our application.

5.3.5 Compressibility of various types of phantoms

The compressibility of the four images is different, due to the very differences in the structure of the phantoms. To assess the compressibility of each image, we compute the c_{wavelet} compression performance for different levels of decomposition. The resulting score is stored in a matrix, and the final result is displayed as a heat map. For the representation of the score, we choose a diverging color map that goes from blue for low values, to white for average values, and finally to red for high values.

To get a good c_{wavelet} compression score, the wavelet must be able to represent the image very well. A rule of thumbs that consistently comes up in the literature is that one should select a mother wavelet that matches the features of the image to be analyzed. In the case of point scatterers for example, we expect a compact wavelet to perform better than a less compact one. If the goal is to reconstruct the point scatterers as bright spots, then a certain level of discontinuity might be preferable. For this study, we are working with the Delay-and-Sum image which is limited by the resolution in the form of a low-pass filter. As a result the Delay-and-Sum image is relatively smooth, even in the case of point scatterers.

As far as the level of decomposition is concerned, one must take into account that the higher the level of decomposition, the more we split the spectrum of the image. As a result, a slowly varying, smooth image will most likely not be well represented by a low decomposition level. If we consider a level 1 decomposition, then the spectrum is split only once, with the high-pass containing little information. The low-pass will contain most of the information, but since our image only has low frequencies, the split won't be optimal in terms of representation efficiency. If we consider the generic signal with a Gaussian bandwidth in figure 5.5, we see that the first split is beneficial but not optimal. The second split of the spectrum is also beneficial, and optimally separates the (non-existent) high-frequency content from the low-frequency content (the actual signal). Now we see that a third split does not bring anything new to the decomposition since it is essentially splitting a part of

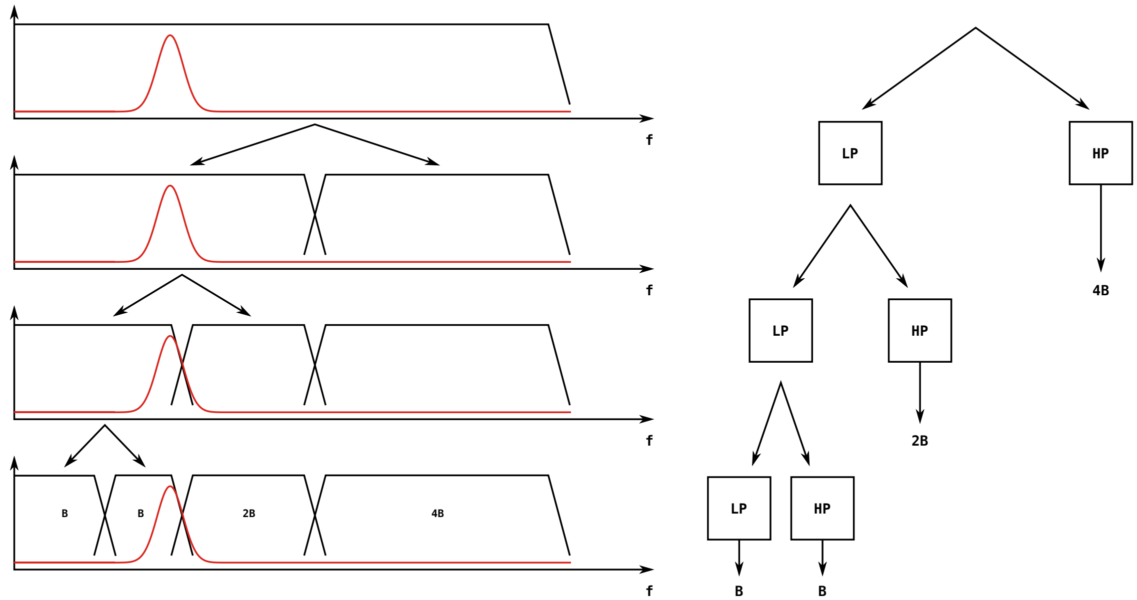

Figure 5.5: *Wavelet decomposition of a generic signal with a Gaussian bandwidth. The level 1 and level 2 decompositions are beneficial since they separate frequencies efficiently. The level 3 decomposition is simply splitting a part of the spectrum that is empty, adding complexity to the transform but not bringing anything advantageous.*

the spectrum that is empty of content. It also increases the complexity of the transform. Therefore, in that case a level 2 decomposition is the most efficient representation.

Point scatterers in a homogeneous medium Phantom 5.4.a is made out of a collection of bright point scatterers on a dark background. The image is actually already sparse in the the pixel domain. However, for the sake of the study, we compute its expansion in the transform space for a number of wavelet families. The results are shown in figure 5.6. As expected, the wavelets with the most compact support of their respective family (Haar, Daubechie$_2$, Symmlet$_2$, and Coiflet$_1$) are the best performers at low decomposition levels. That being considered, we notice that the compression performance at different decomposition levels varies to reach an optimum. On figure 5.6.b, we see that for a very short wavelet such as the Haar wavelet the maximum would be obtained for a hypothetical decomposition level less than 1. In general, we observe that the compression capabilities of more compact wavelets are better at low decomposition levels. For the less compactly supported wavelets of the set, such as Coiflet$_5$ the maximum of compressibility is obtained for a decomposition level greater than 5. Whereas for a shorter wavelet such as Coiflet$_1$, the decomposition level that leads to the maximum of compressibility is 2. The most compressible decomposition is obtained for a Symmlet$_4$ at decomposition level 2.

Hypoechoic cysts in speckle As for phantom 5.4.b, it is a simulated phantom containing cysts in a speckle matrix. The contrast is maximum since the cysts are empty of any diffusers. The speckle level is constant throughout the image. The presence of the speckle along with sharp edges makes the compression of the image somewhat more challenging. As we see on figure 5.7.b, the maximum level of compression obtained is slightly above 88%, when it was over 97% for the previous image. In terms of global compression performance, a similar pattern than previously observed is present: for a given wavelet, *e.g.* Coiflet$_4$, the compression performance increases with the decomposition level up to a certain point, where it reaches a maximum and starts decreasing. Figure 5.7.b shows this trend for all wavelets used. We also note that the HAAR wavelets have by far the worst performance, when the Coiflet$_4$ shows the best performance. For this particular image, the best compression performance is thus obtained with Coiflet$_4$ at decomposition level 3, where the image shows a compressibility of over 88%.

Point scatterers and hyperechoic lesion in speckle Phantom 5.4.c is a physical phantom with a circular lesion and 7 point scatterers in a cross pattern. We notice immediately that the compressibility of image 5.6 is significantly lower than its simulated counterpart. This is due to the fact that the simulated image 5.6 has extensive region of solid black, since it only contains point scatterers and no speckle. However, image 5.8 is closer to what one would observe in tissue. That being said, a similar pattern than previsouly observed hereby emerges. The HAAR wavelet has poor performance and for a given wavelet the compressibility reaches a maximum for a certain decomposition level. The best compression performance is reached for Symmlet$_4$ at decomposition level 2.

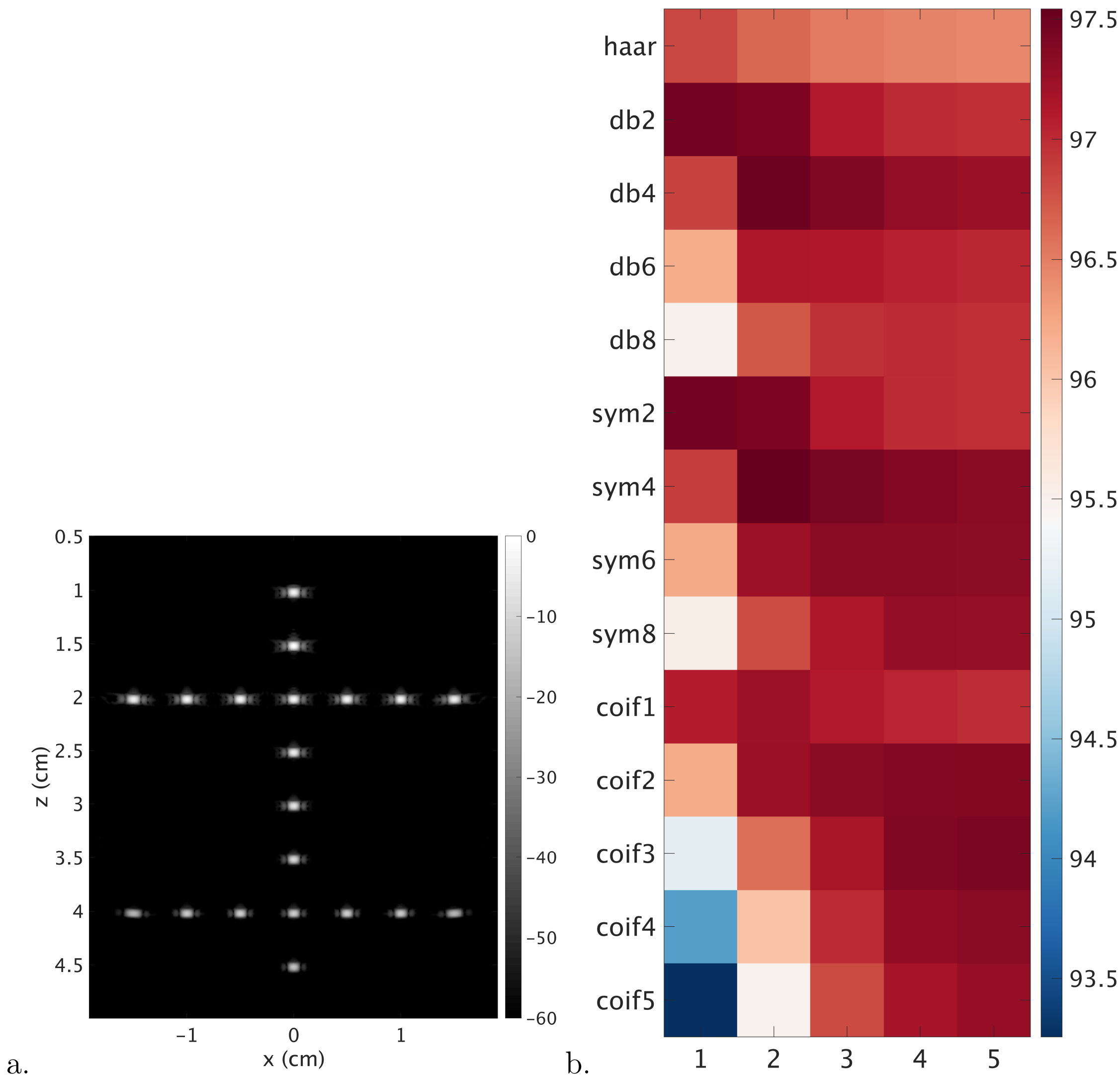

Figure 5.6: *Compression performance for the resolution simulation. Since we are compressing an image of bright points on a black background, the wavelet has to be good at representing points. We notice that the performance decreases as the support of the wavelet increases, regardless of the family.*

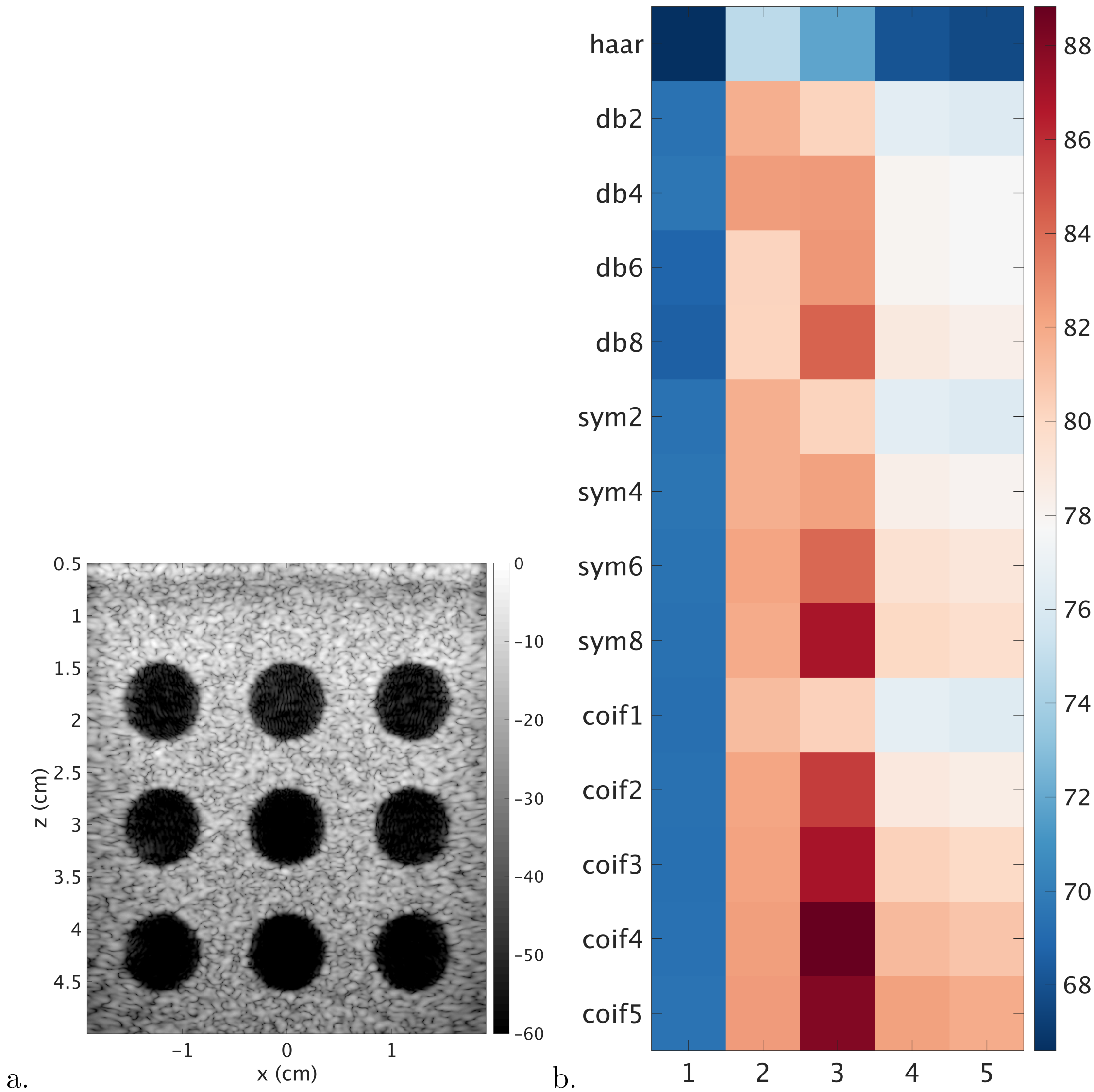

Figure 5.7: *Compression performance for the contrast simulation. We are trying to compress speckle while keeping edges sharp. Wavelets are known to offer poor representations of edges. Compressing speckle is challenging because its very structure depends on both the tissue observed and the system used to image it.*

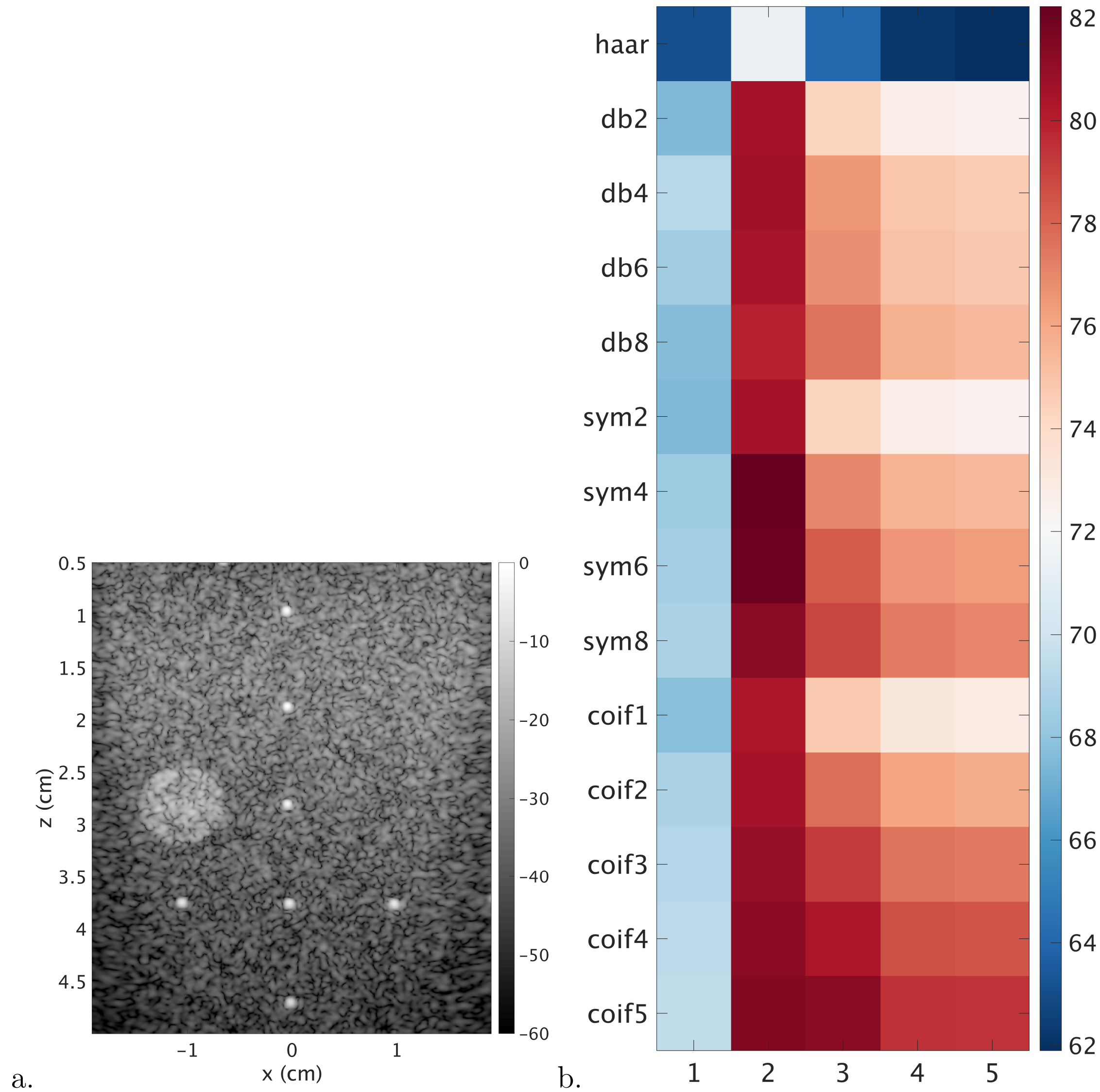

Figure 5.8: *Compression performance for the resolution physical phantom. It is a typical resolution phantom with a circular lesion, and a collection of 7 point scatterers in a cross pattern. The image appears to be less compressible than image 5.6 and 5.7. This might be due to the fact that image 5.6 does not display extensive regions of solid black. To the contrary, the image has no cyst as opposed to image 5.7.*

Hypo and hyperechoic regions in speckle Phantom 5.4.c is a very complete and realistic phantom that contains all the common structures one can observe in tissue:

- a point scatterer, which could be a calcification,
- a low contrast, circular hypoechoic region, which corresponds to a low contrast cyst,
- a low contrat, circular hyperechoic region, which corresponds to a low contrast lesion,
- two high contrast, circular hypoechoic regions, which correspond to high contrast cysts,
- a speckle pattern, commonly observed in tissue.

Probably due to the cysts that are solid black, image 5.9 is more compressible than image 5.6. Once again, the Haar wavelet leads to poor performance, and for a given wavelet the compression score reaches a maximum value for a certain decomposition level, before decreasing again sharply. The best compression score is obtained for a Coiflet$_4$ wavelet, at decomposition level 3.

The best wavelets from the compression standpoint are compiled in table 5.2 for future reference.

The next step is to compute the images using t-CBF and taking into account what we just learned about wavelet and decomposition level choices. Then we compute the images using the JPEG2000 standard Haar wavelet at the best decomposition level for comparison. The goal is to determine if the extra computational cost is worth it in terms of reconstruction quality.

5.3.6 Point scatterers in a homogeneous medium

We start with the sparsest phantom of the study, whose Delay-and-Sum reconstruction is shown in figure 5.10.a. The t-CBF reconstruction is carried out two separate times, using different wavelets in the sparsifying transform:

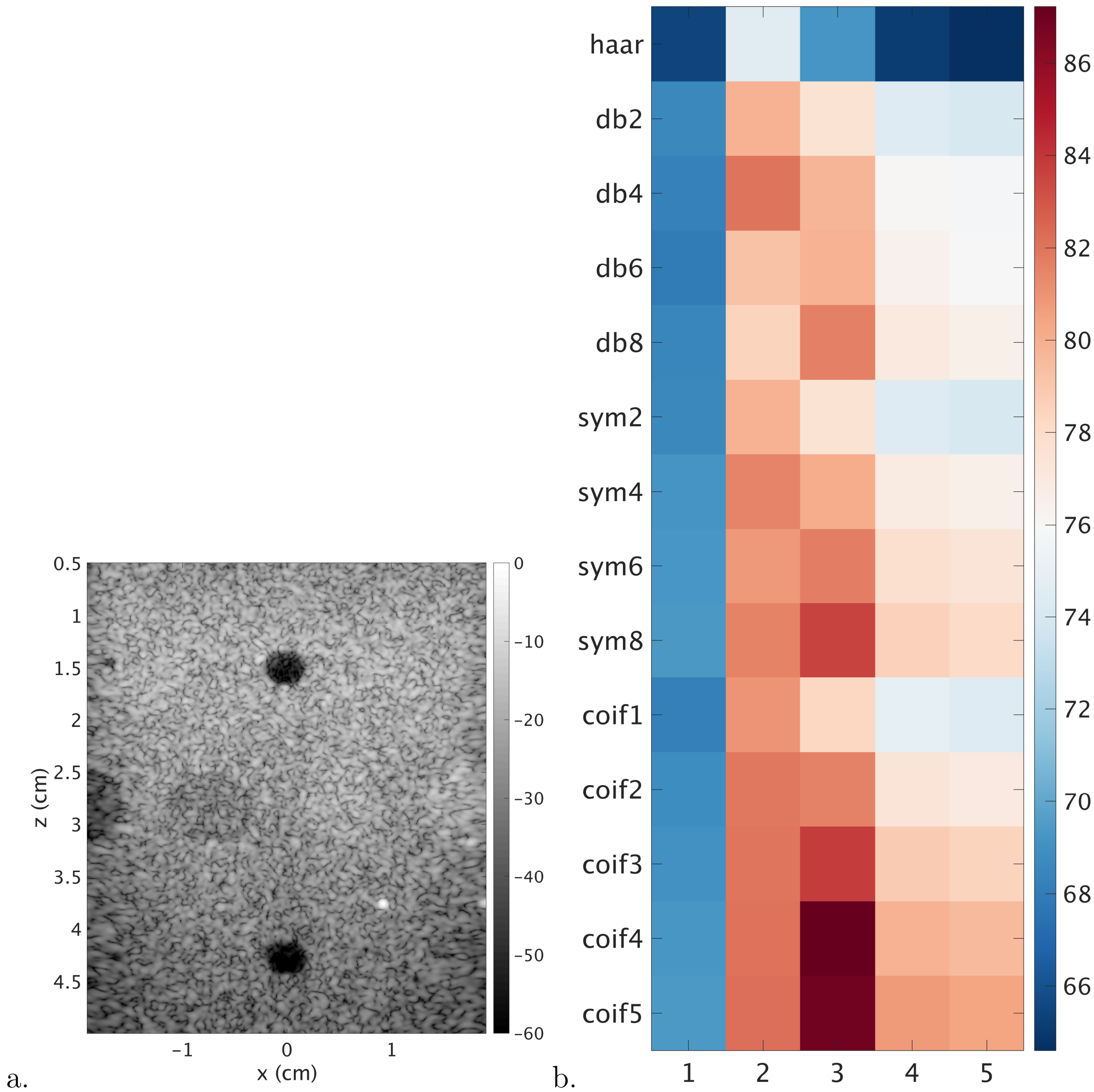

Figure 5.9: *Compression performance for the contrast physical phantom. This phantom contains both high-contrast and low-contrast cysts and lesions, as well as a point scatterer.*

Phantom	5.4.a	5.4.b	5.4.c	5.4.d
Type of data	simulated	simulated	experimental	experimental
Features	point scatterers in free-space	hypoechoic cysts in speckle	point scatterers and hyperechoic lesion in speckle	hypoechoic and hyperechoic regions and point scatterers in speckle
Assessment	resolution	contrast	resolution	contrast
Best wavelet	Symmlet$_4$	Coiflet$_4$	Symmlet$_4$	Coiflet$_4$
Best level	2	3	2	3
Compressibility	97.54%	88.83%	82.22%	87.22%

Table 5.2: *Summary of the best wavelet and compression score results.*

- Haar wavelet at decomposition level 1: the reconstruction is shown in figure 5.10.b. The resolution of the point scatterers is much improved, from the Delay-and-Sum reconstruction. The image was reconstructed in about 10 minutes.

- Symmlet$_4$ wavelet at decomposition level 2: the reconstruction is shown in figure 5.10.c. The resolution is comparable to the Delay-and-Sum reconstruction, by the aspect of the point scatterers is unusual. Their spread is the same in the x- and z-dimensions, giving them a cross-shape. The image was reconstructed in about 7 minutes. It is faster than the Haar reconstruction, but the aspect of the image is not acceptable.

5.3.7 Hypoechoic cysts in speckle

We continue with the other simulated phantom: the contrast phantom whose Delay-and-Sum reconstruction is shown in figure 5.11.a. The t-CBF reconstruction is carried out two separate times, using different wavelets in the sparsifying transform:

- Haar wavelet at decomposition level 2: the reconstruction is shown in figure 5.11.b. The image has a pixelated aspect, but the edges are sharp and the contrast preserved.

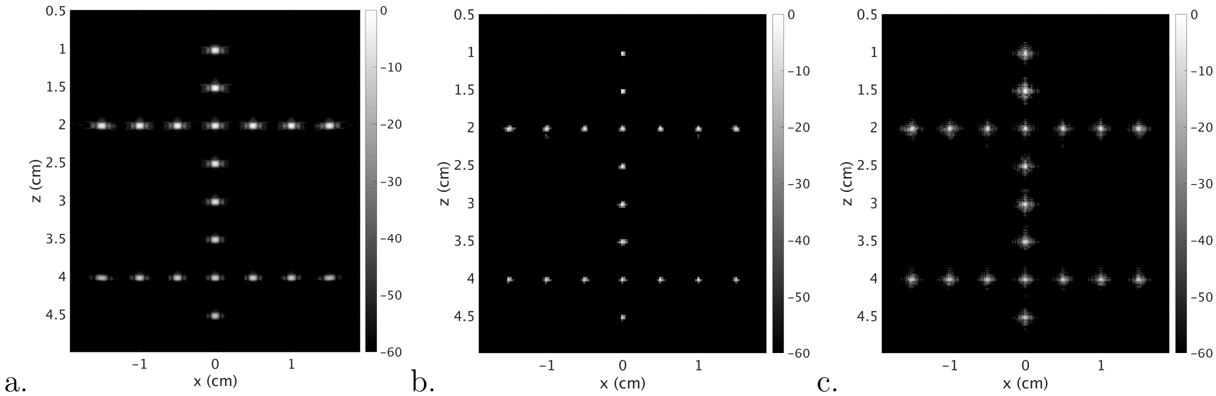

Figure 5.10: *Reconstruction of the simulated resolution phantom:* a. *Delay-and-Sum reconstruction using 75 plane waves,* b. *t-CBF reconstruction using a single plane wave, and* HAAR *wavelet at decomposition level 1,* c. *t-CBF reconstruction using a single plane wave, and Symmlet$_4$ wavelet at decomposition level 2.*

The image was reconstructed in about 8 minutes.

- Coiflet$_4$ wavelet at decomposition level 3: the reconstruction is shown in figure 5.11.c. The contrast is slightly degraded, but the edges are still sharp. The image was reconstructed in about 29 minutes. It is much slower than the HAAR reconstruction, but the image does not have the pixelated aspect of the HAAR image.

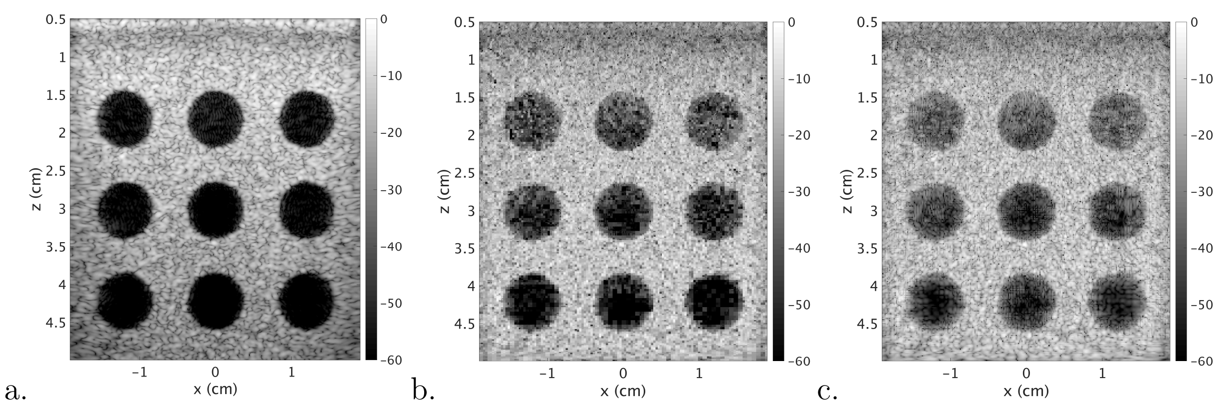

Figure 5.11: *Reconstruction of the simulated contrast phantom:* a. *Delay-and-Sum reconstruction using 75 plane waves,* b. *t-CBF reconstruction using a single plane wave, and* HAAR *wavelet at decomposition level 2,* c. *t-CBF reconstruction using a single plane wave, and Coiflet$_4$ wavelet at decomposition level 3.*

5.3.8 Point scatterers and hyperechoic lesion in speckle

Next, we move on to the first experimental phantom, whose Delay-and-Sum reconstruction is shown in figure 5.12.a. Once again, the t-CBF reconstruction is carried out two separate times, using different wavelets in the sparsifying transform:

- Haar wavelet at decomposition level 2: the reconstruction is shown in figure 5.12.b. Again, the image has a pixelated aspect. The resolution is degraded, and the speckle is not well rendered. The image was reconstructed in about 19 minutes.

- Symmlet$_4$ wavelet at decomposition level 2: the reconstruction is shown in figure 5.12.c. The comments about the resolution and speckle we made previously are also applicable to the Symmlet$_4$ reconstruction. The image was reconstructed in about 14 minutes. It is comparable to the Haar reconstruction, but the image does not have the pixelated aspect of the Haar image.

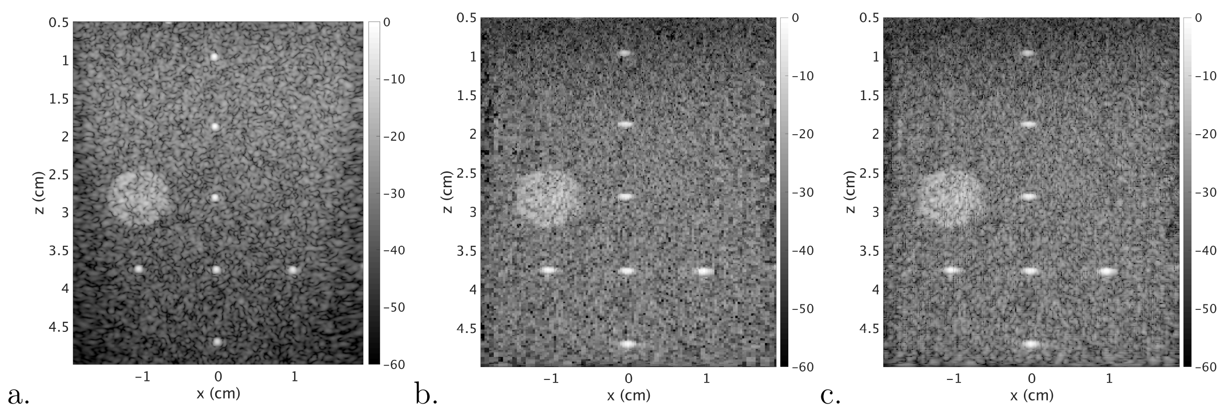

Figure 5.12: *Reconstruction of the experimental resolution phantom:* a. *Delay-and-Sum reconstruction using 75 plane waves,* b. *t-CBF reconstruction using a single plane wave, and* Haar *wavelet at decomposition level 2,* c. *t-CBF reconstruction using a single plane wave, and Symmlet$_4$ wavelet at decomposition level 2.*

5.3.9 Hypo and hyperechoic regions in speckle

Finally, we study the second experimental phantom, whose Delay-and-Sum reconstruction is shown in figure 5.13.a. Once again, the t-CBF reconstruction is carried out two separate times, using different wavelets in the sparsifying transform:

- Haar wavelet at decomposition level 2: the reconstruction is shown in figure 5.13.b. Again, the image has a pixelated aspect. The resolution is slightly degraded, and the speckle is not well rendered. The image was reconstructed in about 11 minutes.

- Coiflet$_4$ wavelet at decomposition level 2: the reconstruction is shown in figure 5.13.c. The comments about the resolution and speckle we made previously are also applicable to the Coiflet$_4$ reconstruction. The image was reconstructed in about 39 minutes. It is considerably more than the Haar reconstruction.

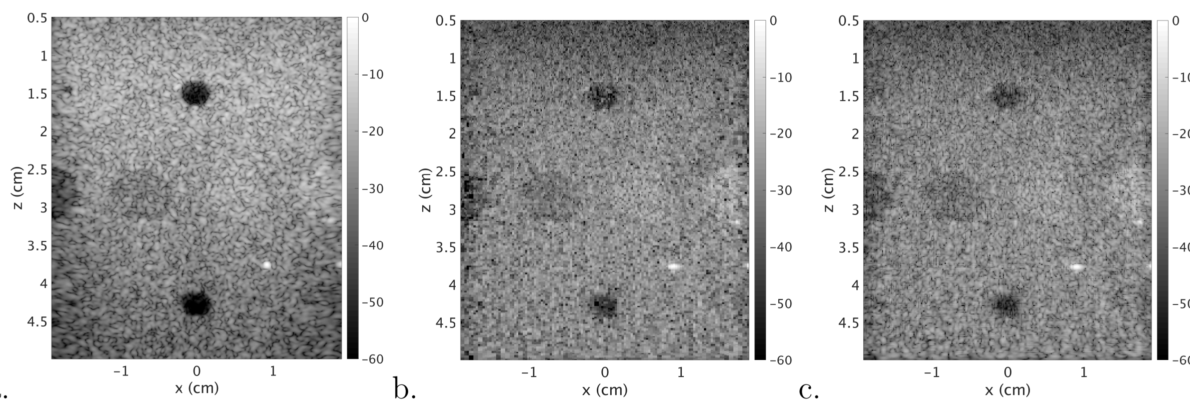

a. b. c.

Figure 5.13: *Reconstruction of the simulated resolution phantom:* a. *Delay-and-Sum reconstruction using 75 plane waves,* b. *t-CBF reconstruction using a single plane wave, and* Haar *wavelet at decomposition level 2,* c. *t-CBF reconstruction using a single plane wave, and Coiflet$_4$ wavelet at decomposition level 2.*

5.3.10 Wrap-up

The conclusion we can draw from this study is that the choice of a particular wavelet against another is far from being trivial. While some wavelets have better compression capabilities than others, the performance of the t-CBF reconstruction does not always correlate. Some of those can be explained. While computing the previous images using t-CBF, all the parameters except for the wavelet used in the sparsifying transform were kept constant. This means that the number of coefficients recovered in the case of the Haar wavelet and in the case of the wavelet leading to the best compression score is roughly the same. However, since the latter wavelet sparsifies the image further, it is easier for the algorithm to pick up more information, and sometimes artifacts. In a way, using a more powerful sparsifying transform while all the other parameters remain constant relaxes the sparsity condition in favor of the fidelity or l_2-error term in equation 5.13. Unfortunately, our model being imperfect in essence, the l_2-constraint brings out more artifacts and we are faced with a tradeoff between the sparsity and the fidelity to our data.

It is found best to choose a wavelet that has the most compact support, and then to work the other parameters around it to get the best image possible without sacrificing the quality. In practice, the wavelet that produces good resolution and visually acceptable results is the Coiflet$_1$ at decomposition level 1. The support of the Coiflet$_1$ wavelet is the most compact of the Coiflets, which ensures the preservation of the resolution. The decomposition at level 1 limits the number of computational operations to apply to the image, making the computation optimally fast.

5.3.11 Decimated or undecimated wavelets?

As seen in chapter 2, the wavelet transform classically includes a decimation by a factor 2. It is the so-called critically sampled wavelet transform. It is the most suitable for image compression in part because the maximum number of coefficients in the transform is bounded by the number of pixels in the image.

However, there exists a version of the wavelet transform that does not decimate the result of the low-pass and the high-pass filters. This transform is commonly referred to as the stationary wavelet transform, or the non-decimated wavelet transform. The stationary wavelet transform brings redundancy to the transform, and its maximum number of coefficients is a function of the level of decomposition. The higher the level, the more coefficients there are in the transform. For that reason, the stationary wavelet transform is not well suited for image compression. However, the added redundancy it brings is beneficial for t-CBF reconstructions in certain cases when it comes to the aspect of the image.

To give a rough example of the improvement in image quality one can expect from the stationary wavelet transform, we applied t-CBF to a numerical phantom displaying lesions, cysts, and speckle. We selected Haar wavelets, decomposed at level 1, and ran t-CBF with the classic decimated wavelet transform first and then the non-decimated wavelet transform. The results are presented in figure 5.14.

As we can see on figure 5.14.b, a Haar wavelet reconstruction leads to an image with a pixelated aspect. This pattern is attenuated when reconstructing the image with the stationary wavelet transform, all other transform parameters kept constant. It is also clear that the resolution of image 5.14.c is better than image 5.14.b, as the point scatterer in the center are far less spread out in the azimuth dimension. The general aspect of the speckle is also closer to the one we would obtain with the Delay-and-Sum algorithm.

However, the stationary wavelet has a major drawback: it makes t-CBF even more computationally intensive since the transform in itself has more operations, and also because there are many more coefficients to recover to get a comparable level of details. Moving forward, it is preferable to simply use a wavelet that does not produce the pixelated artifact, such as the Coiflet_1 at decomposition level 1.

Decimation speeds up minimization. The decimated wavelet transform leads to less potential coefficients to recover, making the minimization easier. Undecimation introduces redundancy as well as smoothness which is a desirable property in our case. A quick comparison of figure 5.14.b and 5.14.c leads to the following observations:

- First, the contrast in the cysts and the lesions is better with undecimated wavelets. The lesions and cysts are well-separated from regular tissue.

- Then, the resolution of the point scatterers is better when using undecimated wavelets. The image reconstructed using decimated wavelets shows a great reduction of the resolution as we go deeper into the tissue. It even seems to be better than the DAS image in figure 5.14.a.

- Finally, figure 5.14.b displays harsh intensity transitions while figure 5.14.c is much smoother.

Those results corroborate with similar experiments we conducted on different types of phantoms. It suggests that using undecimated wavelets is beneficial to t-CBF. However, the computational cost is so high that at the moment it is more efficient to use the critically sampled wavelet transform.

5.4 Reconstructed field-of-view

Ultrasound images are generally subject to clutter noise. The acoustic clutter comes from objects and structures that are off-axis, or outside of the field-of-view. The beamformer does not generally take into account to possibility that off-axis scatterers or outside of the field-of-view scatterers can get insonify during a transmit event. This is due to the very nature of how the transmit wave is generated. Looking at figure 5.15.a we can understand this phenomenon better. Even though we are firing all the elements at the same time to create a plane wave propagating directly *en-face* the probe, the profile of the wave actually generated is quite different. It corresponds to the coherent sum of multiple spherical waves generated at the surface of the probe by each individual element. The spherical waves interfere constructively wherever they are in phase. As a result, the amplitudes add up to form what looks like a plane wave, when we restrict the observation to the field-of-view, represented by a blue rectangle in figure 5.15. However outside of that window the constructive interference stops, and a wave corresponding roughly to the wavefront generated by the extremal elements can be observed. Even though the amplitude is less significant on the sides, they still get

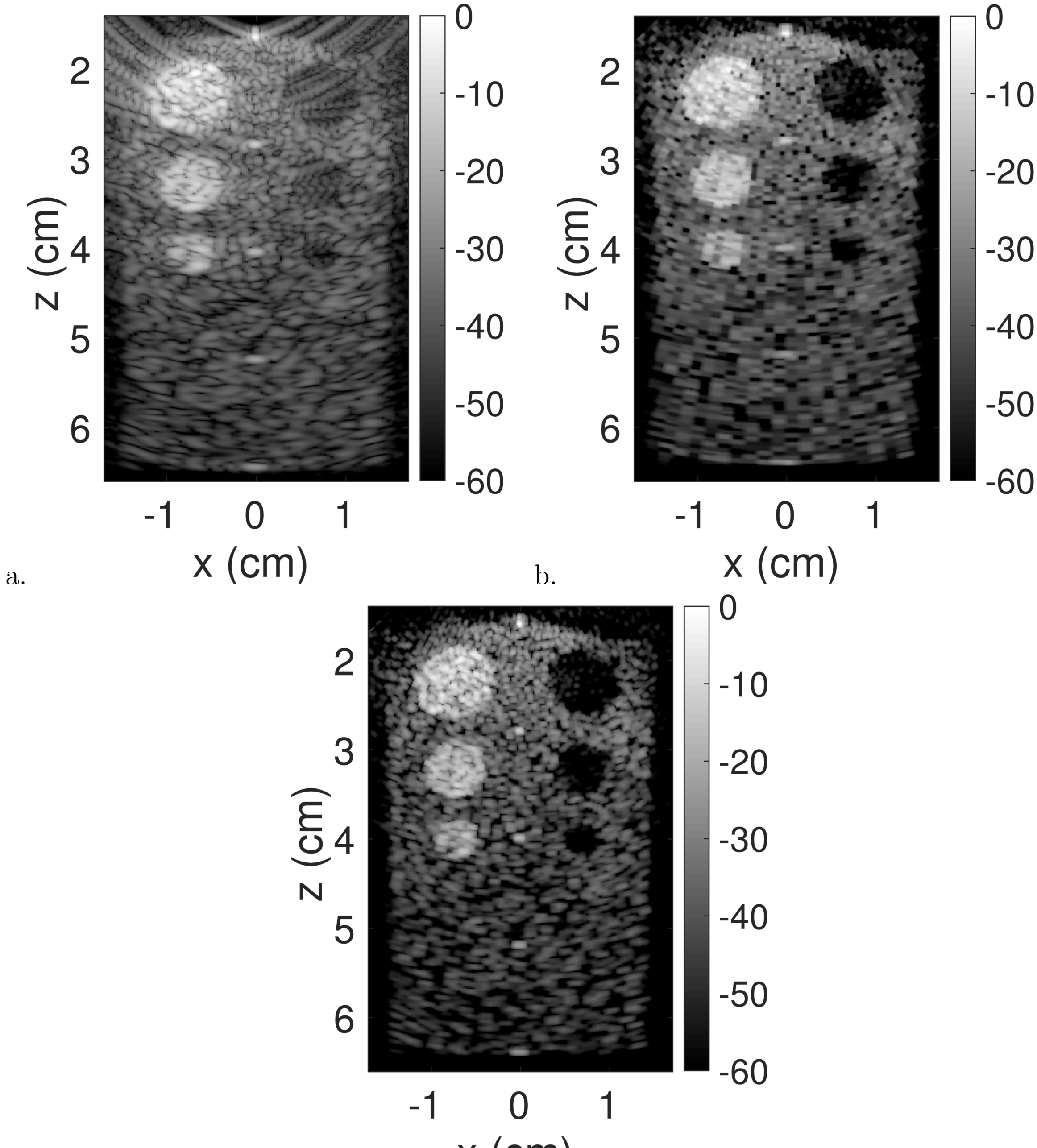

Figure 5.14: *Numerical phantom with lesions, cysts, point scatterers in speckle:* a. *classic Delay-and-Sum reconstruction using a single diverging wave,* b. *t-CBF reconstruction using a single diverging wave, a* HAAR *wavelet at decomposition level 1 and the critically sampled wavelet transform, and* c. *t-CBF reconstruction using a single diverging wave, a* HAAR *wavelet at decomposition level 1 and the stationary wavelet transform.*

insonified.

Figure 5.15.b shows the reflections created by the scatterers in the medium. The two scatterers located in the green area (field-of-view) will produce reflections that will be taken into account by the beamformer. However the scatterer in the red area (outside of the field-of-view), will also produce a wavefront. Since this last wave front will not be taken into account by the beamformer, it will simply add to the noise in the image. This phenomenon is more significant with phased array. The elements in a phased array are usually small enough (about $\lambda/2$) that they are not directive and fire energy in all directions forward as shown in figure 5.16.b. In linear arrays, the phenomenon is still a problem, even though the bigger elements (about λ) are far less directive and fire energy primarily in a $\pi/2$ sector as shown in figure 5.16.a. This difference in directivity can be explained by the size of the elements. In the case of a phased array, the element width is close to $\lambda/2$, making the element physically equivalent to a point scatterer. For a linear array, the element width is usually around λ.

In order to take into account the reflections coming from outside the field-of-view of the image displayed to the user, we increase the width of the field-of-view beyond the width of the probe. This way t-CBF can discriminate the signals that come from *en-face* the probe from the signals that come from the sides.

To illustrate this phenomenon, we reconstruct a cardiac image with different field-of-view sizes. The data is acquired with a single diverging wave, and the parameters of the probe are given in 6.2. The results are shown in figures 5.17 and 5.18. Figure 5.17.a is the reference image. It is reconstructed using the display field-of-view, that is to say a $\pi/4$ sector. In that case, the problem at the boundaries of the field-of-view is ignored. The corresponding reconstruction shows a lot of clutter in the atria resulting in a loss of contrast. The following three images shown in figure 5.17.b, c, and d are reconstructed with progressively wider fields-of-view. We notice a sharp decrease in the amount of clutter in the atria, as well as in the ventricles.

The image can be decluttered further by adopting an even wider field-of-view, as shown

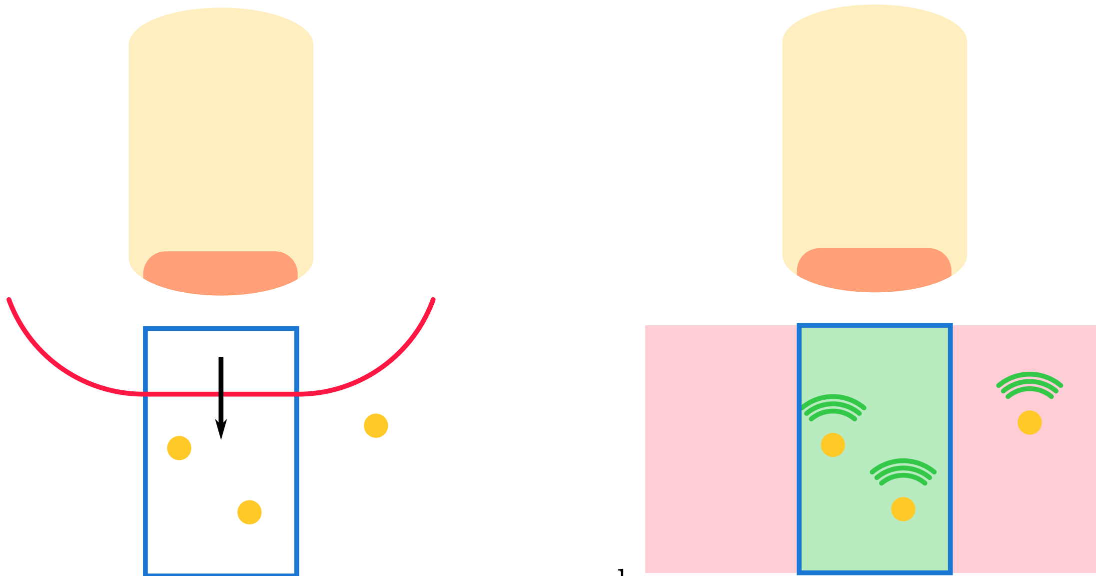

a. b.

Figure 5.15: *Influence of the scatterers outside of the reconstruction field-of-view: a. The transmit wave is not a perfect plane wave, therefore scatterers outside of the reconstruction field-of-view are insonified, b. They produce echoes that travel back to the probe, and create noise in the reconstruction.*

in figure 5.18.a, b, c, and d. Of course, making the reconstruction field-of-view wider comes at the cost of added computations. However, it is a trade-off with the convergence time. A wider field-of-view can help t-CBF making sense of some of the wavefronts that produce the clutter in figure 5.17.a. By doing so, the reconstruction error is decreased, making the convergence faster. When the field-of-view becomes too wide, this advantage is lost because the computational cost becomes too significant. From the present data set, a reconstruction field-of-view 40% larger than the display field-of-view seems to be optimal. It leads to both a decluttered image and a decrease in the total computation time. Above this value, the image quality does not change significantly, but the computation time increases. Below this value, the image shows clutter.

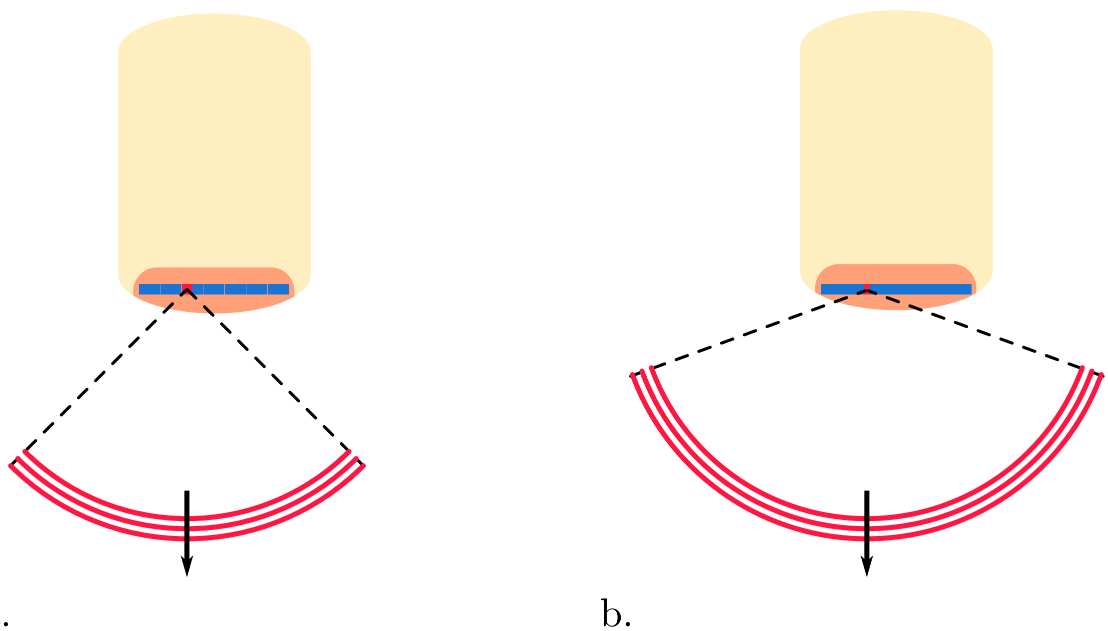

Figure 5.16: *Transducer directivity: a. Elements with a π/2 directivity, typical of a linear probe, b. Almost isotropic, smaller elements that are far less directional, typical of a phased array.*

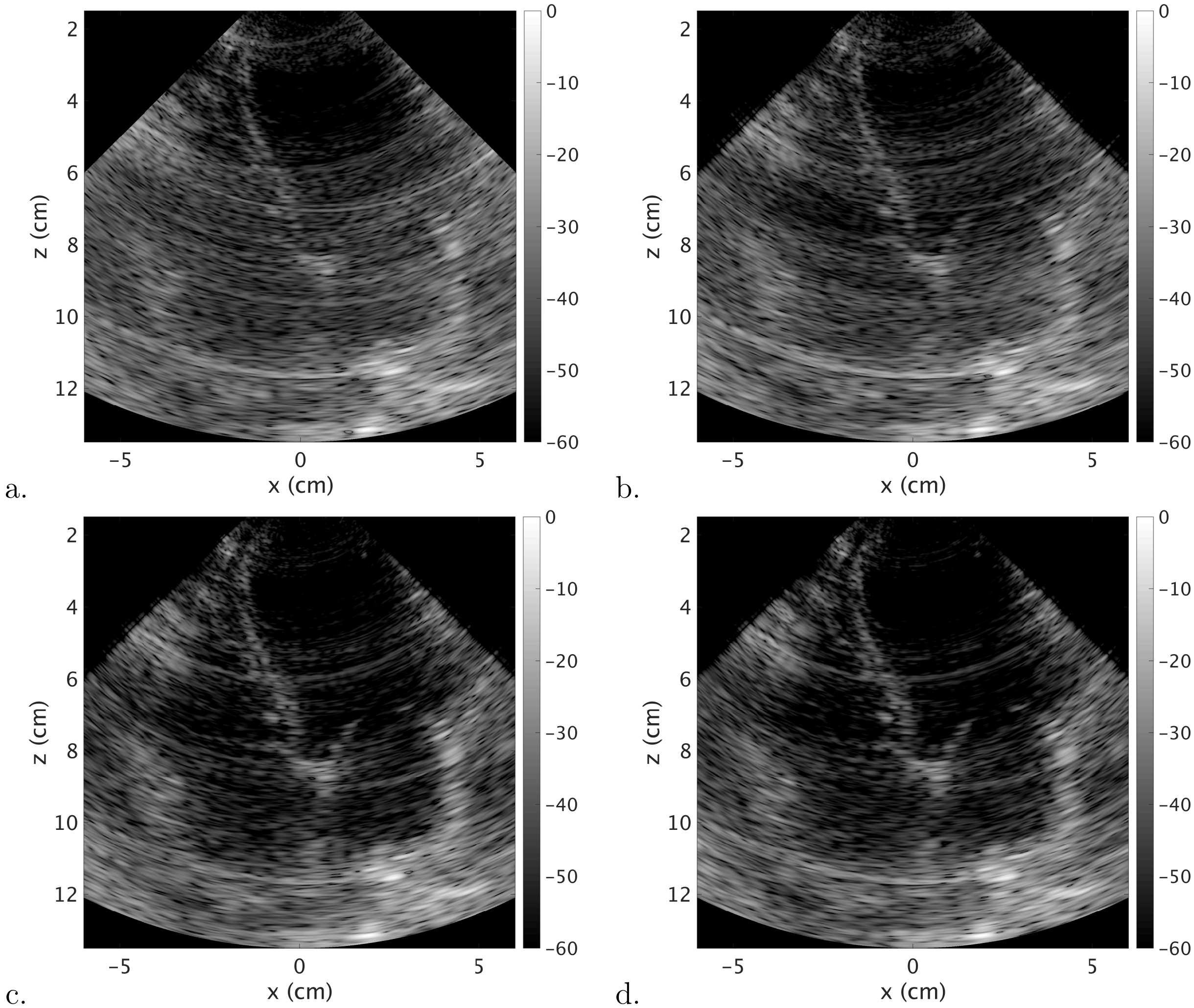

Figure 5.17: *Influence of the reconstruction field-of-view (FOV): a. the reconstruction field-of-view FOV_{recon} is equal to the displayed field-if-view $FOV_{disp} = \pi/4$ and the computation time t_{recon} is 3.2 minutes, b. FOV_{recon} is 10% wider than FOV_{disp} and $t_{recon} = 3.8$ min, c. FOV_{recon} is 20% wider than FOV_{disp} and $t_{recon} = 3.9$ min, d. FOV_{recon} is 30% wider than FOV_{disp} and $t_{recon} = 3.7$ min.*

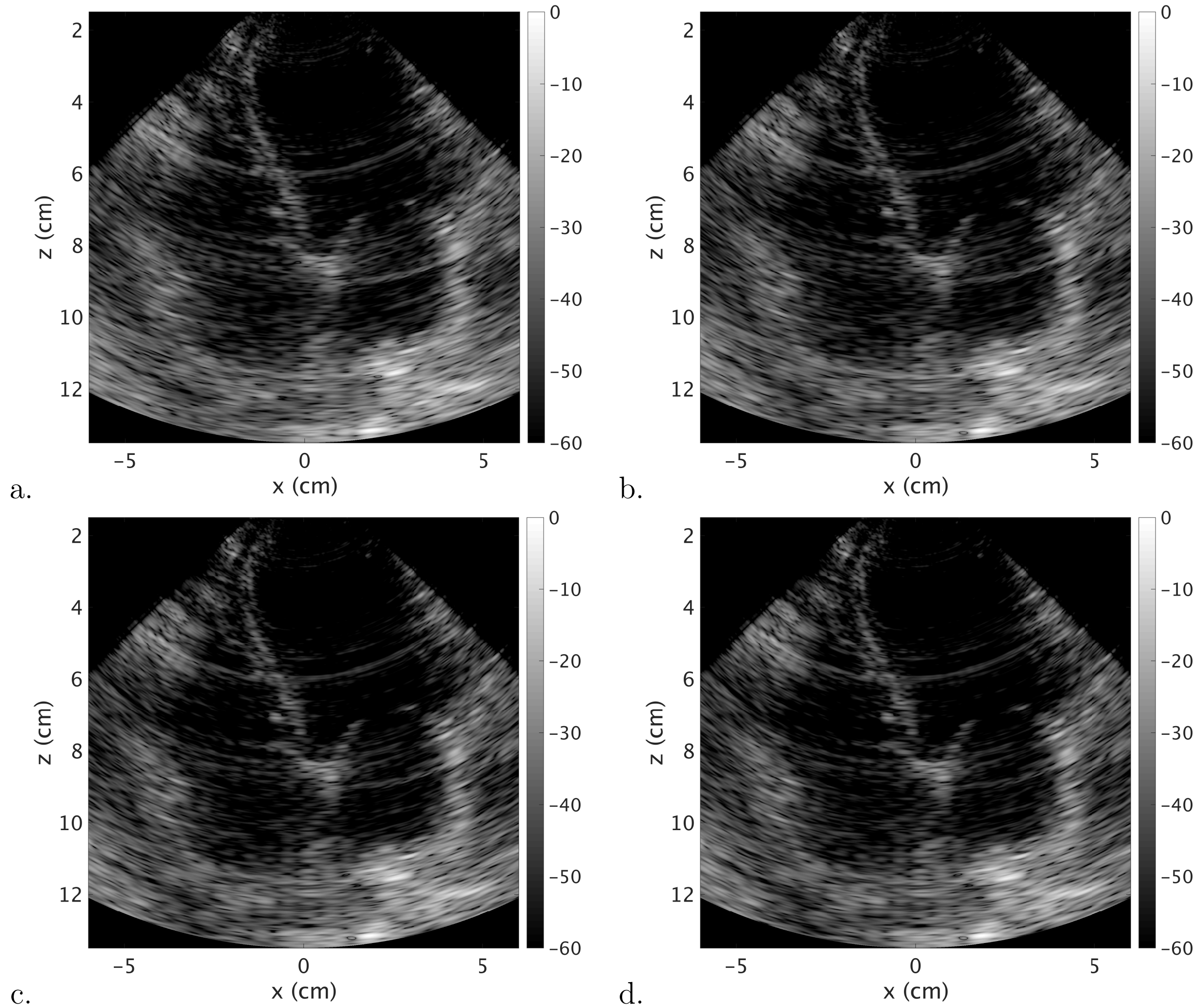

Figure 5.18: *Influence of the reconstruction field-of-view (FOV): a. FOV_{recon} is 40% wider than FOV_{disp} and $t_{recon} = 3.2$ min, b. FOV_{recon} is 50% wider than FOV_{disp} and $t_{recon} = 3.6$ min, c. FOV_{recon} is 75% wider than FOV_{disp} and $t_{recon} = 6.1$ min, d. FOV_{recon} is 100% wider than FOV_{disp} and $t_{recon} = 4.8$ min.*

5.5 Parallelization

Parallelization can speed up the reconstruction. The increase in speed is due to two factors:

- The problem is divided into n_{cores} smaller sub-problems, where n_{cores} is the number of CPU cores we use. Each core reconstructs a portion, or slice of the image.
- The slicing itself allows for a reduction of the amount of RAM used, and the total amount of RAM used by the parallelized problem is less than the amount of RAM used by the complete problem.

In order to parallelize the problem, we need to choose a sub-division of the image we want to reconstruct. Suppose we choose to slice the image in the x-dimension. In that case, the boundaries in the azimuth direction are computed and the data is sliced accordingly. Let us consider a medium with two point scatterers at the same depth. We want to divide the problem into two sub-problems. Thus we compute the boundary between the two sub-problems. Let us assume that one scatterer belongs to sub-problem 1 (SB_1), and the second scatterer belongs to sub-problem 2 (SB_2). Each sub-problem should then easily reconstruct the correct scatterers. However when we consider the slicing of the data, we are faced with a difficulty: there is no way to slice the data that will separate completely the wavefront of the scatterer in SB_1 from the wavefront of the scatterer in SB_2. This phenomenon is shown in figure 5.19. Figure 5.19.c in particular shows that we end up with two sub-images with one scatterer each, but the sub-divided data shows two wavefronts for each sub-problem. Thus this sub-division leads to a greater reconstruction error, since the matrix G does not have the wavefronts necessary to model that data in its dictionary.

As a result, we slice the image in the z-dimension. In that case, the boundaries of the data can be computed by referring to the time-of-flights of the shallowest and the deepest points in each sub-image. This case is illustrated by figure 5.20. In that case, we see that each sub-image contains one scatterer, and each sub-division of the data contains one wavefront.

The maximum number of sub-division is dictated by common sense: if a sub-domain is so small that it cannot contain a complete wavefront, then its size must be increased. In general, we obtain good results with sub-domains spanning about 1 cm of depth.

Figure 5.20.c shows another advantage of this technique. For each sub-image, the corresponding boundaries in the acquisition domain are calculated in order to sub-divide the data. Let us assume that the original data has $3,200$ time samples, and that the reconstruction is carried out using 4 CPUs. If the data is sub-divided into 4 sets of equal size, we end up with a set having 800×64 samples in total. If the total size of the image is 160×128 samples, we are reconstructing 4 sub-images of size 40×128 samples. The implication in terms of memory usage is that each sub-matrix G is going to have $800 \times 64 \times 40 \times 128 = 262,144,000$ samples. The total for the 4 sub-problems is then $1,048,576,000$ samples. However, if we compute the image with the regular t-CBF, the size of the matrix G is $800 \times 64 \times 160 \times 128 = 4,194,304,000$ samples which is 4 times more. Therefore we come to the conclusion that the more CPUs we use the less RAM we need. The time needed to compute an image decreases significantly with this technique, going from several hours to a few minutes. Since the memory requirements are more manageable with parallelized t-CBF, we can also compute bigger images.

5.6 Robustness to noise

Compressive Sensing is generally robust to noise as we saw in section 3.3.8. However, is t-CBF robust to noisy data? In this section, we applied t-CBF to simulated phantom data with different noise levels.

The noise level is expressed in decibels with the reference set at the maximum absolute value of the noiseless signal. We compute the reconstructions for noise levels from -60 dB to 0 dB. At -60 dB, the noise is essentially inconsequential, since it is below the minimum amplitude that we show. At 0 dB the level of noise is higher than most of the signal. As a result, we expect to reconstruct a noisy image lacking all the features of the phantom in

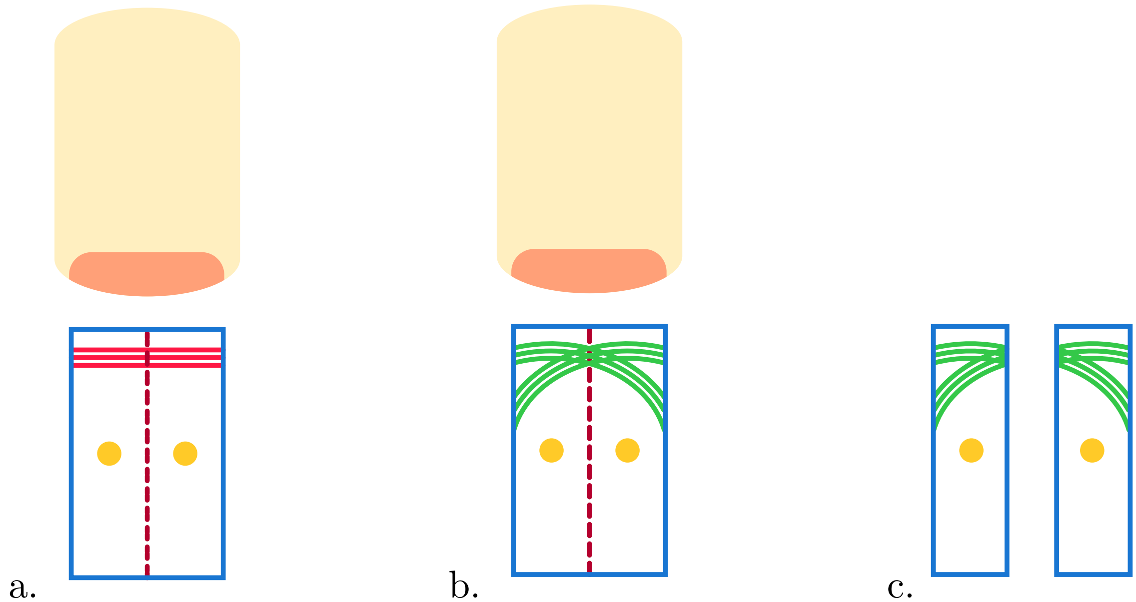

Figure 5.19: *Sub-division of the problem in the x-axis: a. insonification of the medium, b. echoes generated by the scatterers, c. sub-division of the data. Figure c. clearly shows the problem: the sub-images have only one scatterer each, but the sub-divided data shows two wavefronts in both cases.*

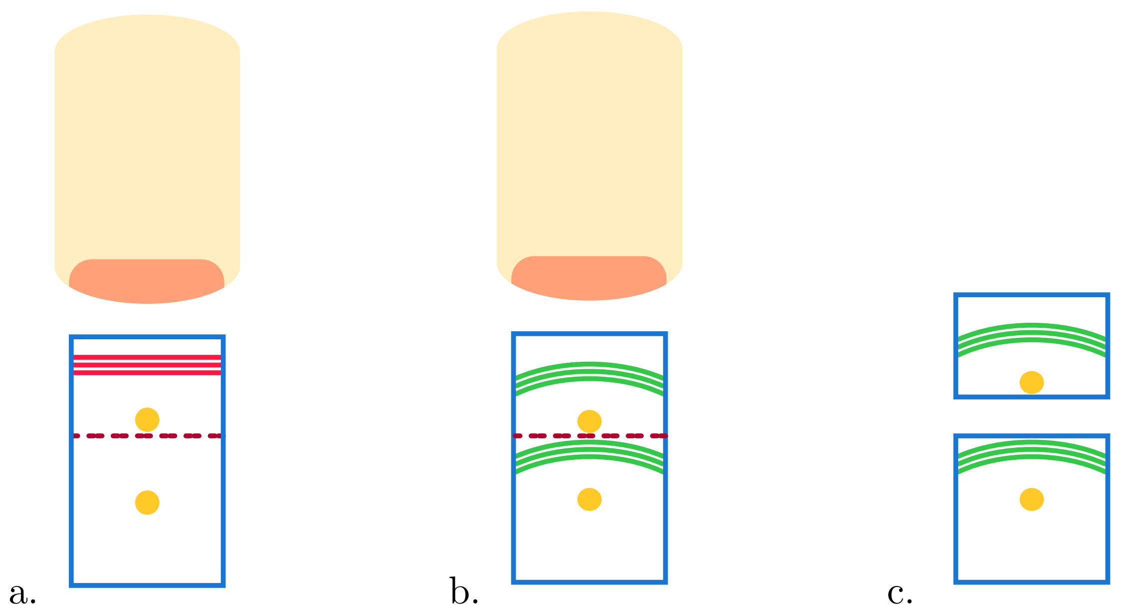

Figure 5.20: *Sub-division of the problem in the z-axis: a. insonification of the medium, b. echoes generated by the scatterers, c. sub-division of the data. Figure c. clearly shows the advantage of such sub-division: each sub-image has one scatterer, and the sub-divided data contains one wavefront in both cases.*

that case.

The noise U is chosen uniformly at random in the interval $[0, 1]$, and scaled later on. The noisy data is obtained by adding U to the noiseless data:

$$R_{\text{noisy}} = R + U \tag{5.17}$$

In figure 5.21.a-c we see that the noise level in the data has little impact on the reconstruction. However starting at 30 dB of noise (figure 5.21.d-f), strong artifacts appear on the reconstruction. The contrast in the cysts decreases drastically, and the deepest scatterer in the center disappears. The resolution does not seem to be affected by the noise.

The same experiment is carried out a second time using wavelet packets. The packet tree is chosen from the first approximation of the image $G^{\top}R$ obtained from the noiseless data. We want to see if the wavelet packet tree that best represents the image will help denoising the reconstruction. The results are shown in figure 5.22.

Figures 5.21 and 5.22 show that the added computational cost of using wavelet packet does not translate to significant improvement of the robustness of t-CBF to noise.

5.7 Conclusion

In this chapter, we showed that t-CBF could be adapted to tissue imaging.

In order to accommodate actual data from a scanner and reconstruct actual ultrasound images, we showed that using the Hilbert transform as a way to decrease the size of G was an acceptable strategy. Further, parallelization made t-CBF even more attractive by accelerating the convergence of the algorithm as well as making it less RAM greedy.

To be able to reconstruct images with thousands of scatterers and displaying a speckle pattern, we showed that using the wavelet transform as a sparsifier was visibly beneficial. Among the many wavelet families and algorithms, we saw that in most cases simpler was better. The critically sampled wavelet transform in conjunction with Coiflet_1 at decomposition

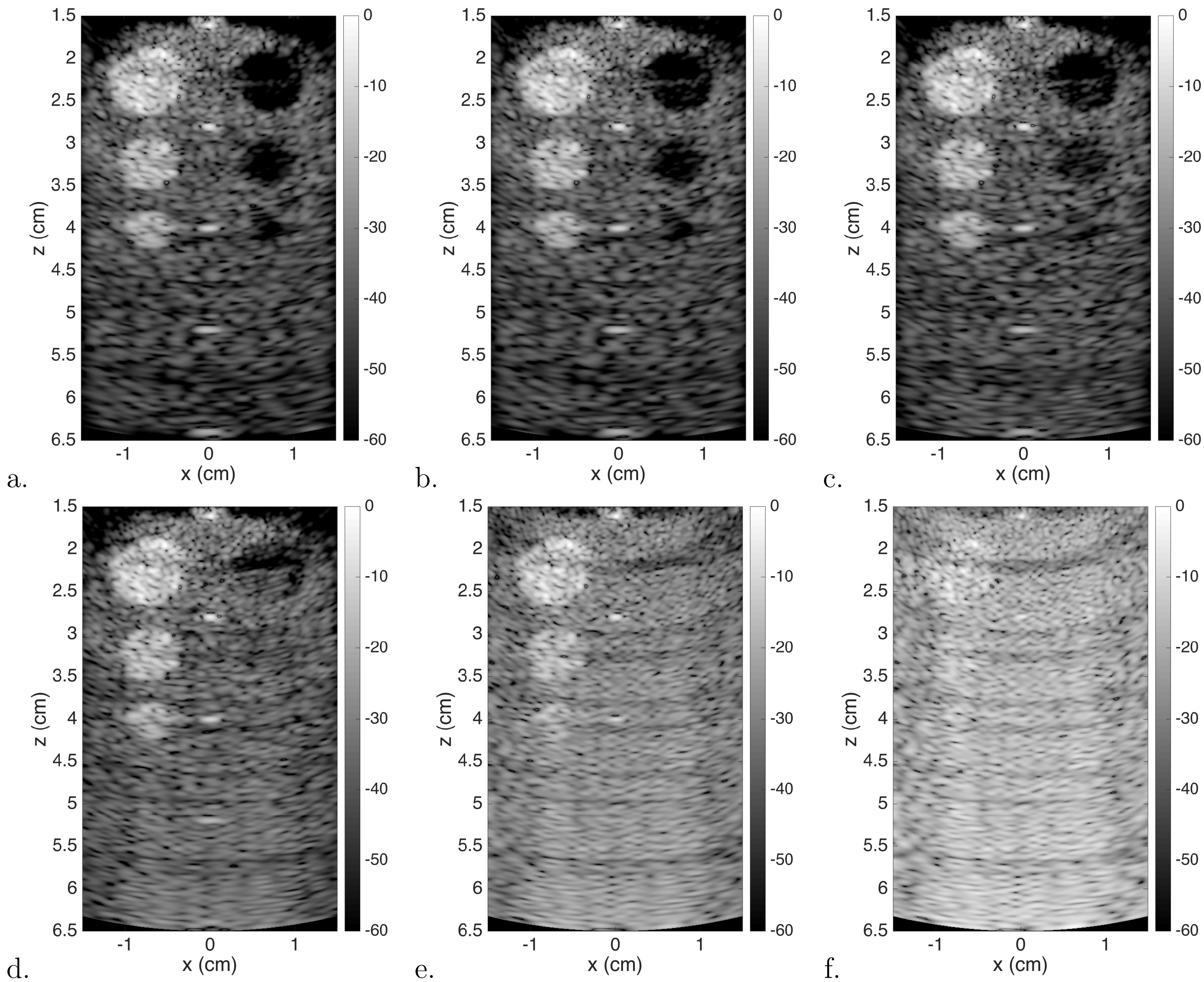

Figure 5.21: *Robustness of t-CBF to noise: a. 60 dB SNR, b. 50 dB SNR, c. 40 dB SNR, d. 30 dB SNR, e. 20 dB SNR, and f. 10 dB SNR.*

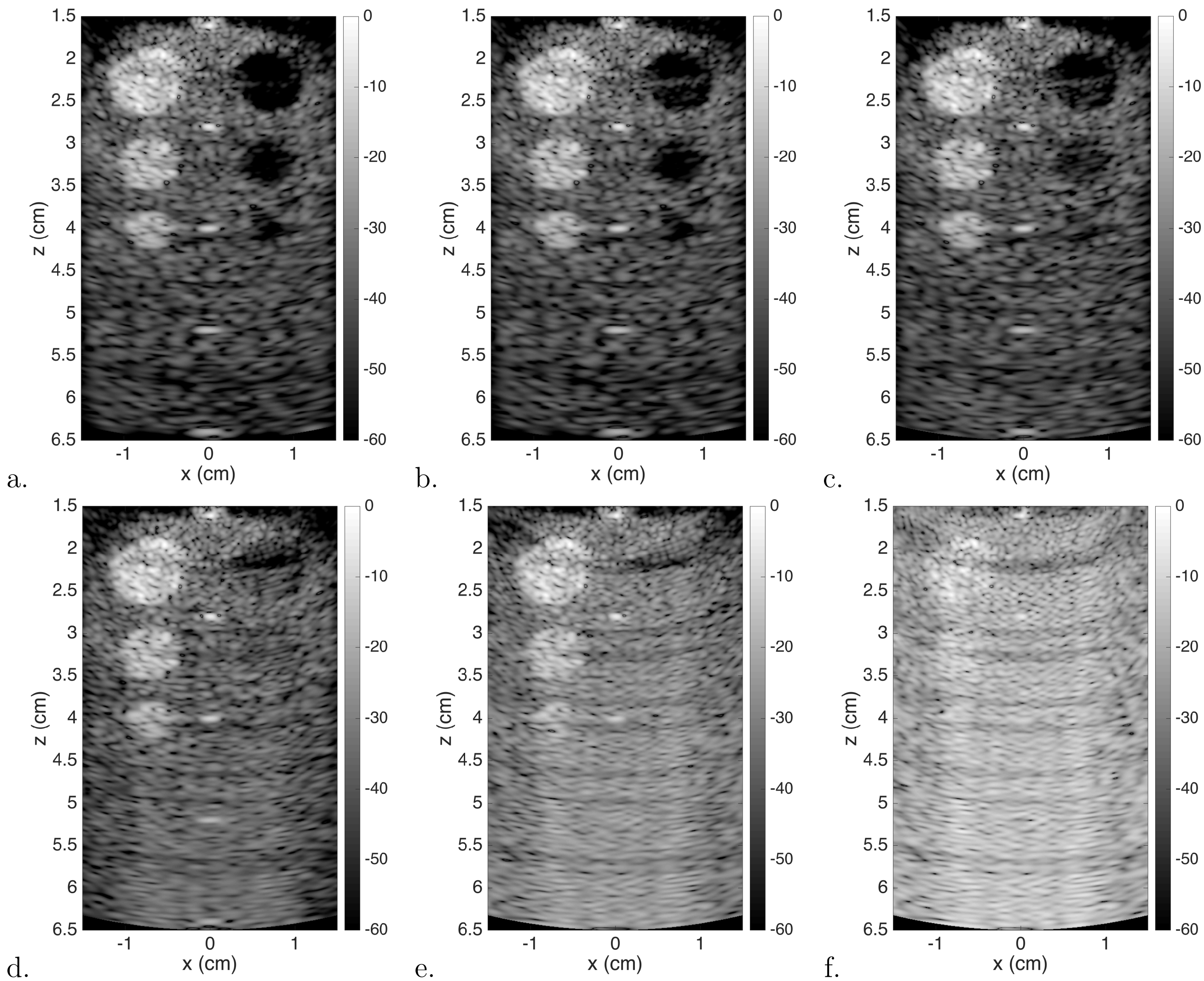

Figure 5.22: *Robustness of t-CBF to noise using wavelet packets: a. 60 dB SNR, b. 50 dB SNR, c. 40 dB SNR, d. 30 dB SNR, e. 20 dB SNR, and f. 10 dB SNR.*

level 1 led to good results in most cases.

Then, we emphasized on the necessity to reconstruct a wider field-of-view than the one displayed to the user. In fact, doing so redued the clutter in the final image. This phenomenon was due to the fact that with a wider field-of-view, t-CBF could understand some of the wavefronts coming from outside the theoretical insonification area. Scatterers outside of this area were insonified because of the lack of directivity of the elements.

We also showed that t-CBF was robust to a certain level of noise, and could produce acceptable results with SNR above 30 dB.

The next chapter is simply an application of all the refinements that were developed to *in-vivo* echocardiography.

Chapter 6

Application to *in-vivo* echocardiography

6.1 Introduction

Some applications of ultrasound imaging require a high frame rate to capture the movement of organs with precision. Such an application is echocardiography, where a physician captures images of a beating heart with an ultrasonic scanner in order to detect a pathology related to its movement, or the movement of its valves. Because such movements are quick, a high frame rate is required to capture them [136].

6.2 Approaching *in-vivo* cardiac imaging

The previous improvements allow us to work on real images. The use of the Hilbert transform in the pre-processing of the data as well as in the building of the matrix G ensures the amount of RAM and computations remain manageable. This step is needed to reduce the number of time samples in the data without aliasing. Indeed, imaging at a 14 cm depth at 32 MHz means that we acquire 5818 samples in depth. However, the analytic signal can be sampled at 3.24 MHz, requiring only 589 time samples.

This mathematical trick allows the use of t-CBF with data acquired with a commercial US scanner. First, we used a hardware modified iU22 from Philips (Best, Netherlands) that

Parameter	f_c	bw	λ	N_{elements}	p	c_{sound}	f_s
Value	2.7 MHz	0.6	570 μm	80	$\lambda/2$	1540 m.s^{-1}	32 MHz

Table 6.1: *Parameters used to build G for our first cardiac dataset.*

allows us to collect raw data, before any kind of processing is applied to the signal. We used the S5-1 probe for those experiments (table 6.1).

Because the pulse sequence we use is not standard, the scanner's software was also modified to emit diverging waves. The modification has not been approved for use on human subjects. For that reason, we used a mathematical trick to produce the data we used for reconstruction. Starting from a cardiac dataset we acquired using a classic pulse sequence made of several focalized transmit waves, we applied the virtual transducers principle [137] to calculate the synthetic aperture data [138]. From there, it was straightforward to calculate the response to a diverging wave.

The t-CBF image showed in figure 6.1c. is much cleaner than the DAS images. It allows us to locate structures that are not easily discernible on the DAS images, such as the left ventricular wall. The other structures are preserved and clear.

Those results are very encouraging and the next step is to now perform the acquisition with a diverging transmit wave directly.

6.3 High frame rate *in-vivo* cardiac imaging

Next, we used data acquired with a Verasonics scanner and a P4-2 probe whose parameters are summarized in table 6.2. That data set we used was critically sampled, meaning that the sampling frequency was strictly equal to the double of the central frequency of the probe. Moreover, the data was acquired using a diverging wave as a transmit wave. A succession of 4,000 consecutive frames was acquired at a 4.9 kHz frame rate. A sample image is shown in figure 6.2.b along with the Delay-and-Sum reconstruction (figure 6.2.a). The Delay-and-Sum image is cluttered and has a low contrast. The t-CBF image is much cleaner, with better

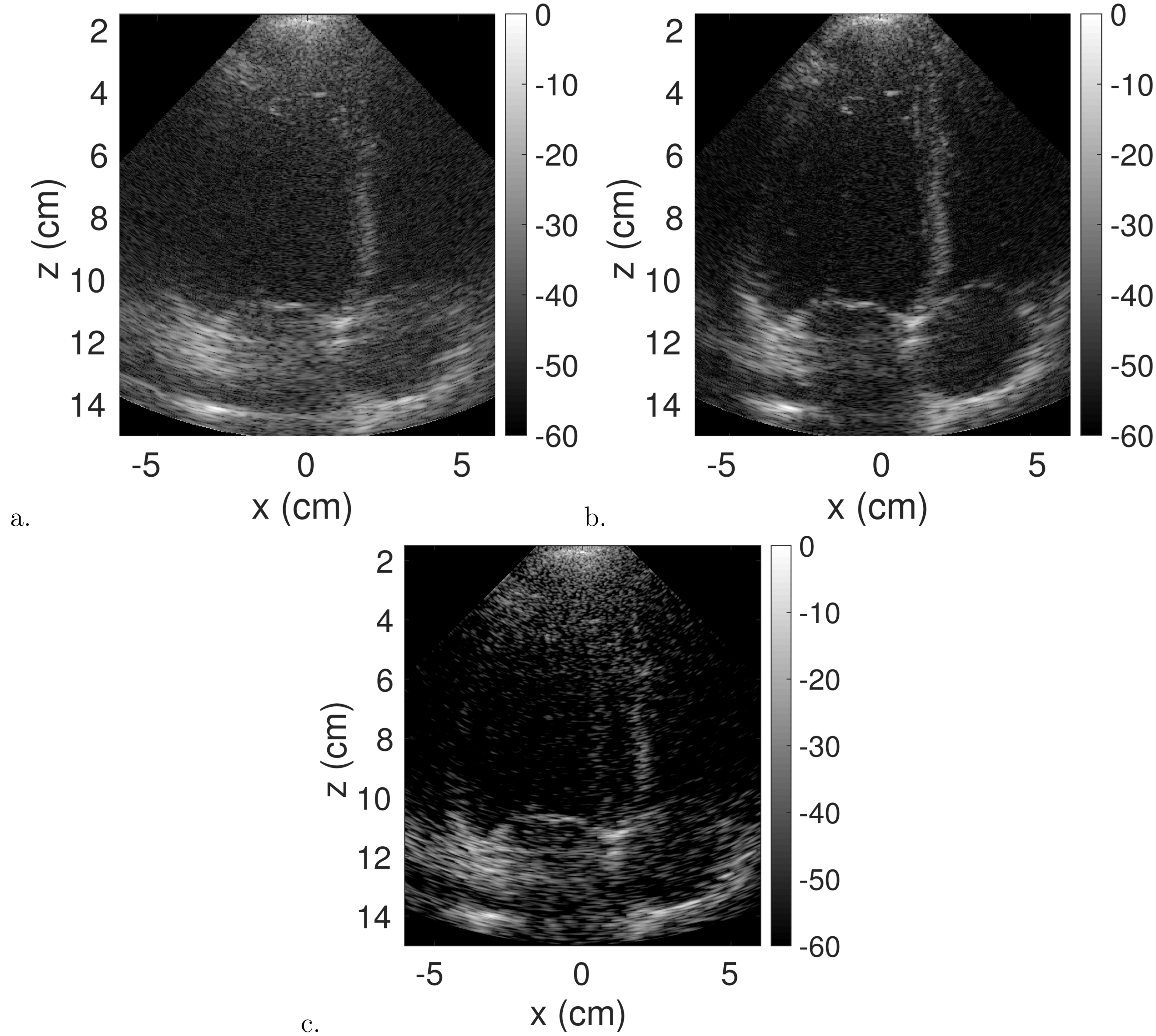

Figure 6.1: a. *DAS image with 1 diverging transmit wave,* b. *DAS with 11 diverging transmit waves, and* c. *t-CBF image with 1 diverging transmit wave.*

contrast in the atria and ventricles. The cardiac walls and the valves are much easier to locate in the t-CBF image.

Overall t-CBF was able to reconstruct an image with better resolution, better contrast, and less clutter than Delay-and-Sum, from the exact same data.

Parameter	f_c	bw	λ	N_{elements}	p	c_{sound}	f_s
Value	2.5 MHz	0.6	616 μm	64	$\lambda/2$	1540 m.s^{-1}	10 MHz

Table 6.2: *Parameters used to build G for the second cardiac dataset.*

6.4 Conclusion

We demonstrated that t-CBF could be used on a cardiac dataset. First, we proposed a way to sparsify the image, making the recovery of speckle patterns by t-CBF more robust. We studied a few wavelet families and selected the most relevant. Then, we investigated the advantages and drawbacks of using a decimated or undecimated wavelet transform. Finally we used the Hilbert transform on our dataset as well as to calculate the matrix G in order to decrease its size and make t-CBF applicable to real life images.

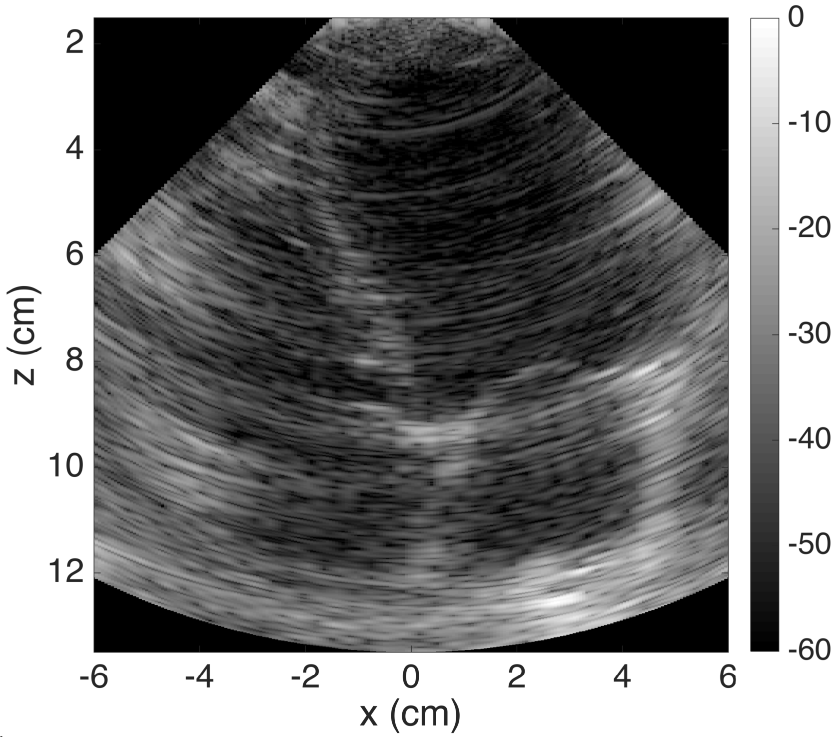

a.

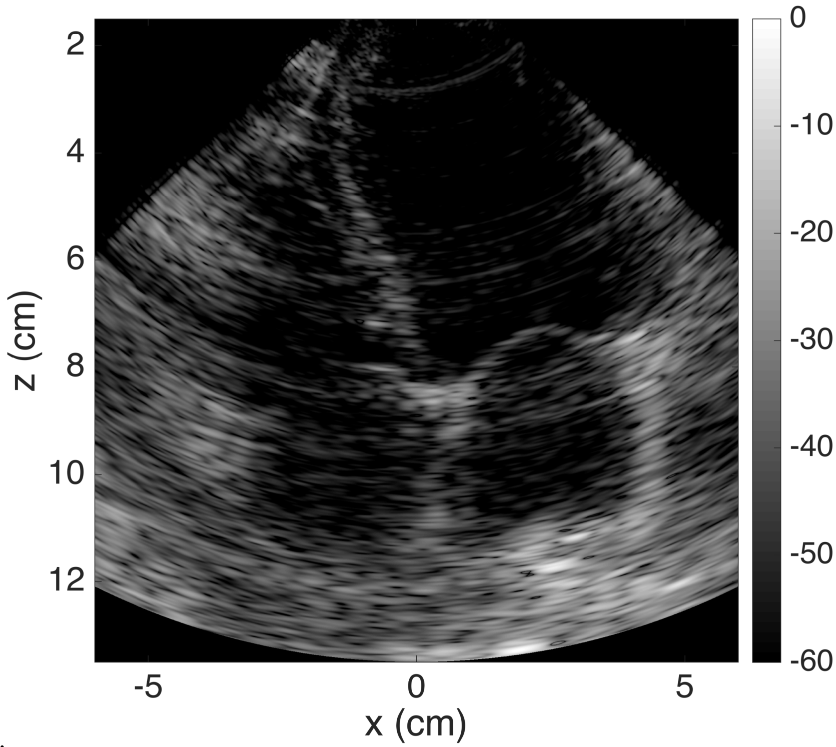

b.

Figure 6.2: in-vivo *cardiac data acquired with a single diverging wave: a. Delay-and-Sum reconstruction, b. t-CBF reconstruction. The t-CBF reconstruction took* 1.4 *minutes. The t-CBF image is much cleaner, with far less clutter in the atria and ventricles, making the cardiac walls and valves easier to see.*

Chapter 7

Concluding remarks

7.1 Introduction

With t-CBF, we built a feature-rich modern beamformer. t-CBF relies on physical models and computational power and can be adapted to scenarios going from plane wave imaging to focalized imaging, coded excitation imaging, or potentially harmonic imaging.

7.2 Focalized t-CBF

7.2.1 Introduction

Time-domain Compressive Beamforming was designed originally for plane wave imaging. It was introduced as a solution to the problem of high quality, high frame rate imaging. Using only one plane wave, t-CBF can achieve resolutions comparable to focalized Delay-and-Sum. It was later adapted to diverging wave imaging, in an effort to generalize it and use it in the context of echocardiography. Once again, diverging wave t-CBF was design with high frame rates in mind, hence it used only one transmit wave.

However, t-CBF can be used in other contexts. Since we have full control over the model that we use to build the matrix G, we can adapt it to focalized transmit waves. Of course, the frame rate in that case would be equivalent to what can be obtained classically with the Delay-and-Sum. However, we can hope to improve the image quality. This assumption comes from the observation that the PSF of the Delay-and-Sum, shown in figure 4.7.b, is much wider than the PSF of t-CBF, shown in figure 4.7.d. Therefore, replacing Delay-and-Sum by t-CBF should allow for an increase in resolution, as well as weaker sidelobes.

In this chapter, we propose to investigate the use of t-CBF in conjunction with focalized transmit waves. A comparison with Delay-and-Sum is then drawn.

7.2.2 Imaging with focalized waves & a linear array

Imaging with a linear array is done by focusing at a fixed depth immediately *en-face* a sub-aperture of the probe. In general, the sub-aperture is half as large as the total aperture. To span the tissue, the sub-aperture is translated across the full aperture as shown in figure 7.1.a. Only the scatterers in the way of the focalized wave are excited by the transmit event, as shown in figure 7.1.b. A Delay-and-Sum reconstruction is then performed to reconstruct the part of the image that corresponds to the insonified region.

This acquisition scheme can be adapted to t-CBF. The focalization is simply built into the matrix G. Thus, we build a matrix G for each focal point, and apply t-CBF to the corresponding data. The result is an image of the tissue where most of the amplitude is reconstructed along the path of the focalized wave, as shown in figure 7.2.a, b and c. We reconstruct as many images as there are focal points, and eventually combine them together to compute the full image. The final reconstruction is thus carried out by selecting the row, or line, that is directly *en-face* the focal point. Figure 7.3.a shows the final reconstruction along with the Delay-and-Sum image (figure 7.3.b). The main difference between the two images is the side lobe levels. Looking at the deepest point scatterers, we see that their PSF is much narrower in the t-CBF reconstruction.

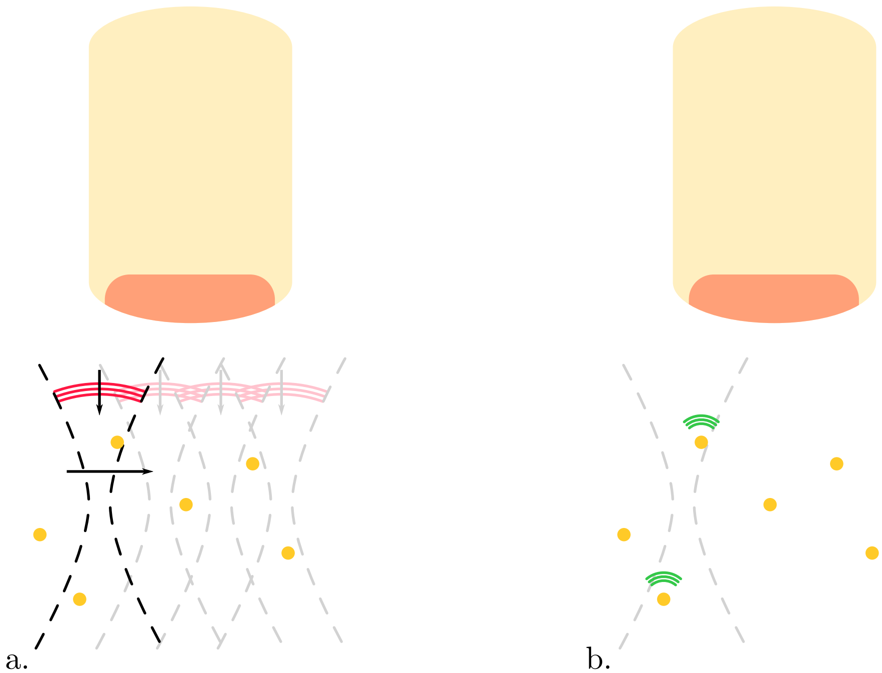

Figure 7.1: *Focalized imaging with a linear array:* a. *the medium is insonified by a translating sub-aperture in a direction orthogonal to the elements. The tissue is primarily insonified in the area delimited by the dashed lines.* b. *The focalization ensures that most of the echoes come from scatterers in the way of the beam, as opposed to anywhere else in the medium.*

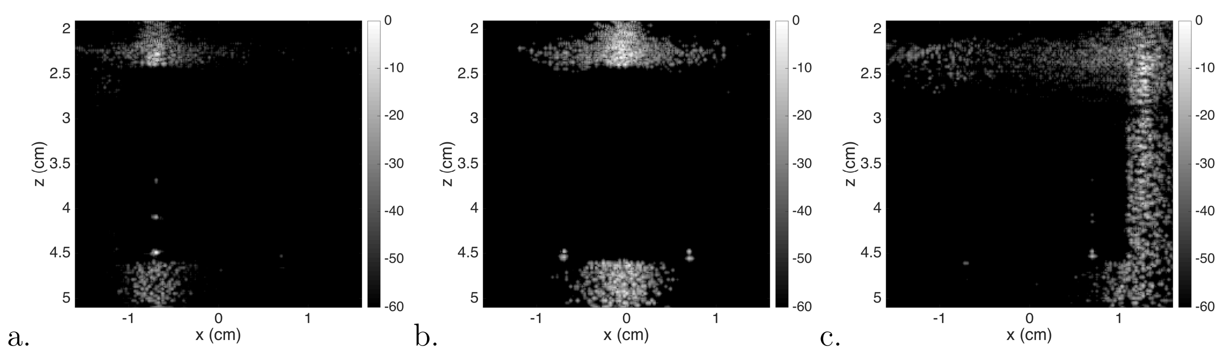

Figure 7.2: *Examples of t-CBF reconstructions from focalized data: the path of the focalized beam can clearly be seen, and the area reconstructed by the algorithm corresponds primarily to the beam path.*

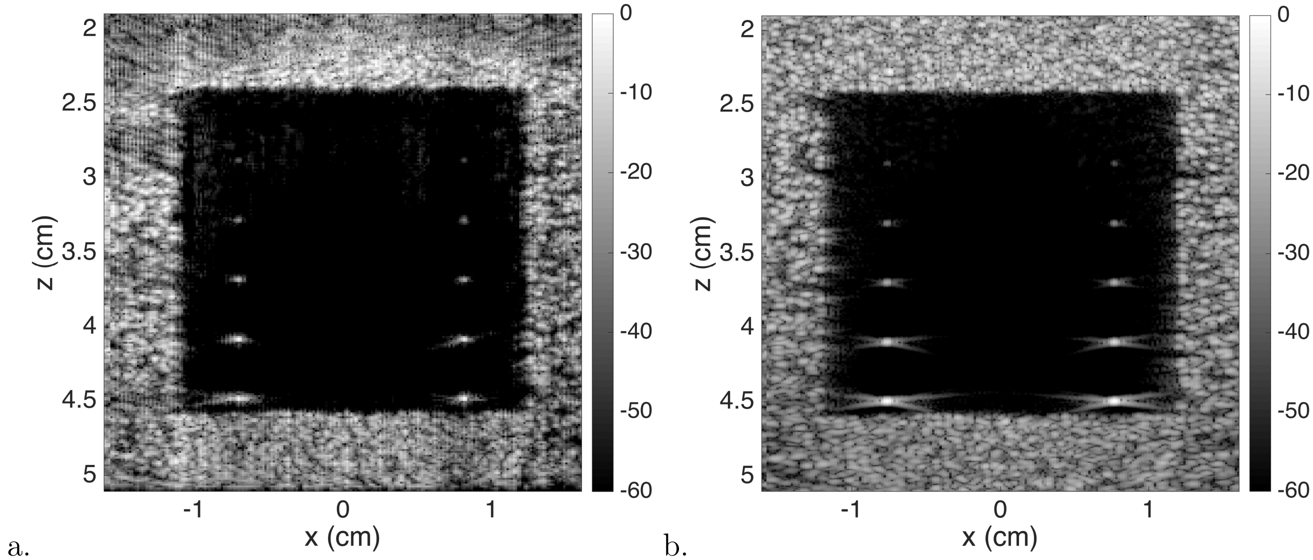

Figure 7.3: *Completed reconstruction:* a. *with t-CBF,* b. *with Delay-and-Sum. The t-CBF image has lower side lobes than the Delay-and-Sum image.*

7.2.3 Imaging with focalized waves & a phased array

Time-domain Compressive Beamforming can also be used in conjunction with a focalized phased array. In that case, the full aperture is used to create beams steered in different directions at constant focal length as shown in figure 7.4.a. Similarly to the case of the linear array, the medium is insonified primarily in the direction of the focalized beam, hence minimizing the potential echoes coming from other locations, as shown in figure 7.4.b.

The t-CBF reconstruction is carried out by computing one image per beam, as shown in figure 7.5.a, b, and c. Then the final image is obtained by selecting the lines along the focal directions and stitching them together. The images computed with 80 lines and 160 lines are shown in figures 7.6.a and b, respectively. As a reference, the Delay-and-Sum image computed with 80 lines is shown in figure 7.6.c. The resolution of the t-CBF image is better, with less distortions than the Delay-and-Sum image. In fact, the circular cysts display an oblong shape in the Delay-and-Sum image. They remain perfectly circular in the t-CBF images.

The 80 line t-CBF image seems to have less contrast in the cysts than the Delay-and-Sum image.

7.3 Coded excitation

Originally used in radars to increase the SNR [139], coded excitation for ultrasound imaging was investigated as early as 1979 [140, 141]. Since then, an extensive literature has been published on the subject. The coded excitation technique come from the observation that in ultrasound imaging, the axial resolution is limited by the duration of the pulse, with shorter pulses leading the best resolution. In other words, pulses of higher frequency and larger bandwidth produce better resolution. However, the attenuation of waves in the human body increases with the frequency of the pulse. To counteract this effect, higher amplitudes could be used. But higher amplitudes lead to side effects, such as tissue heating and damaging. In creasing the pulse duration prevents such side effects, compensates for the attenuation since the total energy being emitted increases, but degrades the resolution.

Coded excitation along with pulse compression provides an answer to the problem. More information can be found in references [142–146].

Time-domain Compressive Beamforming is compatible with coded excitation. This means that the transmit event can be made of several pulses. For example, we can imagine a transmit event composed of three plane waves steered in three different directions, as shown in figure 7.7.

7.4 Data compression by random matrices

In chapter 3, we saw that Compressive Sensing has the ability to recover signals from compressed measurements. In section 3.3.9, we described a few acquisition matrices that have the capability of compressing the signal. They are also fully compatible with the Compressive Sensing framework meaning that when used in a sensing scheme in conjunction with

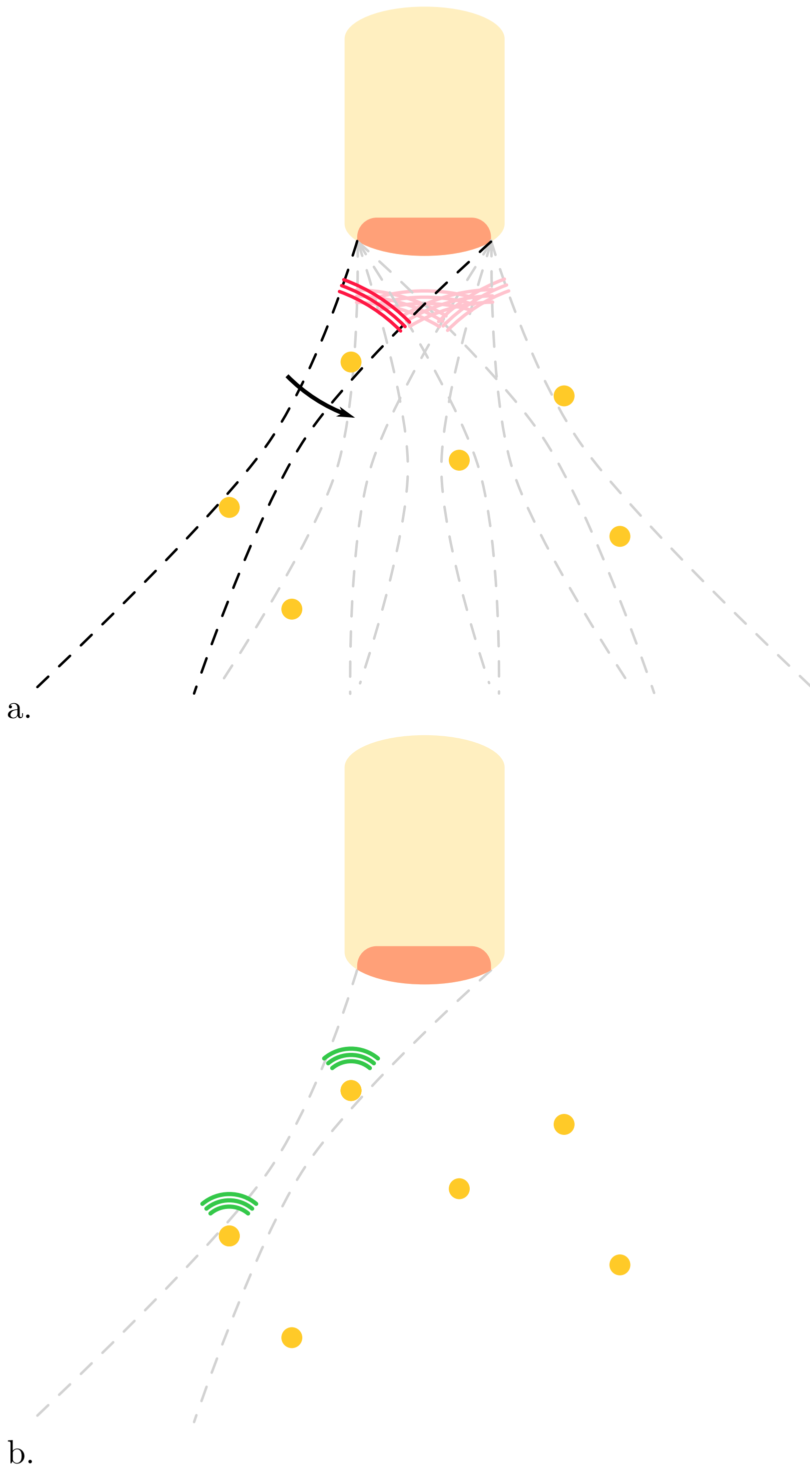

Figure 7.4: *Focalized imaging with a phased array:* a. *the medium is insonified by the full aperture, and the beam is steered in different directions at constant focal length. The tissue is primarily insonified in the area delimited by the dashed lines.* b. *The focalization ensures that most of the echoes come from scatterers in the way of the beam, as opposed to anywhere else in the medium.*

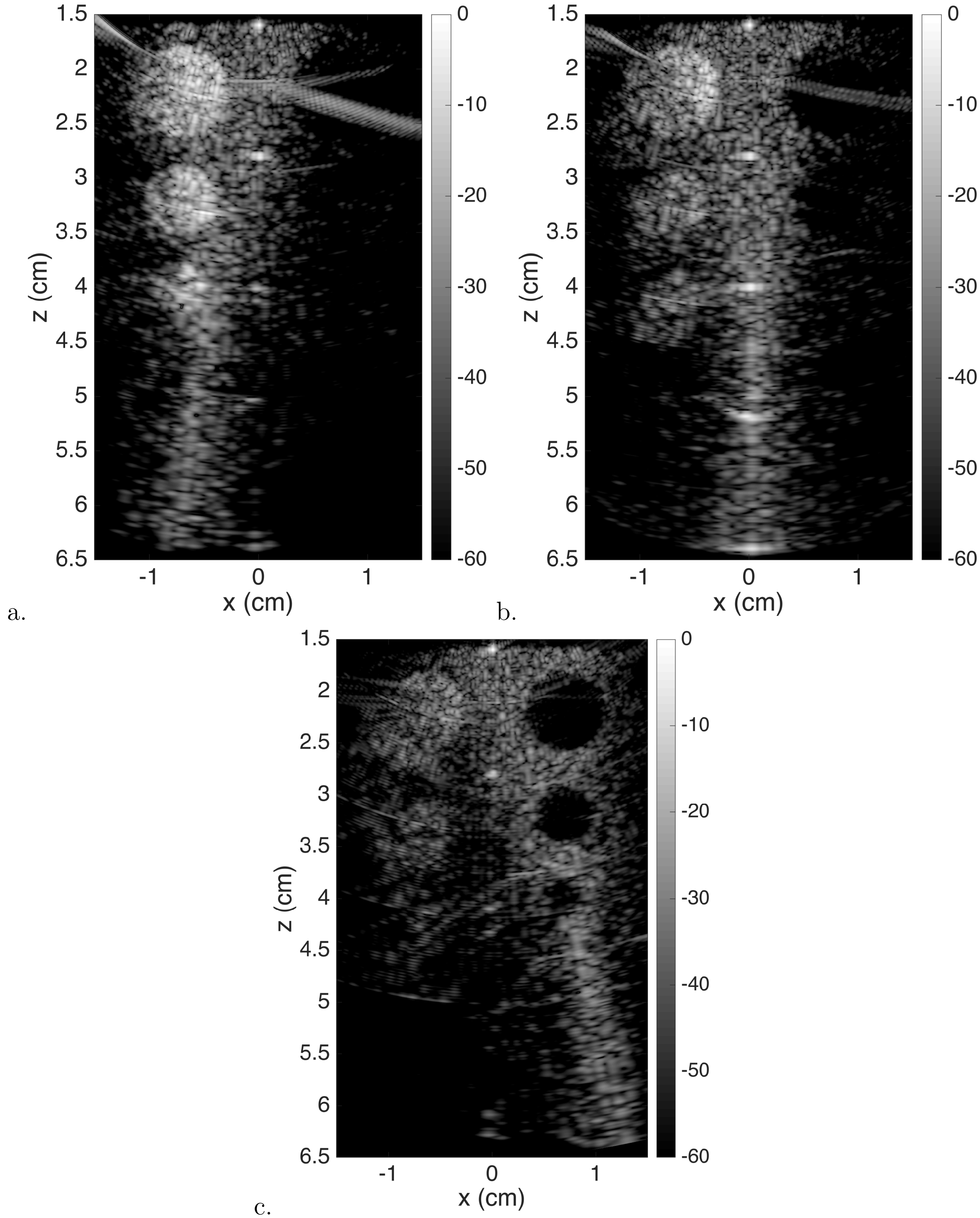

Figure 7.5: *Examples of t-CBF reconstructions from focalized data: the path of the focalized beam can clearly be seen, and the area reconstructed by the algorithm corresponds primarily to the beam path.*

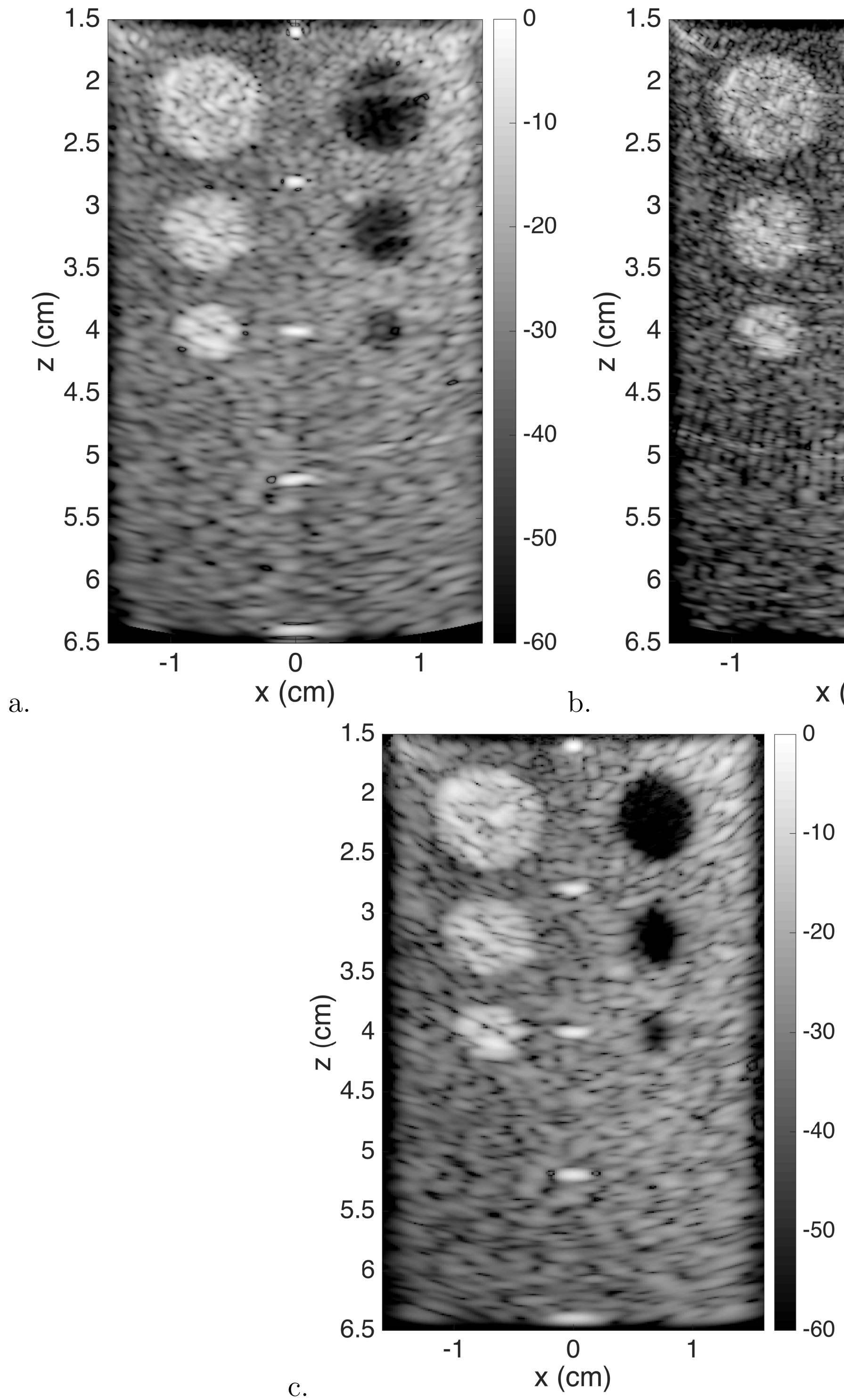

Figure 7.6: *Completed reconstruction:* a. *with t-CBF and* 80 *lines,* b. *with t-CBF and* 160 *lines,* c. *with Delay-and-Sum. The t-CBF images have better resolution than the Delay-and-Sum image, as well as less distortion. It seems the contrast in the cysts for the 80 line t-CBF image could be improved.*

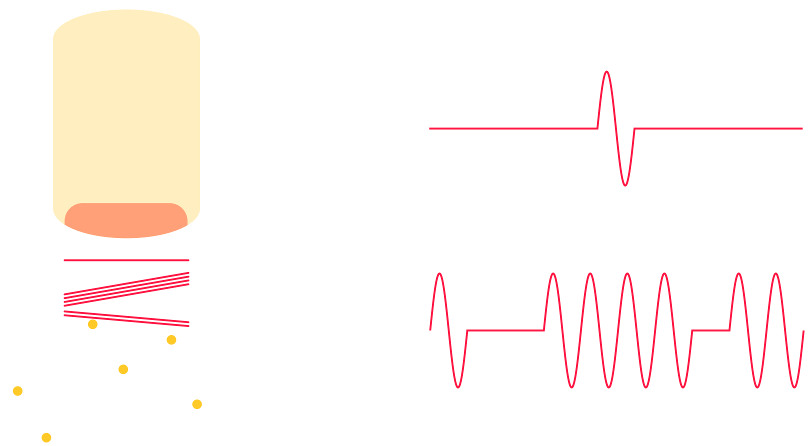

a. b.

Figure 7.7: *Coded excitation:* a. *Insonification with a transmit event made of 3 different ultrasonic pulses of different durations,* b. (top) *Typical ultrasonic impulse,* b. (bottom) *coded excitation.*

convex optimization they introduce no loss of information. In this section, we investigate how random projections can benefit t-CBF.

To take advantage of the data compression offered by Compressive Sensing further, we consider a random compression matrix K at first.

Definition 25. *The compression matrix is a matrix $K \in \mathcal{M}_{N_{comp},N_{data}}(\mathbb{R})$, where $N_{data} = N_t \times N_{el}$ is the number of samples in the data and $N_{comp} < N_{data}$ is the number of compressive acquisitions, such that the compressed data is obtained by:*

$$R_{comp} = KR \tag{7.1}$$

The compression matrix K needs to be taken into account in our minimization scheme.

Corollary 8. *The compression matrix K is incorporated to the model G by projecting the rows of G onto K:*

$$G_{comp} = KG \tag{7.2}$$

with $G_{comp} \in \mathcal{M}_{N_{comp} \times N_{img}}(\mathbb{C})$

The matrix K is built by selecting N_{data}^2 coefficients uniformly a random in $[0, 1]]$. K

is then orthogonalized using the GRAM-SCHMIDT process [147]. Finally, K is truncated to become a $N_{\text{comp}} \times N_{\text{data}}$ matrix.

The t-CBF reconstruction is carried out normally otherwise, that is to say we use SPGL1 [119] to solve the BPDN problem

$$\min_{\hat{I} \in \mathbb{R}^{\mathbb{N}_{\text{img}}}} \|\hat{I}\|_{l_1} \text{ such that } \|G_{\text{comp}}\hat{I} - R_{\text{comp}}\|_{l_2} \leqslant \epsilon \tag{7.3}$$

described in chapter 4.

Figures 7.8.a, b, c, and d show the results obtained with no compression, then 5%, 10%, and 20% respectively. There is no significant difference in image quality between the four reconstructions.

Figures 7.9.a, b, c, and d show the results obtained with 30% 40%, 60%, and 80% respectively. Figure 7.9.a is still comparable to figure 7.8 in terms of image quality. With a compression rate superior to 30% however, the image starts to degrade. The part of the image that is the most affected by the degradation is the part containing the cysts. The contrast tends to decrease as they fill with artifacts. The resolution of the point scatterers stays constant, and the bright lesions are not significantly affected by the compression.

The projections on random vectors could be replaced by the use of the noiselet transform. Noiselets were designed to be incoherent with the HAAR wavelets, and wavelets in general. Therefore, using them in place of the random matrix K would bring two advantages:

1. It would alleviate the need to generate a sizable random matrix K, since the noiselet transform can be computed efficiently in $\mathcal{O}(n \log n)$ operations.

2. It would increase the incoherence between the acquisition space and the reconstruction space.

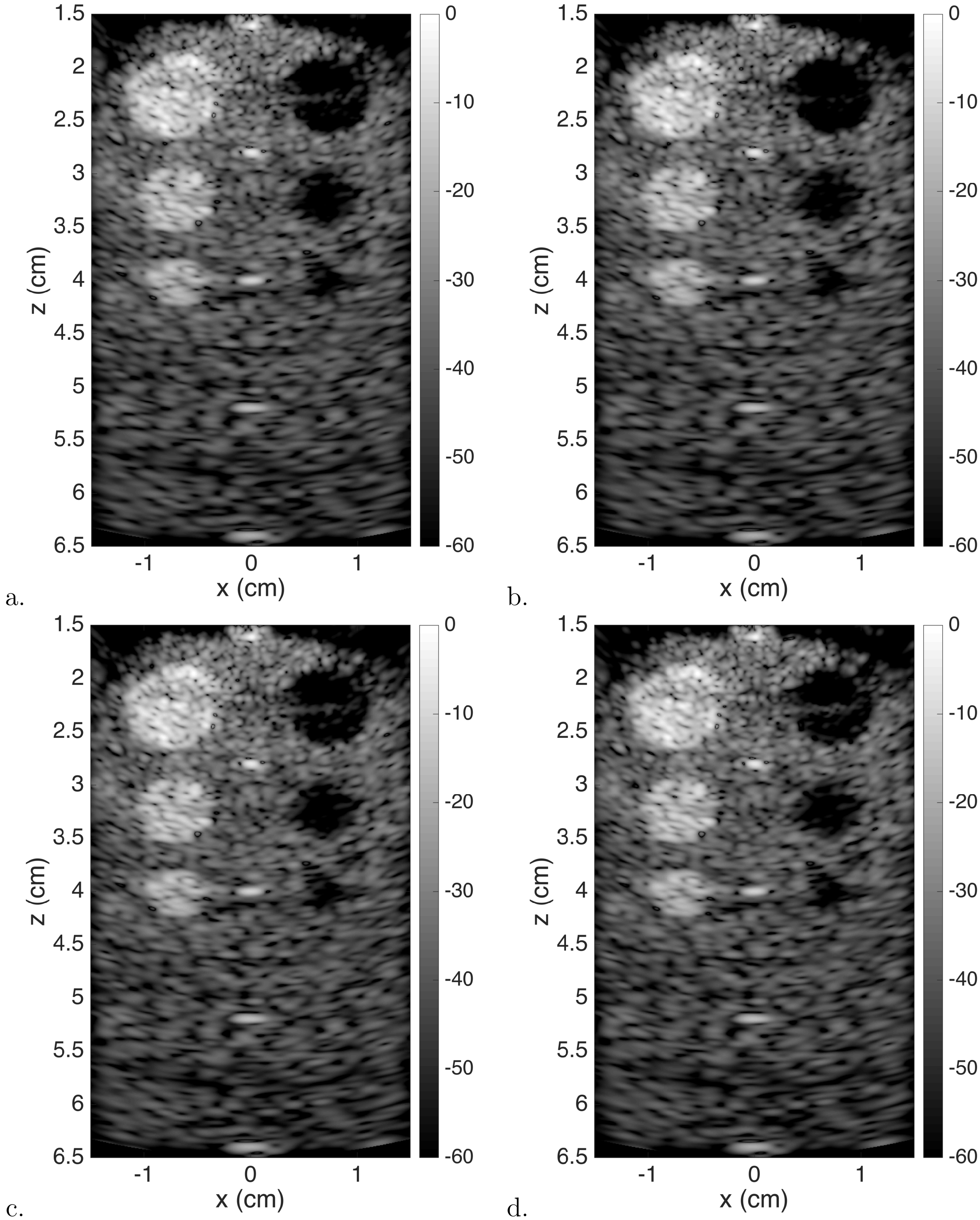

Figure 7.8: *Data compression and t-CBF reconstruction:* a. *Original reconstruction with no compression,* b. 5% *data compression,* c. 10% *data compression,* d. 20% *data compression.*

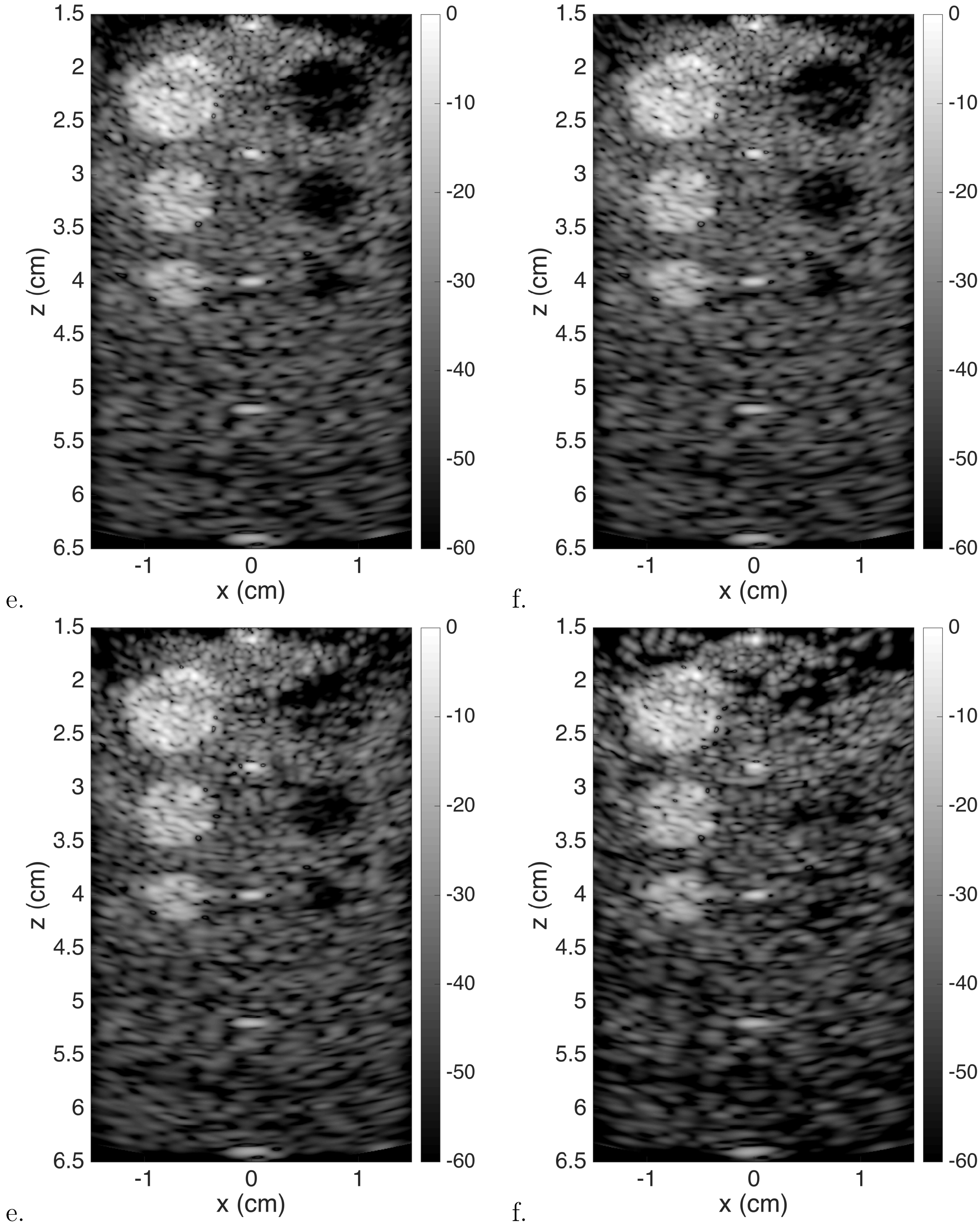

Figure 7.9: *Data compression and t-CBF reconstruction:* a. *30% data compression,* b. *40% data compression,* c. *60% data compression,* d. *80% data compression.*

7.5 Conclusion

This chapter was meant as a glance into the possible next steps for t-CBF. This powerful beamforming technique offers the advantage of being flexible and adaptable to many scenarios.

The applications mentioned in this chapter are some of the logical next steps in the improvement of t-CBF. Some of those have already been investigated and the preliminary results hereby presented are promising.

This work started as a mere observation that the theory of Compressive Sensing was extremely beneficial to MRI. It led to a logical question: could it be similarly beneficial to ultrasound imaging? While this work provided a framework and parts of an answer to that question, it is not isolated. Several ultrasound groups are presently working on this subject, using different approaches and ideas. The excitation around Compressive Sensing has led to hundreds of publications in ultrasound since its inception. The leading ultrasound conferences now have several presentations on the topic every year.

We believe that this work broke new ground in the field of ultrasound imaging. We hope that it will be further developed in the future, and that some of the next steps outlined in this chapter will be tried. Taking this work to the next level would also mean adapting it to 3D imaging. Currently the computational power required to achieve this goal has prevented us from doing so. It would be most interesting to implement this algorithm in the cloud where computational power is cheap and readily available. We believe that the compression capabilities of t-CBF would be a great asset in the development of cloud-beamforming.

We can hope that the continuing development in computer technology will enable the widespread use of computational methods for beamforming which have proven to be superior. Such evolution would certainly make the modality more affordable and accessible to developing countries all over the world.

Bibliography

[1] J. Curie and P. Curie, "Contractions et dilatations produites par des tensions électriques dans les cristaux hémièdres à faces inclinées," *Comptes-rendus de l'Académie des Sciences*, vol. 93, pp. 1137–1140, 1881.

[2] P. Langevin, "Sondage et détéction sous-marine par les ultrasons," *Bull. Assoc. Tech. Marit. Aeronaut.*, vol. 28, p. 407, 1924.

[3] K. T. Dussik, "Über die Möglichkeit, hochfrequente mechanische Schwingungen als diagnostisches Hilfsmittel zu verwerten," *Zeitschrift für die gesamte Neurologie und Psychiatrie*, vol. 174, no. 1, pp. 153–168, 1942.

[4] K. T. Dussik, "Weitere Ergebnisse der Ultraschalluntersuchung bei Gehirnerkrankungen," *Acta Neurochirurgica*, vol. 2, no. 3-4, pp. 379–401, 1952.

[5] H. T. Ballantine, "On the Use of Ultrasound for Tumor Detection," *The Journal of the Acoustical Society of America*, vol. 26, no. 4, p. 581, 1954.

[6] I. Donald, J. Macvicar, and T. Brown, "Investigation of abdominal masses by pulsed ultrasound," *The Lancet*, vol. 271, pp. 1188–1195, jun 1958.

[7] G. D. Ludwig and F. Ludwig, G.D. and Struthers, "Considerations underlying the use of ultrasound to detect gallstones and foreign bodies in tissue.," *Naval Medical Research Institute Reports*, vol. Project #0, no. Report No. 4, p. 23 p., 1949.

[8] E. Brunner, "How ultrasound system considerations influence front-end component choice," *Analog Dialogue*, vol. 36, no. 3, pp. 1–4, 2002.

[9] S.-C. Wooh and Y. Shi, "Optimum beam steering of linear phased arrays," *Wave motion*, vol. 29, no. 3, pp. 245–265, 1999.

[10] K. E. Thomenius, "Evolution of ultrasound beamformers," in *Ultrasonics Symposium, 1996. Proceedings., 1996 IEEE*, vol. 2, pp. 1615–1622, IEEE, 1996.

[11] N. Bom, C. Lancee, J. Honkoop, and P. Hugenholtz, "Ultrasonic viewer for cross-sectional analyses of moving cardiac structures.," *Biomedical engineering*, vol. 6, no. 11, p. 500, 1971.

[12] D. King, "Real-time cross-sectional ultrasonic imaging of the heart using a linear array multi-element transducer.," *Journal of clinical ultrasound: JCU*, vol. 1, no. 3, pp. 196–201, 1973.

[13] W. Anderson, J. Arnold, D. Clark, W. Davids, W. Hillard, W. Lehr, and L. Zitelli, "A new real-time phased array sector scanner for imaging the entire adult human heart," in *Ultrasound in medicine*, vol. 3, pp. 1547–1558, Plenum Publishing New York, 1977.

[14] O. Von Ramm and F. Thurstone, "Thaumascan: design considerations and performance characteristics," in *Ultrasound in medicine*, pp. 373–378, Springer, 1975.

[15] O. T. von Ramm and F. L. Thurstone, "Thaumascan: Improved image quality and clinical usefulness," in *Ultrasound in Medicine*, pp. 463–464, Springer, 1976.

[16] J. Somer, "Electronic sector scanning for ultrasonic diagnosis," *Ultrasonics*, vol. 6, no. 3, pp. 153–159, 1968.

[17] M. Eaton, R. Melen, and J. Meindl, "A flexible, real-time system for experimentation in phased-array ultrasound imaging," in *Acoustical Imaging*, pp. 55–67, Springer, 1980.

[18] J. N. Wright, "Resolution issues in medical ultrasound," in *IEEE 1985 Ultrasonics Symposium*, pp. 793–799, IEEE, 1985.

[19] H. E. Karrer, J. F. Dias, J. D. Larson, R. D. Pering, S. H. Maslak, and D. A. Wilson, "A phased array acoustic imaging system for medical use," in *Acoustical imaging*, pp. 47–63, Springer, 1982.

[20] R. Tancrell, J. Callerame, and D. Wilson, "Near-field, transient acoustic beam-forming with arrays," in *1978 Ultrasonics Symposium*, pp. 339–343, IEEE, 1978.

[21] J. Y. Lu and J. F. Greenleaf, "Nondiffracting x waves-exact solutions to free-space scalar wave equation and their finite aperture realizations," *IEEE Transactions on Ultrasonics, Ferroelectrics, and Frequency Control*, vol. 39, pp. 19–31, Jan 1992.

[22] S. Freeman, P. Li, and M. Odonnell, "Retrospective dynamic transmit focusing," *Ultrasonic Imaging*, vol. 17, no. 3, pp. 173 – 196, 1995.

[23] J. f. Synnevag, A. Austeng, and S. Holm, "Benefits of minimum-variance beamforming in medical ultrasound imaging," *IEEE Transactions on Ultrasonics, Ferroelectrics, and Frequency Control*, vol. 56, pp. 1868–1879, September 2009.

[24] J. Capon, "High-resolution frequency-wavenumber spectrum analysis," *Proceedings of the IEEE*, vol. 57, pp. 1408–1418, Aug 1969.

[25] R. G. Lorenz and S. P. Boyd, "Robust minimum variance beamforming," *IEEE Transactions on Signal Processing*, vol. 53, pp. 1684–1696, May 2005.

[26] S. D. Somasundaram, "Linearly constrained robust capon beamforming," *IEEE Transactions on Signal Processing*, vol. 60, pp. 5845–5856, Nov 2012.

[27] X. Song, J. Wang, and Y. Han, "Robust capon beamforming in the presence of mismatches," in *IEEE International Symposium on Communications and Information Technology, 2005. ISCIT 2005.*, vol. 1, pp. 140–143, Oct 2005.

[28] C. I. C. Nilsen and I. Hafizovic, "Beamspace adaptive beamforming for ultrasound imaging," *IEEE Transactions on Ultrasonics, Ferroelectrics, and Frequency Control*, vol. 56, pp. 2187–2197, October 2009.

[29] H. L. Van Trees, *Optimum Array Processing* in *Detection, estimation, and modulation theory*. John Wiley & Sons, 2004.

[30] A. C. Jensen and A. Austeng, "An approach to multibeam covariance matrices for adaptive beamforming in ultrasonography," *IEEE Transactions on Ultrasonics, Ferroelectrics, and Frequency Control*, vol. 59, pp. 1139–1148, June 2012.

[31] Philips HDI 5000 system: Comparison of Image Clarity Study, "Philips SonoCT real-time compound imaging versus conventional 2D ultrasound imaging," tech. rep., Koninklijke Philips Electronics N.V., 2003.

[32] T. S. Desser and R. B. Jeffrey, "Tissue harmonic imaging techniques: physical principles and clinical applications," in *Seminars in Ultrasound, CT and MRI*, vol. 22, pp. 1–10, Elsevier, 2001.

[33] K. C., J. MA., H. M., and H. M., "Conventional ultrasound and tissue harmonic imaging," *Radiology*, vol. 213P, no. 0033-8419, p. 397, 1999.

[34] N. Nakata, J. Harada, Y. Miyamoto, F. Tsujimoto, S. Tada, and K. Fukuda, "Three-dimensional tissue harmonic imaging and color doppler ultrasound of the abdomen," in *Radiology*, vol. 213, pp. 147–147, Radiological Soc. North Amer. 20th and Northampton Sts, Easton, PA 18042 USA, 1999.

[35] R. S. Shapiro, J. Wagreich, R. Parsons, A. Stancato-Pasik, H.-C. Yeh, and R. Lao, "Tissue harmonic imaging sonography: evaluation of image quality compared with conventional sonography.," *AJR. American journal of roentgenology*, vol. 171, no. 5, pp. 1203–1206, 1998.

[36] T. S. Desser, T. Jedrzejewicz, and C. Bradley, "Native tissue harmonic imaging: Basic principles and clinical applications.," *Ultrasound Quarterly*, vol. 16, no. 1, pp. 40–hyhen, 2000.

[37] L. Hann, A. Bach, L. Cramer, D. Siegel, H. Yoo, and R. Garcia, "Hepatic sonography: comparison of tissue harmonic and standard sonography techniques.," *AJR. American journal of roentgenology*, vol. 173, no. 1, pp. 201–206, 1999.

[38] H. S. Hong, J. K. Han, T. K. Kim, Y. H. Kim, J. S. Kim, J. H. Cha, and B. I. Choi, "Ultrasonographic evaluation of the gallbladder: comparison of fundamental, tissue harmonic, and pulse inversion harmonic imaging.," *Journal of ultrasound in medicine*, vol. 20, no. 1, pp. 35–41, 2001.

[39] H.-J. Jang, H. K. Lim, W. J. Lee, S. H. Kim, K. A. Kim, and E. Y. Kim, "Ultrasonographic evaluation of focal hepatic lesions: comparison of pulse inversion harmonic, tissue harmonic, and conventional imaging techniques.," *Journal of ultrasound in medicine*, vol. 19, no. 5, pp. 293–299, 2000.

[40] J. Kim, J. Han, T. Kim, and H. Hong, "Multifrequency tissue harmonic imaging versus conventional us in imaging focal hepatic lesions," *Radiology*, vol. 213P, no. 0033-8419, pp. 146–147, 1999.

[41] R. Kubale, G. Hetzel, W. Wilhelm, W. Kraemer, C. Bleck, and B. Kramann, "Characterisation of cysts and small structures: Value of ensemble tissue harmonic imaging," in *Radiology*, vol. 213, pp. 147–148, Radiological Soc. North Amer. 20th and Northampton Sts, Easton, PA 18042 USA, 1999.

[42] H. Lim, W. Lee, and J. Lee, "Image quality of gallbladder lesions: Comparison of conventional sonographic, conventional tissue harmonic, and pulse inversion tissue harmonic images," *Radiology*, vol. 213P, no. 0033-8419, p. 381, 1999.

[43] J. Pellerito, C. D'Agostino, B. Burke, D. Miller, and S. Boruchov, "Abdominal applications of non-contrast enhanced tissue harmonic imaging," in *Radiology*, vol. 209, pp. 341–342, Radiological Soc. North Amer. 20th and Northampton Sts, Easton, PA 18042 USA, 1998.

[44] J. Pellerito, C. D'Agostino, B. Burke, D. Miller, and S. Boruchov, "Value of tissue harmonic imaging in non-contrast enhanced renal ultrasonography," in *Radiology*, vol. 209, pp. 342–342, Radiological Soc. North Amer. 20th and Northampton Sts, Easton, PA 18042 USA, 1998.

[45] F. Tranquart, N. Grenier, V. Eder, and L. Pourcelot, "Clinical use of ultrasound tissue harmonic imaging," *Ultrasound in medicine & biology*, vol. 25, no. 6, pp. 889–894, 1999.

[46] T. S. Desser, R. B. Jeffrey, M. J. Lane, and P. W. Ralls, "Tissue harmonic imaging: utility in abdominal and pelvic sonography," *Journal of clinical ultrasound*, vol. 27, no. 3, pp. 135–142, 1999.

[47] T. Muir and E. Carstensen, "Prediction of nonlinear acoustic effects at biomedical frequencies and intensities," *Ultrasound in medicine & biology*, vol. 6, no. 4, pp. 345–357, 1980.

[48] E. Carstensen, W. Law, N. McKay, and T. Muir, "Demonstration of nonlinear acoustical effects at biomedical frequencies and intensities," *Ultrasound in medicine & biology*, vol. 6, no. 4, pp. 359–368, 1980.

[49] A. Baker, "Prediction of non-linear propagation in water due to diagnostic medical ultrasound equipment," *Physics in medicine and biology*, vol. 36, no. 11, p. 1457, 1991.

[50] B. Ward, A. Baker, and V. Humphrey, "Nonlinear propagation applied to the improvement of resolution in diagnostic medical ultrasound," *The Journal of the Acoustical Society of America*, vol. 101, no. 1, pp. 143–154, 1997.

[51] J. Bercoff, M. Tanter, and M. Fink, "Sonic boom in soft materials: The elastic cerenkov effect," *Applied Physics Letters*, vol. 84, no. 12, pp. 2202–2204, 2004.

[52] J. Bercoff, S. Chaffai, M. Tanter, L. Sandrin, S. Catheline, M. Fink, J. Gennisson, and M. Meunier, "In vivo breast tumor detection using transient elastography," *Ultrasound in medicine & biology*, vol. 29, no. 10, pp. 1387–1396, 2003.

[53] L. Sandrin, B. Fourquet, J.-M. Hasquenoph, S. Yon, C. Fournier, F. Mal, C. Christidis, M. Ziol, B. Poulet, F. Kazemi, M. Beaugrand, and R. Palau, "Transient elastography: a new noninvasive method for assessment of hepatic fibrosis," *Ultrasound in Medicine & Biology*, vol. 29, no. 12, pp. 1705 – 1713, 2003.

[54] L. Castéra, J. Vergniol, J. Foucher, B. L. Bail, E. Chanteloup, M. Haaser, M. Darriet, P. Couzigou, and V. de Lédinghen, "Prospective comparison of transient elastography, fibrotest, apri, and liver biopsy for the assessment of fibrosis in chronic hepatitis c," *Gastroenterology*, vol. 128, no. 2, pp. 343 – 350, 2005.

[55] M. Tanter, J. Bercoff, L. Sandrin, and M. Fink, "Ultrafast compound imaging for 2-d motion vector estimation: application to transient elastography," *IEEE Transactions on Ultrasonics, Ferroelectrics, and Frequency Control*, vol. 49, pp. 1363–1374, Oct 2002.

[56] J. Bercoff, M. Tanter, and M. Fink, "Supersonic shear imaging: a new technique for soft tissue elasticity mapping," *IEEE Transactions on Ultrasonics, Ferroelectrics, and Frequency Control*, vol. 51, pp. 396–409, April 2004.

[57] J. Bercoff, M. Tanter, S. Chaffai, and M. Fink, "Ultrafast imaging of beamformed shear waves induced by the acoustic radiation force. application to transient elastography," in *Proceedings of the 2002 IEEE Ultrasonics Symposium*, vol. 2, pp. 1899–1902, 2002.

[58] L. Sandrin, M. Tanter, S. Catheline, and M. Fink, "Shear modulus imaging with 2-d transient elastography," *IEEE Transactions on Ultrasonics, Ferroelectrics, and Frequency Control*, vol. 49, pp. 426–435, April 2002.

[59] L. Sandrin, M. Tanter, J. L. Gennisson, S. Catheline, and M. Fink, "Shear elasticity probe for soft tissues with 1-d transient elastography," *IEEE Transactions on Ultrasonics, Ferroelectrics, and Frequency Control*, vol. 49, pp. 436–446, April 2002.

[60] L. Sandrin, S. Catheline, M. Tanter, X. Hennequin, and M. Fink, "Time-resolved pulsed elastography with ultrafast ultrasonic imaging," *Ultrasonic imaging*, vol. 21, no. 4, pp. 259–272, 1999.

[61] L. Sandrin, S. Catheline, M. Tanter, and M. Fink, "2d transient elastography," in *Acoustical Imaging*, pp. 485–492, Springer, 2002.

[62] G. Montaldo, M. Tanter, J. Bercoff, N. Benech, and M. Fink, "Coherent plane-wave compounding for very high frame rate ultrasonography and transient elastography," *Ultrasonics, Ferroelectrics, and Frequency Control, IEEE Transactions on*, vol. 56, pp. 489–506, March 2009.

[63] D. Mozaffarian, E. J. Benjamin, A. S. Go, D. K. Arnett, M. J. Blaha, M. Cushman, S. R. Das, S. de Ferranti, J.-P. Després, H. J. Fullerton, V. J. Howard, M. D. Huffman, C. R. Isasi, M. C. Jiménez, S. E. Judd, B. M. Kissela, J. H. Lichtman, L. D. Lisabeth, S. Liu, R. H. Mackey, D. J. Magid, D. K. McGuire, E. R. Mohler, C. S. Moy, P. Muntner, M. E. Mussolino, K. Nasir, R. W. Neumar, G. Nichol, L. Palaniappan, D. K. Pandey, M. J. Reeves, C. J. Rodriguez, W. Rosamond, P. D. Sorlie, J. Stein, A. Towfighi, T. N. Turan, S. S. Virani, D. Woo, R. W. Yeh, and M. B. Turner, "Heart disease and stroke statistics—2016 update," *Circulation*, 2015.

[64] M. Pernot, K. Fujikura, S. D. Fung-Kee-Fung, and E. E. Konofagou, "Ecg-gated, mechanical and electromechanical wave imaging of cardiovascular tissues in vivo," *Ultrasound in Medicine & Biology*, vol. 33, no. 7, pp. 1075 – 1085, 2007.

[65] A. Costet, J. Provost, A. Gambhir, Y. Bobkov, P. Danilo, G. J. Boink, M. R. Rosen, and E. E. Konofagou, "Electromechanical wave imaging of biologically and electrically paced canine hearts in vivo," *Ultrasound in medicine & biology*, vol. 40, no. 1, pp. 177–187, 2014.

[66] M. Unser, "Sampling-50 years after shannon," *Proceedings of the IEEE*, vol. 88, pp. 569–587, April 2000.

[67] D. Gabor, "Theory of communication. part 1: The analysis of information," *Journal of the Institution of Electrical Engineers-Part III: Radio and Communication Engineering*, vol. 93, no. 26, pp. 429–441, 1946.

[68] W. Heisenberg, "Über den anschaulichen inhalt der quantentheoretischen kinematik und mechanik," *Zeitschrift für Physik*, vol. 43, no. 3-4, pp. 172–198, 1927.

[69] A. Grossmann and J. Morlet, "Decomposition of hardy functions into square integrable wavelets of constant shape," *SIAM journal on mathematical analysis*, vol. 15, no. 4, pp. 723–736, 1984.

[70] I. Daubechies *et al.*, *Ten lectures on wavelets*, vol. 61. SIAM, 1992.

[71] A. Haar, "Zur theorie der orthogonalen funktionensysteme," *Mathematische Annalen*, vol. 69, no. 3, pp. 331–371, 1910.

[72] D. Taubman and M. Marcellin, *JPEG2000 Image Compression Fundamentals, Standards and Practice: Image Compression Fundamentals, Standards and Practice*, vol. 642. Springer Science & Business Media, 2012.

[73] R. R. Coifman and M. V. Wickerhauser, "Entropy-based algorithms for best basis selection," *IEEE Transactions on Information Theory*, vol. 38, pp. 713–718, March 1992.

[74] E. Candes, L. Demanet, D. Donoho, and L. Ying, "Fast discrete curvelet transforms," *Multiscale Modeling & Simulation*, vol. 5, no. 3, pp. 861–899, 2006.

[75] S. Mann and S. Haykin, "The chirplet transform: A generalization of gabor's logon transform," in *Vision Interface*, vol. 91, pp. 205–212, 1991.

[76] D. L. Donoho, "Fast edgelet transform and applications," *Manuscript, September*, 1998.

[77] D. L. Donoho *et al.*, "Wedgelets: Nearly minimax estimation of edges," *The Annals of Statistics*, vol. 27, no. 3, pp. 859–897, 1999.

[78] M. Aharon, M. Elad, and A. Bruckstein, "K-svd: An algorithm for designing overcomplete dictionaries for sparse representation," *Signal Processing, IEEE Transactions on*, vol. 54, no. 11, pp. 4311–4322, 2006.

[79] C. Shannon, "Communication in the presence of noise," *Proceedings of the IEEE*, vol. 86, pp. 447–457, Feb 1998.

[80] M. Lustig, D. Donoho, and J. M. Pauly, "Sparse MRI: The application of compressed sensing for rapid MR imaging," *Magnetic resonance in medicine : official journal of the Society of Magnetic Resonance in Medicine / Society of Magnetic Resonance in Medicine*, vol. 58, pp. 1182–95, dec 2007.

[81] G. A. Wright, "Magnetic resonance imaging," *IEEE Signal Processing Magazine*, vol. 14, pp. 56–66, Jan 1997.

[82] E. J. Candès, J. Romberg, and T. Tao, "Robust uncertainty principles: Exact signal reconstruction from highly incomplete frequency information," *Information Theory, IEEE Transactions on*, vol. 52, no. 2, pp. 489–509, 2006.

[83] E. J. Candès, "Mathematics of sparsity (and a few other things)," in *Proceedings of the International Congress of Mathematicians, Seoul, South Korea*, vol. 123, Citeseer, 2014.

[84] K. Scheffler and J. Hennig, "Reduced circular field-of-view imaging," *Magnetic Resonance in Medicine*, vol. 40, no. 3, pp. 474–480, 1998.

[85] C. H. Meyer, B. S. Hu, D. G. Nishimura, and A. Macovski, "Fast spiral coronary artery imaging," *Magnetic Resonance in Medicine*, vol. 28, no. 2, pp. 202–213, 1992.

[86] J. I. Jackson, C. H. Meyer, D. G. Nishimura, and A. Macovski, "Selection of a convolution function for fourier inversion using gridding [computerised tomography application]," *IEEE Transactions on Medical Imaging*, vol. 10, pp. 473–478, Sep 1991.

[87] M. Rabbani and R. Joshi, "An overview of the jpeg 2000 still image compression standard," *Signal processing: Image communication*, vol. 17, no. 1, pp. 3–48, 2002.

[88] E. J. Candes and T. Tao, "Near-Optimal Signal Recovery From Random Projections: Universal Encoding Strategies?," *IEEE Transactions on Information Theory*, vol. 52, pp. 5406–5425, dec 2006.

[89] D. Donoho, "Compressed sensing," *IEEE Transactions on Information Theory*, vol. 52, pp. 1289–1306, apr 2006.

[90] J. Romberg, "Imaging via compressive sampling," *Signal Processing Magazine, IEEE*, no. March 2008, pp. 14–20, 2008.

[91] E. J. Candès and M. B. Wakin, "An introduction to compressive sampling," *Signal Processing Magazine, IEEE*, vol. 25, no. 2, pp. 21–30, 2008.

[92] E. Candes and J. Romberg, "Sparsity and incoherence in compressive sampling," *Inverse problems*, vol. 23, no. 3, p. 969, 2007.

[93] E. J. Candes and T. Tao, "Decoding by linear programming," *IEEE transactions on information theory*, vol. 51, no. 12, pp. 4203–4215, 2005.

[94] E. Candès, "Lectures on compressive sampling and frontiers in signal processing," *The Institute for Mathematics and its Applications*, pp. 2006–2007, 2007.

[95] E. J. Candes, J. K. Romberg, and T. Tao, "Stable signal recovery from incomplete and inaccurate measurements," *Communications on pure and applied mathematics*, vol. 59, no. 8, pp. 1207–1223, 2006.

[96] A. Cohen, W. Dahmen, and R. DeVore, "Compressed sensing and best k-term approximation," *Journal of the American mathematical society*, vol. 22, no. 1, pp. 211–231, 2009.

[97] F. Santosa and W. W. Symes, "Linear inversion of band-limited reflection seismograms," *SIAM Journal on Scientific and Statistical Computing*, vol. 7, no. 4, pp. 1307–1330, 1986.

[98] D. Donoho, Y. Tsaig, I. Drori, and J. Starck, "Sparse solution of underdetermined linear equations by stagewise orthogonal matching pursuit 2006," *Preprint*, 2006.

[99] E. J. Candès, "Compressive sampling," in *Proceedings of the International Congress of Mathematicians: Madrid, August 22-30, 2006: invited lectures*, pp. 1433–1452, 2006.

[100] S. Chen and D. Donoho, "Basis pursuit," in *Signals, Systems and Computers, 1994. 1994 Conference Record of the Twenty-Eighth Asilomar Conference on*, vol. 1, pp. 41–44, IEEE, 1994.

[101] R. G. Baraniuk, "Compressive sensing," *IEEE signal processing magazine*, vol. 24, no. 4, 2007.

[102] M. A. Davenport, M. F. Duarte, Y. C. Eldar, and G. Kutyniok, "Introduction to compressed sensing," *Preprint*, vol. 93, 2011.

[103] J. Romberg, "Imaging via compressive sampling [introduction to compressive sampling and recovery via convex programming]," *IEEE Signal Processing Magazine*, vol. 25, no. 2, pp. 14–20, 2008.

[104] J. Hadamard, "Sur les problèmes aux dérivées partielles et leur signification physique," *Princeton university bulletin*, vol. 13, no. 49-52, p. 28, 1902.

[105] J. Hadamard, *Lectures on Cauchy's problem in linear partial differential equations.* New York : Yale University Press ; London : H. Milford, Oxford University Press, 1923.

[106] V. J. Katz, "The history of stokes' theorem," *Mathematics Magazine*, vol. 52, no. 3, pp. 146–156, 1979.

[107] L. D. Landau and E. M. Lifshitz, *Course of theoretical physics.* Pergamon Press, 1965.

[108] J. le Rond DAlembert, "Recherches sur la courbe que forme une corde tendue mise en vibrations," *Histoire de lAcadémie Royale des Sciences et Belles Lettres (Année 1747)*, vol. 3, pp. 214–249.

[109] I. Newton, *Philosophiæ naturalis principia mathematica.* S. Pepys, *Reg. Soc.* Præses, 1686.

[110] A. D. Pierce *et al.*, *Acoustics: an introduction to its physical principles and applications.* McGraw-Hill New York, 1981.

[111] K. Knopp, "The Residue Theorem," in *Theory of functions*, vol. 1, ch. 33, Courier Corporation, 1996.

[112] J. Y. Lu, H. Zou, and J. F. Greenleaf, "Biomedical ultrasound beam forming," *Ultrasound in Medicine and Biology*, vol. 20, no. 5, pp. 403–428, 1994.

[113] M. Tanter and M. Fink, "Ultrafast imaging in biomedical ultrasound," *Ultrasonics, Ferroelectrics and Frequency Control, IEEE Transactions on*, vol. 61, no. 1, pp. 102–119, 2014.

[114] J.-Y. Lu and J. Greenleaf, "Pulse-echo imaging using a nondiffracting beam transducer," *Ultrasound in Medicine & Biology*, vol. 17, no. 3, pp. 265 – 281, 1991.

[115] M. F. Schiffner and G. Schmitz, "Fast pulse-echo ultrasound imaging employing compressive sensing," in *Ultrasonics Symposium (IUS), 2011 IEEE International*, pp. 688–691, IEEE, 2011.

[116] D. Friboulet, H. Liebgott, and R. Prost, "Compressive sensing for raw rf signals reconstruction in ultrasound," in *Ultrasonics Symposium (IUS), 2010 IEEE*, pp. 367–370, IEEE, 2010.

[117] M. Mishali, Y. C. Eldar, and A. J. Elron, "Xampling: Signal acquisition and processing in union of subspaces," *Signal Processing, IEEE Transactions on*, vol. 59, no. 10, pp. 4719–4734, 2011.

[118] B. Angelsen, *Ultrasound Imaging: Waves, Signals, and Signal Processing.* Emantec, 2000.

[119] E. Van Den Berg and M. Friedlander, "Spgl1: A solver for large-scale sparse reconstruction," *Online: http://www. cs. ubc. ca/labs/scl/spgl1*, 2007.

[120] E. Van den Berg and M. P. Friedlander, “Sparse optimization with least-squares constraints,” *SIAM Journal on Optimization*, vol. 21, no. 4, pp. 1201–1229, 2011.

[121] E. Van Den Berg and M. P. Friedlander, “Probing the pareto frontier for basis pursuit solutions,” *SIAM Journal on Scientific Computing*, vol. 31, no. 2, pp. 890–912, 2008.

[122] E. Van Den Berg and M. P. Friedlander, “Theoretical and empirical results for recovery from multiple measurements,” *IEEE Transactions on Information Theory*, vol. 56, no. 5, pp. 2516–2527, 2010.

[123] S. F. Cotter, B. D. Rao, K. Engan, and K. Kreutz-Delgado, “Sparse solutions to linear inverse problems with multiple measurement vectors,” *IEEE Transactions on Signal Processing*, vol. 53, no. 7, pp. 2477–2488, 2005.

[124] E. van den Berg, M. Schmidt, M. P. Friedlander, and K. Murphy, “Group sparsity via linear-time projection,” *Dept. Comput. Sci., Univ. British Columbia, Vancouver, BC, Canada*, 2008.

[125] S. X. Pan and A. Kak, “A computational study of reconstruction algorithms for diffraction tomography: Interpolation versus filtered backpropagation,” *Acoustics, Speech and Signal Processing, IEEE Transactions on*, vol. 31, pp. 1262–1275, Oct 1983.

[126] C. Dorme and M. Fink, “Focusing in transmit–receive mode through inhomogeneous media: The time reversal matched filter approach,” *The Journal of the Acoustical Society of America*, vol. 98, no. 2, pp. 1155–1162, 1995.

[127] J. A. Jensen, “Simulation of advanced ultrasound systems using field ii,” in *Biomedical Imaging: Nano to Macro, 2004. IEEE International Symposium on*, pp. 636–639, IEEE, 2004.

[128] J. Goodman, *Introduction to Fourier optics.* McGraw-hill, 2008.

[129] C. Wachinger, T. Klein, and N. Navab, “The 2D analytic signal for envelope detection and feature extraction on ultrasound images,” *Medical Image Analysis*, vol. 16, no. 6, pp. 1073–1084, 2012.

[130] J. L. R. d’Alembert, *Essai d’une nouvelle théorie de la résistance des fluides.* Chez David l’aîné, 1752.

[131] L. Euler, “Ulterior disquisitio de formulis integralibus imaginariis,” *Nova Acta Academiae Scientarum Imperialis Petropolitinae*, vol. 10, pp. 3–19, (1777) 1797.

[132] A. L. B. Cauchy, *Mémoire sur les intégrales définies, lu à l’Institut le 22 août 1814, remis au secrétariat pour être imprimé, le 14 septembre 1825.* 1827.

[133] R. Bracewell, *The Fourier Transform and Its Applications.* Electrical engineering series, McGraw Hill, 2000.

[134] B. Usevitch, “A tutorial on modern lossy wavelet image compression: foundations of jpeg 2000,” *Signal Processing Magazine, IEEE*, vol. 18, pp. 22–35, Sep 2001.

[135] D. Wei, *Coiflet-type wavelets: theory, design, and applications*. 1998.

[136] H. Geyer, G. Caracciolo, H. Abe, S. Wilansky, S. Carerj, F. Gentile, H.-J. Nesser, B. Khandheria, J. Narula, and P. P. Sengupta, "Assessment of myocardial mechanics using speckle tracking echocardiography: Fundamentals and clinical applications," *Journal of the American Society of Echocardiography*, vol. 23, no. 4, pp. 351 – 369, 2010.

[137] J.-L. Robert and M. Fink, "The time-reversal operator with virtual transducers: Application to far-field aberration correction," *The Journal of the Acoustical Society of America*, vol. 124, no. 6, pp. 3659–3668, 2008.

[138] J. A. Jensen, S. I. Nikolov, K. L. Gammelmark, and M. H. Pedersen, "Synthetic aperture ultrasound imaging.," *Ultrasonics*, vol. 44 Suppl 1, pp. e5–e15, dec 2006.

[139] I. GENESIS, "The early history of pulse co m press ion radar," *IEEE transactions on aerospace and electronic systems*, vol. 24, no. 6, p. 825, 1988.

[140] Y. Takeuchi, "An investigation of a spread energy method for medical ultrasound systems: Part one: Theory and investigation," *Ultrasonics*, vol. 17, no. 4, pp. 175–182, 1979.

[141] Y. Takeuchi, "An investigation of a spread energy method for medical ultrasound systems: Part two: proposed system and possible problems," *Ultrasonics*, vol. 17, no. 5, pp. 219–224, 1979.

[142] T. Misaridis and J. Jensen, "Use of modulated excitation signals in medical ultrasound. Part I: basic concepts and expected benefits," *IEEE Transactions on Ultrasonics, Ferroelectrics and Frequency Control*, vol. 52, pp. 177–191, feb 2005.

[143] T. Misaridis and J. A. Jensen, "Use of modulated excitation signals in medical ultrasound. Part II: Design and performance for medical imaging applications," *IEEE Transactions on Ultrasonics, Ferroelectrics, and Frequency Control*, vol. 52, no. 2, pp. 192–206, 2005.

[144] T. Misaridis and J. Jensen, "Use of modulated excitation signals in medical ultrasound. Part III: high frame rate imaging," *IEEE Transactions on Ultrasonics, Ferroelectrics and Frequency Control*, vol. 52, pp. 208–219, feb 2005.

[145] B. Haider, P. A. Lewin, and K. E. Thomenius, "Pulse elongation and deconvolution filtering for medical ultrasonic imaging," *IEEE transactions on ultrasonics, ferroelectrics, and frequency control*, vol. 45, no. 1, pp. 98–113, 1998.

[146] M. L. Oelze, "Bandwidth and resolution enhancement through pulse compression," *IEEE transactions on ultrasonics, ferroelectrics, and frequency control*, vol. 54, no. 4, pp. 768–781, 2007.

[147] G. B. Arfken, H. J. Weber, and F. E. Harris, "Gram-Schmidt Orthogonalization," in *Mathematical methods for physicists: a comprehensive guide*, ch. 5.2, Academic press, 7 ed., 2011.